Pyrrolidinium Ionic Liquid-based Polymer Electrolytes: Tailoring 3D Printability, Thermal and Electrochemical Properties

Dissertation

zur Erlangung des Doktorgrades der Naturwissenschaften

(Dr. rer. nat.)

der

Naturwissenschaftlichen Fakultät II

Chemie, Physik und Mathematik

der Martin-Luther-Universität

Halle-Wittenberg

Vorgelegt von

Herrn Zviadi Katcharava

Gutachter

1. Prof. Dr. Wolfgang H. Binder

2. Prof. Dr. Liberata Guadagno

Verteidigt am: 13.06.2024

Acknowledgment

I would like to express my sincere gratitude to all those who supported me through the PhD journey. First and foremost, I would like to thank Prof. Dr. Wolfgang H. Binder for providing me with an invaluable opportunity to work under his supervision. I am sincerely grateful for the chance to learn under his guidance.

A special acknowledgment goes to Dr. Anja Marinow for her exceptional support and encouragement. I am truly grateful for all the constructive feedback she consistently provided, and her belief in my abilities has been a motivational force throughout the entire journey. In moments of uncertainty, she was always providing both professional advice and personal support. I sincerely appreciate the time she dedicated to helping me navigate through challenges.

I would like to express my gratitude to Ms. Anke Hassi, who was always ready to answer my questions and assist with any organizational matters. Handling all the bureaucracy was made easier with her support. I am also thankful to Ms. Susanne Tanner and Ms. Julia Grossert for providing all necessary chemicals and laboratory equipment, as well as conducting numerous measurements.

Special thanks to Dr. Rajesh Bhandary for conducting electrochemical measurements, actively engaging in insightful discussions, and providing valuable suggestions.

I am deeply grateful to all the members of the group. The friendly and supportive atmosphere made overcoming challenges truly enjoyable. Thanks to each one of you!

I appreciate Prof. Dr. Mario Beiner for allowing us to use Broadband Dielectric Spectroscopy and conduct necessary measurements. Thanks to Prof. Dr. Michael Bron for permitting LSV measurements.

I extend my thanks to all employees of the analytical department of the Institute of Organic Chemistry for conducting NMR analysis.

Finally, my sincere gratitude extends to my family and friends, who constantly believed in me and provided unwavering emotional support.

Abstract

Lithium-ion batteries, widely used in portable electronics and automotive industry, represent a key technology in the transition to renewable energies and moving towards a carbon-negative future. The current technologies require to improve the safety of batteries for users and enable higher energy density for increased efficiency. Among various possibilities, replacing the flammable organic electrolyte is particularly promising. Polymer electrolytes and ionic liquids (ILs) emerge as auspicious alternatives for lithium-ion batteries. This work aims to harness the strengths of both materials, combining their advantageous properties to enable advanced functionalities such as reprocessing, self-healing, and achieving the required properties for additive manufacturing of batteries. The here used pyrrolidinium-based ionic liquids, known for their superior electrochemical and thermal stability, were integrated into the electrolyte materials using different approaches.

Vitrimeric, dynamic properties were successfully achieved in poly(ionic liquid)s *via* copolymerization and consequent crosslinking with boric acid. Broadband dielectric spectroscopy was employed to investigate the material's conductivity and determine the optimal lithium salt content. Efficient self-healing capabilities were demonstrated, and the material exhibited required rheological properties for creating complex structures *via* fused deposition modeling, holding the potential for future advancements of battery manufacturing. The vitrimeric electrolytes displayed efficient reprocessability, thus addressing environmental sustainability and material circularity.

Nanocomposite-based electrolytes were designed with self-healing poly(ethylene oxide) and nanoparticles. Self-healing was achieved *via* end group modification, facilitating supramolecular interactions. Extensive rheological measurements were conducted to attain the most advanced composition for 3D printing. Surface modification of particles played a crucial role in enhancing the mechanical properties and conductivity, while simultaneously enabling 3D printing.

Fluorination significantly improves the electrochemical performance of electrolytes. In this work, properties of fluorinated dicationic ILs were investigated, examining their conductivities, viscosities, and agglomerate formations. Optimization involved adjusting salt concentration, type of the counterion and the linker between two cations. In the following, the IL was incorporated into a more complex electrolyte type, known as gel polymer electrolyte.

To engineer gel polymer electrolytes with improved mechanical and electrochemical properties, an *in situ* preparation process was used to introduce supramolecular networks in combination with covalent crosslinking. The integration of this dual network resulted in superior mechanical properties, allowing the incorporation of high liquid phase volumes into the polymer matrix. The optimization involved variations in chemical structure of components, ratios, and synthesis techniques. The gels were fine-tuned to achieve the best electrochemical performances without compromising mechanical properties.

Kurzdarstellung

Lithium-Ionen-Batterien sind bereits in der Automobilindustrie und im Bereich der tragbaren Elektronik weit verbreitet. Insbesondere stellen sie eine Schlüsseltechnologie für den Übergang zu erneuerbaren Energien und einer kohlenstoffnegativen Zukunft dar. Die bereits vorhandenen Technologien müssen allerdings verbessert werden, um Batterien für Nutzer sicherer zu gestalten und eine höhere Energiedichte für eine bessere Effizienz zu ermöglichen. Unter den verschiedenen Möglichkeiten ist der Austausch von brennbaren organischen Elektrolyten besonders vielversprechend. Polymerelektrolyte und ionische Flüssigkeiten erscheinen hier als aussichtsreiche Alternativen für die bisher vorrangig genutzten organischen Carbonate.

Ziel dieser Arbeit ist es, die Stärken beider Materialien zu nutzen und ihre vorteilhaften Eigenschaften zu kombinieren, um Rezyklierung und Selbstheilung zu ermöglichen. Gleichzeitig können die erforderlichen Parameter für die additive Herstellung von Batterien optimiert werden. Die in dieser Arbeit genutzten ionischen Flüssigkeiten auf Basis von Pyrrolidiniumsalzen, die für ihre überlegene elektrochemische und thermische Stabilität bekannt sind, wurden mit verschiedenen Ansätzen in das Elektrolytmaterial integriert.

Durch Copolymerisation und anschließende Vernetzung mit Borsäure wurden vitrimerdynamische Strukturen in den polymeren ionischen Flüssigkeiten erreicht. Mittels dielektrischer Breitbandspektroskopie wurde die Leitfähigkeit des Materials untersucht und der optimale Lithiumsalzgehalt bestimmt. Es wurden effiziente, durch das vitrimere Verhalten erzeugte Selbstheilungsfähigkeiten gezeigt. Des Weiteren verfügen die Materialien über die erforderlichen rheologischen Eigenschaften für kontrollierte Extrusion und 3D-Druck mittels Fused Deposition Modeling, was Potenzial für künftige Fortschritte in der Batterieherstellung birgt. Der vitrimere Elektrolyt lässt sich anschließend wiederaufbereiten, was der ökologischen Nachhaltigkeit und Kreislauffähigkeit des Materials zugutekommt.

Nanokomposite, eine weitere vielversprechende Elektrolytart, bestehend aus selbstheilendem Polyethylenoxid und Nanopartikeln wurden hergestellt und untersucht. Die Selbstheilung wurde durch supramolekular wechselwirkende Gruppen ermöglicht, welche durch Modifizierung der Endgruppen an das Polymer angebracht wurden. Durch umfangreiche rheologische Messungen wurde die optimale Zusammensetzung für Extrusion und 3D-Druck gefunden. Die Oberflächenmodifizierung der Partikel spielte eine entscheidende Rolle bei der

Verbesserung der mechanischen Eigenschaften und der Leitfähigkeit und ermöglichte eine Verarbeitung mittels 3D-Druck.

Fluorierung verbessert die elektrochemische Leistung von Elektrolyten erheblich. In dieser Arbeit wurden die Eigenschaften von fluorierten, dikationischen, ionischen Flüssigkeiten in Hinsicht auf Leitfähigkeiten, Viskositäten und Agglomeratbildungen untersucht. Zur Optimierung wurde die Salzkonzentration, die Art des Gegenions und der Linker zwischen zwei Kationen angepasst. Die so optimierte ionische Flüssigkeit wurde im Anschluss als flüssige Phase in komplexeren Gel-Polymer-Elektrolyten eingesetzt.

Um Gel-Polymer-Elektrolyte mit verbesserten mechanischen und elektrochemischen Eigenschaften zu entwickeln, wurde ein *in situ* Präparationsverfahren verwendet, um supramolekulare Netzwerke zusammen mit kovalenten Vernetzungen zu kombinieren. Die Integration dieses dualen Netzwerks führte zu verbesserten mechanischen Eigenschaften und ermöglichte den Einbau eines großen Volumens einer flüssigen Phase in die Polymermatrix. Die Optimierung umfasste Variationen der chemischen Struktur der Komponenten, der Verhältnisse und der Synthesetechniken. Eine Feinjustierung der Gele erzielte optimale elektrochemische Leistungen, ohne die mechanischen Eigenschaften zu beeinträchtigen.

Contents

List of abbreviations

ACN	acetonitrile	DPEPA	dipentaerythritol penta-/hexa-acrylate
AIBN	azobisisobutyronitrile	DSC	differential scanning calorimetry
Al-ion	aluminum-ion	EC	ethylene carbonate
Al_2O_3	aluminium(III) oxide	EMC	ethylmethyl carbonate
AM	additive manufacturing	EME	1-ethoxy-2-methoxyethane
B-O	borate-ester bond	EMIM TFSI	1-ethyl-3-methylimidazolium bis(trifluoromethylsulfonyl)imide
BDS	broadband dielectric spectroscopy	EO	ethylene oxide
BMIm TFSI	1-butyl-3-methylimidazolium bis(trifluoromethylsulfonyl)imide	EU	European union
CAD	computer-aided design	EV	electric vehicles
CAN	covalent adaptive networks	FDM	fused deposition modeling
$CDCl_3$	deuterated chloroform	FEC	4-fluoro-1,3-dioxolan-2-one
CE	composite electrolyte	FRP	free radical polymerization
COF	covalent organic framework	FSI	bis(fluorosulfonyl)imide
CP	cross polarization	FT-IR	Fourier-transform infrared spectroscopy
DBTTC	s,s-dibenzyl trithiocarbonate	2FTMS	α-fluoro-tetramethylene sulfone
DC	direct current	SEC	size-exclusion chromatography
DCM	dichloromethane	HB	hydrogen bonding
DEC	diethyl carbonate	HOMO	highest occupied molecular orbital
DE-IM/TFSI	1,2-dimethyl-3-ethoxyethylimidazolium bis(trifluoromethylsulfonyl)imide	IL	ionic liquid
DIL	dicationic ionic liquid	IMITEA-TFSI	imidazolium-trialkylammonium bis(trifluoromethylsulfonyl)imide
DIW	direct ink writing	Li-air	lithium-air
DLS	dynamic light scattering	LFP	lithium iron phosphate
DMC	dimethyl carbonate	Li-ion	lithium-ion
DMF	dimethylformamide	$LiAlO_2$	lithium aluminate
DMPA	2,2-dimethoxy-2-phenylacetophenone	$LiAsF_6$	lithium hexafluoroarsenate
DMSO	dimethyl sulfoxide	LiB	lithium-ion battery

LiBF$_4$	lithium tetrafluoroborate	NP	nanoparticle
LiBOB	lithium bis(oxalato)borate	PAN	polyacrylonitrile
LiClO$_4$	lithium perchlorate	PC	propylene carbonate
LiCoO$_2$	lithium cobalt oxide	PDA	polydopamine
LiDFOB	lithium difluoro(oxalato)borate	PE	polymer-based electrolyte
LiF	lithium fluoride	PEG	poly(ethylene glycol)
LiFSI	lithium bis(fluorosulfonyl)imide	PEGDME	polyethylene glycol dimethyl ether
LiMeO$_2$	lithium metal oxide	PEGMA	poly(ethylene glycol) monomethacrylate
LiMn$_2$O$_4$	lithium manganese(III,IV) oxide	PEO	poly(ethylene oxide)
Li-O	lithium-oxygen	PFPE	perfluoropolyether
LiPF$_6$	lithium hexafluorophosphate	PIB	polyisobutylene
Li-S	lithium-sulfur	PIL	polymeric ionic liquid
LSV	linear sweep voltammetry	PMAA	poly(methacrylic acid)
LiTFSI	lithium bis(trifluoromethylsulfonyl)imide	PMMA	poly(methyl methacrylate)
LUMO	lowest unoccupied molecular orbital	PPC	poly(propylene carbonate)
MAS	magic angle spinning	PS	poly(styrene)
MeOH	methanol	PVA	poly(vinyl alcohol)
Mg-ion	magnesium-ion	PVdF	poly(vinylidene fluoride)
MgSO$_4$	magnesium sulfate	PVdF-HFP	poly(vinylidene fluoride-co-hexafluoropropylene)
MOF	metal–organic framework	RAFT	reversible-addition-fragmentation chain-transfer
MPPyr TFSI	1-methyl-1-propylpyrrolidinium bis(trifluoromethylsulfonyl)imide	RT	room temperature
Na-S	sodium-sulfur	σ	conductivity
Ni-Cd	nickel-cadmium	SEC	size exclusion chromatography
Na-ion	sodium-ion	SEI	solid electrolyte interface
Na$_2$SO$_4$	sodium sulfate	SH	self-healing
Ni-MH	nickel-metal hydride	SiO$_2$	silica
NMC	nickel-manganese-cobalt	SLS	laser sintering
SLA	stereolithography	SPE	solid polymer electrolyte
NMR	nuclear magnetic resonance	SSE	solid state electrolyte
NMP	N-methyl-2-pyrrolidone	T	temperature

TEA	triethylamine
TEM	transmission electron microscopy
TEP	triethyl phosphate
TFSI	bis(trifluoromethylsulfonyl)imide
T_g	glass transition temperature
TGA	thermogravimetric analysis
THF	tetrahydrofuran
TiO_2	titanium dioxide
TMS	tetramethylene sulfone
T_v	vitrimeric transition temperature
UPy	ureidopyrimidinone
vs.	versus
VTF / VFT	Vogel−Tammann−Fulcher
WAXD	wide-angle x-ray diffraction
Y_2O_3	yttrium oxide
ZrO_2	zirconium dioxide

NMR spectroscopy

d	doublet
dd	doublet of doublets
m	multiple
p	pentet
q	quartet
s	singlet
t	triplet
td	triplet of doublets

Parts of the thesis including the concept, chapter 4 and chapter 5, as well as experimental part were already published:

1. Zviadi Katcharava, Xiaozhuang Zhou, Rajesh Bhandary, Rene Sattler, Heiko Huth, Mario Beiner, Anja Marinow, and Wolfgang H. Binder. "Solvent and catalyst free vitrimeric poly (ionic liquid) electrolytes." *RSC Advances*, 13, (**2023**): 14435-14442.

2. Anja Marinow, Zviadi Katcharava and Wolfgang H. Binder. "Self-Healing Polymer Electrolytes for Next-Generation Lithium Batteries." *Polymers*, 15, (**2023**), 1145.

3. Zviadi Katcharava, Anja Marinow, Rajesh Bhandary, and Wolfgang H. Binder. "3D printable composite polymer electrolytes: influence of SiO_2 nanoparticles on 3D-printability." *Nanomaterials*, 12 (11), (**2022**): 1859.

1 Introduction

1.1 Lithium-ion batteries

Rechargeable batteries, commonly known as secondary batteries, have developed into an indispensable part of modern society. The evolution of rechargeable battery technologies dates back to the late 1800s with the introduction of lead-acid batteries. Over time various technologies were developed, most notably lithium-ion batteries, commercialized by Sony in 1991. Figure 1 displays the specific energy and energy densities of commonly used battery types.[1-15] Lead-acid batteries, the oldest and well established technology, are known for their
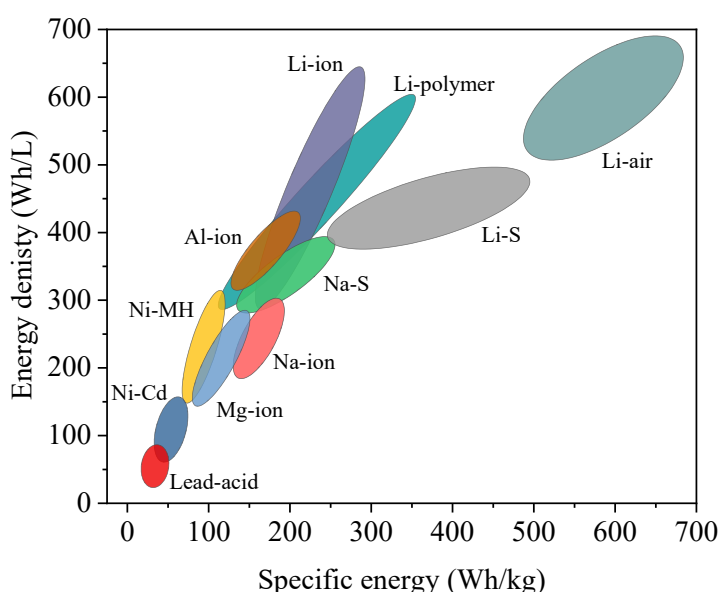
Figure 1. Specific energy (Wh/kg) and energy densities (Wh/L) of different types of rechargeable batteries (approximate values for currently available technologies).

low energy density. They still remain widely used due to their low cost, high recyclability and the ability to deliver high surge of current.[16] The nickel-cadmium (Ni-Cd) rechargeable battery, invented in 1899, provides higher energy densities compared to lead-acid batteries. It employs metallic cadmium and nickel oxide electrodes. The utilization of Ni-Cd batteries is greatly restricted due to the toxicity of cadmium, leading to its ban in the EU for consumer use in the early 2000s. Moreover, Ni-Cd are characterized by high rate of self-discharge and susceptibility to memory effect.[17,18] Similar to Ni-Cd, the nickel-metal hydride (Ni-MH) battery also employs nickel oxide hydroxide as positive electrode. However, Ni-MH battery substitutes the negative electrode with hydrogen absorbing alloys. Ni-MH batteries offer much higher energy density and have addressed environmental concerns, allowing them to remain

useful for various commercial applications.[19] Sodium-sulfur (Na-S) rechargeable batteries, which are more attractive for stationary energy storage devices, comprise liquid sulfur as cathode and liquid sodium as the anode.[20] Usually, Na-S batteries operate within a temperature range of 300 – 350 °C. providing competitive energy densities.[21] Research towards room temperature Na-S battery can be promising direction, which requires further advancement of cell design and associated materials.[22] Conversely, lithium sulfur (Li-S) batteries are more advanced, operating at RT and theoretically achieving exceptional specific energy. Yet, the challenge with Li-S batteries that needs addressing is their poor long-term cyclic stability.[23,24]

The growing demand for energy-efficient battery technologies necessitates improved energy and power densities, safety enhancements, and cost savings. This also brings forth ethical considerations like sustainability, repurposing, or recycling. Thus, there have been flourishing research activities in different directions to fulfill these prospective requirements. Since a large group of batteries are operating based on metal ions traveling between electrodes during charging and discharging, one favored approach involves diversifying energy storage systems by transitioning towards more abundant resources like sodium (Na), potassium (K), calcium (Ca), magnesium (Mg), zinc (Zn), or aluminum (Al). Sodium ion (Na-ion) batteries present an emerging technology, driven by the abundance of Na and environmental friendliness. Although, the development of Na-ion batteries has been particularly rapid owing to their analogous chemistry with the lithium-ion battery system, due to sodium being three times heavier and having a lower standard electrochemical potential than lithium, it remains challenging for Na-ion to surpass LiBs in terms of energy density, specific capacity, or rate capability. The active material of Na-ion energy storage devices requires further improvement for gaining more commercial interest.[25] Magnesium-ion (Mg-ion) batteries, which are still in its early stage of research, have a potential to reach exceptionally high specific energy above 700 Wh/L. However, the existing technologies and available materials limit its performance, promoting the further research and development.[26,27] Aluminum-ion (Al-ion) systems stand as another emerging technology distinguished by its excellent cyclic lifespan, even under high charging rates. The current limitation lies in the low energy density of these cells, a factor that could potentially be enhanced in the future.[28,29] Another attractive technology are lithium air (Li-air) batteries, theoretically capable of surpassing the energy densities of all exciting systems. Li-air batteries employ metallic lithium as anode and either aqueous or non-aqueous electrolytes.[30] The current technologies have not yet reached their full potential, and existing battery cells suffer from drastically lower energy densities and short cycle lifespan.[31-33]

2

The battery market has been dominated by lithium-ion (Li-ion) batteries in the last three decades. Li-ion batteries (LiBs) cover wide range of application including, consumer electronics, electric vehicles and energy storage devices for renewable sources.[34,35] LiBs are very versatile and compact devices and a few characteristic features makes them irreplaceable by other technologies. They offer high energy density, long cyclic life, low self-discharge and almost neglectable memory effect.[36-39] The basic structure of LiBs is presented in Figure 2.[40] LiBs are composed of two electrodes, the positive (cathode) and negative (anode), along with separator that electrically isolates the electrodes, and an electrolyte responsible for transporting lithium ions. Additionally, current collectors (aluminum for the cathode and copper for the anode) are used for providing the pathway for electron flow during battery cycling.[41]

The most commonly used material for the anode in LiBs is graphite. Its crystalline structure facilitates the intercalation of Li ions between layers during charging and the release of ions during discharge.[42] Graphite is widely available, has low cost and low toxicity. Moreover, it exhibits good reversibility (impacting the cyclic life of batteries) and stands as a well-established material within the industry. However, along with this advantageous properties,

Cathode: $LiCoO_2 \leftrightarrows Li_{(1-x)}CoO_2 + xLi^+ + xe^-$ $0 \leq x \leq 0.5$

Anode: $6C + yLi^+ + ye^- \leftrightarrows Li_yC_6$ $0 \leq y \leq 0.5$
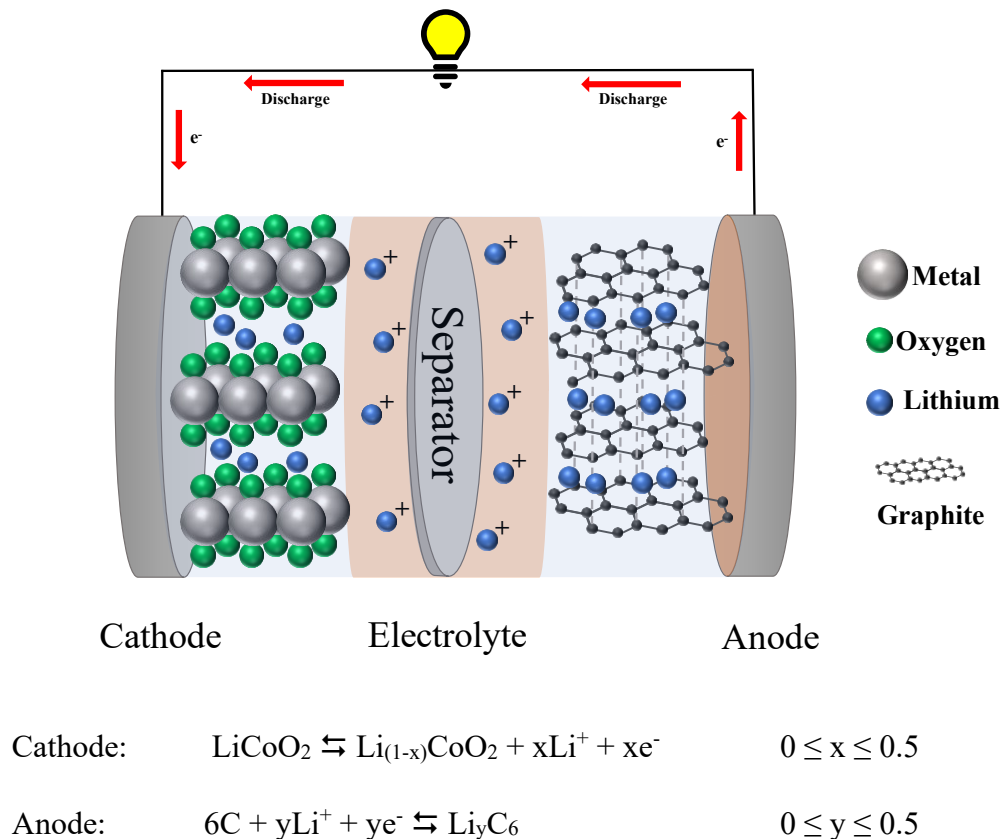
Figure 2. Simplified structure of LiBs and corresponding electrochemical reactions for $LiMeO_2$/graphite cell. Adapted with permission from [40].

graphite does have some drawbacks, predominantly its limited capacity of 372 mAh/g, which restricts the accessibility to next generation high-capacity batteries.[43] Alternative materials, mostly silicon-based, can drastically increase the specific capacity of LiBs.[44] This field is still in its research phase, primarily because current silicon materials are known for their low cyclic life and significant volumetric changes during charging and discharging.[45] The extreme volume changes can cause the pulverization of active material and promote the degradation of battery.[46]

Cathode materials for LiBs play a crucial role in cell performance. J. Goodenough and co-workers pioneered the development of various materials designed specifically as cathodes, which can be categorized into three types.[37,38] Layered oxide, spinel oxide and polyanion oxides (Figure 3)[47-49] are widely recognized and commercially thriving materials used in LiBs.[50] Layered $LiCoO_2$ consists of monovalent Li ions situated between anionic sheets made of cobalt and oxygen. Such structures enable the operation at higher voltage (up to 4 V) but restrict the charge capacity to 140 mAh/g. Similar to $LiCoO_2$, other transition metals can replace cobalt, which is associated with high cost and limited availability. Among various investigated structures cobalt combined with manganese and nickel (NMC) $LiNi_{1-y-z}Mn_yCo_zO_2$ has emerged as a commercially successful alternative.[51] Incorporation of three transition metals serves the purpose to combine advantageous properties and achieve chemical and structural stability of the materials.[52] Spinel oxides is the second class of cathode materials for LiBs. $LiMn_2O_4$ forms cubic spinel structure and enables Li-ion intercalation. The main advantage of $LiMn_2O_4$ is the exclusion of more expensive cobalt and nickel. The main drawback is the relatively low cyclic lifespan compared to layered structure cathodes.[53] The third class known
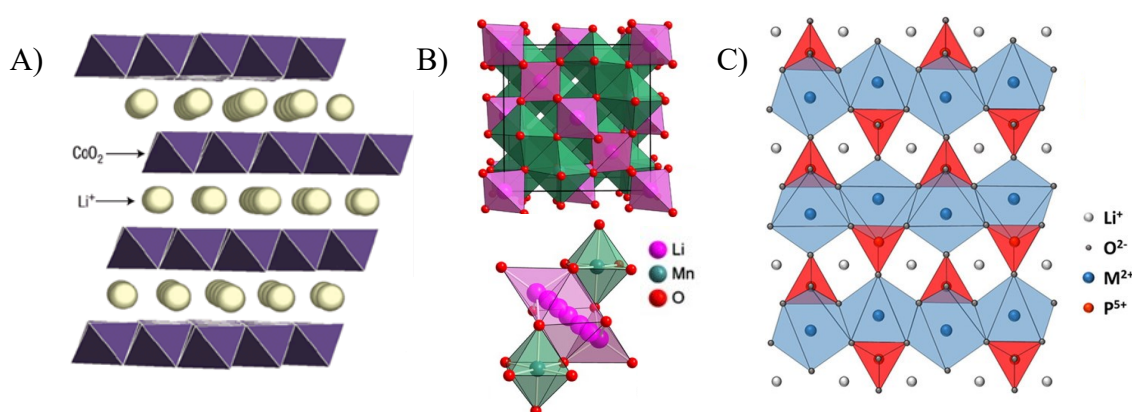
Figure 3. A) Layered structure of $LiCoO_2$. Taken from [47]. Copyright © 2003, Springer Nature Limited. B) Structure of spinel $LiMn_2O_4$ and diffusion pathway of lithium. Taken with the permission from [48]. Copyright © 2013 Chinese Materials Research Society. Production and hosting by Elsevier B.V. C) Structure of polyanion cathode material. Taken from [49]. Copyright © 2021, American Chemical Society.

as polyanion oxides consist of metal cation surrounded by polyatomic anion and forming three dimensional structure.[54] Among numerous researched structures, lithium iron phosphate (LiFePO$_4$, LFP) stands out notably, gaining widespread application.[55] LFP is achieving excellent cycling life and stability at elevated temperatures. However, the specific energy is relatively lower compared to other types (due to necessary coating of LFP particles), making it less attractive for portable application, but more desirable for stationary energy storage batteries.[56]

The third key component of LiBs is the electrolyte, responsible for transporting lithium ions during charge/discharge cycles. They are required to operate within a wide temperature range, endure redox environments, and maintain high conductivity (above 5 mS/cm). Commercial electrolytes typically comprise non-aqueous solutions containing dissolved lithium salt in carbonate esters. Commonly used electrolytes contain a mixture of two or more solvents, because, to date, a single solvent does not provide high enough dielectric permittivity, good ionic transport capabilities and sufficient interfacial stability on electrodes simultaneously.[57] Ethylene carbonate (EC), propylene carbonate (PC), dimethyl carbonate (DMC), diethyl carbonate (DEC) and ethylmethyl carbonate (EMC) are commonly used in the electrolyte formulations.[58,59] EC is the crucial part of the mixture due to its ability to form solid electrolyte interfaces (SEI) with the anode, the protective, electrically isolating but ionically conductive layer.[60,61] Conducting lithium salt is added to carbonate mixture to allow ion transport and form final electrolyte mixture. Furthermore, small amounts of additive are used in the commercial scale for improving the SEI formation capabilities and adjusting some electrochemical properties.[57] The additional lithium salt is required to have the ability to dissociate in the electrolyte, exhibit electrochemical and thermal stability, retain chemical inertness toward all battery components and be cost-effective to support large-scale manufacturing.[62] Lithium hexafluorophosphate (LiPF$_6$) is the commonly used Li salt due to its balanced properties that fulfil the majority of requirements, but there are few drawbacks which can be improved.[63] Safety concerns arise due to the decomposition at elevated temperatures. Additionally, chemical stability may pose challenges; LiPF$_6$ can form hydrofluoric acid even at few ppm concentrations of moisture, inducing battery degradation.[64] Alternative Li salts are being developed and investigated, most notable and promising ones are lithium perchlorate (LiClO$_4$), lithium tetrafluoroborate (LiBF$_4$), lithium hexafluoroarsenate (LiAsF$_6$), lithium bis(oxalato)borate (LiBOB), lithium bis(trifluoromethylsulfonyl)imide (LiTFSI) and lithium bis(fluorosulfonyl)imide (LiFSI) (Figure 4).[57,62,63] LiClO$_4$ exhibits desirable electrochemical
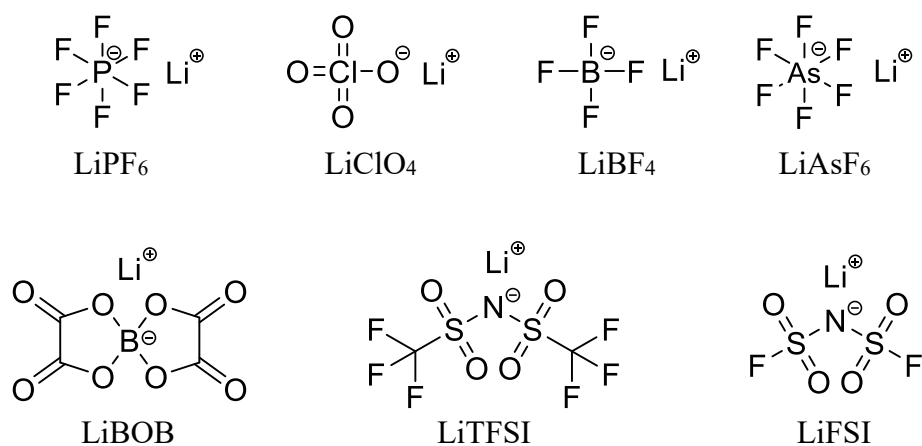
Figure 4. Chemical structures of different Li-salts.

properties and low sensitivity towards moisture, but is prone to explosion and other safety issues, limiting the application only for research purposes.[65,66] LiBF$_4$ is characterized by desired electrochemical and thermal stability, but ionic conductivity is the main constraint.[67-69] LiAsF$_6$ outperforms other alternatives in almost all aspects, however, irrespective of its excellent electrochemical performance, the salt is not used due to its high toxicity.[70] LiBOB demonstrates good ionic conductivity, low toxicity and wide electrochemical stability window. However, poor solubility in organic solvents restricts its application in LiBs.[71,72] Imide-based salts, LiTFSI and LiFSI, represent one of the most promising alternatives for LiPF$_6$. They exhibit excellent electrochemical and thermal stability, chemical inertness, superior ionic conductivity and solubility in organic solvents.[73,74] The main drawback is the inability to passivate aluminum current collector at high potential which results in corrosion.[62]

The fourth component of LiBs is the separator. Although it is not an electrochemically active component, it plays a crucial role in ensuring the safety of LiBs while facilitating the lithium-ion transfer.[75] The separator needs to demonstrate high ionic conductivity, electrochemical and thermal stability, excellent electrolyte wettability, superior mechanical properties and high porosity.[76,77] Typically polymeric porous membranes from polyethylene and/or polypropylene with defined thickness are used as separators.[78] Alternatively, poly(vinylidene fluoride) (PVdF), polyacrylonitrile (PAN), polydopamine (PDA) and poly(methyl methacrylate) (PMMA) can function as a separator, potentially enhancing the performance, adjusting the requirements and enduring compatibility with the new generation batteries.[79,80]

1.2 Drawbacks of Li-ion batteries

Despite the widespread demand for LiBs, the current technology is far from being perfect. Addressing numerous shortcomings is imperative to successfully design next generation systems with higher energy and power densities. Safety concerns are the most notable critical issues with LiBs,[81,82] followed by significant drawbacks such as sustainability, recyclability and limited lifespan.[83-85] The potential for fire and explosion in LiBs poses serious safety risk, especially with the world transitioning towards electric vehicles (EV) relying on large number of battery cells. The fire risk is linked with the flammable organic solvent-based electrolyte. Various factors can trigger the irreversible and dangerous degradation of LiBs, with thermal runaway being the most dangerous failure event which can result in explosion and/or fire.[86] A thermal runaway is the cascading series of uncontrollable exothermic processes. When the internal temperature of LiBs exceeds > 80 °C, it triggers further exothermic reactions within the cell, leading to a further increase in temperature.[81,87] Overheating, the initial step of thermal runaway, can be initiated by overcharging (charging a battery beyond its recommended voltage), external mechanical damage or heating, internal short circuit and manufacturing defect.[88-92] An important concern is the occurrence of the internal short circuits, which can take place due to direct electric contact between the cathode and anode. This issue can be caused by the formation and growth of lithium dendrites during battery´s charge/discharge cycles (Figure 5). Dendrites are needle-like structures made of metallic lithium that form on the anode and expand gradually over time.[93] The formation of these structures at random nucleation sites is associated with improper operation of the cell, for example, high charging at high current densities, overcharging and charging at low temperatures. Dendrites can penetrate the separator and initiate thermal runaway.[94-96] The formation and propagation of dendrites can be suppressed by using different types of electrolytes.[97,98] Moreover, replacing conventional electrolyte can resolve the flammability issue if non-flammable alternatives are used.[99,100] More detailed discussion on alternative electrolytes will be presented in the following chapter (Section 1.3). In the pursuit of achieving higher energy density in next generation batteries, alternative electrode materials are considered. For example, switching to silicon-based or
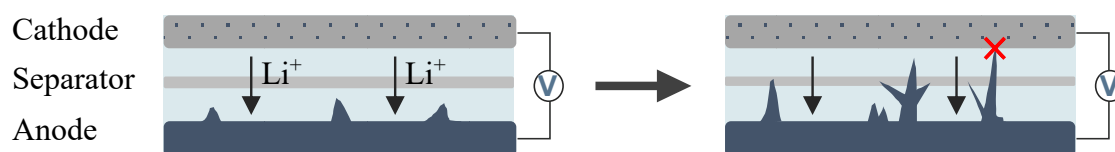

Figure 5. Schematical presentation of dendrite formation and growth in LiBs.

metallic anodes can substantially increase the energy density, but it comes with drawbacks, particularly low cyclability.[101] Silicon-based anode, for instance, experience significant volume changes during charging/discharging (up to 300%), leading to reduced interfacial contact and cell degradation. Lithium metal, on the other hand, is very prone to dendrite formation, which diminishes cycling life and raises safety concerns.[101]

The high demand and consumption of LiBs raise concerns regarding sustainability and responsible consumption of resources. Extraction of materials required for LiBs, especially cobalt and nickel, is connected to environmental and ethical problems. Moreover, the global economy is striving for carbon negativity/neutralization and endorsing the circular economy, which necessitates adjustments within the LiBs industry. These changes require adaptation and improvement of traditional materials to make them more readily recyclable and reusable.[102-104]

1.3 Electrolytes for Li-ion batteries

Lithium-ion batteries currently rely on organic-solvent based electrolytes, posing safety concerns due to their leachability and flammability. To address the flammability issue, replacing flammable solvents with non-flammable alternatives has been explored. However, these alternative materials often struggle to form a solid electrolyte interface (SEI), a crucial factor for the long-life cycle of LiBs. The quest for an ideal electrolyte is complex and numerous different chemistries have been intensively investigated in the last few decades. In general, electrolyte materials can be classified in different ways.[57,58,105] In the following discussion, electrolytes will be divided into several categories (Figure 6): conventional electrolytes including fluorinated and nonfluorinated compounds, polymer-based materials, ionic liquids and derived poly(ionic liquid)s, gel polymer electrolytes, all solid-state materials and composite materials.
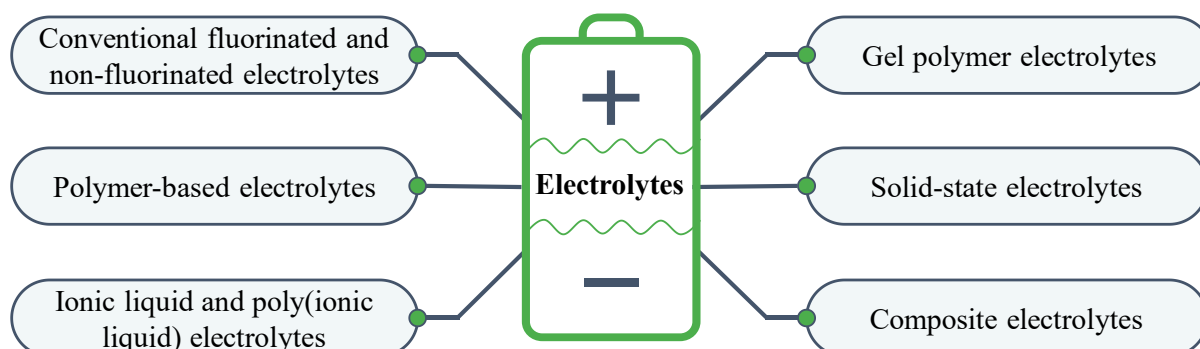
Figure 6. Electrolyte materials for LiBs.

1.3.1 Conventional fluorinated and non-fluorinated liquid electrolytes

Fluorinated solvents, primarily due to their superior electrochemical and thermal stability, can potentially replace traditional liquid organic carbonate-based electrolytes. These solvents typically exhibit oxidative stability exceeding 4.5 V and are non-flammable. The electrochemical window of electrolytes is associated with the highest occupied molecular orbital (HOMO) and the lowest unoccupied molecular orbital (LUMO) (Figure 7). The reduction of liquid electrolyte occurs when the electrochemical potential of the anode exceeds the electrolyte LUMO, while oxidation occurs when the electrochemical potential of the cathode falls below the HOMO.[38] Ideally, a liquid electrolyte should possess a high LUMO
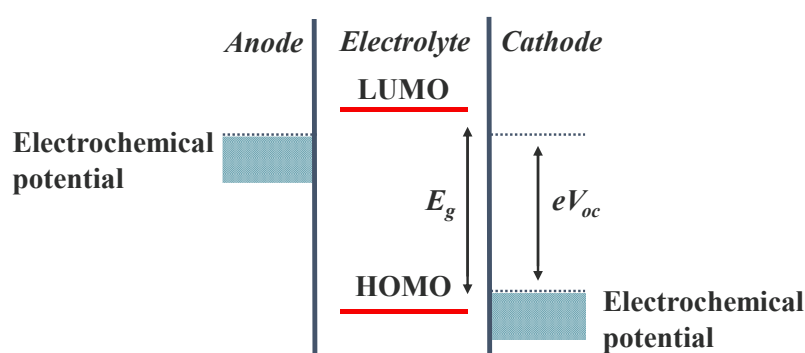
Figure 7. Relative energies of the electrolyte window (E_g) and the electrodes electrochemical potentials for liquid electrolyte with solid electrodes. (V_{oc} open circuit voltage and e electron charge). Adapted with permission from [38]. Copyright © 2013, American Chemical Society.

and a low HOMO.[38,106] The formation of SEI restricts the further reduction/oxidation of an electrolyte during cycling. Introducing electro-withdrawing fluorine in the structure reduces the HOMO and further improves SEI formation capabilities.[107-109] Fluorinated compounds contribute to the formation of LiF-rich SEI layer, offering more efficient protection against electrolyte degradation and effectively suppressing dendrite growth.[110,111]

Fluorinated esters and ethers have garnered considerable interest for their excellent separator wettability and compatibility with electrodes, including also lithium metal batteries.[112] Selected fluorinated compounds and corresponding nonfluorinated counterparts are presented in Table 1. Ethylene carbonate (EC) derivatives with different number of incorporated fluorine atoms have been characterized.[113] The number of fluorine substituents is significantly changing physiochemical properties. For instance, melting temperature, boiling temperature and dielectric constant decrease with an increasing number of F atoms. The dielectric constant plays a pivotal role in determining the possible application of solvent in an electrolyte, as it assesses the ability of molecules to solvate/dissociate salts. However, viscosity of EC derivatives

follows different trends initially increasing and then gradually reducing with the increasing number of fluorine atoms. This deviation is assumed to be influenced by the impact of fluorination on intermolecular interactions. Furthermore, 4-fluoro-1,3-dioxolan-2-one (FEC) outperforms EC electrolyte in cycling stability in batteries with silicon anodes, attributed to more stable SEI formation.[114] Comparatively, linear carbonates and corresponding fluorinated structures display different behavior. Unlike cyclic EC, diethyl carbonate (DEC) exhibits an increase in dielectric constant after introduction of fluorine atoms. Additionally, the boiling temperature initially rises and subsequently reduces. The viscosity of fluorinated DEC increases with the degree of fluorination, leading to a reduction of ionic conductivity.[113] Fluorinated ethers display significant initial changes in dielectric constant upon introducing fluorine into the structure, but only minor differences emerge between varying the degree of modification. Moreover, they exhibit changes in viscosity and conductivity. As an example, in the case of 1-ethoxy-2-methoxyethane (EME), the difluoro substituted analog displays the highest viscosity, followed by mono substituted, trisubstituted and non-modified versions. The conductivity trends indicate reduction with a higher number of fluorine, although the mono-substituted compound surpasses the conductivity of non-fluorinated reference at elevated temperatures.[115]
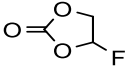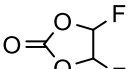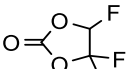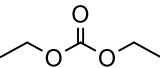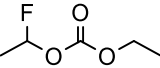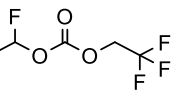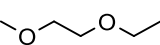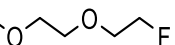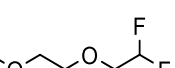
Apart from carbonates and esters, various compounds can serve as electrolytes, such as sulfones, for higher voltage batteries, or organic phosphates as flame-retardant agents.[100,116,117] Tetramethylene sulfone (TMS), which displays an excellent electrochemical window up to 5.5 V, faces challenges due to poor separator and electrode wettability, high viscosity, and a high melting temperature.[118] Fluorination can affect sulfones, enhancing wettability and reducing viscosity. However, α-fluoro-tetramethylene sulfone (2FTMS) exhibits lower oxidation stability compared to TMS. The position of substitution is crucial; significant oxidation stability reduction occurs only when fluorine is introduced at the α-carbon position.[119] Triethyl phosphate (TEP) is one of the potential flame-retardant additives for electrolytes. However, it lacks the ability to form a stable SEI, leading to the degradation of the graphite anode.[99,120] Fluorinating the phosphate results in reduced viscosity, enhanced flame retarding efficiency and outperforms non-fluorinated counterpart in battery testing.[121]

Recently, a new class of fluorinated ethers has emerged, featuring varied fluorinated backbones and lengths of non-fluorinated ether end groups.[122] The synthesized compounds combine the electrochemical stability and enhanced ionic conductivity, attributed to the presence of non-modified ether groups. DME-FTriEG (Table 1), when combined with 1 M LiFSI, exhibits
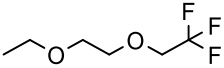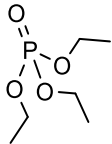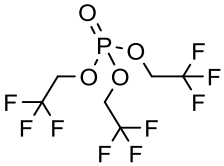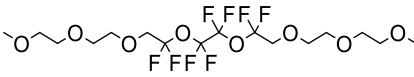
conductivity as high as 2.7×10^{-4} S/cm at 30 °C. While its conductivity remains below that of its non-fluorinated counterpart (tetraglyme), its electrochemical performance drastically improves, reaching 5.6 V compared to 4 V (tetraglyme). Notably, a battery employing DME-FTriEG (1 M LiFSI) with NMC as the cathode and Li metal as the anode successfully functioned over 100 cycles.

Thus, fluorinating solvents for electrolytes can enhance properties but requires careful design for optimal performance. Considering not only the number of F atoms but also their position is essential for achieving the best properties.

Table 1. Selected fluorinated and non-fluorinated electrolytes for lithium batteries.

Compound	Chemical structure	T_m (°C)	T_b (°C)	Viscosity (cP)	Dielectric constant
Ethylene carbonate (EC)[112,113]		37.5	238	1.94 *	90.5 *
4-Fluoro-1,3-dioxolan-2-one (FEC)[112,113]		20	210	4.40 *	79.7 *
4,5-Difluoro-1,3-dioxolan-2-one (F$_2$EC)[112,113]		8.5	129	2.70 *	35.4 *
4,4,5-Difluoro-1,3-dioxolan-2-one (F$_3$EC)[112,113]		-54.5	91	1.28 *	18 *
Diethyl carbonate (DEC)[112,113,123]		-75	126	0.82 *	2.8 *
Ethyl(1-fluoroethy)-carbonate (F$_1$DEC)[112,113,123]		-	135	1.21 *	7.5 *
2,2,2-Trifluoroethyl(1-fluoroethyl) carbonate (F$_4$DEC)[112,113,123]		-28.5	127	1.87 *	8.3 *
1-ethoxy-2-methoxyethane (EME)[115]		-	103	0.52 #	5.7 #
2-Fluoroethoxymethoxy-ethane (FEME)[115]		-	-	1.01 #	16.6 #
1-(2,2-Difluroethoxy)-2-methoxyethane (DFEME)[115]		-	-	1.06 #	16.6 #

Name	Structure				
1-(2,2,2-Tifluroethoxy)-2-methoxyethane (TFEME)[115]		-	125	0.78 [#]	16.9 [#]
Tetramethylene sulfone (TMS)[116,124,125]		27	285	10.28 [##]	60 *
α-fluoro-tetramethylene sulfone (2FTMS)[112,116,119]		-	-	-	-
Triethyl phosphate (TEP)[121,126]		-56.4	215	1.6 [#]	13 *
Tris(2,2,2-trifluoroethyl)phosphate (TFP)[121,126]		-19.6	148	4.6 [#]	10.5 *
DEG-FTriEG[122]				18.1 *	-

* - at 20 °C, [#] - at 25 °C, [##] - at 30 °C.

1.3.2 Polymer-based electrolytes

Polymer-based electrolytes (PEs) are considered as one of the most promising alternatives to commercial flammable liquid electrolytes in LiBs. Polymers address safety concerns due to their non-flammable nature and offer superior mechanical properties. They can resist deformation and hinder or prevent dendrite formation, thus, consequently extending overall battery lifespan. Despite their advantageous properties, it is crucial to note that conductivity remains the main limiting factor in replacing the currently employed electrolytes. Typically, polymers exhibit low dielectric constant making them unsuitable as electrolytes, due to their limited capacity to efficiently dissociate Li salts. Consequently, this hampers the ion transport within the system. However, polymers with electron withdrawing groups in the backbone demonstrate enhanced ability to dissociate salt, making them particularly promising candidates for use as PEs.[127] The most extensively studied PE is poly(ethylene oxide) (PEO/PEG).[59,128,129] Ethylene oxide groups in PEO are able to coordinate with lithium ion. The labile lithium-oxygen bond can break and reform, which promotes the intermolecular and/or intramolecular ion hopping.[130] Schematically the transport of Li-ion *via* hopping mechanism is presented in Figure 8. This mechanism is more applicable for amorphous polymers, where segmental
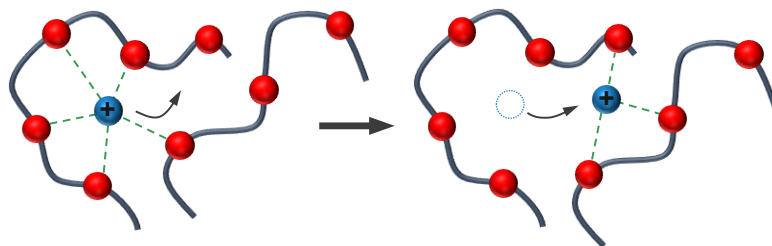
Figure 8. Lithium-ion conduction in amorphous poly(ethylene oxide).

relaxations contribute to conductivity. In the crystalline structures of PEs, the conductivity remains inadequately understood. The prevailing theory explaining conductivity in crystalline PEO involves the transport of lithium ions through three dimensional tunnels within polymers crystalline structure *via* hopping, while anions are located outside of these tunnels.[131] Nonetheless, a deeper comprehension is needed to ascertain whether the greater contribution to overall conductivity is attributed to crystalline or amorphous segments.[127,132]

Ion transport is strongly related to segmental motions of polymer chains and the efficiency of salt dissociation. The common approach to distinguish their contributions is to use the Arrhenius equation (eq. (1), where σ_0 is pre-exponential factor associated with the number of charge carriers, k_b denotes the Boltzmann constant, and E_a signifies activation energy)[133,134] and the Vogel−Tammann−Fulcher (VTF) (also known as Vogel−Fulcher−Tammann (VFT)) equation (eq. (2), where A is the pre-exponential factor related to the number of charge carriers, , B stands for pseudo-activation energy related to segmental motions of polymer, and T_0-known as Vogel temperature, typically 50 °C below T_g).[134,135] The Arrhenius equation can be applied to polymers below T_g when the chain dynamics become constrained. Under such conditions, ion conductivity occurs solely *via* hopping to the nearest vacant site, enabling the formation of new coordination sites.[134,136] The temperature dependence of the Arrhenius model is commonly represented on an inverse temperature scale, allowing for the extraction of activation energy from the fitting process. Conversely, the VTF model comprehensively describes the temperature-depended conductivity, considering both polymer motions and ion hopping. Chain dynamics can influence conductivity by creating free volume and consequently increasing diffusion of ions. Moreover, these dynamics affect the coordination of lithium ions by facilitating the forming or breaking of Li-O coordination. Unlike the linear trend observed in Arrhenius plots, VTF displays nonlinear behavior and is typically observed for polymers above T_g. Another crucial parameter, aside from conductivity, is the lithium transference number. It is defined as the fraction of the total current conveyed through the electrolyte by lithium ions.[137]

The lithium transference number below 0.5 indicates that the main contributor to ionic conductivity is the counterion, while the Li$^+$ remains solvated within a bulky shell of anions.[138]

$$\sigma = \sigma_0 \exp(-\frac{E_a}{k_b T})$$ (1)

$$\sigma = A \exp(-\frac{B}{T - T_0})$$ (2)

In general, polymer electrolytes can be categorized into solid PEs (SPEs) and gel PEs (GPEs). GPEs will be discussed separately in Chapter 1.3.4. SPEs typically contain additional lithium salt and can potentially replace both liquid electrolyte and separator. Among these, PEO-based electrolytes have been extensively researched for their favorable properties, such as high dielectric constant and good electrochemical stability. However, PEO exhibits low ionic conductivity ($< 10^{-7}$ S/cm) and low transference number ($0.2 - 0.3$) at RT.[137,139] Its conductivity becomes suitable for batteries only at elevated temperatures (above 60 °C). PEO melts at $65 - 70$ °C, thus the polymer displays poor mechanical properties at elevated temperatures.[140] Different approaches can be used to enhance the conductivity and simultaneously maintain high mechanical strength of SPEs. Most common approaches include the addition of plasticizers, the synthesis of co-polymers, blending and the addition of nanofillers.[129,141-143] The addition of lithium salt to PEO does improve conductivity, but the RT values remain inadequate for practical applications (Table 2). Moreover, salts with large anions tend to dissociate more effectively in PEO, reducing crystallinity but elevating the glass transition temperature.[129]

The preparation of blends has demonstrated to be a successful approach for enhancing the conductivity of polymer electrolytes by expanding the amorphous phase. Additionally, using the appropriate polymers ensures the dimensional stability of the PE. PEO mixed with poly(methacrylic acid) (PMAA) can reach the conductivity up to 1.3×10^{-5} S/cm at 60 °C while maintaining film formation ability.[144] Poly(propylene carbonate) (PPC) stands as another viable option for blended PE preparation, displaying the ionic conductivity of 6.8×10^{-5} S/cm at RT.[145] Blending proves to be a successful technique in precisely controlling the degree of crystallinity of low molecular PEO and perfluoropolyether (PFPE). The incorporation of a fluorinated backbone further improves the electrochemical properties of the mixture. Moreover, the optimal composition with LiTFSI exhibits amorphous properties over the broad temperature range, achieving the conductivity up to 2×10^{-4} S/cm.[146] PEs consisting of PEO

can undergo further enhancement through chemical modifications, such as synthesizing copolymers with varied architectures or preparing grafted copolymers.[147,148]

These modifications provide opportunities to fine-tune properties, as demonstrated by the block copolymer of poly(styrene) (PS) and PEO. PS-b-PEO displays the ability of self-assembly and yields in hexagonally perforated lamella, hexagonally packed cylinders and lamellae dependent on the volume fraction of PEO and PS.[149] The different morphologies provide the conducting pathways for lithium ions. Samples doped with $LiClO_4$ reach the conductivity up to 8.8×10^{-5} S/cm at 100 °C, a comparable value to $PEO/LiClO_4$ composition. Jeffamine® (amine terminated polyether oligomers) was also successfully incorporated in PEs.[150,151] Comb like morphologies were prepared in the presence of LiTFSI and LiFSI. Synthesized PEs not only exhibit enhanced conductivity, even at RT, but also demonstrate superior electrochemical stability for LiFSI containing samples.[151] Introducing covalent crosslinking offers a route to obtain excellent mechanical properties while maintaining high conductivity. Such approach was used for preparing PE based on semicrystalline polyethylene crosslinked with PEO containing chains.[97] The prepared PE was further doped by incorporating PEO oligomers and the conductivity reached values above 10^{-4} S/cm while simultaneously retaining remarkable mechanical properties, with the ability to suppress dendrites growth in lithium-metal battery.[97]
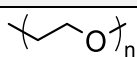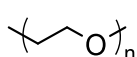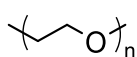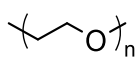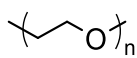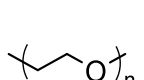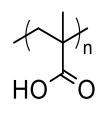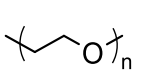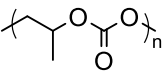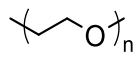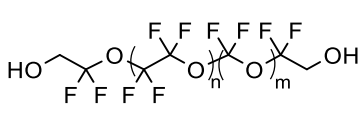
Poly(siloxane)s represents another promising class of materials for PEs. Poly(siloxane)s typically exhibit high thermal and electrochemical stability, low toxicity and low glass transition temperature due to flexible Si-O-Si bond.[152,153] However, mechanical properties and the salt dissolution ability requires enhancement which is usually achieved by copolymerization, blending, grafting or/and crosslinking. Siloxane-based polymer network containing ethylene oxide side chains and crosslinking displays high conductivity up to 1.33×10^{-4} S/cm while benefiting from improved mechanical properties.[154,155]

An interesting approach of improving electrochemical properties of solid state polymer electrolyte was reported recently.[156] The poly(ionic liquid) (PIL)-based electrolyte was prepared by mixing an IL-monomer with a fluorinated crosslinker, vinyl ethylene carbonate and LiTFSI. The mixture was crosslinked by means of UV polymerization. The addition of the fluorinated crosslinker positively impacted the electrochemical stability, reaching values above 5 V and additionally supporting SEI formation in battery cell. Moreover, incorporation of carbonate moieties in the polymer backbone enhances conductivity (1.4×10^{-3} S/cm at 25 °C).
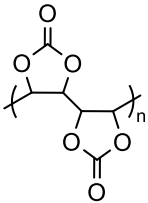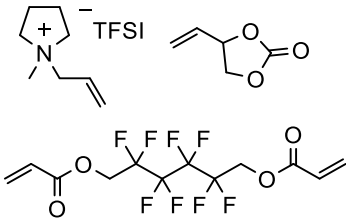
The solid polymer electrolyte displayed the ability to resist dendrite growth during battery testing.

Polymer electrolytes offer advantageous properties and many promising materials have been investigated.[137] However, the lower ionic conductivity remains the challenge and hinders their widespread application. This challenge has motivated research not only in solid-state polymer electrolytes but also in more complex designs, which will be discussed in the following chapters.

Table 2. Selected polymer electrolytes for lithium batteries.

Polymer (Mn - kDa)	Structure	Li salt	T (°C)	Conductivity (mS/cm)
PEO[137]		-	RT	$10^{-8} - 10^{-7}$
PEO (200)[157]		LiAsF$_6$ (10 wt%)	20	6.67×10^{-4}
PEO (4.2)[158]		LiTFSI (17 wt%)	50	3.63×10^{-4}
PEO (6000)[159]		LiPF$_6$ (20 wt%)	RT	4.10×10^{-5}
PEO (100)[160]		LiBOB (13 wt%)	40	1×10^{-4}
PEO (0.4) / PMAA (700)[144]	68 mol% 17 mol%	LiClO$_4$ (15 mol%)	60	1.3×10^{-5}
PEO (620) / PPC (50)[145]	45 wt% 45 wt%	LiClO$_4$ (10 wt%)	RT	6.83×10^{-5}
PEO (0.4) / PFPE (1)[146]	20 wt% 80 wt%	LiTFSI (r = 0.026)	30	2×10^{-4}
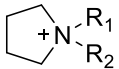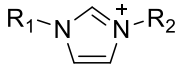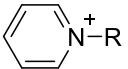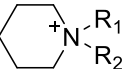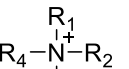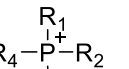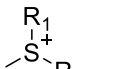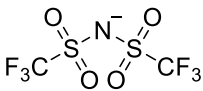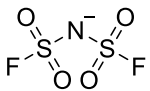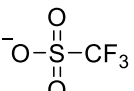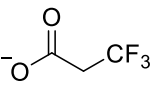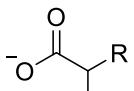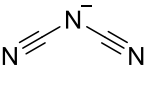
Material	Structure	Salt	Temp (°C)	Conductivity (S/cm)
PEO (900) / PVdF (534)[161]	18 wt% 72 wt%	LiClO₄ (10 wt%)	RT	2.62×10^{-5}
PS-b-PEO[149]		LiClO₄ (r = 0.042)	100	8.8×10^{-5}
PS-b-PEO[162]		LiTFSI (r = 0.02)	90	3.6×10^{-4}
PE-PEO cross-linked[97]		LiTFSI (r = 0.055)	25	2.7×10^{-5}
Jeffamine-based comb-like[151]		LiTFSI (r = 0.05) or LiFSI (r = 0.05)	40	2×10^{-4}
Siloxane-based[154]		LiTFSI (r = 0.05)	25	1.33×10^{-4}
Poly(siloxane)[163]		LiPF₆ (r = 0.025)	25	1.2×10^{-3}
PEC (220)[164]		LiFSI (80 wt%)	60	2.2×10^{-4}

PVCA[165]		LiDFOB (12.5 wt%)	50	9.82×10^{-5}
PIL[156]		LiTFSI	25	1.4×10^{-3}

/ - blend, r-ratio of Li^+/ EO group.

1.3.3 Ionic liquids and poly(ionic liquid)s

Ionic liquids (ILs) and polymeric ionic liquids (PILs) have gained increasing attention as potential electrolytes for LiBs due to their unique properties. ILs, defined as salts with melting points below 100 °C, are consisting solely of ions, typically organic cations and organic/inorganic anions (Figure 9).[166,167] ILs are distinguished by their advantageous features such as low volatility, high thermal and chemical stability, wide electrochemical window, non-flammability, good solubility of salts and good ionic conductivity.[168-171] One of the prominent features of ILs is their self-assembly behavior, leading to a subtle micro- and nanostructural organization, attributed to the distinct aggregation of apolar and ionic regions.[172-174] Moreover, their properties can be tailored by selecting the cation/anion pair from the large pool of options,

Figure 9. Chemical structures of common cations and anions for ILs.

18

making them suitable for various applications, including LiBs.[169,175,176] However, some challenges hinder the widespread use of ILs as electrolytes. The main drawbacks include their high viscosity, which diminishes the conductivity, especially in the lower temperature range.[177] Additionally the production of ILs is costly process, which requires more efficient approaches.[178,179]

The commonly researched ILs intended for potential use as electrolytes usually contain fluorinated anions, whereas as cations choices like imidazolium, pyrrolidinium and phosphonium are preferred, due to their relatively low viscosity and exceptional stability.[180,181] The selection of the cation significantly impacts both the viscosity and conductivity. For instance, increasing the size of the cation leads to higher viscosity and, consequently, resulting in reduced ionic conductivity. Moreover, the presence of ether group in the cation lowers the viscosity. Similar trends do not consistently apply to anions, where molecular interactions, such as Coulombic interactions, van der Waals and hydrogen bonding, also play considerable roles.[178,182] Using relatively smaller FSI (radius ≈ 0.264 nm) compared to TFSI (radius ≈ 0.379 nm) anion could reduce the viscosity, thus improving conduction capabilities.[177] Most commonly, imidazolium and pyrrolidinium based ILs are investigated as potential electrolytes. Imidazolium-based ILs exhibit high ionic conductivity, but are limited by lower electrochemical stability window, hindering their use in high voltage batteries. In contrary, pyrrolidinium-based ILs exhibit relatively lower conductivity, but offer a stability window above 5 V and better thermal stability, provided the right selection of anion group.[183-185] The main challenge remains in achieving the highest conductivity without compromising electrochemical stability when determining the optimal IL composition.

Similar to organic electrolytes, when employed as electrolytes, ILs also incorporate lithium salt. The interaction between Li^+ and cation/anion of ILs considerably influences the mobility of charge carriers. The anion tends to form clusters with the lithium cation, where the size of these clusters and the strength of coordination serve as crucial parameters for overall conductivity.[178,186,187] Anions possessing better delocalized charge or weaker electron pair donating ability ensure easier decomplexation and faster Li ion transfer. Studies on the ion mobility within $TFSI^-$, BF_4^- and imidazolium-based ionic liquids indicate that lithium mobility differs from that observed in conventional liquid electrolytes.[188] Li^+ transport is correlated to motion of negatively charged clusters (containing Li^+) and its mainly driven by the concentration gradient.

Another interesting class of ILs are so called dicationic ILs (DILs) or geminal ILs, containing two cationic groups connected *via* spacer chain.[189] DILs offer one more option (other than cation and anion choice) to tune properties by varying the spacer (link between two cations) length and its chemical nature. In the meantime, various DILs based on imidazolium, pyrrolidinium and other common types of cations have been reported.[190] The selected examples with their corresponding structures and conductivities are displayed in Table 3. The benefits of DIL preparation can be seen on the example of imidazolium-trialkylammonium DIL (IMITEA-TFSI). Combination of these two cations results in the IL that exhibits advantageous properties of both incorporated groups, displaying simultaneously high ionic conductivity $(2.7 \times 10^{-4}$ S/cm$)$ and electrochemical stability (5 V).[191]
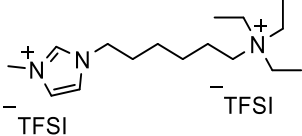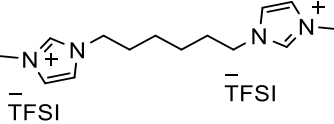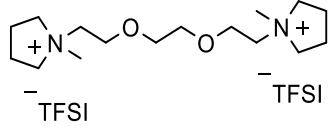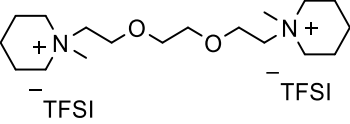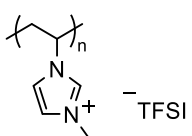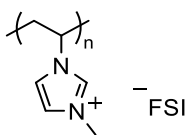
Furthermore, incorporating polymerizable functionalities onto IL cations or anions, offers the possibility to use ILs as monomers, thereby facilitating the creation of corresponding polymeric ionic liquids. The resulting polymers, containing IL species in each monomer, are referred as poly(ionic liquid)s (PILs) and represent another promising material for LiBs.[192] They exhibit advantageous properties of ILs combined with the enhanced mechanical properties of polymers. Synthesized PILs come in various architectures, including polycationic, polyanionic and zwitterionic PILs (Figure 10), and can be obtained as homopolymers, copolymers or crosslinked networks.[193] Combination of the polymers with ILs leads to a more sophisticated morphology of the PILs.[194-197] Similarly to conventional liquid electrolytes, the fluorination of the IL and PIL-components may induce favorable properties, potentially enhancing segregation by forming additional fluorinated domains.[198] This ionic clustering and self-aggregation within PILs can contribute to an elevation in ionic conductivity, with the added possibility that the fluorinated domains might further stabilize the SEI layer, rendering them suitable for applications as valuable polyelectrolytes.[194,199,200] Generally, PILs are synthesized using two different techniques. The first approach involves the synthesis of IL monomer with the desired

Polycation   Polyanion   Zwitterion
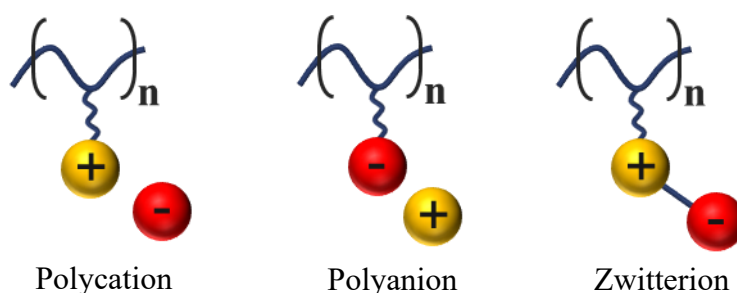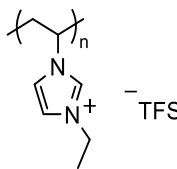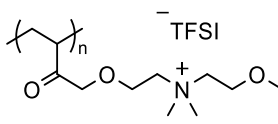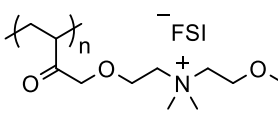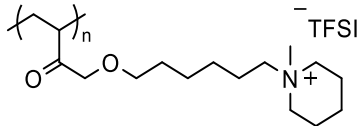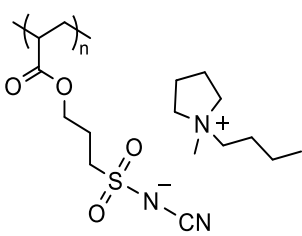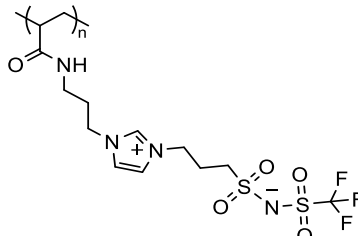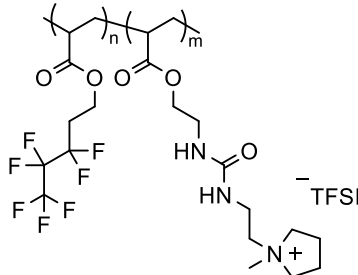
Figure 10. Schematical structure of various types of PILs.

counterion, usually trough an anion exchange reaction, followed by direct polymerization. The second approach entails polymerizing IL monomers with halide counterions, and subsequent anion exchange reaction.[201] The first approach may be advantageous for creating polymers with more complex structures, but it involves more meticulous work and purification to obtain the desired IL monomer. On the other hand, the second approach requires a smaller number of steps for monomer purification but might encounter challenges during the subsequent anion exchange. However, the post-polymerization modification can be advantageous in cases where co-polymers are not easily accessible *via* direct polymerization.[192] Typically, vinyl, methacrylate and methyl methacrylate-based ILs are used for polymerization and selected PILs are presented in Table 3. The conductivity of PILs typically reaches up to 10^{-6} S/cm at RT, although with suitable architectures, such as zwitterionic PIL, higher conductivity values can be achieved even at lower temperatures.

Table 3. Selected DILs and PILs.

DIL/PIL	Structure	Li salt	T (°C)	Conductivity (mS/cm)
IMI-TEA-TFSI[191]		-	25	2.7×10^{-4}
		LiTFSI (1 M)	25	7.1×10^{-5}
Di-imidazolium-TFSI[202]		LiTFSI (0.6 M)	30	1.02×10^{-3}
Di- pyrrolidinium-TFSI[203]		-	25	7.8×10^{-4}
		LiTFSI (1 M)	25	1.0×10^{-4}
Di- piperidinium-TFSI[203]		-	25	2.2×10^{-4}
		LiTFSI (1 M)	25	2.1×10^{-5}
Poly(1-vinyl-3-methylimidazolium) TFSI[204]		LiTFSI (r = 1)	30	8.8×10^{-9}
Poly(1-vinyl-3-methylimidazolium) FSI[204]		LiFSI (r = 1)	30	8.3×10^{-6}

Name	Structure	Salt	Temp	Conductivity
Poly(1-vinyl-3-ethylimidazolium) TFSI[205]		LiTFSI (r = 1)	30	7.5×10^{-6}
Quaternary ammonium-based PIL[206]		-	30	2.2×10^{-6}
Quaternary ammonium-based PIL[206]		-	30	4.0×10^{-6}
Methylpiperidin-iumbased PIL[207]		-	30	6.2×10^{-6}
1-Cyano-1-[(3-(methacryloy-loxy)propyl-sulfonyl)]imide-based PIL[208]		-	25	1.6×10^{-7}
Zwitterionic PIL[209]		LiTFSI (r = 0.9)	0	1.6×10^{-5}
Co-polymer PIL[210]		-	80	3.4×10^{-7}

r = [Li$^+$] / [monomer unit]

1.3.4 Gel polymer electrolytes

The performance of solid polymer electrolytes and PILs can be further enhanced by incorporating the liquid electrolyte to form a gel polymer electrolyte (GPE). Gels, defined as materials with a three-dimensional polymer network with imbedded substantial amount of solvent/liquid,[211,212] possess the unique ability to retain features from both liquids and solids.[213] In GPEs, the mobility of liquid components contribute to conductivity, while the polymer network provides the mechanical strength and flexibility.[214] According to the preparation method, GPEs can be classified into two main categories: physical gels and chemical gels. In physical GPEs the liquid electrolyte is imbedded within a polymer network without any bond
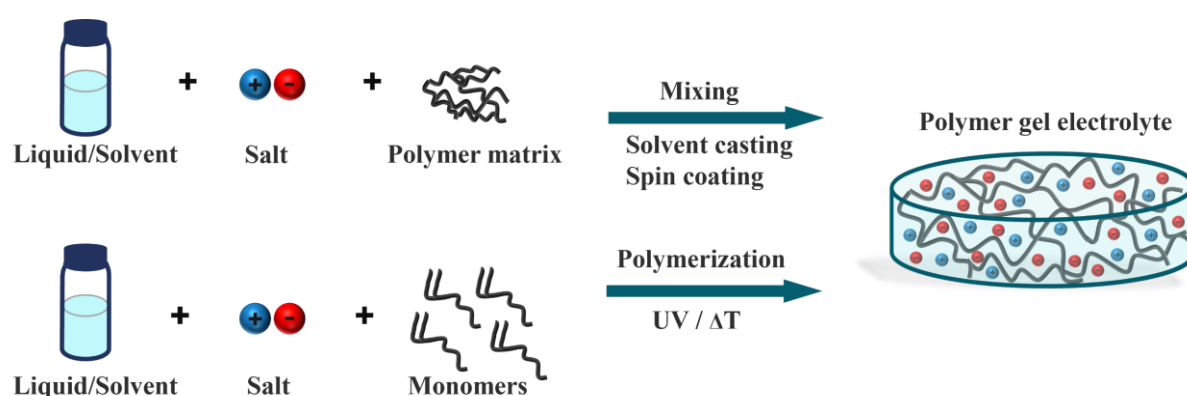
Figure 11. Schematic representation of gel polymer electrolyte preparation.

formation between the polymer and the solvent. On the other hand, in chemical gels, functional groups are crosslinked with the polymer network.[215] In more complex systems the boundary between physical and chemical gels can blur, representing the combination of both types. Furthermore, among various synthesis routes, two common approaches for polymer gel electrolyte are depicted schematically in Figure 11. The first one involves dissolution of polymer in presence of conductive lithium salt and plasticizer, typically followed with the solution casting or spin coating. Alternatively, *in situ* polymerization includes gel preparation form monomers mixed with the liquid electrolyte, lithium salt and consequently polymerizing *via* thermal or photoinitiation. Various polymers have been explored for GPEs including PEO, poly(vinyl alcohol) (PVA), PVdF, poly(methyl methacrylate) (PMMA), poly(acrylonitrile) (PAN), poly(vinylidene fluoride-co-hexafluoropropylene) (PVdF-HFP) etc.[214,216] Selected examples are presented in Table 4.

PAN is one of the most extensively researched polymers for GPEs. An effective method for successful preparation of PAN-based GPE involves the incorporation of IL/Li salt into a
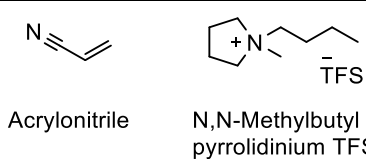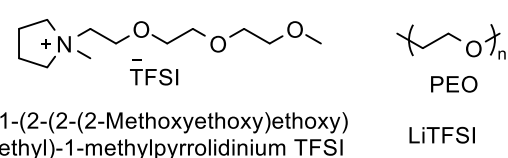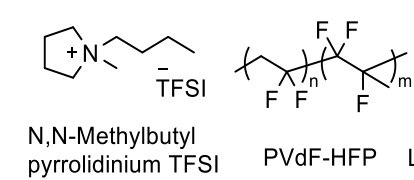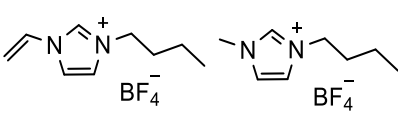
polymer matrix *via in situ* thermal polymerization. *N,N*-Methylbutylpyrrolidinium-TFSI was combined with LiTFSI and acrylonitrile and subsequently polymerized in the formed electrolyte solution.[217] The resulting GPE displays exceptional conductivity up to 1.7×10^{-3} S/cm. Furthermore, the sample maintains mechanical stability, with no observed phase separation. Moreover, resulted GPE outperforms ionic liquid in battery testing and displays capacity up to 141 mAh/g.[217] PEO based GPEs are also extensively explored, encompassing gels containing conventional or IL based electrolytes. For instance, PEO based GPEs with incorporated ether functionalized IL were characterized and investigated. The resulting gel has the ability to form self-standing film *via* hot press, while exhibiting excellent conductivity, reaching up to 6.2×10^{-4} S/cm at 40 °C.[218] The mechanical properties of GPEs can be further enhanced by using PVdF-HFP, known for its semi crystalline structure. PVdF is excellent in terms of structural integrity and electrochemical stability, while the amorphous HFP is effectively trapping large amounts of ionic liquid.[219] Furthermore, PVdF-HFP is characterized by high dielectric constant and pronounced hydrophobicity, leading to numerous PVdF-HFP-based GPEs reported in the literature.[220] For an example, a N-butyl-N-methylpyrrolidinium bis(trifluoromethylsulfonyl)imide/LiTFSI PVdF-HFP GPE was prepared *via* solution casting method using NMP as solvent.[221] The obtained self-standing film exhibits excellent thermal stability above 300 °C, high ionic conductivity of 3.5×10^{-4} S/cm at RT and electrochemical stability up to 4.8 V. Numerous PVdF-HFP based GPEs with various types of ionic liquids and salts and corresponding concentrations have demonstrated impressive ionic conductivity above 10^{-4} even at RT.[222-226]

Poly(ionic liquid)s can serve as polymer matrix for further enhancing GPE performance. An imidazolium-based GPE was synthesized with IL monomer, hyperbranched crosslinker and additional 1-butyl-3-methylimidazolium tetrafluoroborate IL. Such gels display excellent stretchability, superior conductivity (5.8×10^{-4} S/cm at RT) and good thermal stability. Furthermore, the versatility of the material enables fabrication *via* 3D printing for obtaining complex structured specimens.[227] Another noteworthy PIL-based GPE was synthesized by using 2-methacryloyloxyethyl phosphorylcholine and sulfobetaine vinylimidazole as monomers for *in situ* synthesis in the presence of tetraglyme/LiTFSI equimolar solution. Obtaiined zwitterionic copolymer gel electrolyte displays conductivity of 7×10^{-4} S/cm at RT. Interestingly, the elastic moduli can be doubled by changing the monomers ratio, while maintaining the conductivity in the similar range. The zwitterionic gel contains physical crosslinking allowing high degree of plastic deformation and efficient self-healing at elevated

temperatures.[228] By modifying integrated components GPE properties can be tuned. The introduction of an imidazolium ionic liquid monomer bearing a fluorinated alkyl chain into the GPE, along with poly(ethylene glycol) methacrylate and dipentaerythritol penta-/hexa-acrylate as covalent crosslinkers result in the gel with outstanding performance.[229] Fluorinated chain enhances both the ionic conductivity (9.3×10^{-3} S/cm at 20 °C) and lithium transference number. Appetecchi *et al.* prepared solvent free polymer-based electrolyte containing poly(diallyldimethylammonium) bis(trifluoromethylsulfonyl)imide, LiTFSI salt and 1-butyl-1-methylpyrrolidinium bis(trifluoro-methanesulfonyl)imide as ionic liquid. The prepared sample can be classified as gel and is characterized with high conductivity (1.6×10^{-4} S/cm at 20 °C), while displaying the capability to deliver the capacity of 140 mAh/g at 40 °C (Li/LiFePO$_4$ battery cell).[230]

The diverse molecular structures of ionic liquids (ILs) and IL monomers when combined with other GPE components, offer immense potential to tailor properties and unveil cutting-edge materials for the next generation of batteries.

Table 4. Properties of selected gel-polymer electrolytes (GPEs).

Entry	Gel structure / components	T (°C)	Conductivity S/cm	Ref.
1	Acrylonitrile, N,N-Methylbutyl pyrrolidinium TFSI, LiTFSI	25	1.7×10^{-3}	[217]
2	1-(2-(2-(2-Methoxyethoxy)ethoxy)ethyl)-1-methylpyrrolidinium TFSI, PEO, LiTFSI	40	6.2×10^{-3}	[218]
3	N,N-Methylbutyl pyrrolidinium TFSI, PVdF-HFP, LiTFSI	RT	3.5×10^{-4}	[221]
4	1-Vinyl-3-butyl imidazolium tetrafluoroborate, 1-Butyl-3-methyl imidazolium tetrafluoroborate, Hyperbranched acrylate	RT	5.8×10^{-4}	[227]

5	Tetraglyme / Zwitterioninc PIL / LiTFSI	RT	7×10^{-4}	[228]

Tetraglyme

Zwitterioninc PIL

LiTFSI

5 RT 7×10^{-4} [228]

F-ionic liquid

DPEPA

R = H or

PEGMA

6 20 9.3×10^{-3} [229]

PIL

TFSI

N,N-Methylbutyl pyrrolidinium TFSI

LiTFSI

7 20 1.6×10^{-4} [230]
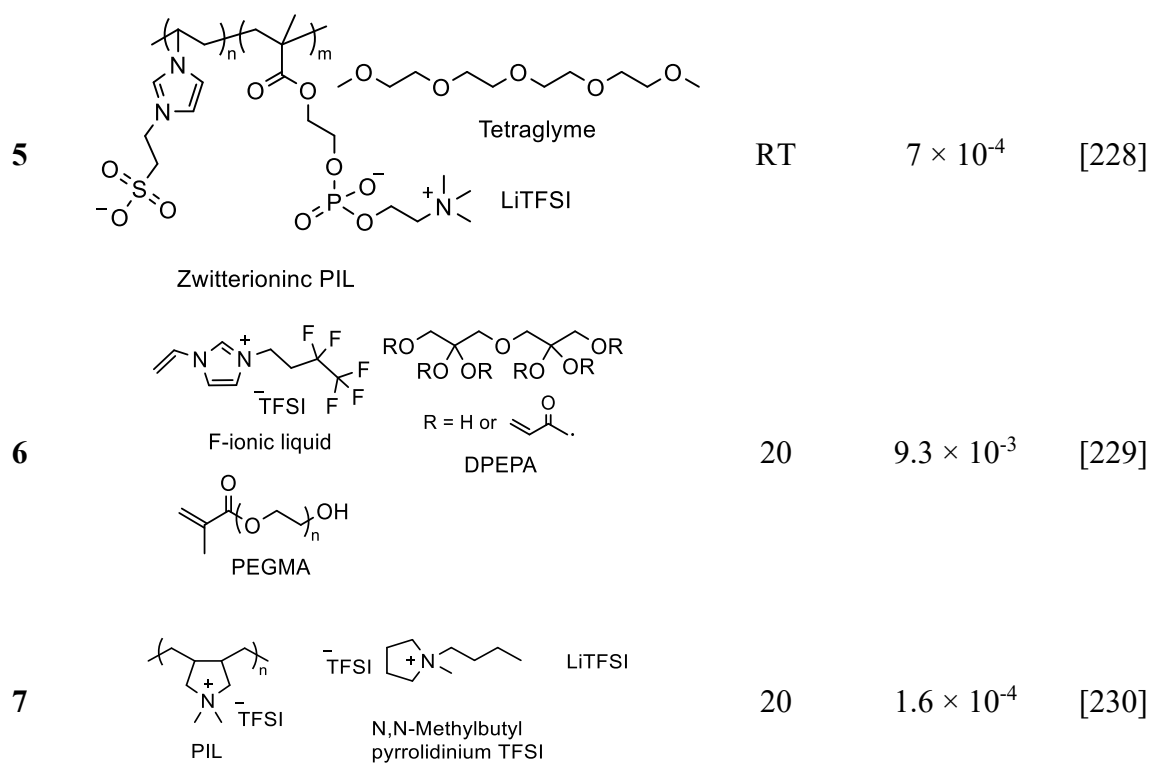
1.3.5 Solid-state electrolytes

Solid state electrolytes (SSEs) stand out as one of the safest alternative materials for lithium batteries, with lithium-ion conductive ceramics being a part of this category.[231] These ceramics are typically characterized with outstanding moduli (> 1 GPa), effectively addressing dendrite formation and growth concerns while demonstrating remarkable thermal and electrochemical stability.[127] However, to make SSEs commercially competitive, certain limitations need to be tackled. Despite their superior moduli, these materials tend to be brittle/stiff, posing challenges for modern battery manufacturing processes that necessitate some degree of elasticity, such as roll-to-roll techniques.[232] The issues related to interfacial stability between electrolyte and electrode impacts the performance of SSE, impeding ion transport. Moreover, the complex procedures involved in manufacturing ceramic electrolytes, including sintering and high-temperature treatments, significantly elevate their production costs. The ionic conductivity of SSEs, while capable of reaching moderate values, still requires further enhancement to achieve conductivity values around 1×10^{-3} S/cm at RT. Numerous types of SSE materials have been developed in the past 50 years. The most notable inorganic solid electrolytes are NASICON, Hydride, LiPON, Sulfides, Perovskite, Antiperovskite and Garnet.[233-239] The ionic conductivities of common SSEs with selected material compositions are shown in Table 5.

Although, the conductivities are reaching the values of conventional electrolytes, SSEs still requires further understanding and improvement to potentially overcome performance and manufacturing challenges and direct the industry towards advanced, high energy density solid state batteries.

Table 5. Selected solid state inorganic electrolytes.

SSE	Chemical formula	Conductivity S/cm	Ref.
NASICON	$LiM_2(PO_4)_3$	$10^{-7} - 10^{-3}$	[127,240]
Hydride	$Li_2(BH_4)(NH_2)$, $LiBH_4-LiX$	$10^{-7} - 10^{-4}$	[127,231]
LiPON	LiPON	10^{-6}	[231]
Sulfides	$Li_{10}GeP_2S_{12}$, $Li_2S-P_2S_5$	$10^{-7} - 10^{-3}$	[127,231]
Perovskite	$Li_{0.34}La_{0.51}TiO_{2.94}$	$10^{-6} - 10^{-3}$	[240]
Antiperovskite	$Li_3O(Cl, Br)$	$10^{-5} - 10^{-3}$	[231]
Garnet	$Li_7La_3Zr_2O_{12}$	$10^{-6} - 10^{-3}$	[231]

M = Ti, Ge, Zr, Sn,   X = Cl, Br, I

1.3.6 Composite electrolytes

Composite or hybrid electrolytes (CEs) emerge as a promising class of materials for potential electrolyte applications with advanced properties. Typically, CEs involve blending a polymer with inorganic/ceramic nanofillers (Figure 12), a combination that not only improves the mechanical properties of polymers but also enhances the ionic conductivity. The initial discovery highlighting the positive impact of ceramic nanofillers (α-alumina particles) on PEO-based electrolyte,[241] led to extensive investigations of numerous compositions.[242] Inorganic fillers are classified into two distinct categories based on their nature: passive and active fillers.[243] Passive fillers, although not conductive by nature, promote the conductivity of host polymer. In contrast, active fillers (Section 1.3.5) exhibit inherent ionic conductivities. In the context of this work, the more relevant category is that of passive fillers, which commonly encompasses nanoparticles like Al_2O_3, $LiAlO_2$, SiO_2, TiO_2 and ZrO_2 (Table 6).[244-247] The addition of nanoparticles impacts the polymer morphology, lowers the degree of crystallinity and consequently promotes ion transport.[248] The extend of this effect is strongly depended on the type and size of added particles.[249]
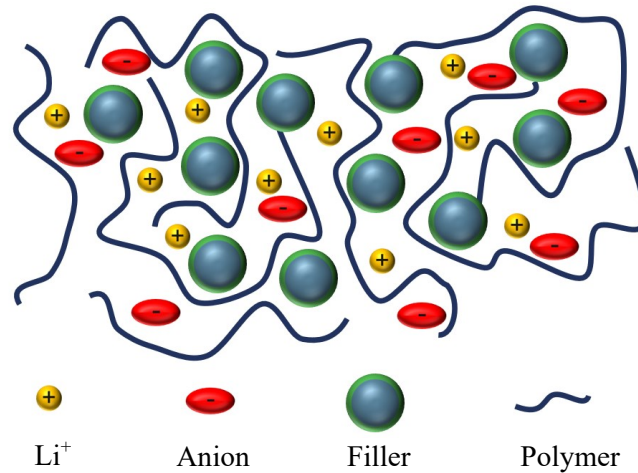
Figure 12. Schematic structure of a composite electrolyte.

Inorganic fillers not only increase conductivity by reducing crystallinity but also create percolation channels with fast ion transport capabilities. The formation of these channels is the consequence of Lewis acid-base interaction between the fillers surface, the polymer and added lithium salt. SiO_2 has been one of the most widely used fillers due to the hydroxyl rich surface, which enables strong interaction and consequently leads to drastic improvement of mechanical properties. In a PEO-LiClO$_4$ electrolyte, blending of SiO_2 nanoparticles with two different surface chemistries (one with silanol groups and the other with octyl chains on the surface), resulted in a significant increase in conductivity from $10^{-8} - 10^{-7}$ S/cm to 2.3×10^{-5} S/cm at room temperature.[250] Silica nanoparticles with different morphology can further improve the properties of polymer electrolyte. Incorporated SiO_2 three-dimensional framework into PEO based electrolyte acts as a robust backbone for the electrolyte, elevating the elastic modulus by an order of magnitude. Simultaneously the large surface area of SiO_2 promotes anion adsorption, consequently enhancing the conductivity (6×10^{-4} S/cm at 30 °C).[251] In another study, silica nanoparticles in combination with Al_2O_3 were blended with PVdF-HFP and the conductivity reached the 10^{-3} S/cm range.[252] A more effective approach for incorporation of silica nanoparticles into polymer matrix was reported recently. Unlike the traditional blending method PEO composite was prepared by *in situ* synthesis of SiO_2 in a polymer electrolyte.[253] This approach established much stronger interactions within the sample and more effective reduction of PEO crystallization. The composite with LiClO$_4$ achieved the conductivity of 1.2×10^{-3} S/cm at 60 °C and excellent electrochemical stability of 5.5 V. In another study, a less commonly used nanofiller, Y_2O_3 doped ZrO_2 nanowires containing positively charged oxygen vacancies, was incorporated into PAN-based CE.[254] The ionic conductivity compared to particle free polymer electrolyte was increased to 1.07×10^{-5} S/cm from 3.62×10^{-7} S/cm

at 30 °C. The positive-charged oxygens in these nanowires are presumed to facilitate lithium-ion release through association with anion groups.

Table 6. Selected composite electrolyte materials.

Polymer/salt	Filler	Filler (wt%)	T (°C)	Conductivity (S/cm)
PEO/LiClO$_4$[250]	SiO$_2$	10	25	2.3×10^{-5}
PEO/LiTFSI[251]	SiO$_2$[#]	≈ 22	30	6×10^{-4}
*PVdF-HFP/ LiFAP[252]	Al$_2$O$_3$/ SiO$_2$	2.5	25	10^{-3}
PEO/LiClO$_4$[253]	SiO$_2$	≈ 10	60	1.2×10^{-3}
PAN/LiClO$_4$[254]	Y$_2$O$_3$/ ZrO$_2$	15	30	3.62×10^{-7}
PEO/LiClO$_4$[246]	Al$_2$O$_3$	10	30	1.5×10^{-5}
PEO/LiClO$_4$[246]	TiO$_2$	10	30	2.3×10^{-5}

* Contains EC/ DEC, # aerogel

Surface modification of nanoparticles is another possible approach for tuning properties of CEs. Recently, successful introduction of imidazolium-based ionic liquids on the silica nanoparticles was reported.[255-257] The performance of these modified nanoparticles was tested with a propylene carbonate/LiTFSI mixture. Although the resulting blend does not include a polymer, it can arguably be considered a composite electrolyte. The blend demonstrated the positive influence of ionic liquid modification: the incorporation of nanoparticles drastically improved mechanical properties and the dendrite suppression ability. Simultaneously, ionic conductivity was further enhanced, approaching 10^{-3} S/cm at RT. Furthermore, modified particles exhibited better dispersity, highlighting the importance and potential application of surface modification.

1.4 Additive manufacturing of batteries

Additive manufacturing (AM), also known as 3D printing, gained an increased attention for manufacturing of batteries. Implementing 3D printing offers several advantages over traditional methods such as design flexibility, complex battery architecture, reduced waste materials, cost-effectiveness and potentially improved electrochemical performance.[258-261] The current technology relies on two-dimensional current collectors, which can negatively impact the performance due to extended ion transport channels. In contrast, 3D architecture can amplify the surface area, consequently increasing the energy density. Furthermore, it reduces ion transport pathways and lowers resistance.[262] Most common AM techniques encompass materials extrusion (including fused deposition modeling (FDM) and direct ink writing (DIW)), powder bed fusion (laser sintering (SLS)), vat polymerization (stereolithography (SLA)), material jetting (inkjet printing (IJP)), binder jetting, sheet lamination and directed energy deposition.[263,264] The initial step in additive manufacturing involves digital modeling, where a desired 3-dimensional structure is created using computer-aided design (CAD), followed by the printing process. However, the currently used materials for batteries do not meet the requirements for successful AM. Each printing technique has its distinct advantages but also some limitations.[258,265,266] For instance, FDM (Figure 13) is mainly suitable for thermoplastic polymers. It is a very cost-effective and convenient method for printing but offers the lowest resolution (≈ 50 µm) compared to other techniques. In the FDM process, a polymer filament is fed into the 3D printer, where it is heated and extruded through the nozzle. An alternative FDM device is equipped with the storage tank (Figure 14).[267] In this case, the process does not rely on the filament fed; instead, the solid polymer is directly placed into a heatable storage tank. With increasing temperature, the polymer flows to the printing head and
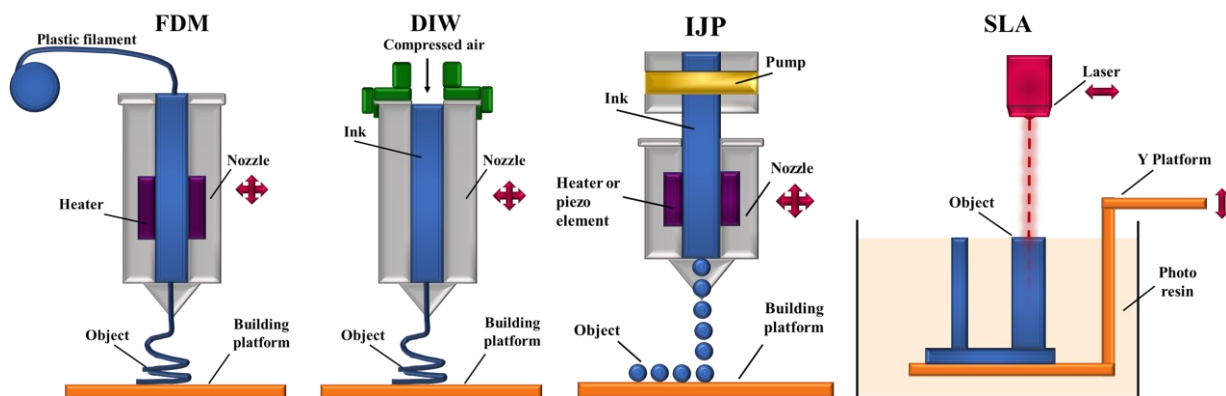
Figure 13. Common 3D printing techniques for battery manufacturing. Redrawn with permission from [259]. © 2020 Elsevier Inc.
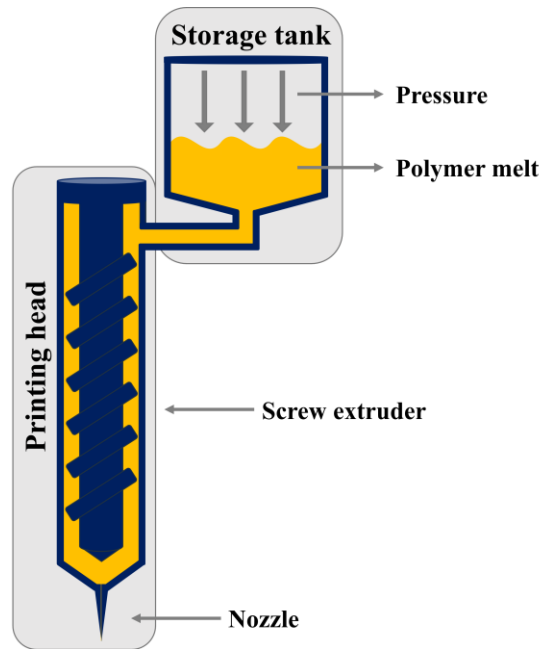
Figure 14. Schematic representation of extrusion-based 3D printer.

is extruded from the nozzle, rapidly solidifying and fusing with the previously printed layer. It's important to note that various parameters of the 3D printer can significantly influence the print quality and overall printability. Achieving optimal print quality includes adjusting temperature, nozzle diameter, extrusion speed, and the speed of printing head movement. The printable material is also required to have distinct mechanical properties. The melt flow/viscosity should not be too low otherwise the extrusion is too liquid, and no shape stability can be obtained. Moreover, high viscosity restricts the continuous extrusion of the polymer. One possible approach to investigate the materials printability is to conduct rheology measurements, which simulate the shear behavior of printer and can be compared to required/predetermined optimal values. DIW (Figure 13), another widely employed technique, can offer much higher resolution (≈ 1 µm) and is simultaneously the cost-effective method applicable for plastics and composites. Nevertheless, materials suitable for DIW often require additives to meet mechanical property requirements. SLA (Figure 13) relies on UV curing to produce resin structures with the resolution ≈ 10 µm, providing high efficiency and material versatility due to relatively flexible viscosity requirements. However, it faces challenges with multicomponent printing and requires photo responsive additives. SLS also can be applied for polymeric materials offering relatively high resolution (≈ 30 µm) but is one of more expensive and less time-efficient methods. Materials jetting is suitable for printing polymers and ceramic materials (Figure 13), enabling the creation of 3D structure, but it might have slower processing

31

speeds than other techniques and lower surface quality, potentially posing problems in the final product. Binder jetting, on the other hand, can be advantageous for producing multi-component products with good resolution, yet the weak mechanical properties can become an issue. The current state of additive manufacturing for batteries encounters various challenges, particularly in integrating a specific formulation of battery components that meet both physical and electrochemical property requirements for printing. Extensive efforts have been devoted towards improving the electrodes printability and numerous publications highlight the significant advancement over the past few years.[265] However, the electrolyte remains a bottleneck of the technology.[262]

The successful printability of graphene-based anode has been demonstrated by FDM. To achieve the required properties a graphite polylactic acid filament was prepared. The introduction of plasticizers, such as PEGDME, effectively reduced ductility and stiffness, enabling high resolution printing. Moreover, the theoretical capacity was reached with the optimized composition containing 10 wt% carbon conductive additives.[268] In the case of a silicon-based anode, inkjet printing was effectively utilized. The choice of additives plays a crucial role in achieving optimal printability. The printed film silicon anode with poly(3,4-ethylenedioxythiophene)-poly(styrene sulfonate) binder exhibits excellent cyclability (over 1000 cycles) and capacity retention ability.[269]

Various cathode materials can be fabricated *via* AM with considerable research focused on LiFePO$_4$. Li$_4$Ti$_5$O$_{12}$ (LTO) (as anode)/LFP micro batteries were printed, demanding meticulous compounding of printable inks to ensure printability, enabling reliable flow and adhesion between layers.[270] In the final stage, inks containing approximately 60% of active material were printed on the gold current collector in an interdigitated structure. Assembling the batteries involved placing a PMMA form on the structure, filling it with liquid electrolyte, and sealing it. The resulted 3D printed batteries exhibit a high areal energy density of 2.7 mW/cm^2.

Electrolytes are typically printed *via* extrusion or SLA techniques. Printing electrolyte can partially solve the interfacial problem for solid state batteries and form strong interfaces.[258] In a successful application, a 3D Archimedean spiral structure was printed *via* SLA using PEO diacrylate, succinonitrile, and LiTFSI mixture. This printed structure effectively shortens the pathway for lithium-ion conduction, displaying conductivity up to 3.7×10^{-4} S/cm. Furthermore, the observed reinforced interface enhances the performance of the cell, reaching superior cyclability compared to the structure-free cell (128 mAh/g vs. 32 mAh/g after

250 cycles).[271] DIW is also applicable for electrolyte printing. $Li_7La_3Zr_2O_{12}$ containing ink was printed in various patterns with the resolution ranging from 12.5 to 125 µm. Cell testing reveals low area specific resistance (22 Ω cm^2) presumably due to improved interfacial contact.[272]

Implementing 3D printing techniques with enhanced materials can be beneficial for next generation batteries. Yet, several challenges need to be addressed to make AM more attractive for larger scale manufacturing. The rapid development of printing technologies combined with the recent significant achievement at the laboratory scale unveils exciting possibilities for future battery manufacturing.

1.5 Concept of self-healing and re-processability

Batteries play a critical role in transitioning towards renewable energy sources and electrifying transportation sector. The large scale of manufacturing and increasing demand arises concerns about responsible resource consumption and sustainability.[84] The next generation of batteries is expected not only to exhibit enhanced performance but also to exhibit extended lifespan and facilitate efficient recyclability. Integration of smart functionalities in batteries represents one of the possible approaches to extend cycle life. Enabling self-healing, the ability to repair certain types of damage on itself, enhances the overall performance and lifespan of energy storage devices.[273,274]

Inspired by remarkable ability to self-heal (SH) observed in living organisms, extensive research and development have been dedicated for enabling autonomous self-healing of materials. This encompasses polymers capable of self-repair *via* incorporation of various functional groups. The SH material can be classified into two primary groups based on the
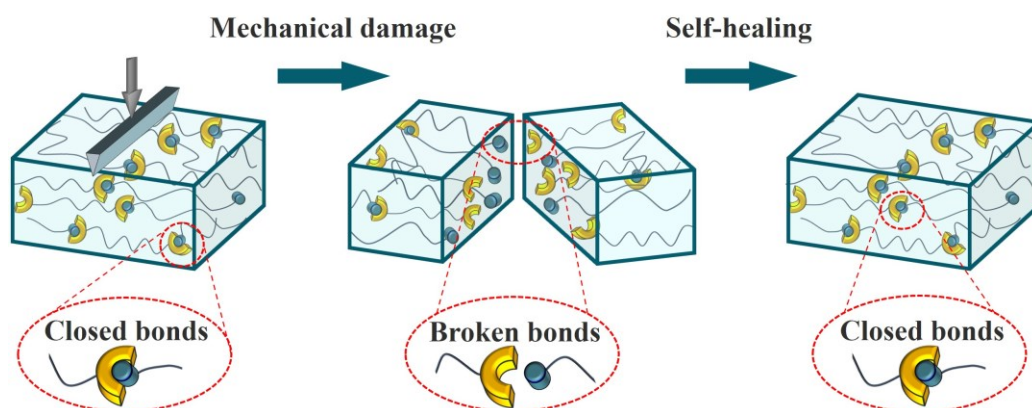
Figure 15. Illustration of intrinsic self-healing *via* dynamic/reversible bonds.

underlying mechanism of SH: extrinsic and intrinsic. The extrinsic materials exhibit SH by utilizing embedded encapsulated agents, which are released upon mechanical damage, thereby initiating reactions to facilitate repair. Currently two different approaches are employed for enabling extrinsic SH: microcapsules and vascular networks.[275] Microcapsules are spherical structures that carry the self-healing agent (e.g. monomers, catalysts, resins, adhesives etc.) dispersed in polymeric materials. Inspired by the circulatory system of living organisms, vascular systems involve the imbedded interconnected network within the polymeric materials that carries the healing agent. Upon sustaining mechanical damage, the healing agent is released, rapidly initiating repair with high efficiency. Although extrinsic SH is effective and efficient, its limitations often revolve around supporting multiple rounds of self-repair and ensuring the compatibility of the polymer matrix with the vascular system or capsules. In contrast, intrinsic SH achieve reversible self-repair by incorporating dynamic/reversible covalent bonds or supramolecular interactions within the material,[276-278] with an ability to reform after being broken during the SH processes (Figure 15). Polymeric materials can be
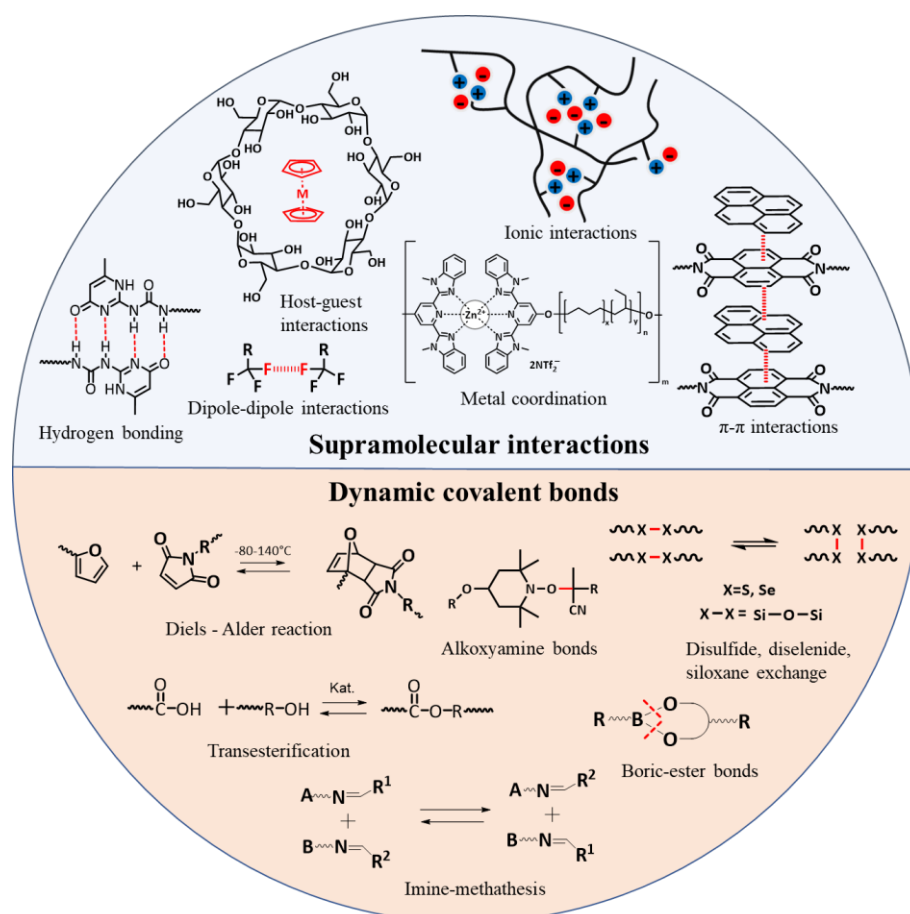
Figure 16. Various supramolecular interactions and dynamic covalent bonds for achieving self-healing ability in polymers. Taken with permission from [40].

tailored to modulate strength and dynamics *via* altering their chemical nature, and consequently the type of interaction they possess. The Figure 16 displays the most commonly used chemical interactions employed to achieve intrinsic self-healing.

1.5.1 Supramolecular interactions in self-healing polymers

Supramolecular self-healing polymers feature the presence of a multitude of dynamic, reversible non-covalent intermolecular interactions, which are equilibrating between open and closed state. Designing a polymer with the ability for multiple self-healing events requires a more sophisticated approach beyond merely introducing supramolecular interactions. These interactions significantly impact the physical properties of polymers such as viscosity, elasticity, strength and can change the arrangement of polymer chains. When a self-healing polymer is subjected to mechanical stress or damage, the relatively weak supramolecular interactions break, creating unconnected species. These spices have the ability to recombine, facilitating the healing of the material. The process can be repeated many times, making such polymers attractive candidates for various applications, including battery technologies.

Supramolecular networks can be achieved *via* plethora of interactions such as hydrogen bonding, π-π stacking, metal-ligand coordination, ionic interactions, dipole-dipole interactions, host-guest interactions and van der Waals interactions.[40,279,280] Hydrogen bonding (HB),

$$K_{assn.} = \frac{[AB]}{[A] \times [B]} = \frac{k_a}{k_d}$$
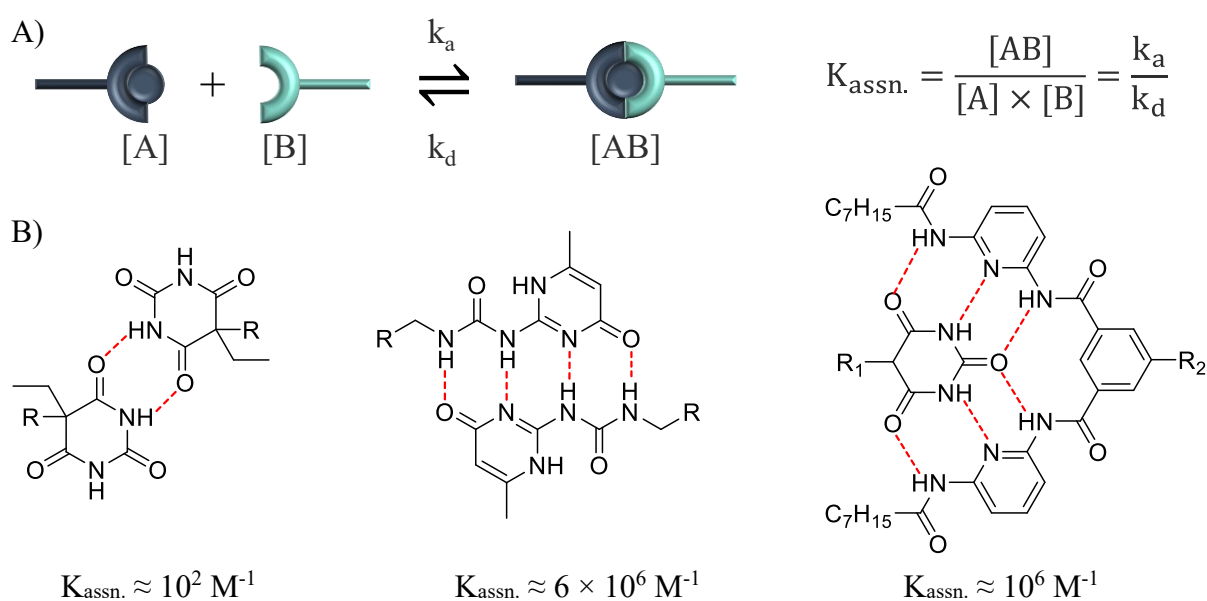
Figure 17. A) Equilibrium between hydrogen bond forming moieties, B) Selected hydrogen bond forming moieties and corresponding $K_{assn.}$ in solution.

35

although weaker than ionic and covalent bonds with energy between 5 − 40 kJ/mol, plays an important role in SH polymers and it is one of the most frequently involved type of interactions in supramolecular chemistry. The strength of the interaction is drastically increasing when multiple bonds are formed. Moreover, the binding strength varies based on the arrangement of donor and acceptor units. Examples of such enhanced interactions include ureidopyrimidinone (UPy), barbiturate groups and Hamilton wedges. The hydrogen forming moieties are always in equilibrium, which can be expressed by the association constant ($K_{assn.}$) (Figure 17A). $K_{assn.}$ can be calculated as a ratio of the rate of association and rate of dissociation, $K_{assn.}$ expressing the binding constant of the system and indicating the degree of bonds association. A higher $K_{assn.}$ value refers to a stronger affinity between the hydrogen forming moieties. Moreover, the rate of dissociation is considered as a measure of bond and interaction strength. Selected hydrogen bonding systems with corresponding $K_{assn.}$ in solution are shown in the Figure 17B. Within a bulk polymer system, the interactions are complex, with hydrogen bonds typically surrounded by polymer chains or other self-healing moieties. This configuration introduces the potential for additional influences, significantly impacting the materials self-healing abilities. Numerous supramolecular polymeric materials with the self-healing abilities have been reported.[276,279,281-283] One approach for achieving SH is end group functionalization. Polyisobutylene (PIB) after the end group modification with Hamilton wedge or barbituric acid displays the formation of solid-like material.[284] The material not only exhibits drastic improvement of mechanical properties but also displays the ability of self-healing. The specimen cut into two pieces can reconnect and restore its integrity in 24 hours and in 48 hours the damage is fully invisible. Rubber like polymer was reported by Cordier *et al.*.[285] The material was prepared based on functionalized di- and triacids, which were condensed with diethylene triamine and then reacted with urea. After adding a distinct amount of dodecane for lowering the T_g rubber like material was formed. It displayed superior mechanical properties but more impressively the SH ability and recovery of mechanical properties.

Supramolecular polymers are also attractive for extrusion-based 3D printing. Low T_g PIB was successfully tuned for 3D printability by end group modification with hydrogen bond forming moieties (barbiturates).[267] Such approach is based on the formation of supramolecular clusters, resulting in increased mechanical strength. The clusters can be destroyed at elevated temperatures during FDM and reformed when the polymer cools down instantly after the extrusion. Moreover, adding nanofillers to supramolecular polymers enhances the cluster formation and improves printability.

Supramolecular chemistry holds promise for improving current battery technologies. It not only introduces the potential for batteries to possess partial self-healing abilities, but also has the capability to enhance the manufacturing processes *via* AM.

1.5.2 Supramolecular interactions in polymer electrolytes

Incorporating SH capabilities into batteries presents a substantial opportunity to prolong their lifespan. This can be achieved by employing polymeric materials with SH ability as passive or active component of the system, e.g. as polymer electrolyte or as a binder. Remarkable progress have emerged in self-healable polymer electrolytes over the past decade.[40,286] Self-healing polymer-based electrolytes can be classified into three main types: solid polymer electrolytes, composites and polymer gel electrolytes. As discussed previously in the section 1.3.2 solid PEs are typically consisting of polymer mixed with lithium conductive salts. The selected samples of PEs without the inclusion of supplementary plasticizers or liquid electrolytes, while simultaneously exhibiting SH features are presented in Table 7. Hydrogen bonding stands as widely explored supramolecular interaction in the pursuit of achieving SH properties in electrolytes. Successful incorporation of UPy moieties in PEO-based electrolyte was realized *via* reversible addition-fragmentation chain transfer (RAFT) polymerization of PEGMA and UPy containing methacrylate monomer (entry 1).[287] The synthesized random copolymer was dissolved with LiTFSI for fabricating PE *via* solution casting. The supramolecular interactions have remarkable influence on PEO electrolyte. The material demonstrates self-healing ability at ambient temperature, achieving elongation greater than 2000 %, simultaneously reaching conductivity up to 1.1×10^{-4} S/cm at 60 °C. Furthermore, the material shows stable battery cycling performance with retained initial capacity. The mechanical properties of PE can further be increased by combining supramolecular and covalent crosslinking. Similar composition with covalent crosslinking was prepared by adding the third monomer polyethylene glycol-bis-carbamate dimethacrylate (entry 2). Forming the dual network, combination of hydrogen bonding and covalent bonding ensures structural stability while simultaneously sustaining the SH capability. The efficiency of SH characterized by tensile testing is reaching 84 %. However, covalent crosslinking has its drawbacks in terms of ionic conductivity, which is reduced almost one order of magnitude compared to non-crosslinked sample with similar salt content.

UPy moieties were successfully incorporated in poly(vinyl alcohol) (PVA).[288] The PE composition contained dangling PEO chains for enhancing the conductivity reaching

1.5 × 10⁻⁴ S/cm at 60 °C and providing wide electrochemical stability window (5.0 V vs. Li/Li$^+$). More interestingly, the combination of UPy/PVA/PEO exhibits shape memory properties, transforming from temporary to permanent shape under application of heat. The PVA main chains and PEG side chains played a crucial role in controlling the temporary shape, while the permanent shape was sustained by a physical crosslinking *via* UPy moieties. Moreover, quadrupole hydrogen bonds maintain the self-healing ability of PE. The material is a functional electrolyte in lithium metal battery, displaying high discharge capacity (145 mAh/g) and high columbic efficiency (99 % at 0.1 C).

Although hydrogen bonding systems are predominantly used, other types of supramolecular interactions are also applicable for polymer electrolytes. Imidazolium-based ionic liquid monomer was copolymerized with ethyl acrylate monomer, exhibiting SH ability due to ionic interactions.[289] The PIL contains bulky TFSI anion, which further increases the polymers segmental mobility of polymer chains and enables self-healing (at 55 °C). Additionally, the material displays excellent mechanical properties, reaching elongation of 877 % on tensile test. However, ionic conductivity (1.6 × 10⁻⁷ at RT) requires further improvements. Another PIL with supramolecular ionic interaction for SH and enhanced conductivity was reported by Zhu *et al.*[290] The PE is composed of PEO-PIL block copolymer, which was incorporated into PEO (entry 5). The composition exhibits outstanding mechanical properties (tensile stress > 3.4 MPa, elongation > 860%) and self-healing ability in under 30 min at 60 °C. Moreover, the block architecture reduces the crystallinity of PE, inducing microphase separation and promoting faster lithium-ion transport.
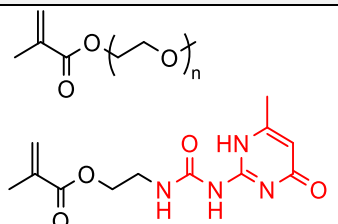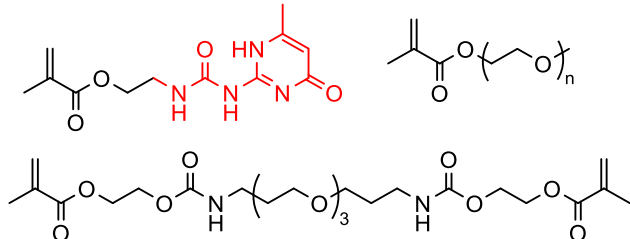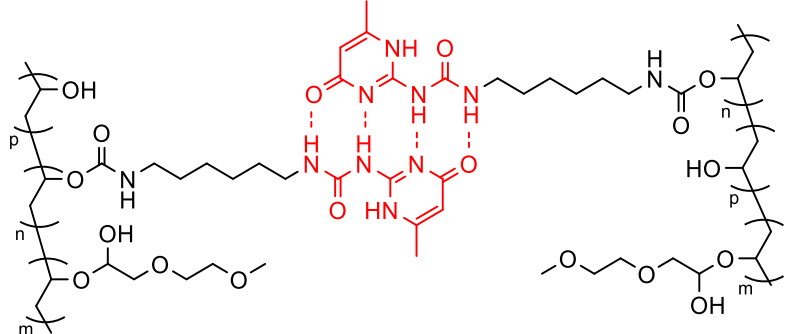
Composite material preparation offers another avenue for enhancing the properties of PEs. A self-healing PE was prepared by blending surface modified silica nanoparticles (with UPy moieties) with PEG-UPy copolymer (entry 6).[291] The surface modification not only influences the mechanical stability (tensile stress up to 120 kPa) of the final PE but also positively impacts the conductivity (8 × 10⁻⁴ S/cm at 30 °C). The conductivity is increased due to better dispersity compared to the sample with non-modified particles. UPy surface forms strong supramolecular interactions (hydrogen bonds) enabling self-healing and good compatibility with Li metal for solid state batteries. Self-healing composites electrolytes can also be created based on ionic interactions (entry 7). PIL based on dicationic repeating unit was employed as a host for composite PE containing boron nitride nanosheets and additional imidazolium-based IL.[292] Nanofillers act as mechanical reinforcements and provide lithium ion transfer channels. The
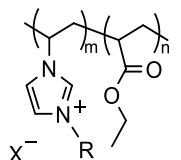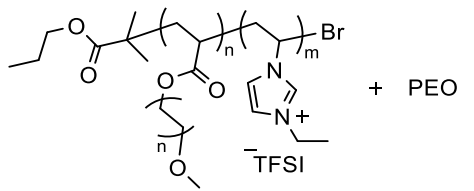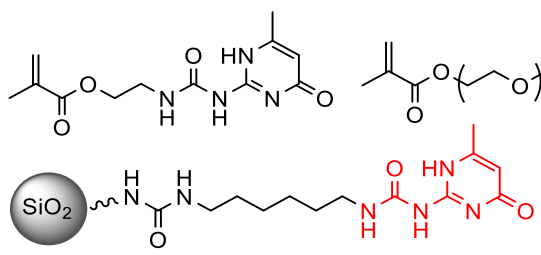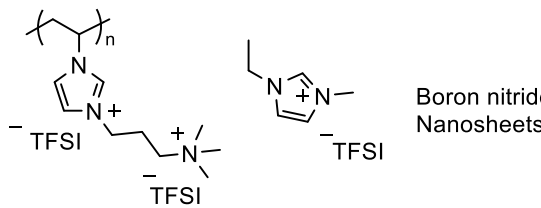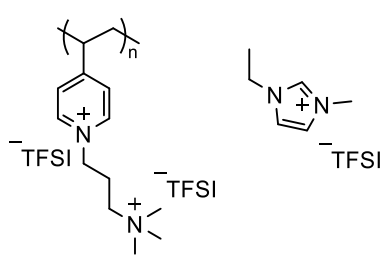
optimized PE exhibits conductivity up to 1.6×10^{-4} S/cm at 25 °C while the ionic interactions ensure SH ability even at RT.

The concept of self-healing *via* supramolecular interactions can also be successfully introduced into gel polymer electrolytes. Dicationic PIL was combined with the additional 1-ethyl-3-methylimidazolium bis(trifluoromethylsulfonyl)imide (EMIMTFSI) and LiTFSI to form a self-heling electrolyte (entry 8).[293] The GPE can retain 45 wt% of the additional ionic liquid, which enhances the conductivity (1.3×10^{-4} S/cm). The amount of IL plays a crucial role as after reducing the content down to 40 % the conductivity drops almost one order of magnitude (3.6×10^{-5} S/cm). Self-healing GPE exhibits high initial capacity in lithium metal battery. PIL can be combined with UPy moieties in the polymer backbone creating additional supramolecular interaction (HB and ionic interaction) (entry 9).[294] The prepared random copolymer is mixed with 69 wt% 1,2-dimethyl-3-ethoxyethylimidazolium bis(trifluoromethylsulfonyl)imide (DE-IM/TFSI) to form the highly conductive (1.5×10^{-4} S/cm at RT), non-flammable SH gel. Moreover, GPE exhibits the ability to suppress dendrite growth, demonstrated in excellent battery performance with 99.7 % columbic efficiency after 120 cycles (at rate of 0.2 C). Another method for preparation of GPE includes soaking the polymer precursor in liquid electrolyte. This approach was applied for the preparation of UPy containing GPE (entry 10).[295] The polymeric material contained PVdF-HFP/PEO/PEG-UPy as polymer matrix and it displays good self-healing ability combined with high ionic conductivity. Highly crosslinked GPE containing commercial electrolyte was also reported (entry 11).[296] The polymer matrix consists of end-group modified PEG (with UPy groups) which was subsequently incorporated into the GPE *via* UV polymerization. The precursor mixture, containing all electrolyte components and photo initiator was cured under UV in 5 min making the preparation method very convenient and easily accessible. The resulting GPE displays good mechanical properties, self-healing ability at elevated temperature due to supramolecular interactions and excellent ionic conductivity.

Supramolecular chemistry combined with different types of polymeric electrolytes and additives holds potential for creating safer, self-healable, high-performance materials. However, it requires careful design and component selection to optimize properties without compromising other features.

Table 7. Selected self-healing solid polymer electrolytes (entry 1–6), composite electrolytes (entry 6–7) and gel polymer electrolytes (entry 8–11) with supramolecular interactions.

Entry	Composition	Healing Mechanism	Healing condition	Additives	Conductivity S/cm	Ref.
1		HB	RT, 2 h	LiTFSI (r = 20)	1.1×10^{-4} (60 °C)	[287]
2		HB	60 °C, 2 h	LiTFSI (r = 16)	1.72×10^{-5} (60 °C)	[297]
3		HB	60 °C, 1 h	LiClO$_4$ (r = 11)	1.5×10^{-4} (60 °C)	[288]

		Interaction	Conditions	Salt	Conductivity	Ref.
4		Ionic interaction	55 °C, 7.5 h	-	1.6×10^{-7} (RT)	[289]
5	+ PEO	Ionic interaction	60 °C, 0.5 h	LiTFSI (10 %wt)	1.1×10^{-5} (30 °C)	[290]
6	SiO₂	HB	RT, 1 h	LiClO$_4$ (r = 16)	8×10^{-4} (30 °C)	[291]
7	Boron nitride Nanosheets	Ionic interaction	RT, 1 h	LiTFSI	1.6×10^{-4} (25 °C)	[292]
8		Ionic interaction	RT, < 1 h	LiTFSI (10 %wt) EMIMTFSI (45 %wt)	1.3×10^{-4} (RT)	[293]

#		Interaction	Conditions	Electrolyte	Conductivity	Ref
9		HB, ionic interaction	55 °C, 1 h	LiTFSI (13.8 %wt) DE-IM/TFSI (69 %wt)	1.5×10^{-3} (RT)	[294]
10		HB	RT, 15 h	Soaked in electrolyte	7.5×10^{-4} (25 °C)	[295]
11		HB	40 °C, 3 h	1 M LiPF$_6$ in EC/DMC (67 wt%)	1×10^{-3} (40 °C)	[296]

HB – Hydrogen bond, r = EO/ Li$^+$

1.5.3 Dynamic covalent bonds in self-healing polymers

Covalent Adaptive Networks (CANs) represent a novel class of materials characterized by dynamic covalent crosslinking. Unlike supramolecular networks, dynamic covalent bods are characterized with higher bond energy, leading to a more substantial impact on mechanical properties. Polymer materials are commonly categorized into two main classes: thermoplastics and thermosets. Thermosets are polymer networks which offer three-dimensional stability and rigidity, making them attractive for a wide range of applications. The permanent crosslinking in thermosets poses challenges to reprocessability and reshaping, consequently restricting the reusability of such materials. On the other hand, thermoplastics, characterized by weak or no crosslinking, allow for reprocessibility, recyclability, and reshaping. However, their mechanical properties are inferior compared to thermosets, which limits their suitability in applications where dimensional stability is crucial. CANs, by their nature, are situated between thermoplastic and thermoset polymers.[298,299] They offer dimensional stability (like thermosets) due to crosslinking but simultaneously they can be reprocessed (like thermoplastics) due to the dynamic nature of crosslinking. CAN materials offer a compelling solution for replacing conventional thermosets and addressing their recyclability issues. Dynamic covalent crosslinking significantly affects materials properties, endowing them with self-healing, stimuli responding and more importantly recycling abilities. CANs can be classified into two groups based on the dynamic bond exchange mechanism.[300-302] The first group relies on dissociative crosslinkers (Figure 18A). The bond must break before reconnecting to other species, which temporarily reduces the crosslinking density during the bond exchange process. In contrast, CANs based on associative mechanism (Figure 18B) maintain the consistent crosslinking density. The new covalent bond forms solely when the associative position is established. Dissociative CANs encompass various covalent bonds such as Diels-Alder cycloaddition, amine urea exchange, aminal transamination, imine transamination, thioacetal exchange etc. [278,303] Diels-Alder type CANs are the most widely studied design of dissociative mechanism, which upon heating becomes reversable and enables topology rearrangement due to the dynamic nature of bonds.[304] After the seminal work for Leibler[305] numerous types of associative CANs, also known as vitrimers, were developed.[301,306] Leibler and co-workers developed material based on epoxy network, which undergoes topology rearrangement by transesterification reactions. The malleable material displays features similar to a vitreous silica, which inspired the term "vitrimer". The recently developed vitrimers are based on transesterification, disulfide exchange, boric ester exchange, imine metathesis, silyl ether

A) Dissociative exchange

Bond breakage
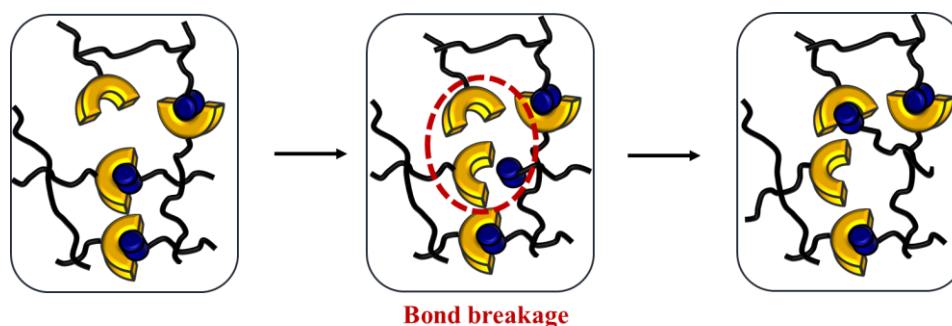
B) Associative exchange (Vitrimers)

No breakage
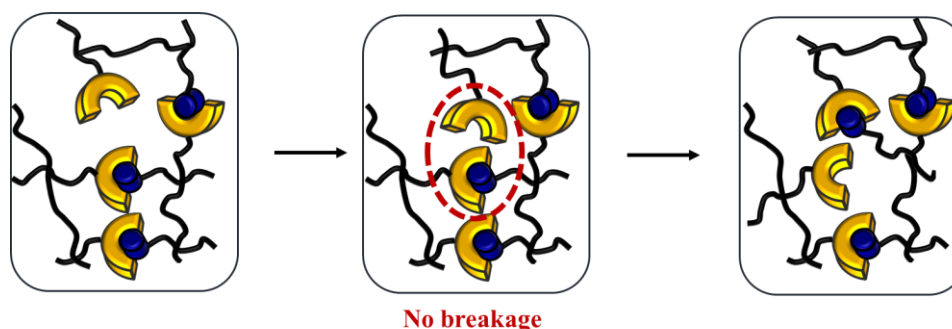
Figure 18. Schematic representation of A) Dissociative exchange CANs, B) Associative exchange CANs. Redrawn with permission from [302].

exchange, urea exchange etc.[298,306] The field is rapidly developing, exploring various chemistries to achieve vitrimers-like behavior. In this context, borate esters have become a primary interest for creating vitrimers. The bond exchange mechanism of boronic ester is directly impacted by the design of CANs. The presence of aqueous environment determines the exchange mechanism, dictating whether it follows associative or dissociative pathway.[307-310] The dissociative mechanism of boronic ester in aqueous environment is displayed in Figure 19A. Initially, the bond undergoes hydrolysis, leading to a reduction in crosslinking density, followed by the subsequent formation of a new bond. In a moisture-free environment, a boronic ester exhibits vitrimeric behavior. When a free alcohol group is present in the composition, the species associate and form intermediate state, yet the overall crosslinking density remains unchanged (Figure 19B). Similarly, for metathesis when no hydroxyl groups or moisture is present the bond exchange happens through the associative mechanism (Figure 19C). Thus, the boronic ester bond can be tuned to create associative or dissociative CAN by careful design of material.

Unlike other materials, vitrimers viscoelastic behavior is characterized by two distinct transition temperatures.[311,312] The first, typical for amorphous polymers, glass transition

A) Dissociative exchange mechanism of boronic ester in aqueous environment
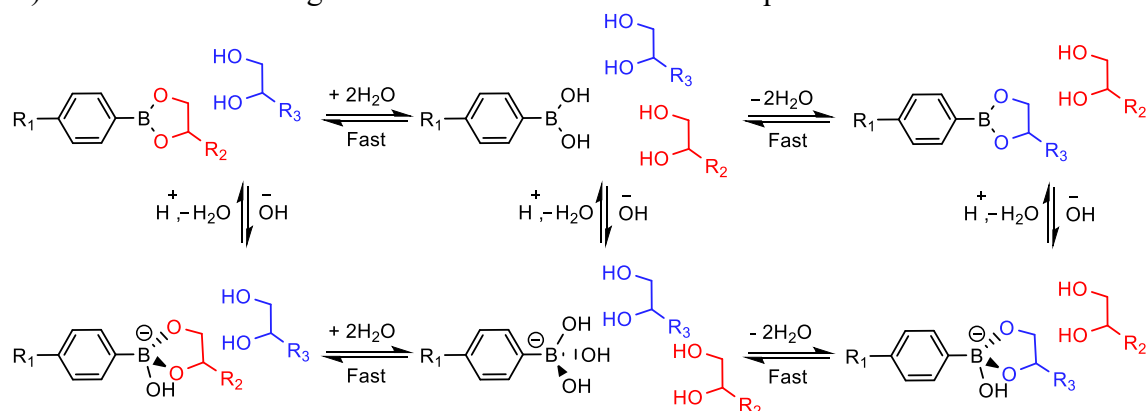
B) Associative exchange mechanism of boronic ester under dry conditions and excess diol
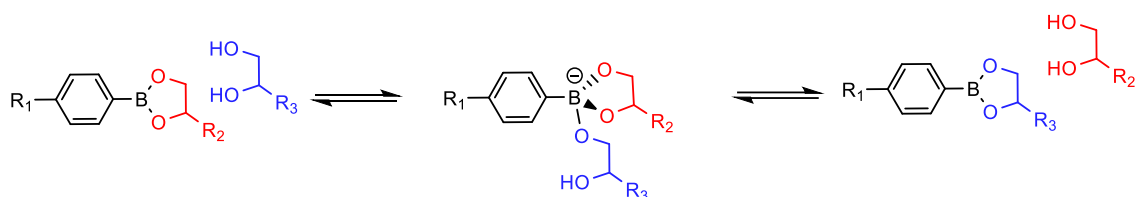
C) Associative exchange mechanism of boronic ester under dry conditions
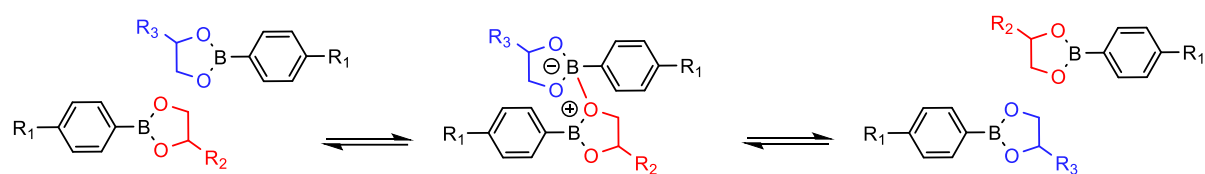
Figure 19. Boronic ester exchange mechanism in different environments. Redrawn from [310]. Copyright © 2022, American Chemical Society.

temperature, describes the segmental motions. The second is known as topology freezing temperature (T_v). T_v is very characteristic for vitrimers, and it defines the temperature where bond exchange rate is considerable, allowing the material to undergo topology changes. Below T_v material transitions from viscoelastic liquid to viscoelastic solids, with viscosity typically assumed to be 10^{12} Pa s. In general, two scenarios are discussed: one when T_v is higher that T_g and another when T_v is lower than T_g. If $T_v > T_g$ the vitrimers transition from glassy to rubbery state accompanied by gradual decrease in viscosity upon reaching T_v. For $T_v < T_g$ the topology rearrangement is not easily accessible below T_g, as the structure remains in glassy state, hindering the bond exchange.

Vitrimers chemistry is rapidly advancing, especially in the design of new materials tailored for diverse applications. An emerging area is batteries, wherein polymer electrolytes can be

customized with vitrimeric properties to enhance mechanical properties, introduce self-healing, recycling, and reprocessability capabilities.
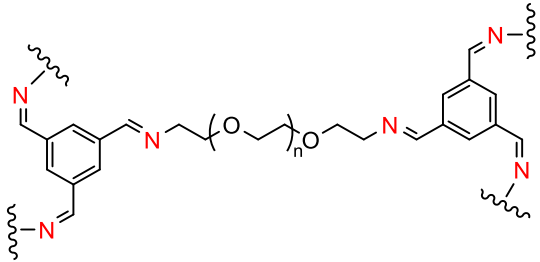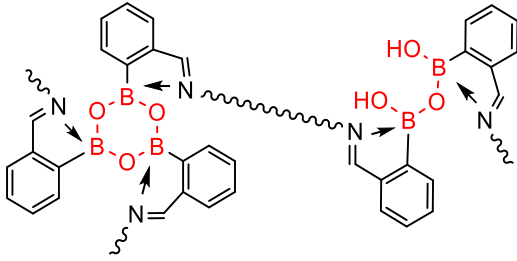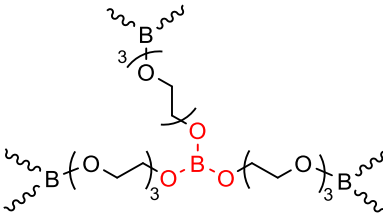
1.5.4 Dynamic covalent bonds in polymer electrolytes

The inherent vitrimeric nature facilitates self-healing and reprocessing of the material. The successful incorporation of dynamic bonds into polymer electrolyte materials signifies a noteworthy achievement. Despite the relatively recent emergence of vitrimers, their application in electrolytes is still in its infancy stage. Some remarkable progress has been made (Table 8) by incorporating, imine, disulfide and borate dynamic bonds. PEO-based vitrimer was prepared by reaction of diamine PEG with 1,3,5-triformylbenzene (entry 1).[313] The formed imine bond enables self-healing and superior mechanical properties (stretchable up to 524 %) due to the crosslinking. The vitrimer electrolyte possesses high ionic conductivity (7.48×10^{-4} S/cm at 25 °C), wide electrochemical stability windows up to 5 V vs. Li/Li$^+$ and maintains discharge capacity of 126 mAh/g for 300 cycles. The material's mechanical property is almost fully restored after the self-healing at RT, indicating the advantages of dynamic crosslinking. Disulfide bonds in the combination with supramolecular interactions were incorporated in polymer electrolyte (entry 2).[314] To create such dual network RAFT polymerization was used with the corresponding monomers, including PEG diacrylate. The resulted vitrimeric electrolyte can restore the cut without external stimuli in immersive 30 min at RT and in 1 min at higher temperature (80 °C). Although the ionic conductivity is on the lower end of the required values, reaching 1.78×10^{-4} S/cm (at 80 °C), the electrolyte displays the capacity retention of 97% after 100 cycles in battery testing. Borate bonds with the imine bonds were also successfully incorporated into a polymer electrolyte (entry 3).[315] PEG diamine was used as a polymer backbone which was crosslinked and consequently soaked in the liquid electrolyte mixture containing lithium difluoro(oxalato)borate (LiDFOB), fluoroethylene carbonate (FEC), ethylene carbonate, LiTFSI and LiPF$_6$. The vitrimeric material displays very fast bond exchange reactions and can heal the mechanical damage in 4 hours at RT with the efficiency of 97 %. Moreover, it exhibits excellent conductivity (5.08×10^{-3} S/cm at 30 °C) and cycling performance for polymer-based material. Another PEO based vitrimer electrolyte was prepared by crosslinking PEO with boric acid (entry 4).[316] The electrolyte was prepared with the varying amount of LiTFSI and corresponding conductivity displayed initial increase followed by the reduction at higher salt concentration. The higher value of 3.5×10^{-4} S/cm at 90 °C was reached. The different content of LiTFSI is impacting the mechanical properties of the vitrimer, proved by rheology measurement where shear modulus varied in one order of magnitude and

stress relaxation in two orders of magnitude. More importantly, the composition is fully recyclable with the right choice of solvent and self-healable with very high efficiency (97 %). PILs, another promising candidate for polymer electrolytes, can also be combined with dynamic bonds for further enhancement. The self-healing PIL was prepared by crosslinking allyl PIL copolymer and thiol terminated PEG with boronic ester bonds (entry 5).[317] Properties of the synthesized vitrimer are influenced by the crosslinking density. Higher crosslinking density enhances the mechanical properties but simultaneously decreases the ionic conductivity. The PIL also exhibits vitrimer-like features such as very good recyclability and restored properties after reprocessing. Self-healing vitrimeric electrolytes has been reported with other types of dynamic bonds such as imine bonds (entry 6 and 7)[318,319] and dynamic vinylogous urethane.[320] Vinylogous urethane moieties were incorporated in PEO/LiFSI mixture (entry 8). The resulting network can be reprocessed in 30 min at 90 °C *via* hot press and the ionic conductivity (10^{-5} S/cm) was consistently maintained even after multiple reprocessing cycles of the material. However, the mechanical properties undergo considerable decrease, presumably attributed to potential side reactions catalyzed by lithium cations. Recently successful incorporation of silyl ether dynamic bond in PIL electrolyte has been demonstrated by our group.[321] The vitrimeric sample exhibits self-healing and reprocessability *via* catalyst-free exchange of dynamic bonds. Moreover, the polymer network can retain additional 1-methyl-1-propylpyrrolidinium bis(trifluoromethylsulfonyl)imide (Mprets)/LiTFSI mixture up to 80 wt%. The resulting gel electrolyte displays high ionic conductivity up to 1.3×10^{-4} S/cm at 20 °C.

Vitrimers are gaining interest in creating recyclable materials, particularly in polymer electrolytes for lithium batteries. Recent advancements in this area are promising, leveraging the dynamic features of vitrimers for reprocessing, not just through methods like hot pressing but also with more sophisticated technologies like additive manufacturing.

Table 8. Selected vitrimeric polymer electrolytes.

Entry	Composition	Healing Mechanism	Healing condition	Additives	Conductivity S/cm	Ref.
1		Imine dynamics	RT, 24 h	LiPF$_6$ (r = 10)	7.48×10^{-4} (RT)	[313]
2		Disulfide dynamics, HB	RT, 0.5 h	LiTFSI (r = 16)	1.78×10^{-4} (80 °C)	[314]
3		Borate and imine dynamics	RT, 4 h	0.02 M LiPF$_6$ + 0.3 M LiDFOB + 0.8 M LiFSI in FEC/EC	5×10^{-3} (30 °C)	[315]
4		Borate dynamics	60 °C, 34 h	LiTFSI (r = 12)	3.5×10^{-4} (90 °C)	[316]

No.	Structure	Mechanism	Conditions	Electrolyte	Conductivity (S cm⁻¹)	Ref.
5		Borate dynamics	120 °C, 2 h	-	1.6×10^{-5} (30 °C)	[317]
6		Imine dynamics	RT, 10 s	0.1 M LiTFSI in BMImTFSI	3.1×10^{-4} (5 °C)	[318]
7		Imine dynamics	-	-	1×10^{-4} (30 °C)	[319]
8		Vinylogus urethane dynamics	90 °C, 0.5 h	LiFSI (r = 16)	10^{-5} (RT)	[320]
9		Silyl ether dynamics	180 °C, 12 h	LiTFSI/ MPPyrTFSI (80 wt%)	1.3×10^{-4} (20 °C)	[321]

2 Aim

Current commercially available Li-ion battery technologies rely on organic solvent-based electrolytes. Despite their advantageous properties, significant drawbacks and challenges must be addressed. Safety concerns due to electrolytes flammability,[117,322] formation and growth of lithium dendrites,[323,324] voltage limitation[118,325] and negative environmental impact[124,326] can be overcome by using alternative materials as electrolytes. The aim of this thesis is to address some of these drawbacks by designing novel electrolyte materials for the next-generation Li-ion batteries. The focus is on addressing the self-healing ability and reprocessability of the materials. Ionic liquids[57,62] are used due to exceptional electrochemical properties, thermal stability, low volatility, non-flamma bility and environmentally friendliness.[189] As ILs are versatile compounds easily integrated into materials, or combined with polymers to impart additional desired properties such as mechanical integrity, self-healing ability or 3D-printability, the various IL-based materials developed within the scope of this thesis are schematically presented in Figure 20:
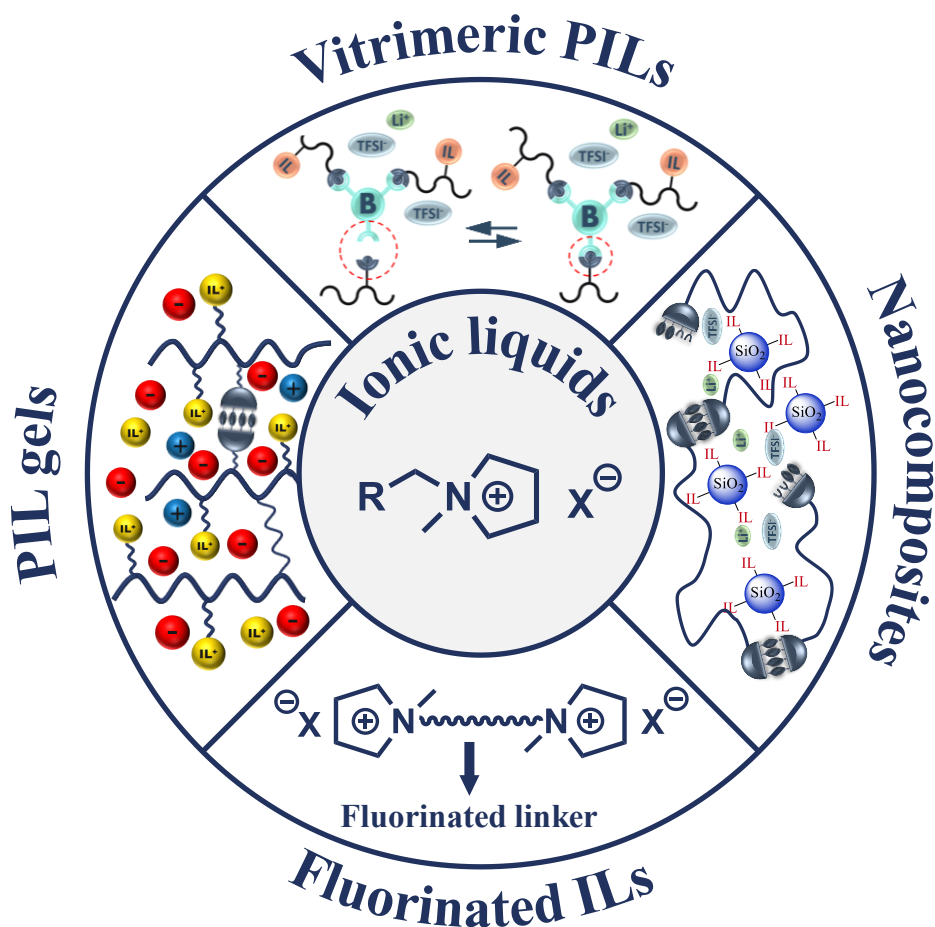
Figure 20. Schematical representation of ionic liquid-based materials.

I. *Vitrimeric poly(ionic liquid)s* – are investigated to merge the unique characteristics of vitrimers by introducing dynamic covalent bonds into polymerized ionic liquids. This integration should result in materials that are reprocessable, 3D-printable and sustain high ionic conductivity.

II. *Nanocomposites* – introduce IL properties by incorporating surface modified nanoparticles into polymer electrolyte. The presence of NPs with IL-modified surface is expected to improve mechanical properties and enable 3D printing (for otherwise non-printable polymer materials) while simultaneously enhancing the ionic conductivity.

III. *Fluorinated ionic liquids* – are designed and investigated to further enhance electrochemical performance. Dicationic ILs will be investigated and characterized together with their non-fluorinated analogous compounds to better assess property enhancements and evaluate their potential use as electrolyte materials for Li-ion batteries.

IV. *Poly(ionic liquid) gel electrolytes* – aim to achieve dynamic and non-dynamic crosslinking properties to establish a strong but still conductive polymer network. The integration of ionic liquids and lithium salt aims to enhance the conductivity of the crosslinked material. The optimization of the gel electrolyte involves varying compositions and components to identify the most suitable samples for potential use in Li-ion batteries.

3 Concept

Lithium-ion batteries demand enhancements in safety, sustainability, and performance to meet market requirements. Replacing conventional electrolytes with alternative, more advanced and smart materials could be a possible solution. Ionic liquids (ILs) and poly(ionic) liquids (PILs) stand out from other alternatives by their superior electrochemical and physical properties. This work is designed to leverage the advantageous properties of ILs and PILs in combination with diverse polymeric or macromolecular structures to tailor electrochemical, thermal and mechanical properties. Additionally, self-healing ability, reprocessability and 3D printability of developed materials are investigated. Different approaches for incorporation of IL features into polymeric materials followed in the scope of this work are schematically represented in
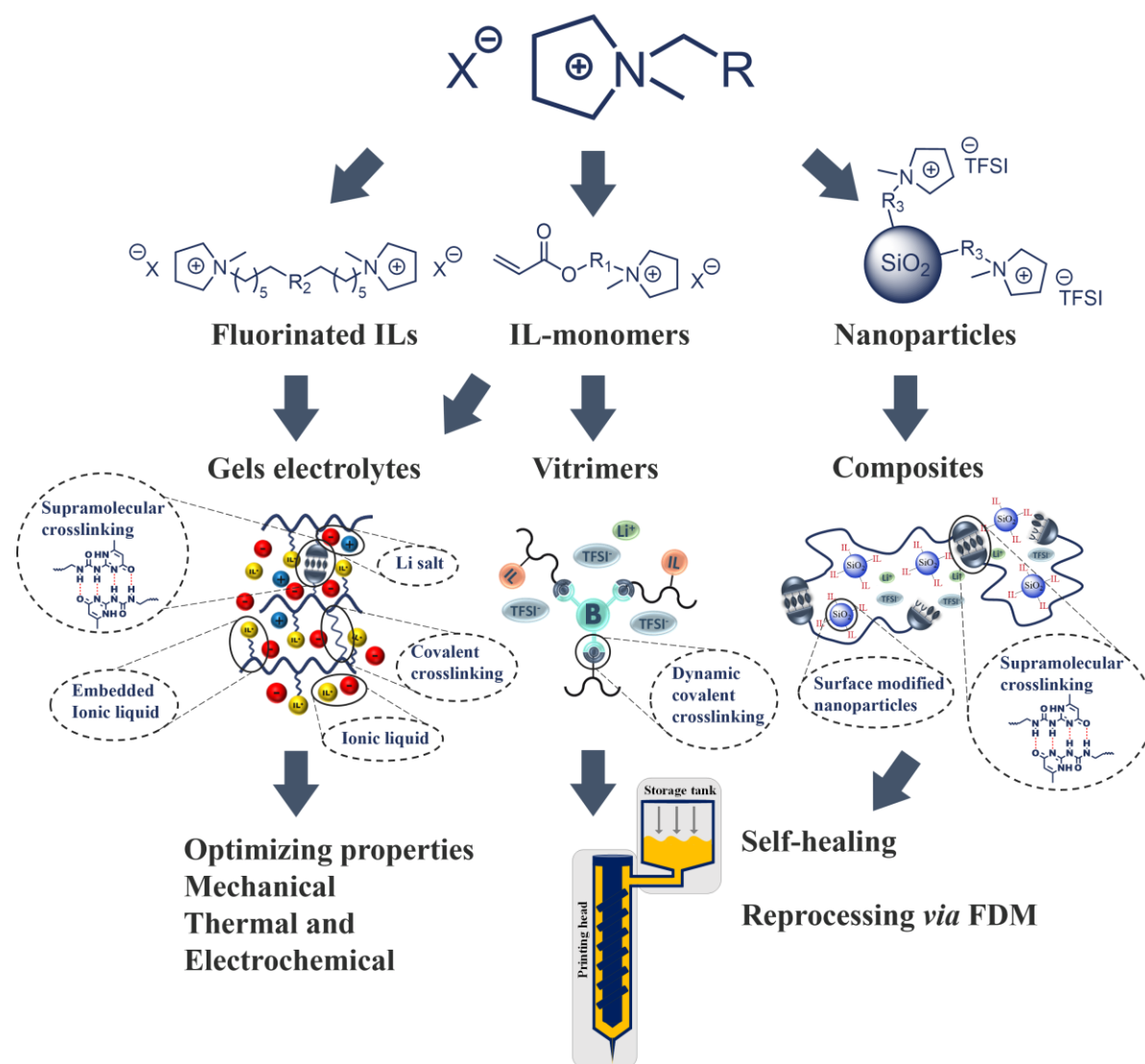
Figure 21. General scheme of embedding pyrrolidinium IL compounds into electrolyte materials.

Figure 21. Among the vast number of ILs, the pyrrolidinium cation is selected due to its excellent electrochemical stability window and superior thermal properties. By the selection of the counterion of IL and lithium salt the focus is set on TFSI and FSI anions, due to their favorable thermal and electrochemical properties, and the ability to stabilize the SEI layer.

Approach I Vitrimeric poly(ionic liquid)s. In order to introduce the unique features of vitrimers dynamic covalent bonds are incorporated into polymeric ionic liquids. The corresponding synthetic concept is presented in Figure 22. By attaching polymerizable groups onto IL-cation two different types of IL-monomers are prepared. Additional ethylene oxide groups present in the second IL-monomer are expected to actively involve in Li^+ transport, thus enhancing the conductivity of PILs. Due to the favorable dynamic features of the borate-ester bond (B-O), boric acid was chosen for the introduction of the vitrimeric properties into the material. 2-[2-[2-[(4-ethenylphenyl)methoxy]ethoxy]ethoxy]ethanol was used as a second monomer, serving the dual purpose of reinforcing mechanical strength and providing binding sites for dynamic covalent bonding *via* the OH group. The synthesis involves two steps: firstly, the preparation of corresponding pre-copolymers, followed by the creation of vitrimeric electrolytes in the second step by the addition of boric acid and Li salt as source of Li-ions. In order to optimize the properties and performance of the materials, various factors are systematically varied, including monomer ratios and the quantity of Li salt.
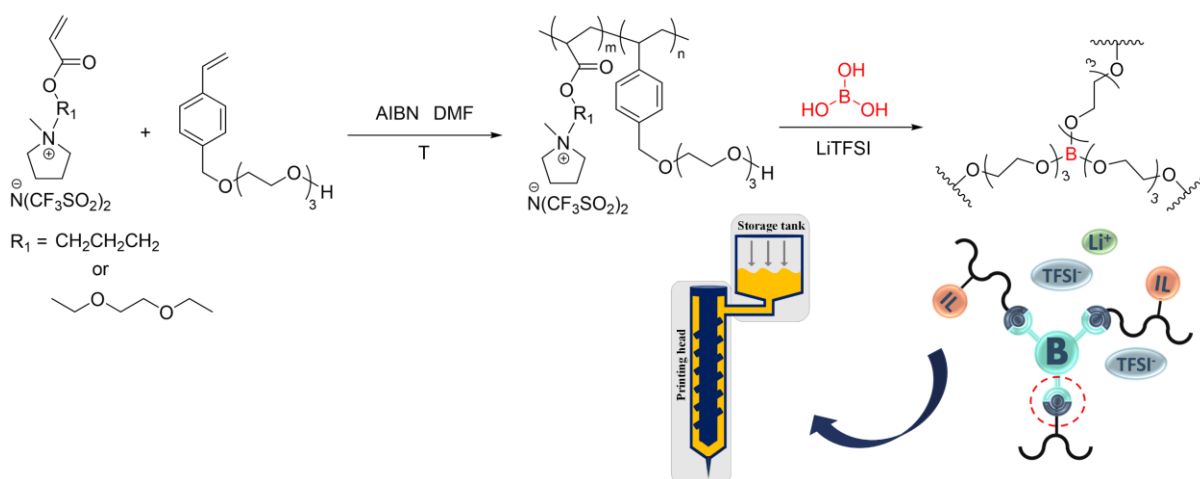
Figure 22. General scheme of *Approach I*.

All prepared materials are comprehensively characterized *via* SEC, NMR spectroscopy, TGA and DSC. The optimization of ion conductivity was continuously followed by broadband dielectric spectroscopy (BDS) measurements. Tensile testing is employed to assess the mechanical integrity of the polymer films, while the rheological investigations are conducted

to investigate the 3D printability of the prepared materials *via* FDM. Finally, the self-healing ability and reprocessability of the optimized vitrimeric PILs is evaluated. All obtained results are presented and discussed in Chapter 4. Parts of the chapter have been already published:

Katcharava Zviadi, Xiaozhuang Zhou, Rajesh Bhandary, Rene Sattler, Heiko Huth, Mario Beiner, Anja Marinow, and Wolfgang H. Binder.* "Solvent and catalyst free vitrimeric poly (ionic liquid) electrolytes." *RSC advances,* 13, (**2023**): 14435-14442.

Approach II Nanocomposites. Composite electrolytes are prepared based on PEG and silica nanoparticles. For improving the mechanical properties of PEG, while potentially introducing self-healing ability, supramolecular interactions are created by end group modification of PEO with UPy or barbiturate moieties (Figure 23). Different hydrogen forming moieties enable to adjust the interaction strength. IL incorporation is achieved by surface modification of silica nanoparticles with pyrrolidinium ILs. For this purpose, N-[3-(trimethoxysilyl)propyl]-N-methylpyrrolidinium chloride IL was synthesized and attached to NP surface *via* two step processes (Figure 23). For better accessing the importance of surface modification on properties, alkyl chain modified particles are also prepared. The successful modification of silica NPs is confirmed *via* liquid and solid-state NMR (CP-MAS NMR), FT-IR spectroscopy and TGA. A range of composite materials is prepared by altering the type of supramolecular polymer matrix, varying the type and quantity of the modified NPs, and adjusting the amount of added lithium salt. The primary aim is to optimize the composite electrolyte material
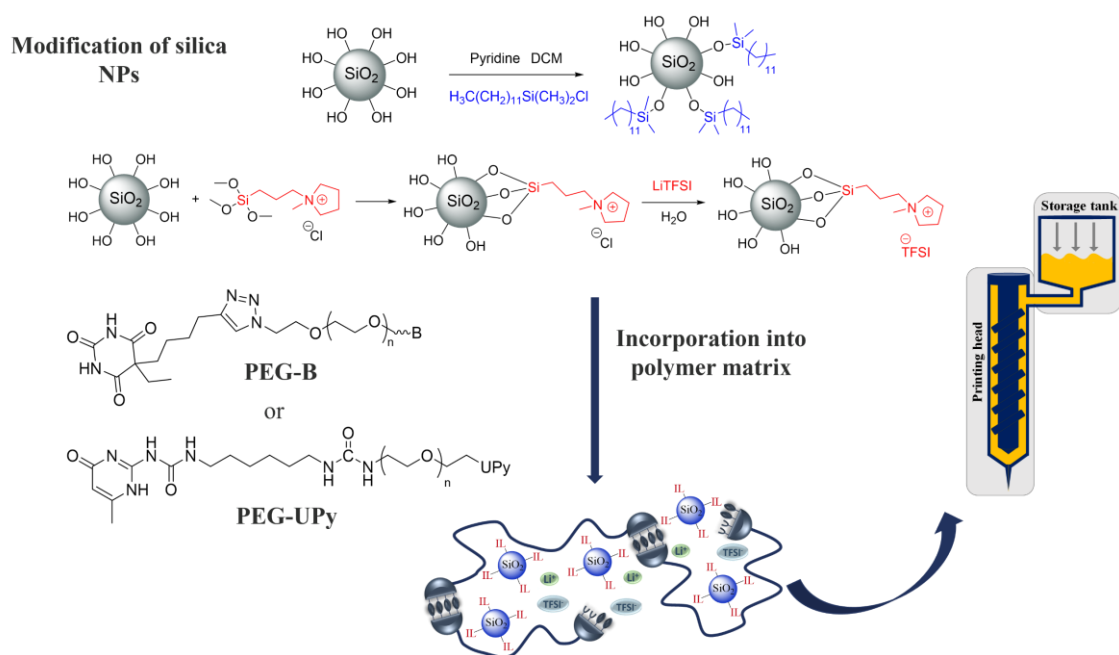
Figure 23. General scheme of *Approach II*.

specifically for enhanced 3D printability using FDM. Intensive rheological investigations are conducted in order to choose the most promising composition. Furthermore, the influence of the 3D-printing process on the ion conductivity of the composite electrolyte is investigated *via* BDS. Obtained results are summarized and discussed in Chapter 5. Parts of the chapter have been already published:

Katcharava Zviadi, Anja Marinow, Rajesh Bhandary, and Wolfgang H. Binder.* "3D printable composite polymer electrolytes: influence of SiO$_2$ nanoparticles on 3D-printability." *Nanomaterials*, 12 (11), (**2022**): 1859.

Approach III Fluorinated ionic liquids. Since fluorinated compounds are known to have excellent chemical, electrochemical and thermal stability, while positively influencing the stability of the SEI layer, the objective of this approach is to assess the suitability of the novel fluorinated dicationic ionic liquids for use in electrolyte materials. Two types of fluorinated pyrrolidinium ILs containing fluorinated ether linker and different anions (TFSI and FSI), as well as their nonfluorinated analogs are investigated (Figure 24). Properties of the ILs are examined *via* DSC, TGA, BDS, LSV and rheology (Chapter 6.1). Moreover, fluorinated ILs tend to segregate into ionic, apolar, and fluorinated domains, creating a complex morphology that potentially influences ion transport. Thus, the WAXD measurements are conducted to get an insight into internal ordering of ILs as well as to investigate the influence of the Li salt on the morphology. Subsequently, the dicationic ILs are used for the preparation of the gel polymer electrolytes in the scope of the Approach IV.
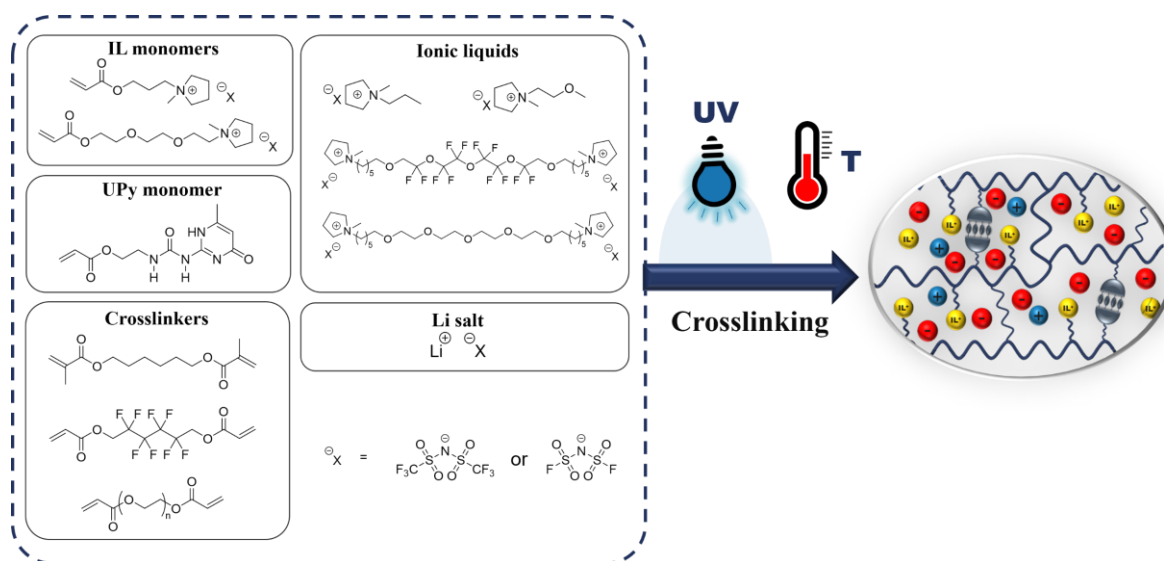
Figure 24. General scheme of *Approach III* and *IV*.

Approach IV Poly(ionic liquid) gel electrolytes. A promising approach to introduce the unique properties of ILs into polymeric materials involves the preparation of GPEs, comprising of a polymer matrix and an additional liquid phase for enhancing ionic conductivity. The polymer matrix provides a three-dimensional structure, restricting the free flow of the liquid phase. ILs can be integrated either as a monomer within the polymer matrix or as a liquid phase. Gel electrolytes are typically formulated by mixing components followed by a crosslinking reaction. In Figure 24 various components used for preparing of GPEs in the scope of this thesis are illustrated. Two types of the IL monomers with variating side chains are applied, alongside UPy-containing monomer to introduce supramolecular networks into the polymer matrix. Furthermore, the type of crosslinker as well as of IL is varied, with the emphasis on exploring how the presence of fluorinated or EO-containing chains affects the properties of gel electrolytes. Due to the complexity of the GPE composition, systematical investigation is needed to identify the optimal composition for the desired application. For this purpose, different gel components are systematically varied including type of IL monomer, content of the UPy group, type of crosslinker, type and amount of the IL as well as type and quantity of added salt. Additionally, the impact of the polymerization method (thermal vs. photochemical) is investigated. The influence of all these factors on the properties of the final GPE is intensively examined by combining different analytical methods like TGA, DSC, BDS, LSV and tensile testing. Comprehensive findings are summarized and discussed in Chapter 6. In order to further enhance the properties of GPEs as well as to combine different approaches explored in the scope in this work, combined compositions are also investigated. This involves the addition of dynamic covalent bonds (incorporation of borate ester bonds into GPEs) or the exploration of composite GPEs by integrating MOFs.

4 Vitrimeric poly(ionic liquid)s

Poly(ionic liquid)s, an appealing class of polymers, known for their favorable mechanical properties and elevated ionic conductivity, underwent further enhancement trough the incorporation of versatility of vitrimeric materials. Dynamic crosslinking, which can undergo associative exchange reactions enables self-healing, reprocessability and 3D printability. To combine the PILs with vitrimeric nature our strategy involved synthesizing copolymers with pyrrolidinium IL-based monomer and styrene derivate monomer with terminal hydroxyl group to act as a crosslinking site for boric acid. The formed borate-ester linkage can undergo the reversible break/formation cycles as illustrated in Figure 25. The ratio of two monomers consequently determines the crosslinking density and thus, the properties of the final polymer. Hence, the copolymers with different ratios were prepared and accessed the optimal composition for the superior performance material. The incorporation of several monomers into copolymer structure depends on their compatibility and can deviate from the intended values. Here the incorporation of both monomers was verified using ^{1}H NMR and the actual values were in very close proximity to the intended ones. Additionally, a second type of IL monomer with ethylene oxide-based linker was used for investigating the impact on the ionic conductivity of the material. For the preparation of PEs lithium salt is added, as a source of Li-ions. In the preparation process of vitrimers LiTFSI with varying concentration was added and obtained PEs are subsequently analyzed *via* BDS. Vitrimeric samples were investigated with TGA for determining the degradation temperature and verifying that copolymerization or dynamic crosslinking is not negatively affecting the thermal properties. For addressing the sustainability and recyclability the prepared samples were also tested for self-healing and 3D printability. The presence of dynamic crosslinking is very suitable for FDM, as it requires polymer extrusion at elevated temperatures. Higher temperature increases the dynamic bond exchange rate of vitrimer polymer electrolyte, thus reducing the viscosity to the required level
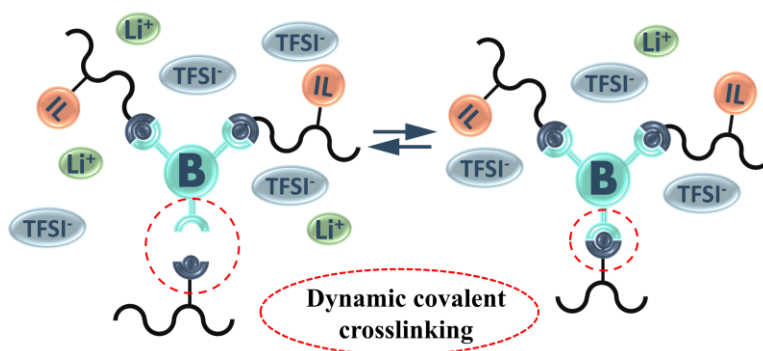
Figure 25. Schematical representation of vitrimeric PIL and dynamic nature of crosslinking.

while subsequently retaining the dimensional stability as the sample cools down after the extrusion.

4.1 Preparation of vitrimeric electrolytes

Vitrimeric poly(ionic liquid) electrolytes were synthesized *via* two step reaction (Figure 26). Initially precursor polymers were prepared using ionic liquid monomer (**4**) and 2-[2-[2-[(4-ethenylphenyl)methoxy]ethoxy]ethoxy]ethanol (**1**) by free radical polymerization in DMF. The IL monomer introduces advantageous properties of ionic liquids, whereas the second monomer serves as both a reinforcement for mechanical strength and as a binding site for
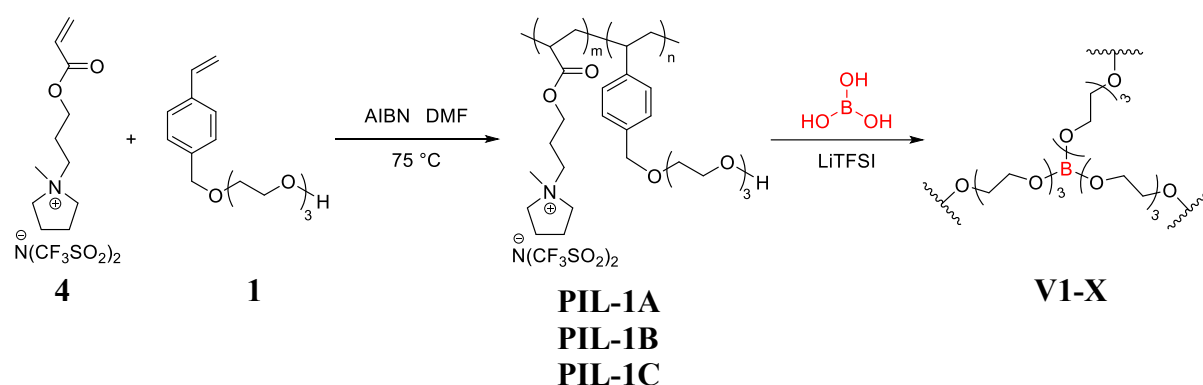
Figure 26. Synthesis of vitrimeric PILs (**V1**) from N-[(2-acryloyloxy)propyl]-N-methylpyrrolidinium bis(trifluoromethylsulfonyl)imide (**4**) and 2-[2-[2-[(4-ethenylphenyl)methoxy]ethoxy]ethoxy]ethanol (**1**) *via* FRP and subsequent crosslinking.

dynamic covalent bonding over the OH group. The ratio of monomers is a critical parameter that dictates the material's performance, allowing for the fine-tuning of properties between heightened mechanical strength and high conductivity of the material. Three compositions were prepared with varying monomer ratios: **PIL-1A** with the ratio m:n = 9 : 1, **PIL-1B** with m:n = 1 : 1 and **PIL-1C** with m:n = 1 : 9. Obtained and purified polymers were analyzed on SEC for determining the average molecular weight and molecular weight distribution (Figure 27). The following values were extracted: **PIL-1A** − Mn = 12 kDa, Mw = 94 kDa, Đ = 7.67; **PIL-1B** − Mn = 77 kDa, Mw = 225 kDa, Đ = 2.93 and **PIL-1C** − Mn = 75 kDa, Mw = 318 kDa, Đ = 4.2. However, the molecular weight obtained from SEC can be imprecise due to presence of IL moieties, which could be affecting the hydrodynamic radius of polymer chains and the interactions with the columns. For accurate data extraction, it is necessary to use PIL standards (which are rarely available commercially) rather than commercial PS and PEO
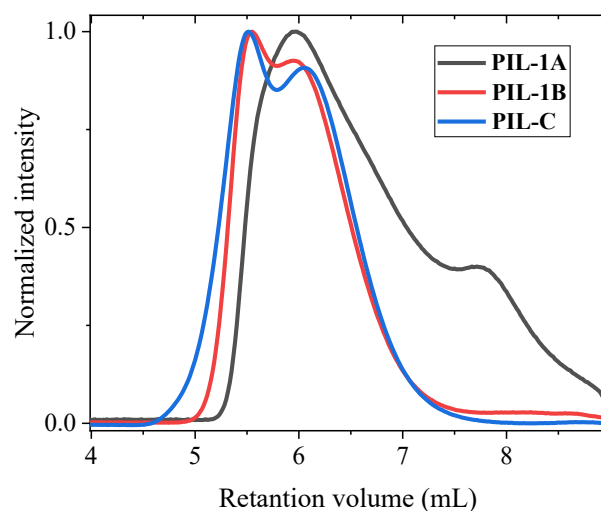
Figure 27. SEC curves of **PIL-1A**, **PIL-1B** and **PIL-1C** in DMF.

standards.[327,328] Thus, proton NMR was used for verifying the successful copolymerization and for calculating the actual monomer ratios in PILs. In Figure 28 ^{1}H-NMR spectra of prepared PILs are presented. The ratio of aromatic protons of monomer **1** and of methyl group from IL monomer was used for calculating the monomer ratio, resulting in very similar values to the intended ones.

Knowing the dynamic features of the borate-ester bond (B-O),[307,329,330] boric acid was chosen for the introduction of the vitrimeric properties into the material. After drying of precursor PILs at 120 °C for 24 h (under vacuum) crosslinking reaction was conducted. For the typical procedure PIL was dissolved in dry ACN and equimolar amount (to free OH groups) of boric acid and appropriate amount of LiTFSI was added to the mixture (exact procedure and compositions are given in the Experimental section 8.3.5). Boric acid forms dynamic boronic
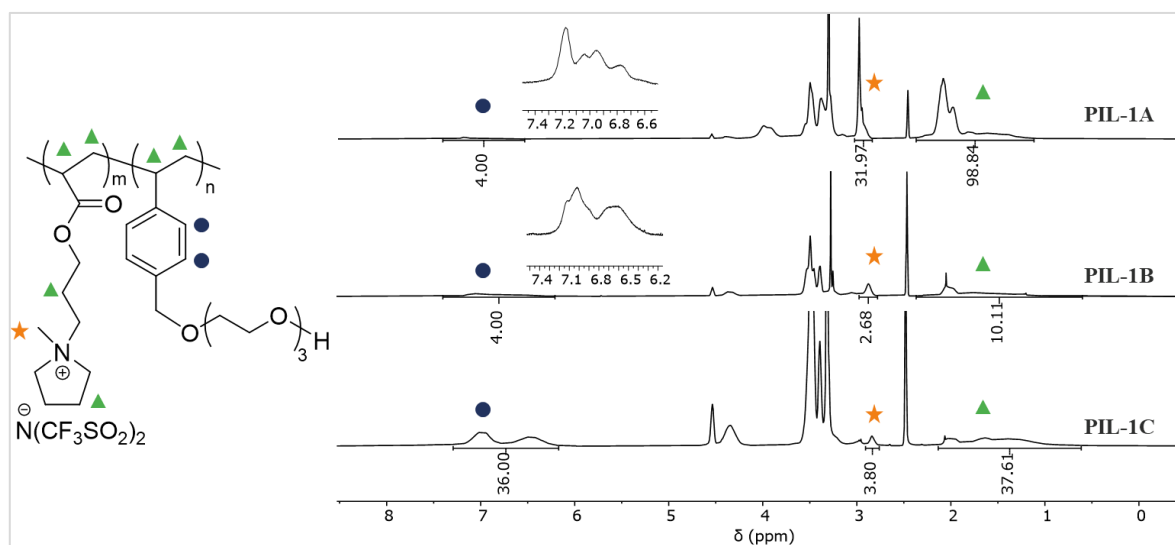
Figure 28. ^{1}H NMR spectra of **PIL-1A**, **PIL-1B** and **PIL-1C** in DMSO-d$_6$.

ester bonds with the terminal OH groups whereas the additional salt serves as the source of lithium ions in the system. LiTFSI amount was varied and the concentrations are presented with respect to the quantity of ethylene oxide (EO) groups within the structure. Obtained compositions are given in Table 9. In respect to their potential application as electrolytes, the final vitrimeric PILs are required to be dried under vacuum at high temperatures (120 °C) to eliminate any traces of water, which can affect the electrochemical properties, potentially resulting in misleading outcomes.

Table 9. Composition of vitrimeric PILs (**V1-X**), projected molar ratio of monomers in the polymer precursor, molar ratio of additional LiTFSI with respect to EO groups and corresponding conductivities at 30 °C.

Entry	Precursor	Molar ratio of monomers (m:n)	LiTFSI/EO	Conductivity at 30 °C (S/cm)
V1-1	PIL-1A	9 : 1	0	1.9×10^{-7}
V1-2	PIL-1A	9 : 1	0.1	8.8×10^{-7}
V1-3	PIL-1A	9 : 1	0.2	1.7×10^{-6}
V1-4	PIL-1A	9 : 1	0.3	2.5×10^{-6}
V1-5	PIL-1A	9 : 1	0.4	1.6×10^{-6}
V1-6	PIL-1A	9 : 1	0.5	1.2×10^{-6}
V1-7	PIL-1A	9 : 1	1	5.1×10^{-7}
V1-8	PIL-1A	9 : 1	2	4.8×10^{-7}
V1-9	PIL-1C	1 : 9	0	1.5×10^{-7}
V1-10	PIL-1B	1 : 1	0	1.7×10^{-7}
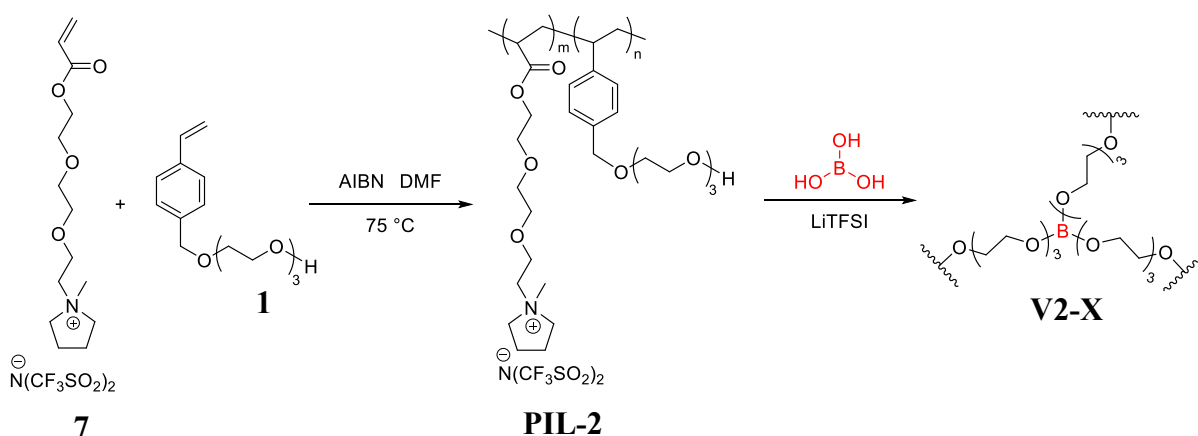
Figure 29. Synthesis of vitrimeric PILs (**V2-X**) from N-(2-(2-(2-(acryloyloxy)ethoxy)ethoxy)ethyl)-N-methylpyrrolidinium bis(trifluoromethylsulfonyl)-imide (**7**) and 2-[2-[2-[(4-ethenylphenyl)methoxy]ethoxy]ethoxy]ethanol (**1**) *via* FRP and subsequent crosslinking.

In the similar approach vitrimeric PILs were prepared by utilizing the second IL monomer N-(2-(2-(2-(acryloyloxy)ethoxy)ethoxy)ethyl)-N-methylpyrrolidinium bis(trifluoromethyl-sulfonyl)imide (**7**) (Figure 29). The used IL monomer contains additional ethylene oxide groups, which are expected to enhance the conductivity of PILs *via* actively involving in Li$^+$ transport, as previously reported for the conventional PEO-based solid-state electrolytes.[331] Successful polymerization of a precursor copolymer was verified *via* proton NMR (Figure 30). Incorporation of both monomers with the intended amount can be seen on the spectrum when comparing aromatic protons of the styrene monomer and alkyl protons of the IL monomer. Crosslinking and introduction of boric ester dynamic covalent bonds was conducted in dry ACN, while additionally different amounts of LiTFSI were added to the polymer samples and the obtained compositions are presented in the Table 10.
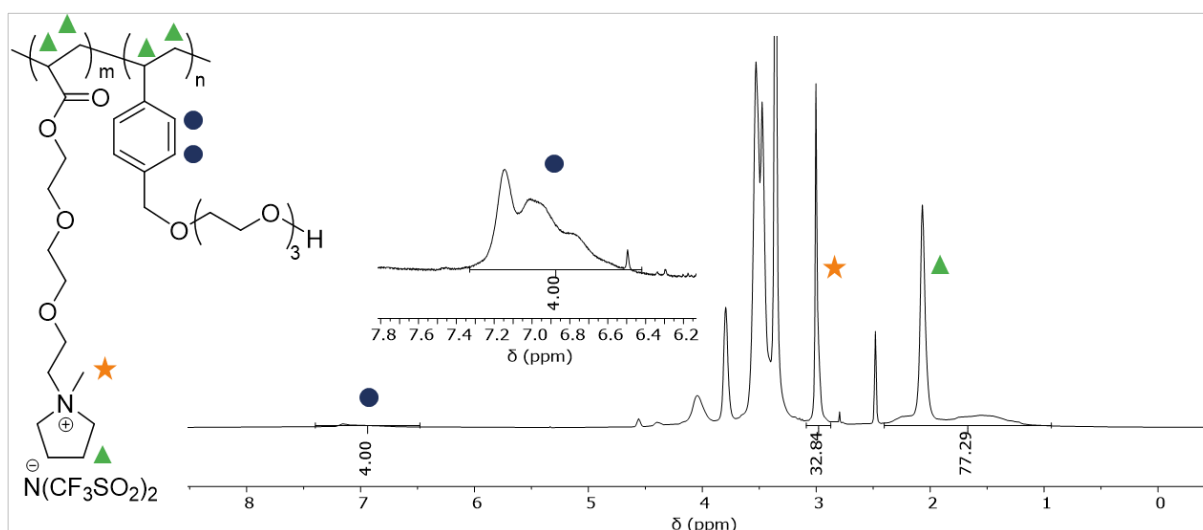
Figure 30. ^{1}H NMR spectrum of **PIL-2** in DMSO-d$_6$.

Table 10. Composition of vitrimeric PILs (**V2-X**), projected molar ratio of monomers in the polymer precursor, molar ratio of additional LiTFSI with respect to EO groups and corresponding conductivities at 30 °C.

Entry	Molar ratio of monomers (m:n)	LiTFSI/EO	Conductivity at 30 °C (S/cm)
V2-1	9 : 1	0	2.35×10^{-5}
V2-2	9 : 1	0.1	8.82×10^{-6}
V2-3	9 : 1	0.2	2.58×10^{-6}
V2-4	9 : 1	0.3	5.97×10^{-7}
V2-5	9 : 1	0.5	4.75×10^{-8}
V2-6	9 : 1	1	1.47×10^{-8}

4.2 Characterization of vitrimeric electrolytes

Precursor polymers were analyzed by TGA under inert atmosphere for investigating the thermal stabilities and for ensuing the incorporation of both monomers (Figure 31). **PIL-1A** displayed one step weight lost starting at 300 °C, indicating high thermal stability of the sample. **PIL-1B** and **PIL-1C** also show stability above 300 °C, however with increasing ratio of the styrene monomer a two-step weight loss can be observed. The observed thermal stability is in accordance with the data reported for other IL-based polymers and copolymers.[332]
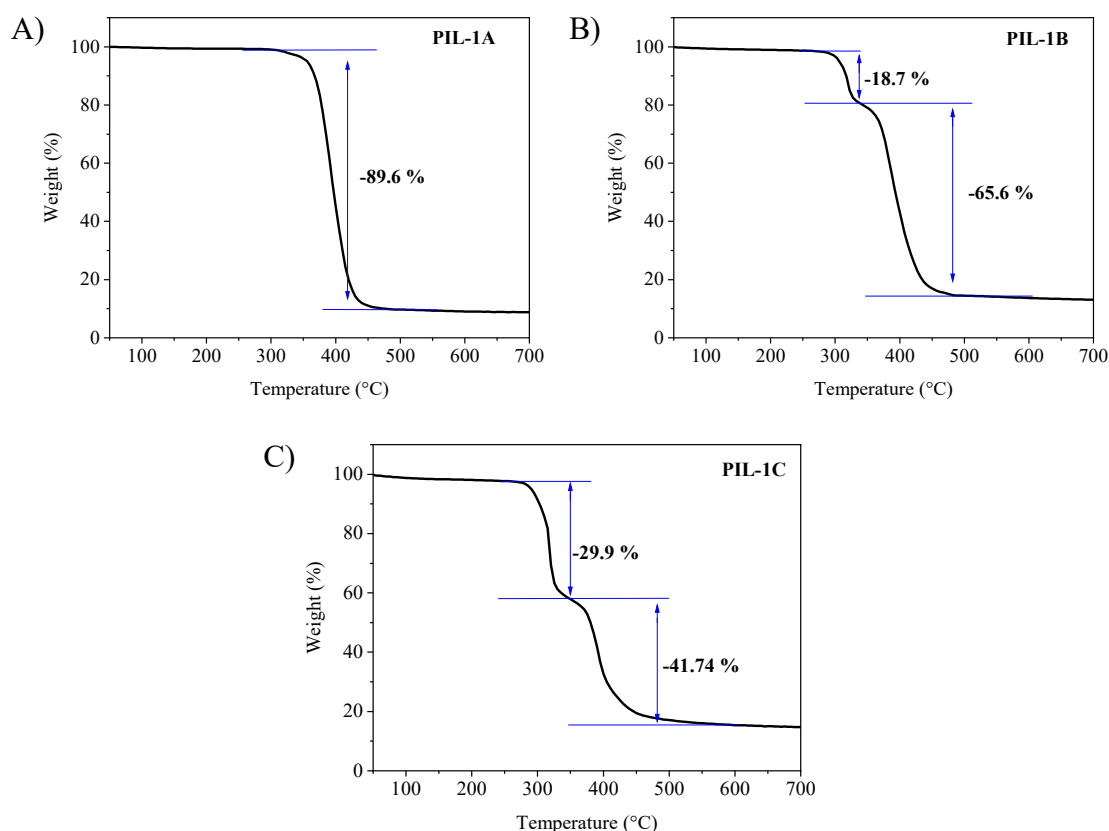
Figure 31. TGA measurement of A) **PIL-1A**, B) **PIL-1B** and C) **PIL-1C** under N_2 up to 700 °C.

Prepared vitrimeric PILs before and after crosslinking with boric acid but without addition of Li salt were tested using tensile measurements to characterize their mechanical properties. These properties are crucial when considering the material's suitability for potential application as a polymer electrolyte. Superior mechanical properties not only diminish the rate of lithium dendrite growth but also grant the batteries more resilience against mechanical damage.[57,153] Testing mechanical properties involves the determination of materials toughness, the energy which is absorbed before the fracture point. Tensile curves and corresponding calculated toughness values (area under the tensile curve) are shown in Figure 32. Initially, significant

improvements in mechanical properties are evident upon the introduction of dynamic crosslinking when comparing **PIL-1A** to other samples. **PIL-1A** shows a distinct degree of elastic deformation, but it can resist and absorb the least amount of energy before reaching a breaking point. If we compare vitrimeric PILs the trend can be observed that when we are increasing the crosslinking density in materials ultimate tensile strength is increasing but the
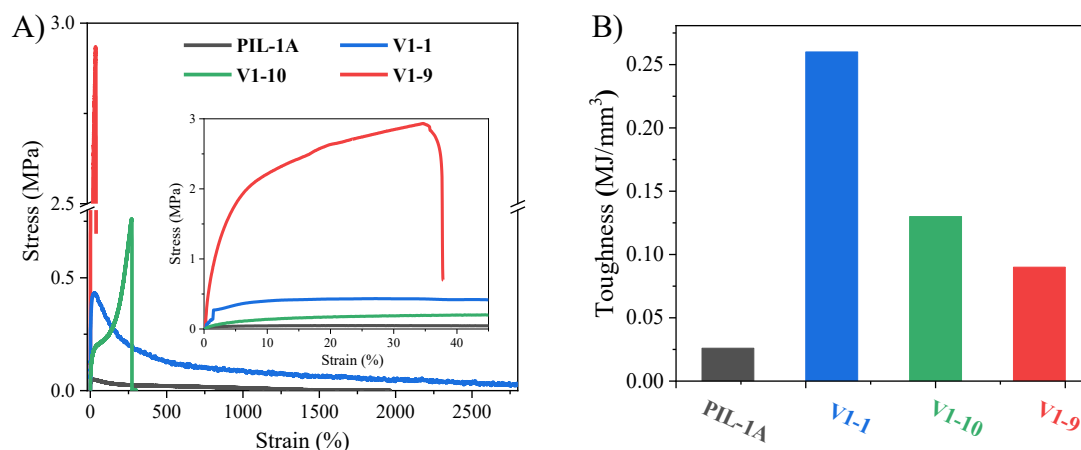
Figure 32. A) Tensile testing of **PIL-1A**, and (inserted section-zoomed in curve in the strain range of 0-50 %), B) Toughness values of **PIL-1A**, **V1-1**, **V1-9** and **V1-10**.

material becomes more brittle and cannot resist the deformation. **V1-1** displays the highest value of toughness reaching ≈ 0.25 MJ mm^{-3}.

The key parameter and usually limiting factor for polymers to be used as electrolyte is the ionic conductivity. Broadband dielectric spectroscopy (BDS) was used for investigating the conductivity (σ), and typical BDS measurement curves are shown in Figure 33A, where the plateaued values from the frequency vs. conductivity curves are considered as σ for each
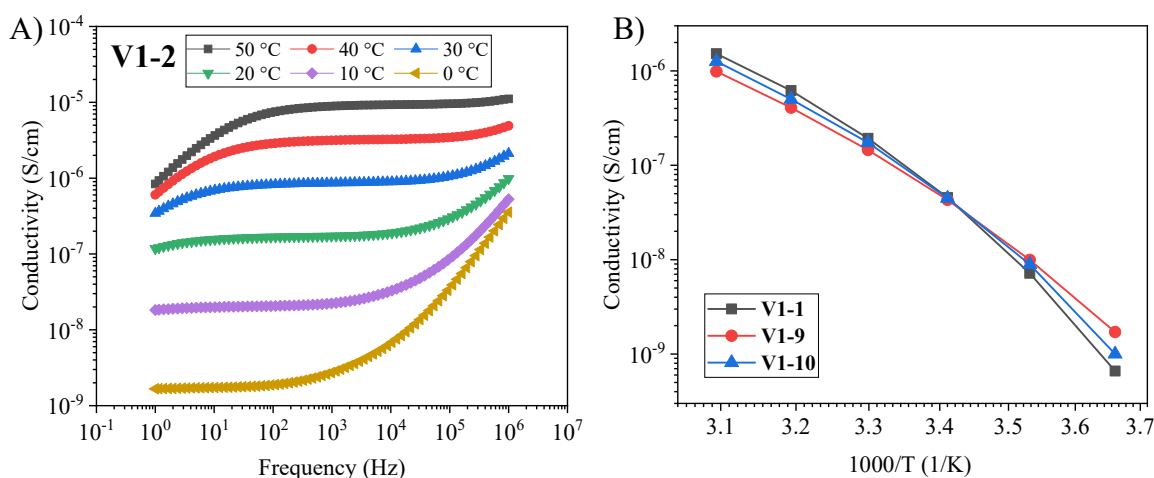
Figure 33. A) BDS measurement of **V1-2** in the temperature range of 0 °C to 50 °C with 10 °C increments, the frequency range between 1 to 10^6 Hz, B) Conductivity as a function of temperature of **V1-1**, **V1-9** and **V1-10**.

composition. As expected, the values are dropping with reducing temperature from 70 °C to 0 °C and varying in the range of 10^{-5} to 10^{-9} S/cm, while the lowest value is observed for **V1-2**, which does not contain any additional LiTFSI. **V1-9** and **V1-10**, vitrimeric samples with higher degree of crosslinking also displayed the conductivities in range of 10^{-6} to 10^{-9} S/cm (Figure 33B). The conductivity for all vitrimeric PILs without additional LiTFSI salt are below the minimum requirements for PEs, however we expect that the samples with additional LiTFSI are more realistically applicable for practical use as electrolyte. Thus, vitrimeric PILs with various content of LiTFSI were investigated in the temperature range of 0 °C to 50 °C (Figure 34A). The conductivity shows three orders of magnitude increase with increasing temperature. The highest value of 1.8×10^{-5} S/cm was reached at 50 °C for **V1-4**. The trend
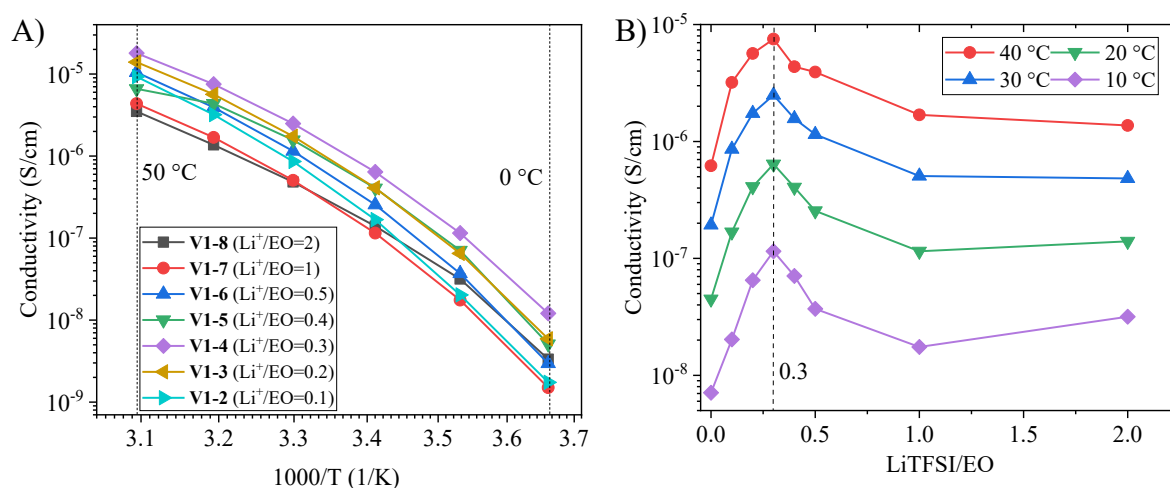
Figure 34. A) Conductivity as a function of inverse temperature (0 − 50 °C) for **V1-2**, **V1-3**, **V1- 4**, **V1- 5**, **V1-6**, **V1-7** and **V1-8**, B) Conductivity as a function of lithium content (LiTFSI/ EO) at different temperatures.

aligns with typical Vogel-Fulcher-Tammann behavior, suggesting that the polymer network retains a certain level of dynamics. The VFT model can be described with the following equation $\sigma = \sigma_0 \exp[-B/(T-T_0)]$,[333] where σ_0 is constant pre-exponential factor, B – constant related to energy and T_0 also known as Vogel temperature typically taken 50 °C below experimental T_g. Concentration vs. σ curves in Figure 34B display the increase of conductivity with increasing LiTFSI concentration and subsequent decrease above critical point. Such behavior in dependence of salt content was reported before for PEO based materials and it can be explained by formation of anion clusters above critical concentration, which hinders the ion mobility resulting in reduced conductivity.[316,334] The observed behavior remains similar at different temperatures and reaches maximum values for LiTFSI/ EO = 0.3.
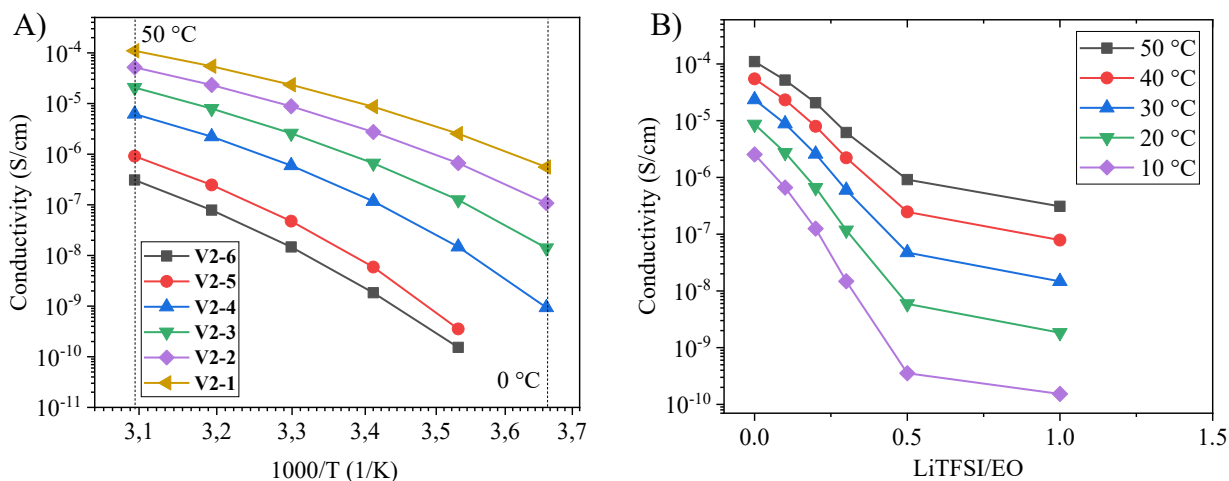
Figure 36. A) Conductivity as a function of inverse temperature (0 − 50 °C) for **V2-1**, **V2-2**, **V2-3**, **V2-4**, **V2-5** and **V2-6** B) Conductivity as a function of lithium content (LiTFSI/ EO) at different temperatures.

Ionic conductivity of **V2** samples having ionic liquid monomer with EO linker was measured in an analogous manner in the temperature range of 0 °C to 50 °C (Figure 35A). **V2-1** displayed the highest conductivity, reaching 1.1×10^{-4} S/cm at 50 °C. After addition of LiTFSI the conductivities are gradually reducing (Figure 35B), in contrast to the behavior observed for **V1** compositions. The reduction of σ is even more distinct for higher salt concentrations decreasing to 10^{-10} S/cm for **V2-6** (LiTFSI / EO = 1). Presumably Li ion mobility is decreased due to the coordination to the EO groups.[335] **V2** compositions also show typical VFT behavior, which was also reported for other types of poly(ionic liquid)s.[336,337] Results obtained for **V1-2** and **V1-2** with corresponding VFT fitting are presented in Figure 36. The fitting shows minimal deviation with $R^2 = 0.9999$ and extracted constants are presented in Table 11.
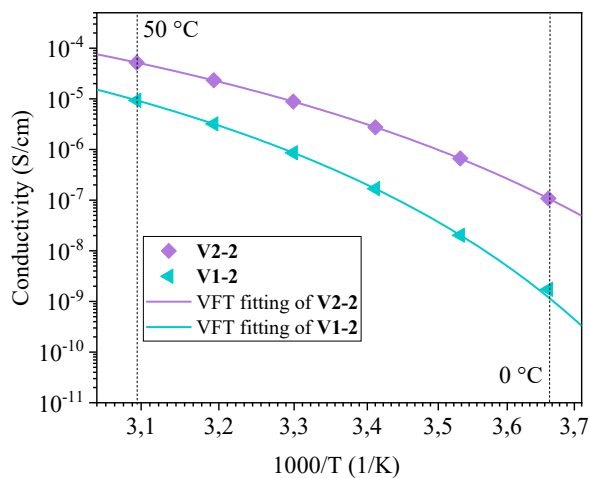
Figure 35. Conductivity as a function of temperature for **V1-2** and **V2-1** and the corresponding VFT fitting.

Table 11. VFT fitting parameters of **V1-2** and **V2-1** for conductivity.

Sample	$\sigma_0/10^{-1}$ S/cm	$B/10^3$ K	T_0/ K	R^2
V1-1	3.83 ± 0.25	1.16 ± 0.01	213.8 ± 0.4	0.9999
V2-1	6.41 ± 0.85	1.19 ± 0.03	196.8 ± 1.0	0.9999

Vitrimeric samples were analyzed *via* TGA under inert atmosphere for investigating thermal stability. In Figure 37A TGA curves display the thermal stability above 300 °C, which is much higher than the operating temperature of LiBs. The degradation pattern is similar for all samples irrespective of salt content, indicating that additional LiTFSI exhibits similar stability as the polymer matrix.[338] Additionally, there is not significant difference when comparing **V1** samples to **V2-1**, suggesting that the IL monomer with ethylene oxide linker is not affecting the stability negatively. Thermal transitions were investigated using DSC (Figure 37B), samples where initially kept isotherm at 120 °C for 30 min for removing the thermal history and for ensuring moisture removal. Vitrimers show behavior typical for amorphous polymers with one glass transition temperature (T_g) which is related to the segmental motions. T_g is affected by the addition of salt and it is reducing from 7 °C to -12 °C with increasing salt concentration, but the nature of the samples remains similar with one distinct glass transition. Change in T_g is also affecting the conductivity, **V1-8** (LiTFSI / EO = 2) exhibits higher conductivity than **V1-7** (LiTFSI / EO = 1) at lower temperatures due to the lower T_g value. The
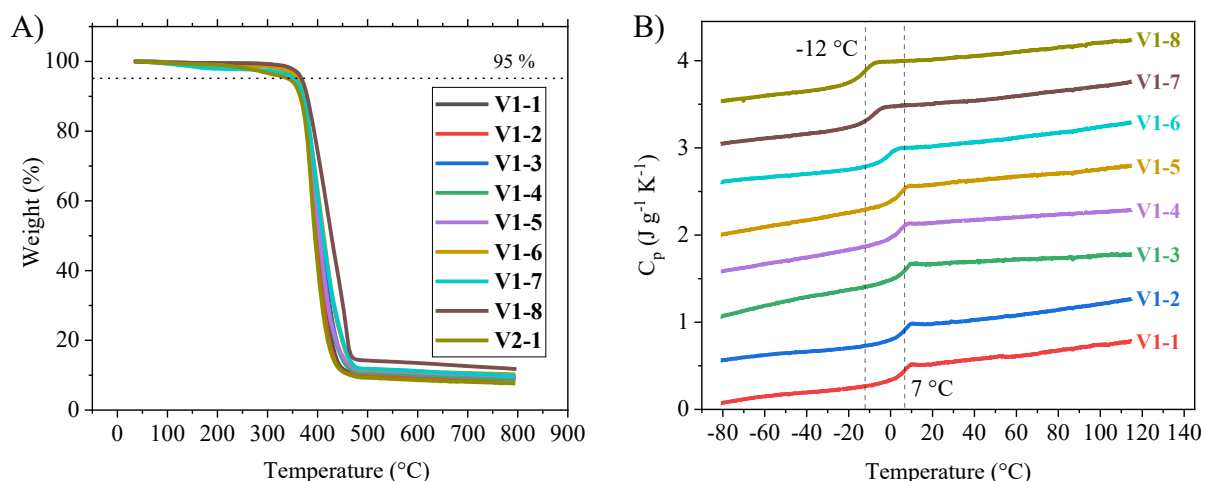
Figure 37. A) TGA measurements of vitrimeric samples (**V1-1 − V1-8**, **V2-1**) in the temperature range of 35 °C to 800 °C under nitrogen atmosphere, B) DSC measurements of vitrimeric samples (**V1-1 – V1-8**) in the temperature range of -80 °C to 120 °C with the heating rate of 5 K min⁻¹ under nitrogen atmosphere.

difference can be associated with the higher chain mobility in **V1-8** at the temperature close to T_g which promotes Li ion transport.

Vitrimers can be characterized by topology freezing temperature also referred as vitrimeric transition temperature (T_v), above which polymer network can undergo topology arrangement due to considerable dynamic bond exchange rate. Below T_v network is "frozen" and the bond exchange rate is neglectable. Moreover, the activation energy for this exchange represents a characteristic parameter for vitrimers, serving as a measure of the energy barrier for dynamic bond exchange.[339,340] For extracting both of these values rheology relaxation experiments were conducted. Share was applied to the sample and the corresponding relaxation modulus was measured over time at different temperatures. The experiment was conducted under continuous flow of nitrogen to prevent moisture absorption by hygroscopic LiTFSI. Two samples were chosen to investigate the influence of additional salt on vitrimeric properties. Figure 38A and
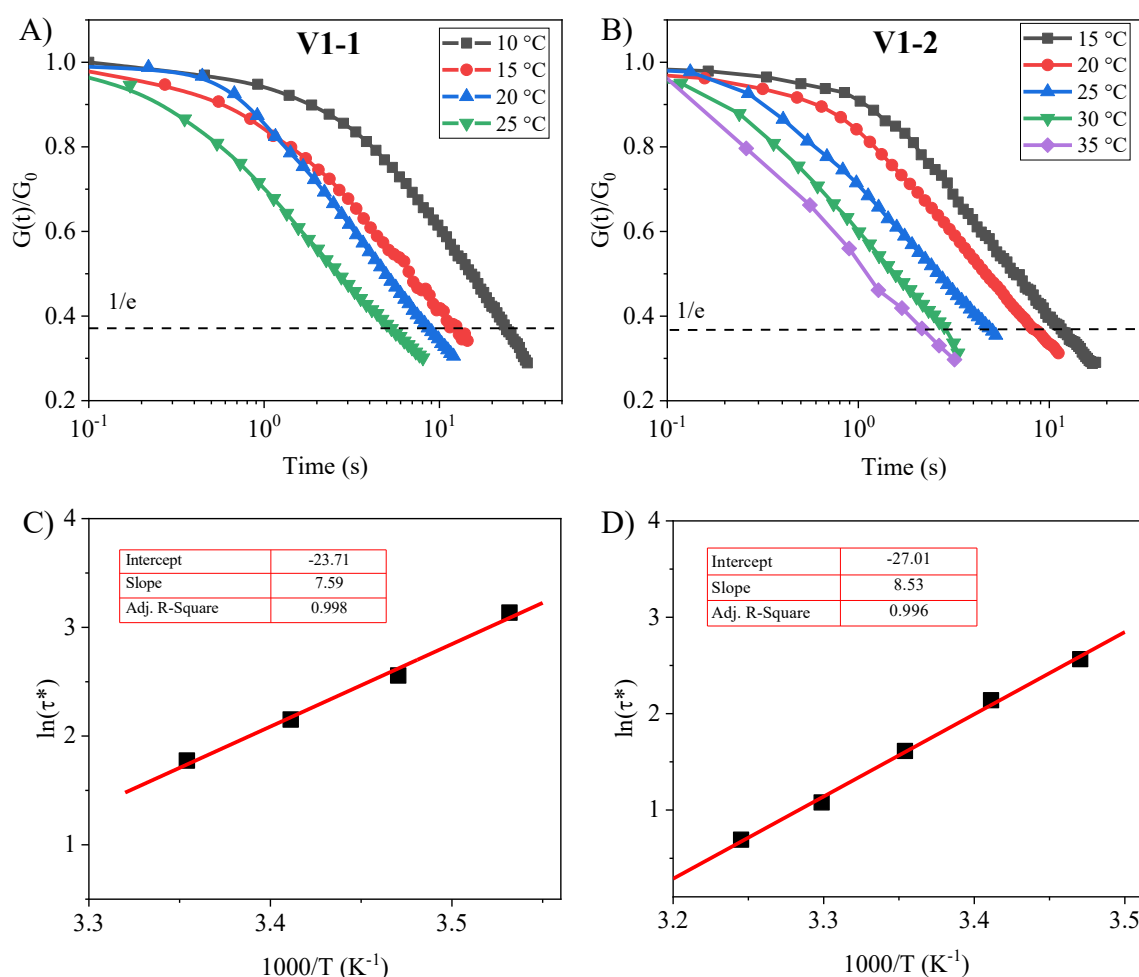
Figure 38. Normalized stress relaxation curves of A) **V1-1** and B) **V1-2** at different temperatures, relaxation time vs. inverse temperature and Arrhenius fitting of C) **V1-1** and D) **V1-2**.

Figure 38B shows the normalized stress-relaxation behavior of **V1-1** (LiTFSI / EO = 0) and **V1-2** (LiTFSI / EO = 0.1). The Maxwell model for viscoelastic fluids describes time-dependent response for materials and corresponding relaxation time. This model is represented as a combination of a spring and a dashpot in series, where each element contributes to the overall response. The normalized relaxation modulus is decaying exponentially, thus the time when modulus becomes 1/e is taken as relaxation time.[341-343] Corresponding times at different temperatures can be used to construct Arrhenius plot (Figure 38C and Figure 38D) which follows the equation $\ln(\tau^*) = \ln(\tau_0) + E_a/RT$. τ_0 is the characteristic relaxation time, E_a – activation energy, R – universal gas constant and T – temperature. E_a can be extracted as a slope of the fitting on Arrhenius plot, and it equals 61.7 kJ mol^{-1}for **V1-1** and 70.9 kJ mol^{-1} for **V1-2**, respectively. Extracted values are in accordance with the previously reported vitrimers based on boronic ester.[307,344,345]
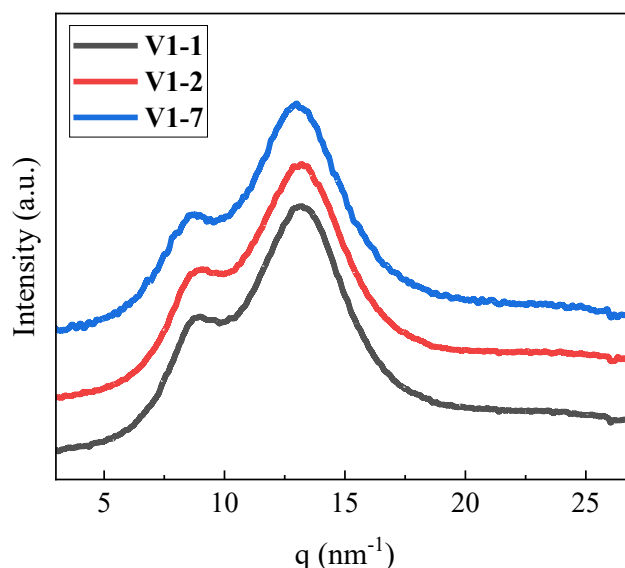
Figure 39. Wide angle X-ray diffraction (WAXD) measurements of **V1-1**, **V1-2** and **V1-7**.

The topology freezing temperature is defined as a temperature when materials viscosity equals to 10^{12} Pa × s.[300,305] Such high value of viscosity is experimentally difficult to measure, thus alternative methods have been applied for dynamic networks to extract T_v. By using stress relaxation measurements and Maxwell relation, T_v can be approximated as a temperature when relaxation time reaching 10^6 seconds. The curves in Figure 38C and Figure 38D are extrapolated to $\ln(10^6)$ and corresponding topology freezing temperature is calculated revealing T_v (**V1-1**) = - 71 °C and T_v (**V1-2**) = - 64 °C, respectively. However, the obtained values can have some inaccuracy especially when Arrhenius behavior of relaxation is reaching nonlinear region[300] close to glass transition temperature. When we compare two chosen samples small

changes in T_v and E_a can be observed due to the additional LiTFSI, however the effect is not significant. Additionally, the WAXD measurements conducted for **V1-1** (LiTFSI / EO = 0), **V1-2** (LiTFSI / EO = 0.1) and **V1-7** (LiTFSI / EO = 1) (Figure 39) confirm that no structural changes take place with the incorporation of Li salt. Obtained scattering vectors can be correlated to sizes of the heterogeneities by applying Bragg's law,[346] which relates x-ray wavelength to interplanar distances by the equation $n\lambda = 2d\sin\Theta$, where n is the order of diffraction, λ – wavelength, Θ – refraction angle, d – interplanar spacing. q on the other hand can be described by the combination of incident vector and refraction vector which follows the equation $q = 4\pi\sin\Theta/\lambda$.[347] By combining the scattering vector equation and Bragg's low the dependence of distance and q can be derived as $q = 2\pi/d$, hence $d = 2\pi/q$. Two clear signals at $q_1 = 8.3$ nm^{-1} (corresponding to domain size of d = 0.757 nm) and $q_2 = 13$ nm^{-1} (d = 0.483 nm) can be observed already in **V1-1**, indicating the segregation of polar and nonpolar domains within PILs, and addition of LiTFSI is not affecting the initially formed structures.

4.3   Reprocessing and 3D printing of vitrimeric electrolytes

Vitrimers have an ability of self-healing due to the presence of dynamic covalent bonds. Self-healing experiment of **V1-1** is presented in Figure 40A where a rectangular specimen was cut into two pieces and placed in the oven at 80 °C for 30 minutes. The restoration of the specimen can be visually observed. Additionally, self-healing efficiency was characterized *via* tensile testing (Figure 40B) before and after SH. The toughness of the sample was restored by 65 %. Enhanced efficiency can be achieved by applying additional pressure to the sample, ensuring tight contact between cut pieces and reducing the probability of imperfect surface formation, which can subsequently induce crack propagation and reduction in mechanical properties. Furthermore, allowing more time can further improve the self-healing effectiveness.

Sample **V1-1** was successfully used for demonstrating reprocessability of the material. In Figure 41 the sample is cut into small pieces and placed under hot-vacuum-press at 40 °C for 4 hours. The sample is forming a self-standing rectangular shape. Elevating the temperature can accelerate the process by intensifying bond exchange dynamics, thereby achieving a quicker restoration of the original shape. This unique property is also successfully used for extrusion-based 3D printing. For fused deposition modeling (FDM) the material should have the viscosity in the specific range (depending on the dimensions and properties of the 3D printer). Analyzing viscosity can be an effective approach to predict whether material is 3D
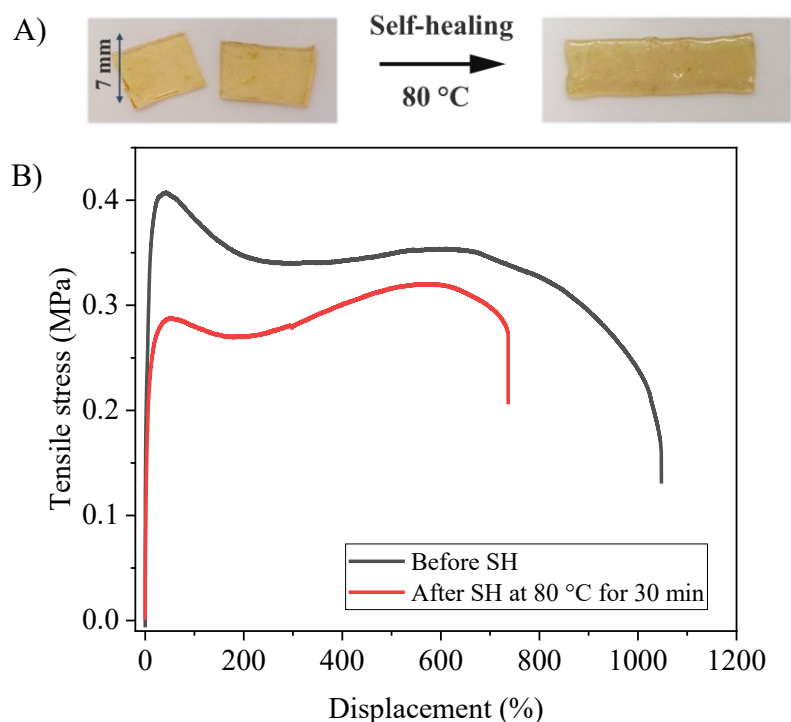
Figure 40. A) Self-healing experiment of **V1-1**, B) Tensile testing of **V1-1** before and after self-healing (SH).

printable or not. Figure 42A displays the viscosity dependence of **V1-3** on shear rate. The intersecting point of the green and yellow segments represents the printing windows. Within these windows, the low shear rate mirrors the flow behavior in the storage tank, while the high shear rate replicates the extrusion behavior. **V1-3** displayed printability in the wide range of temperature and similarly other compositions can be also used for FDM processes (Figure 42B). Successful printing was achieved on the glass plate in normal laboratory conditions. The resulted star shape (Figure 42C) consisting of 7 layers, showed good adhesion between each layer and good mechanical stability in water free environment. The presence of moisture can negatively affect the batteries performance therefore, the manufacturing process relies on materials drying procedures and operating in controlled dry environments.[348]
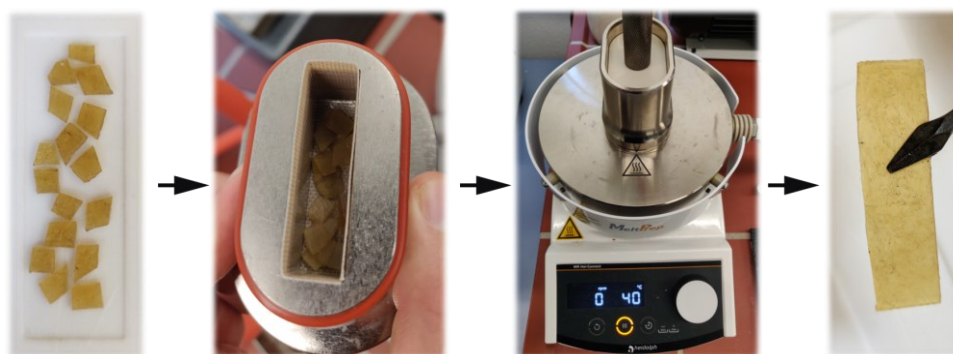
Figure 41. Reprocessing of **V1-1** *via* hot-vacuum-press at 40 °C for 4 hours.
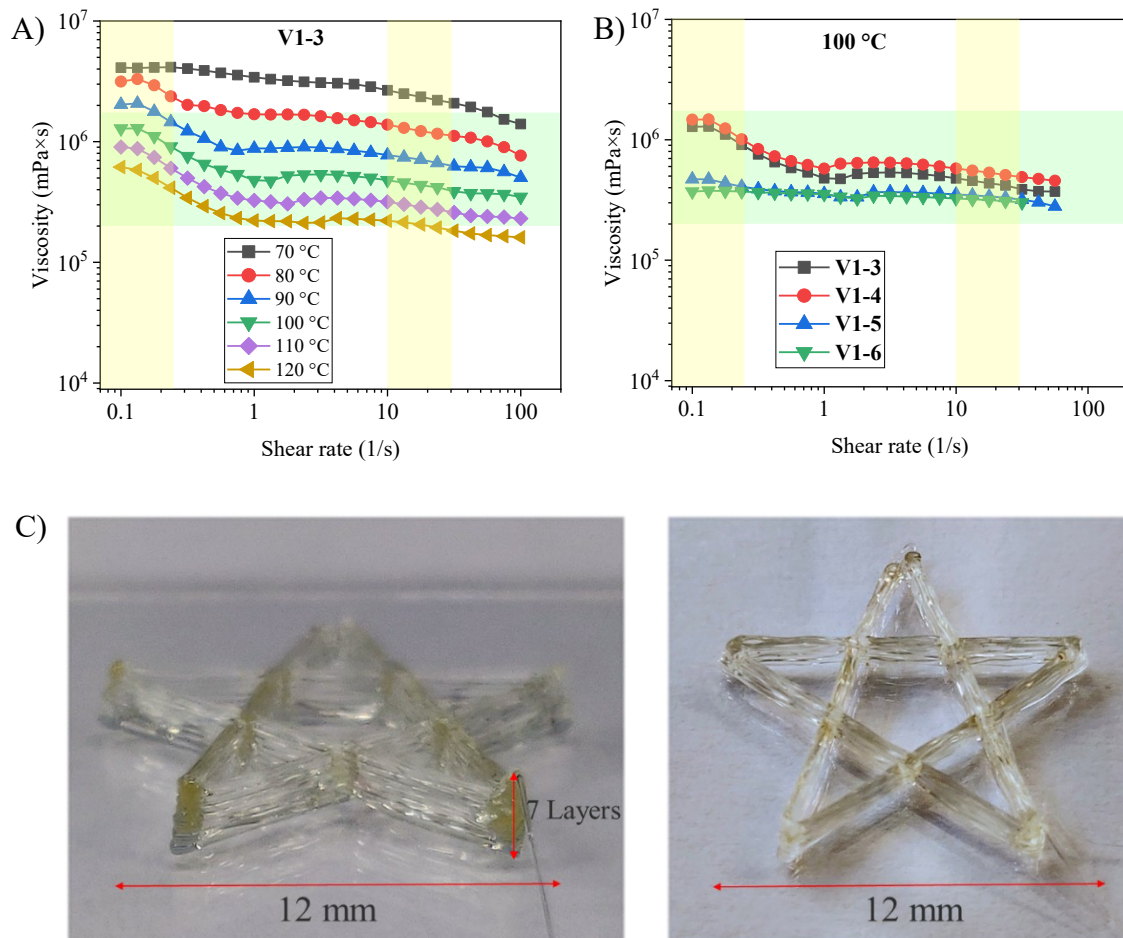
Figure 42. A) Viscosity dependence on shear rate of **V1-3** between 70 °C and 120 °C and highlighted printing windows, B) Viscosity dependence on shear rate of **V1-3**, **V1-4**, **V1-5** and **V1-6** at 100 °C and highlighted printing windows, C) FDM of **V1-3** at 120 °C into start shape.

5 Composite electrolytes

As previously mentioned, incorporation of ILs into electrolytes can be achieved in various ways.[349-351] CEs achieve the mechanical and electrochemical improvements by using nanofillers as additives for polymer electrolytes. In the scope of this work PEG based CEs were prepared by incorporating nanoparticles into polymer matrix. Initially the polymer was end group modified with UPy and barbiturate moieties for introducing supramolecular interaction, enhancing the mechanical properties and introducing advanced self-healing functionality. Silica based nanoparticles were used as nanofillers and they were surface functionalized with different groups for improving the impact on CPEs. Considerations when selecting functional groups were as follows: ionic liquids due to their advantageous conductivity and electrochemical stability; alkyl chains to change the dispersity and interactions with polymer matrix, and finally the hydroxyl functionalized particles to be considered as reference sample and better understand the impact of the modification. Furthermore, the nanoparticles were analyzed prior to incorporation to ensure covalent attachment to the surface and estimate the degree of modification. Composite electrolyte preparation is schematically depicted in Figure 43. The final electrolyte material includes conductive lithium salt dispersed together with NPs within polymer matrix. To explore the possibility of achieving superior material properties in terms of conductivity and mechanical integrity, the concentrations of salt and NPs were varied. The prepared compositions were extensively analyzed *via* rheology for investigation of the 3D printability of materials, which can be beneficial for next generation batteries.
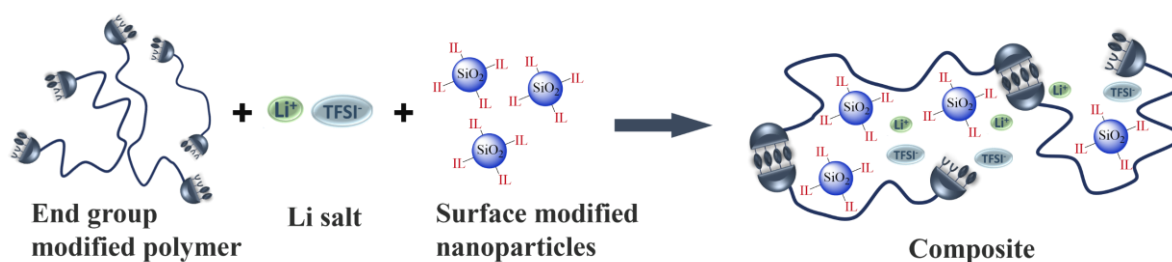
Figure 43. Schematical representation of composite electrolyte preparation.

5.1 *Surface modification of silica nanoparticles*

Silica nanoparticles (NPs) were surface modified with alkyl chains and pyrrolidinium-based ionic liquid, as depicted in Figure 44. Alkyl chains were attached to silica NPs (Nanopowder) *via* following procedure (Figure 44A): Nanopowder was dried under high vacuum at 170 °C to

ensure the removal of moisture, which could otherwise reduce the active sites on the surface of NPs and negatively impact the degree of modification. The particles were dispersed in DCM in the presence of pyridine as a base, followed by the addition of chloro(dodecyl)-dimethylsilane. Modified nanoparticles were obtained after 8 hours of stirring at room temperature and subsequent washing/purification.

For modification with ionic liquid LUDOX® SM colloidal silica was used and the modification procedure was adopted from previously reported procedure.[257] Initially N-[3-(trimethoxysilyl)propyl]-N-methylpyrrolidinium chloride (**10**) was synthesized and attached to the NP surface *via* two step processes (Figure 44B). In the first step colloidal silica was diluted

A)

B)
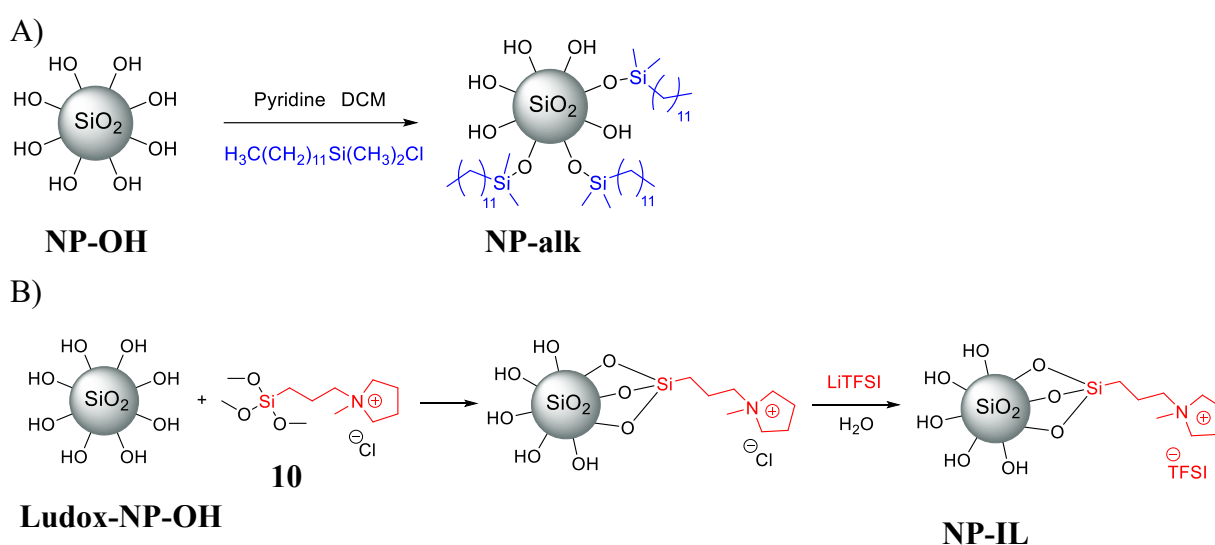
Figure 44. A) Surface modification of silica Nanopowder with chloro(dodecyl)dimethylsilane, B) Surface modification of LUDOX® SM colloidal silica with N-[3-(trimethoxysilyl)propyl]-N-methylpyrrolidinium chloride (**10**) and subsequent anion exchange with LiTFSI.

in deionized water and N-[3-(trimethoxysilyl)propyl]-N-methylpyrrolidinium chloride (**10**) was added to the solution. After stirring at 80 °C for 24 hours modified particles were collected by solvent removal under reduced pressure, followed by a washing step using acetone. Subsequent anion exchange reaction was conducted in water (for 8 hours at room temperature) to replace chloride with TFSI anions. NPs with chloride ions were water soluble but after anion exchange with a hydrophobic TFSI anion they precipitate, enabling facile collection of the product by centrifugation. The excess LiTFSI salt as well as byproducts were removed by washing several times with deionized water. Modified NPs were dried under vacuum at 70 °C for 48 hours and stored over P_2O_5.

Modified nanoparticles were characterized by FT-IR spectroscopy and TGA (Figure 45). Figure 45A shows IR spectra of surface modified and non-modified NPs. **NP-alk** displays

characteristic alkyl C-H stretching vibration at 2800-3000 cm^{-1}, which cannot be observed in case of **NP-OH**, indicating successful surface modification. **NP-IL** also displays alkyl C-H stretching resulting from N-[3-(trimethoxysilyl)propyl]-N-methylpyrrolidinium on the surface. Additionally, peaks characteristic for TFSI anion can be also observed: SO$_2$ stretching at 1348 cm^{-1}, CF$_3$ stretching band at 1179 cm^{-1}, S-N-S stretching at 1086 cm^{-1} and C-S stretching
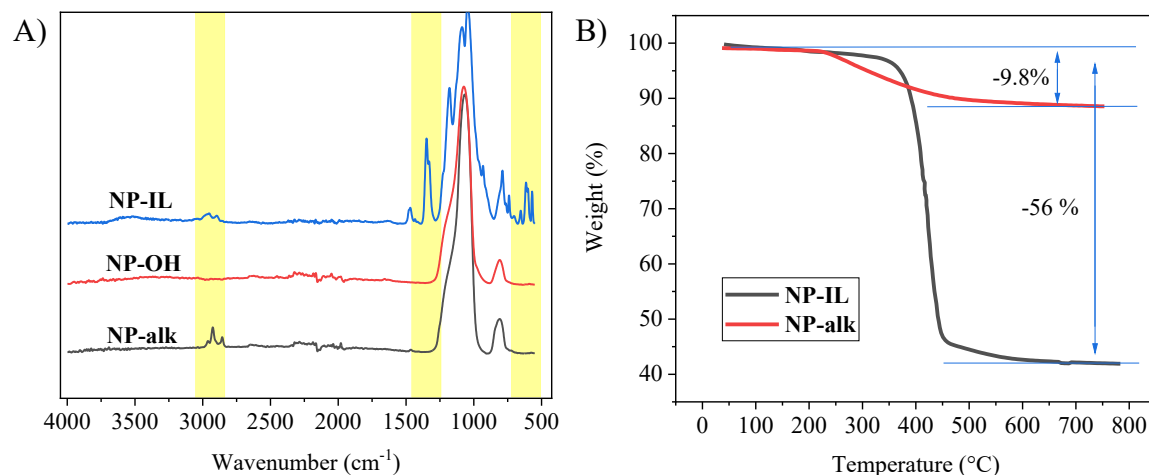
Figure 45. A) FT-IR spectra of **NP-IL**, **NP-OH** and **NP-alk**, B) TGA measurement of **NP-IL** and **NP-alk** in the temperature range of 35 °C to 800 °C under nitrogen atmosphere.

band at 788 cm^{-1}. Furthermore, all types of NPs show strong absorption at 1055 cm^{-1} corresponding to Si-O-Si bond stretching. TGA was also used to verify successful modification of the surface. Attached organic groups can decompose at high temperature and corresponding weight loss can be the indication of modified surface. In Figure 45B **NP-alk** and **NP-IL** display high thermal stability, the decomposition of **NP-alk** starts at around 250 °C, which is sufficiently high for potential use as electrolyte nanofiller. **NP-IL** exhibits higher thermal stability up to 350 °C, which is in the expected range for pyrrolidinium / TFSI ionic liquid groups.[327] Additionally, the quantity of weight loss can be used to estimate the degree of modification. Assuming that moisture loss and dehydroxylation contribute negligibly to the weight loss on TGA curves, and the recorded loss exclusively represents the modified surface, the degree of modification is estimated at approximately **NP-IL** ≈ 1.34 mmol/g and **NP-alk** ≈ 0.8 mmol/g, respectively.

NP-IL was also analyzed using solid state and solution NMR. **NP-IL** can be dissolved in DMSO-d$_6$ and corresponding spectrum is shown in Figure 46A. The signals from pyrrolidinium groups and the integral values additionally prove the attachment of IL groups to the surface. Solid-state Cross-Polarization Magic Angle Spinning (CP-MAS) NMR, as a method for obtaining high resolution solid state NMR spectra, was used for further investigations. In general solid state spectra exhibit broad signals caused by the orientation-depended interactions

Figure 46. A) ^{1}H NMR spectrum of **NP-IL** in DMSO-d$_6$, B) ^{29}Si MAS NMR spectra of **NP-IL** and **NP-OH**, C) Possible surface attachment of N-[3-(trimethoxysilyl)propyl]-N-methylpyrrolidinium to silica nanoparticles.

within the sample. Cross polarization coupled with magic angle spinning can increase the resolution by introducing artificial motion of sample rotor at the 54.74 ° angle (magic angle) to magnetic field. Under such conditions, the orientation-dependent interactions become negligible (becoming zero). The cross-polarization technique is increasing the signal intensities by transferring abundant spins (^{1}H or ^{19}F) to dilute spins such as ^{13}C or ^{15}N, or ^{29}Si, which is the relevant element for investigating the surface of silica nanoparticles. Figure 46B displays the MAS NMR spectra of **NP-IL** and **NP-OH** allowing us to compare nanoparticles before and after modification. On the red curve, we can observe the appearance of two new peaks. When ionic liquids adhere to the surface there are three possible ways of chemical bonding (Figure 46C, the IL group can be attached *via* 1 bond, 2 bonds or 3 bonds). On the spectrum formation of two types of connections can be seen, indicating formation of one and two covalent bonds, since the simultaneous formation of three bonds is less probable. Additionally, the signal at -115 ppm is reducing, which can be the result of the reduction of Si-OH groups on the surface due to the desired modification reaction.

The size of NPs was analyzed using TEM and DLS. Figure 47A and Figure 47B shows the TEM images of **NP-IL** and **NP-OH**, correspondingly. As expected, **NP-IL** exhibits a size under 10 nm compared to the starting material LUDOX® SM, which has a diameter of 7 nm.

Conversely, **NP-alk** displays a larger size than expected. While the initial material Nanopowder was reported to have a diameter of 12 mm, TEM analysis of the modified particles reveals significantly larger sizes reaching the range of 100 nm. Comparable results for the size of **NP-alk** are also obtained with DLS (Figure 47C) showing the average value of 155 nm, with 11.2 % of polydispersity.
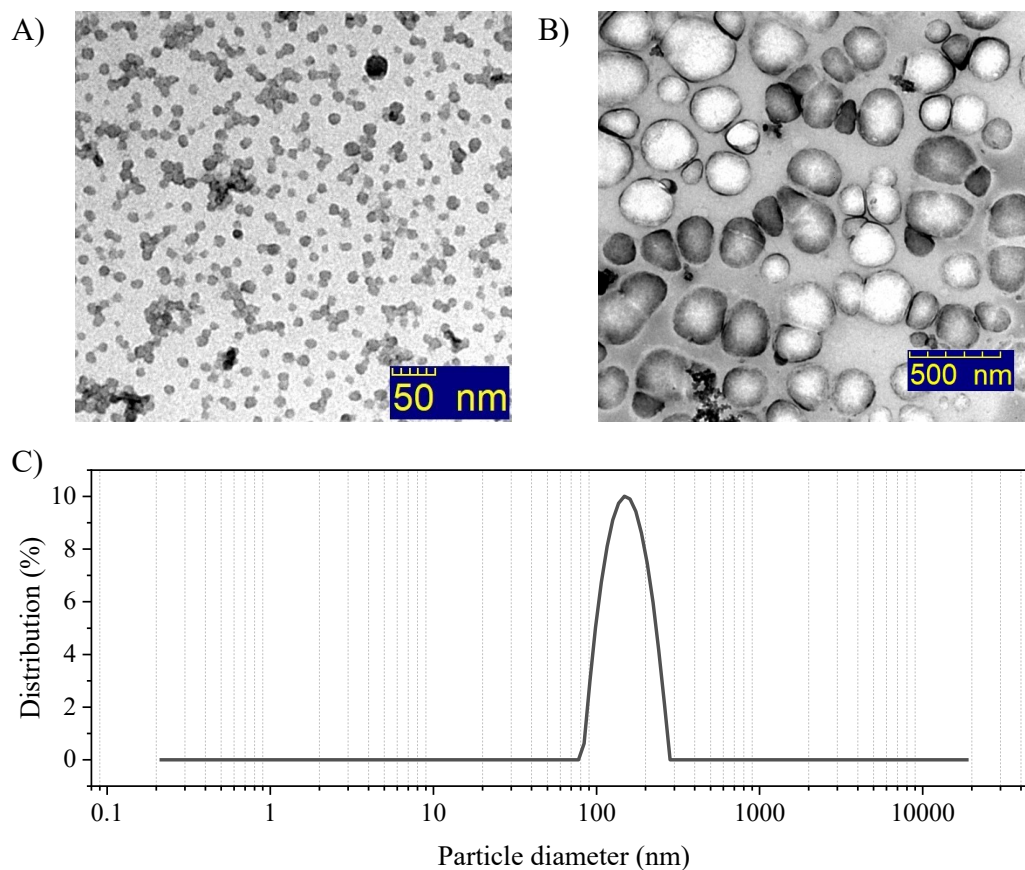
Figure 47. A) TEM image of **NP-IL**, B) TEM image of **NP-OH**, C) DLS measurement of **NP-OH** in THF.

5.2 Synthesis and preparation of composite materials

PEG 1500 and PEG 8000 were used for preparing composite electrolytes. Polymers were end group modified with UPy and barbiturate groups for integrating hydrogen bonding ability, thus improving mechanical properties and introducing self-healing functionality. The two chosen moieties differ in the strength of formed hydrogen bonded networks, barbiturate is forming much weaker interactions while UPy is forming strong quadrupolar hydrogen bonds. The
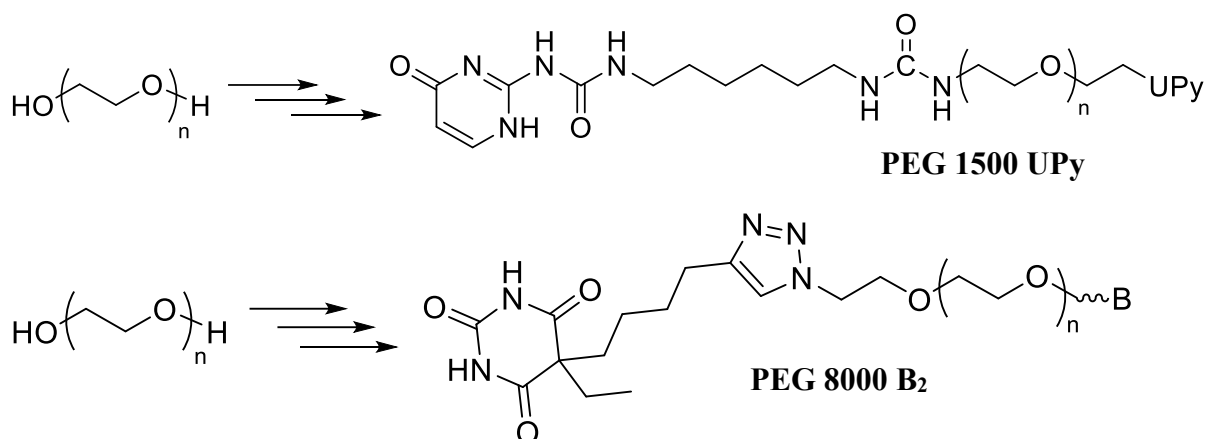
Figure 48. Structures of end group modified **PEG 1500 UPy** and **PEG 8000 B₂**.

structures of end group modified polymers are presented in Figure 48 and the modification procedures are presented in the Experimental section (8.5). Polymers were analyzed using proton NMR for confirming the successful modification. Figure 49 displays the ^{1}H NMR spectrum of **PEG 1500 UPy** in chloroform-d. The characteristic signals of UPy group can be
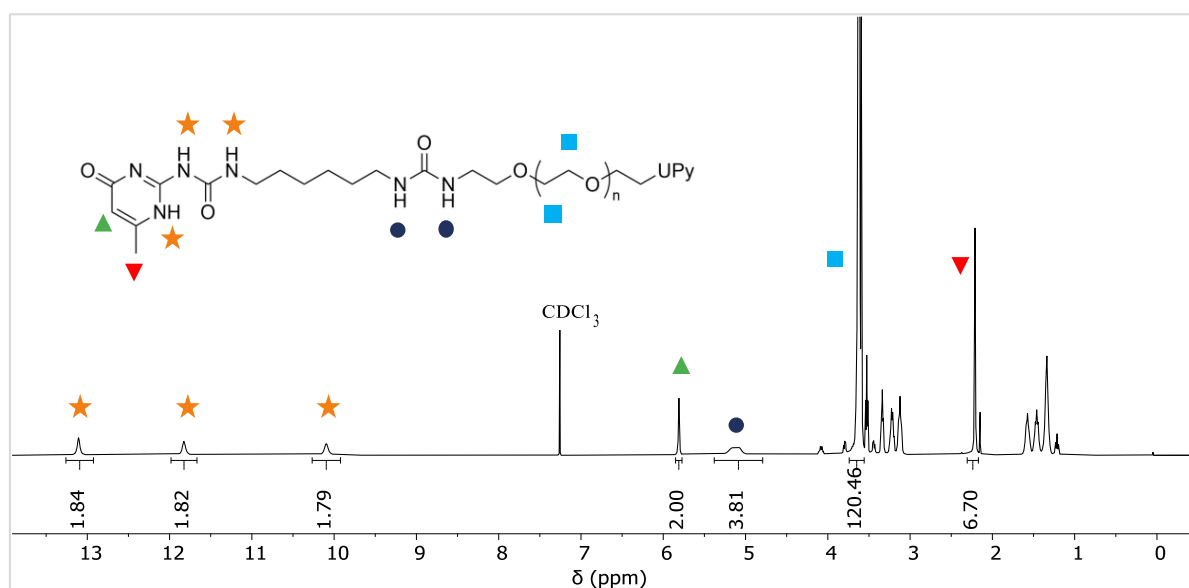
Figure 49. ^{1}H NMR spectrum in CDCl₃ of **PEG 1500 UPy**.

observed at higher ppm values; furthermore, formation of urea bond is evident which is formed when reacting UPy isocyanate (**12**) with PEG-diamine (**15**) in the final step of modification. Proton NMR is also used to calculate the degree of polymerization and molecular weight of the sample (DP = 32, Mn = 2000 Da) by establishing the ratio of end group protons *vs.* protons from polymers repeating unit. Similarly, **PEG 8000 B$_2$** was analyzed using ^{1}H NMR in chloroform-d. The spectrum (Figure 50) shows the successful modification of PEG by barbiturate groups. The signal of triazole ring can be observed at 7.5 ppm, indicating the attachment of barbiturate group to PEG *via* click reaction. With the ratios and the integral values of polymer backbone the degree of polymerization and molecular weight was calculated (DP = 206, Mn = 9600 Da).
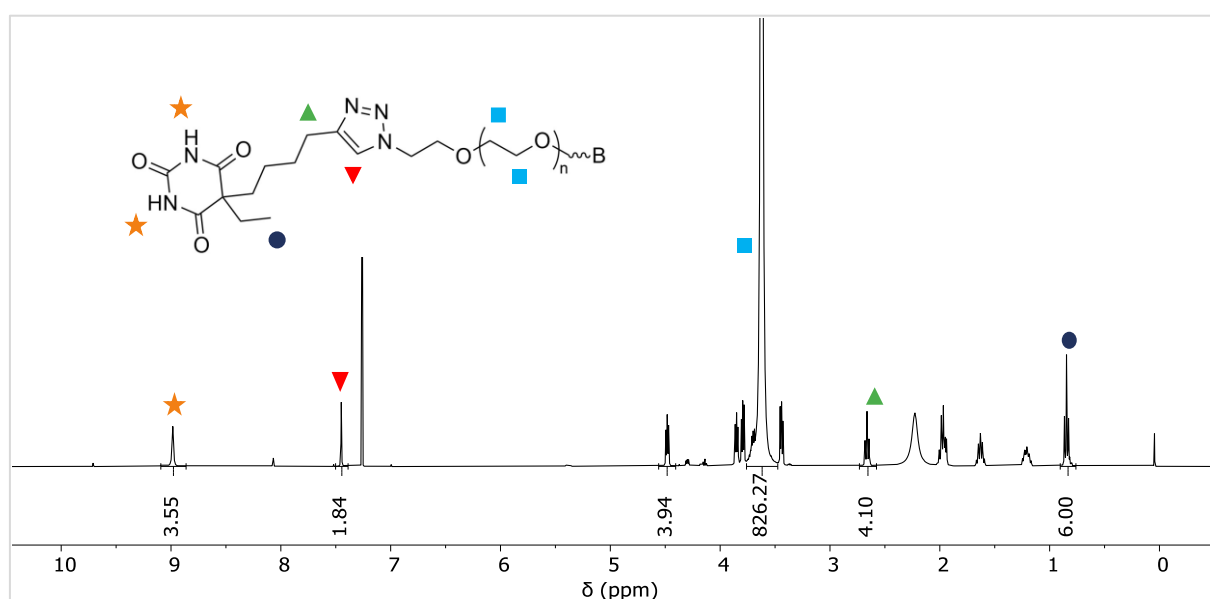
Figure 50. ^{1}H NMR spectrum in CDCl$_3$ of **PEG 8000 B$_2$**.

Modified PEG polymers and surface modified nanoparticles were used for preparing composite electrolytes. Incorporating the nanofillers enhances both the mechanical properties and has the potential to improve ionic conductivities.[246,352-354] Compositions were prepared by mixing polymer samples with NPs and LiTFSI in dry ACN, followed with the solvent removal in the oven at 80 °C and subsequent drying in vacuum at 80 °C. Samples containing NPs were ultrasonicated before solvent removal for ensuring the good dispersity. Prepared and investigated compositions are given in Table 12. Sample **PEG-5**, **PEG-6**, **PEG-7** were prepared with LUDOX® SM colloidal silica which was dried *via* freeze-drying. **PEG-15**, **PEG-16** and **PEG-17** were prepared with dry Nanopowder silica.

Table 12. Composition of PEG-composites containing **PEG 1500 UPy** and **PEG 8000 B$_2$** mixed with **NP-IL**, **NP-alk** and **NP-OH** and different amounts of LiTFSI.

Sample	Polymer-type	EO/LiTFSI	NPs-type	NPs (wt%)
PEG-1	PEG 1500 UPY	5	-	
PEG-2	PEG 1500 UPY	5	NP-IL	5
PEG-3	PEG 1500 UPY	5	NP-IL	10
PEG-4	PEG 1500 UPY	5	NP-IL	15
PEG-5	PEG 1500 UPY	5	NP-OH	5
PEG-6	PEG 1500 UPY	5	NP-OH	10
PEG-7	PEG 1500 UPY	5	NP-OH	15
PEG-8	PEG 8000 B$_2$	5	-	-
PEG-9	PEG 8000 B$_2$	10	-	-
PEG-10	PEG 8000 B$_2$	20	-	-
PEG-11	PEG 8000 B$_2$	5	NP-alk	5
PEG-12	PEG 8000 B$_2$	5	NP-alk	10
PEG-13	PEG 8000 B$_2$	5	NP-alk	15
PEG-14	PEG 8000 B$_2$	5	NP-IL	10
PEG-15	PEG 8000 B$_2$	-	NP-OH	5
PEG-16	PEG 8000 B$_2$	-	NP-OH	10
PEG-17	PEG 8000 B$_2$	-	NP-OH	15
PEG-18	PEG 8000 B$_2$	-	NP-alk	5
PEG-19	PEG 8000 B$_2$	-	NP-alk	10
PEG-20	PEG 8000 B$_2$	-	NP-alk	15

5.3 Analysis and characterization of PEG composites

The materials were investigated for 3D printability and for understanding how different surface modification of NPs is influencing the melt flow behavior. Initially thermal behavior of PEG/LiTFSI systems was probed *via* DSC measurements in the temperature range of -15 °C to 170 °C. **PEG 1500 UPy** was reported to have amorphous properties in presence of high concertation of LiTFSI.[355] **PEG 8000 B$_2$** displays similar behavior (Figure 51). Pure end group modified polymer exhibits one melting peak appearing at 52 °C. The presence of Li salt in **PEG-10** (EO / LiTFSI = 20) led to lowering of melting temperature to 37 °C. Presumably, LiTFSI is coordinating with the oxygen in PEG backbone, disrupting the interactions between polymer chains and impeding the formation of ordered crystalline structure. Moreover, salt can enhance the segmental mobility of the polymer, consequently affecting the glass transition temperature. Additionally, an exothermic peak is appearing at 10 °C on DSC heating curve, which can be interpreted as cold crystallization peak. The cooling rate applied during the measurement is likely to have quenched crystallization process. Upon heating above T$_g$ reordering of polymer chains takes place. Presumably, the glass transition temperature of **PEG-10** falls outside the range of measured temperature. **PEG-9** (EO / LiTFSI = 10) did not display presence of melting peak, indicating that the sample is fully amorphous and corresponding T$_g$ can be seen at 15 °C. Further increasing the salt content is increasing the T$_g$ which is 22 °C for **PEG-8** (EO / LiTFSI = 5).
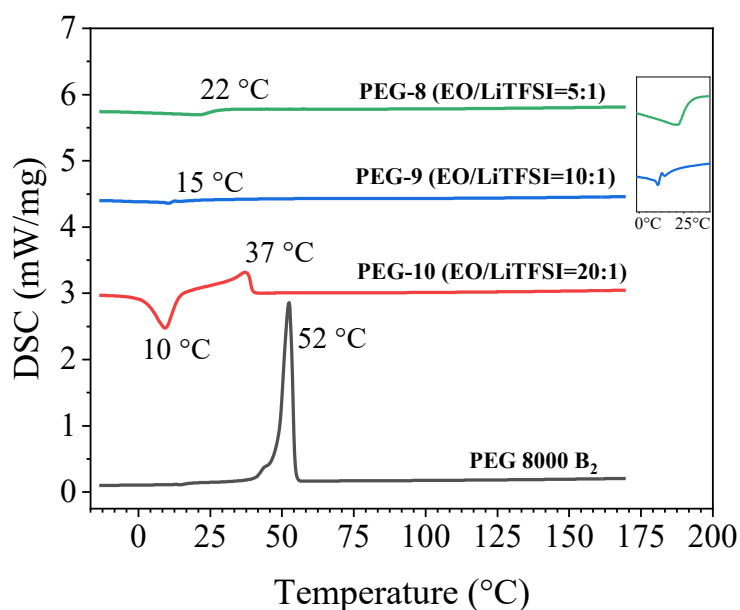
Figure 51. DSC measurements of **PEG 8000 B$_2$**, **PEG-8**, **PEG-9** and **PEG-10** in the temperature range of -15 °C to 170 °C with the heating rate of 5 K min^{-1} under nitrogen atmosphere.

3D printability of the prepared nanocomposites was investigated above melting and glass transition temperatures *via* rheology, by measuring the melt flow properties at varying shear rate. As it was discussed in the previous chapter the sample should be characterized by specific viscosity values to be applicable for FDM. Typical viscosity vs. shear rate of pure **PEG 8000 B$_2$** is presented in Figure 52A. The sample's viscosity falls under 10 Pa × s above its melting temperature, which is extremely low for FDM. According to the previously published work of our working group,[355] **PEG 1500 UPy** displays undesirable melt flow properties that fall beyond the required printing windows. However, although the addition of Li salt is changing the behavior of polymer melt resulting in shear rate independent viscosity (reaching the values of 100 Pa × s) for samples **PEG-8** (EO / LiTFSI = 5), **PEG-9** (EO / LiTFSI = 10) and **PEG-10** (EO / LiTFSI = 20) (Figure 52B), the melt flow still falls beyond the required printing windows. The increase in viscosity is more distinct with **PEG-8**, which contains the highest Li salt concentration. In order to adjust the melt flow behavior to the
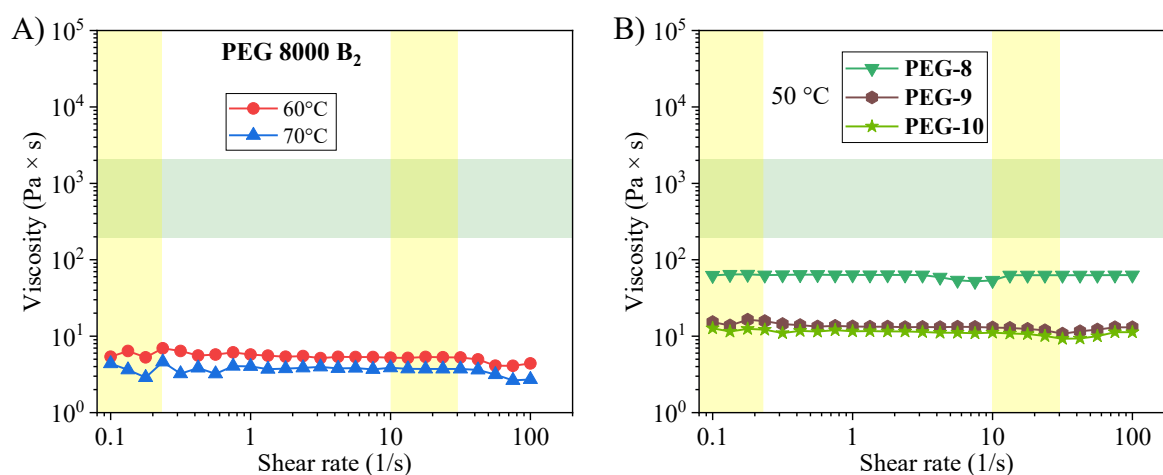
Figure 52. A) Viscosity dependence on shear rate of **PEG 8000 B$_2$** at 60 °C and 70 °C and highlighted printing windows, B) Viscosity dependence on shear rate of **PEG-8**, **PEG-9** and **PEG-10** at 50 °C and highlighted printing windows.

requirement properties NPs were introduced, and comparable measurements were carried out. Figure 53A illustrates the viscosity behavior of **PEG-11**, **PEG-12** and **PEG-13** samples with the additional **NP-alk** at different concentrations. Notably, **PEG-13** shows the highest viscosity in the full range of shear rate due to the highest amount of nanofillers (15 wt%), additionally the shear thinning behavior is observed. The viscosity of the mixture is decreasing under shear stress, which can be the result of the alkyl-like surface of the added NPs, probably reducing the incorporation in the polymer matrix, which becomes more predominant with increasing shear rate. The hydrophobic surface might result in less dispersed sample formation due to the weaker
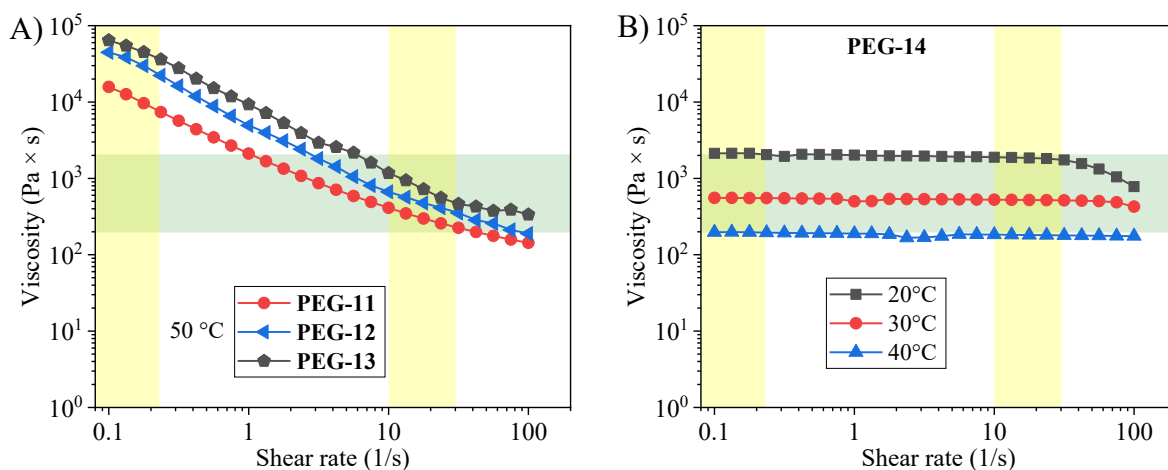
Figure 53. A) Viscosity dependence on shear rate of **PEG-11**, **PEG-12** and **PEG-13** at 50 °C and highlighted printing windows, B) Viscosity dependence on shear rate of **PEG-14** at 20 − 40 °C and highlighted printing windows.

interactions with the polymer matrix. Under the low shear rate the viscosity is influenced by agglomerates leading to an increase in viscosity. However, at high shear rate agglomerates break down and correspondingly the viscosity value is dropping. The samples **PEG-11**, **PEG-12** and **PEG-13** lacked the desired rheological properties for 3D printability. **PEG-14** consisting of **PEG 8000 B₂** and **NP-IL** displayed shear independent viscosity (Figure 53B). The surface modification *via* ionic liquid groups improves the dispersion ability within the PEG based polymer, enhancing the compatibility of NPs with a polymer matrix. The liner viscosity behavior is also fitting in the printability windows in the temperature range of 20 − 40 °C. Unfortunately, elevated temperatures near RT are reducing the shape stability. After the 3D printing the material retains the ability to flow. Thus, **PEG-14** is not applicable for 3D printing.
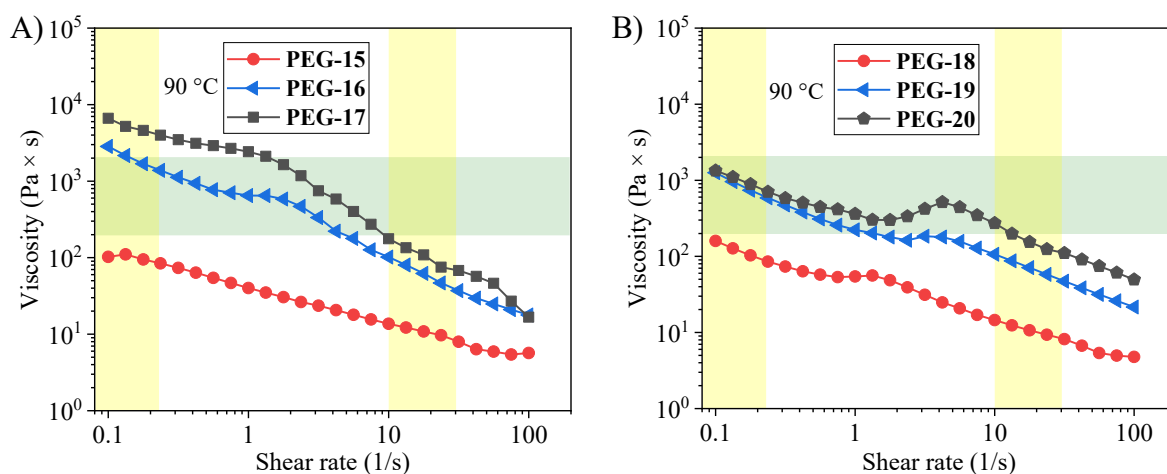
Figure 54. A) Viscosity dependence on shear rate of **PEG-15**, **PEG-16** and **PEG-17** at 90 °C and highlighted printing windows, B) Viscosity dependence on shear rate of **PEG-18**, **PEG-19** and **PEG-20** at 90 °C and highlighted printing windows.

PEG 8000 B$_2$ was also tested with Naopowder and **NP-alk** with the content of 5 wt% (**PEG-15**), 10 wt% (**PEG-16**) and 15 wt% (**PEG-17**) without any additional salt. Nanopowder-based composites exhibited shear thinning behavior (Figure 54A) indicating the issue with the dispersity or the incompatibility with the polymer matrix. The viscosity values are falling outside of the printability windows. Modifying the surface with alkyl chains does not alter the interaction significantly. **PEG-18**, **PEG-19** and **PEG-20** continue to show the shear thinning behavior (Figure 54B) and the values are beyond the acceptable range. In summary, **PEG 8000 B$_2$** with all prepared compositions did not fulfil the requirements for printing. The decrease in T$_g$ enables the material to maintain its flow properties near room temperature, yet the challenge lies in achieving proper nanoparticle dispersion and interaction with the polymer, which remains the limiting factor. **PEG 1500 UPy** was investigated with the additional salt and NPs. In the Figure 55 **PEG-2** (EO / LiTFSI = 5, **NP-IL**-5 wt%), **PEG-3** (EO / LiTFSI = 5,
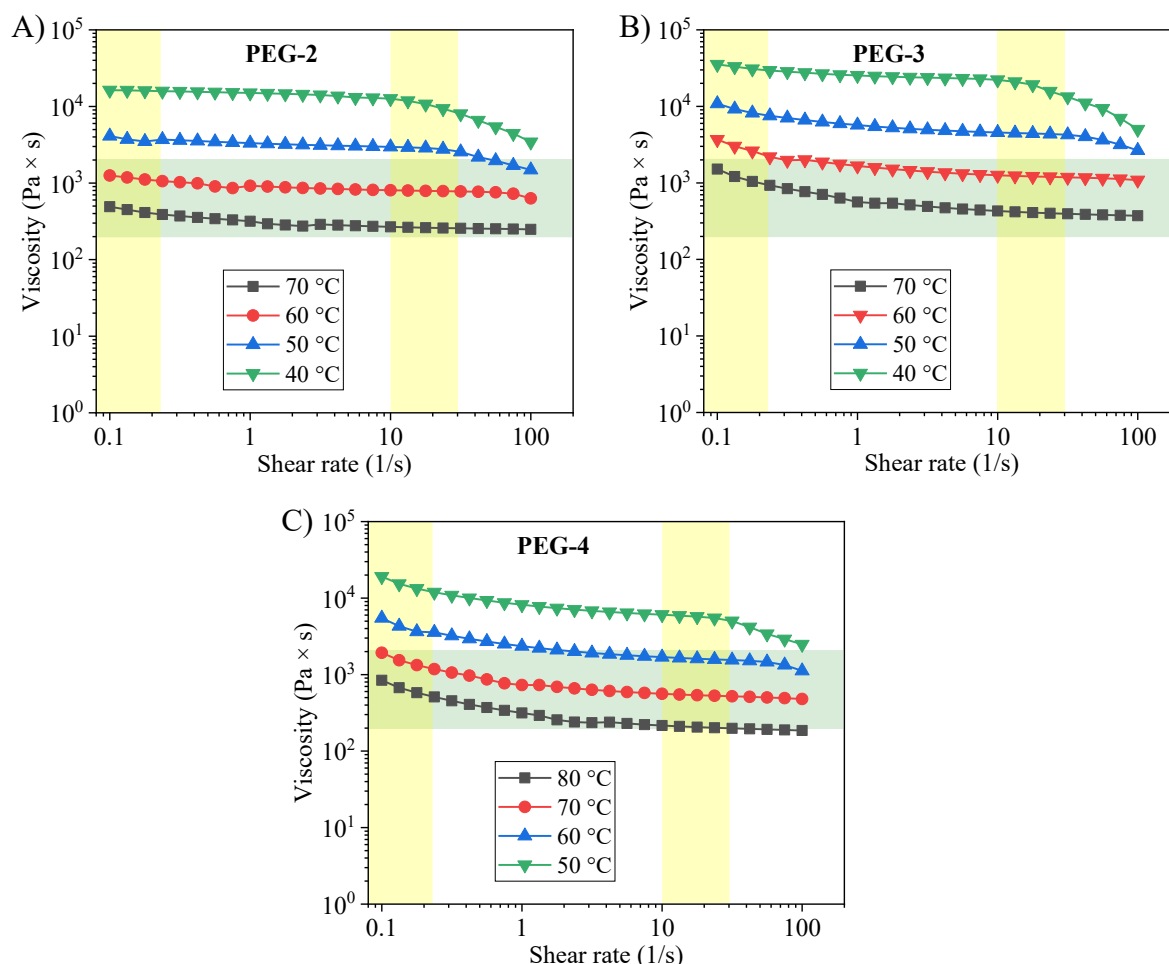
Figure 55. A) Viscosity dependence on shear rate of **PEG-2** at 40 − 70 °C and highlighted printing windows, B) Viscosity dependence on shear rate of **PEG-3** at 40 − 70 °C and highlighted printing windows, C) Viscosity dependence on shear rate of **PEG-4** at 50 − 80 °C and highlighted printing windows.

NP-IL-10 wt%) and **PEG-4** (EO / LiTFSI = 5, **NP-IL**-15 wt%) samples exhibited shear independent viscosity. Samples can be printed and moderately high temperature (70 − 60°C) viscosities fall in the printing windows. Modified nanoparticles display better incorporation in the polymer, evident in the absence of shear thinning behavior. **PEG 1500 UPy** was similarly tested with LUDOX® SM colloidal silica (dried *via* lyophilization). **PEG-5** (EO / LiTFSI = 5, **NP-OH**-5 wt%), **PEG-6** (EO / LiTFSI = 5, **NP-OH**-10 wt%) and **PEG-7** (EO / LiTFSI = 5, **NP-OH**-15 wt%) also display linear relation between viscosity and shear rate in the temperature range of 50 − 80 °C (Figure 56). The presence of NPs is positively affecting the melt flow properties, whereupon **PEG-7** exhibits the most viscous properties. Moreover, all prepared composites materials with LUDOX® SM colloidal silica are printable in the temperature range above 60 °C.
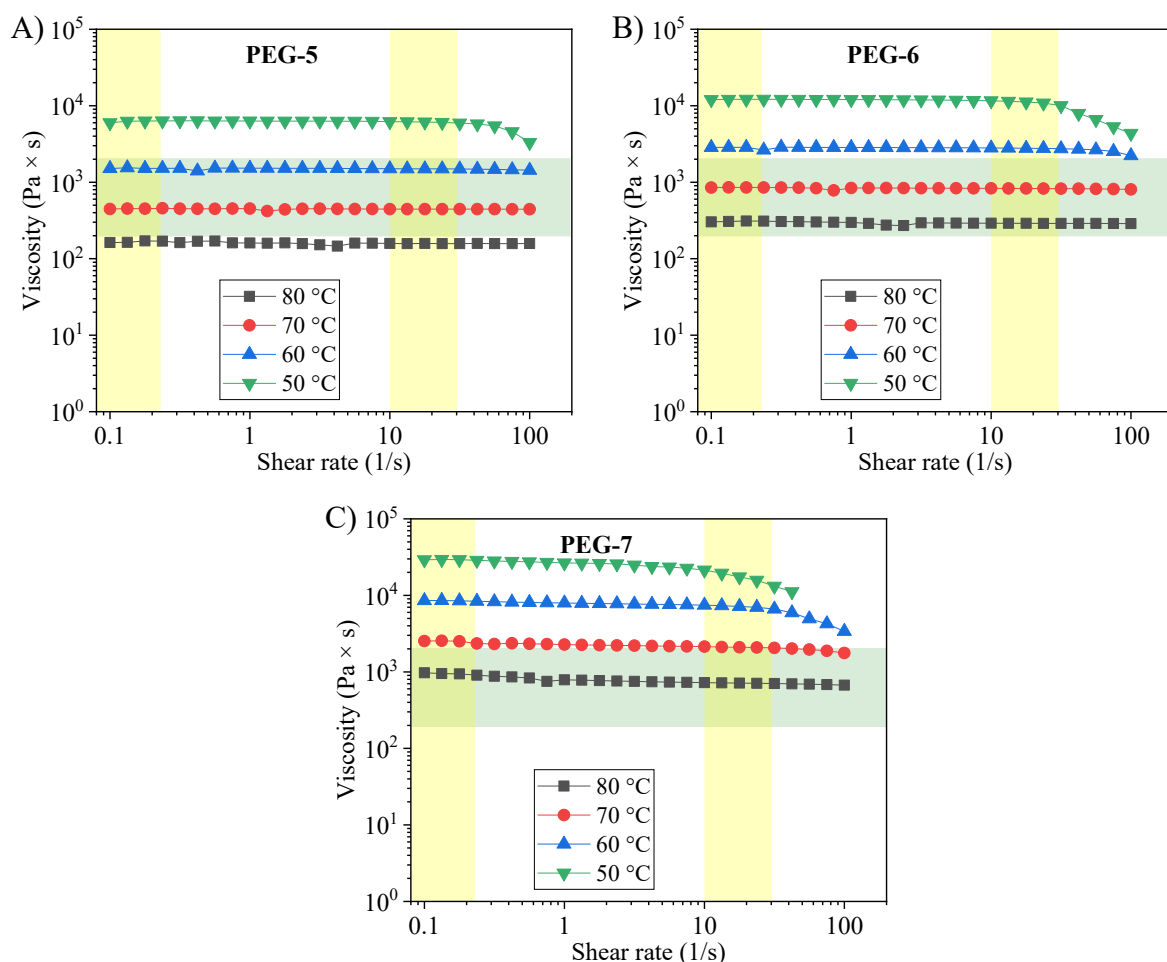
Figure 56. A) Viscosity dependence on shear rate of **PEG-5** at 50 − 80 °C and highlighted printing windows, B) Viscosity dependence on shear rate of **PEG-6** at 50 − 80 °C and highlighted printing windows, C) Viscosity dependence on shear rate of **PEG-7** at 50 − 80 °C and highlighted printing windows.

To estimate the applicability of prepared composites as electrolytes the samples were investigated *via* BDS. DC conductivity was extracted from BDS measurements as the value of the plateau of conductivity vs. frequency measurement. Figure 57 shows the plot of **PEG-1**, **PEG-4** and **PEG-7**. The conductivities cannot be extracted at 0 °C due to considerable overlap of electrode polarization with the plateau. **PEG-1** containing only additional LiTFSI (EO / LiTFSI = 5) displayed the conductivity up to 2.8×10^{-5} S/cm at 80 °C. The samples with nanofillers (**NP-IL**, **NP-OH**) displayed conductivity in the similar range. Moreover, **PEG-4** containing **NP-IL** (modified surface) has a positive impact not only on mechanical properties but also on the conductivity which is as well reaching 3.2×10^{-5} S/cm (Figure 57B). In contrast, **PEG-7** with unmodified nanoparticles shows reduced conductivity of 1.7×10^{-5} S/cm (Figure 57C). However, the conductivity values at RT (ranging from 10^{-7} to 10^{-8} S/cm) still
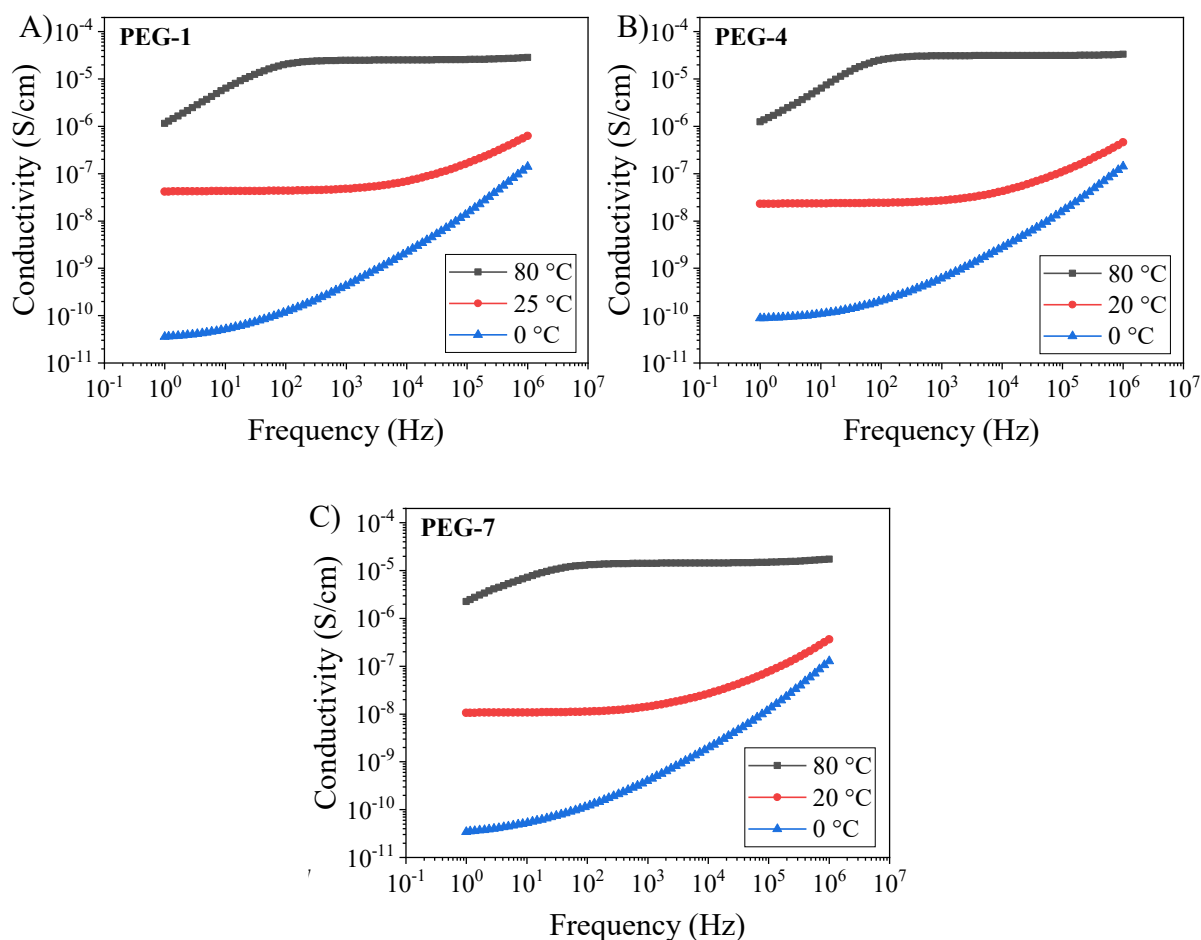
Figure 57. A) BDS measurement of **PEG-1** at different temperatures with the frequency range between 1 to 10^6 Hz, B) BDS measurement of **PEG-4** at different temperatures with the frequency range between 1 to 10^6 Hz, C) BDS measurement of **PEG-7** at different temperatures with the frequency range between 1 to 10^6 Hz.

require further enhancement to make the printable composites competitive to the commercial liquid electrolytes.

PEG 8000 B₂ was also analyzed *via* the BDS spectroscopy, although **PEG 8000 B₂** did not exhibit the required melt flow behavior for 3D printing. Consequently, only the samples with LiTFSI were investigated to understand how varying salt concentration can impact the conductivity. σ reached 10^{-3} S/cm for **PEG-9** (EO/ LiTFSI = 10) (Figure 58B). The conductivity for **PEG-8** (EO/ LiTFSI = 5) (Figure 58A), containing the highest concentration of LiTFSI, displayed a slight reduction of σ attributed to the agglomeration. Such behavior was previously reported for PEG based electrolytes.[158,356] **PEG 8000 B₂** exhibits higher conductivities than **PEG 1500 UPy**, Although, according to the literature a higher molecular weight is usually leading to the reduction of ionic conductivity,[357,358] the end group
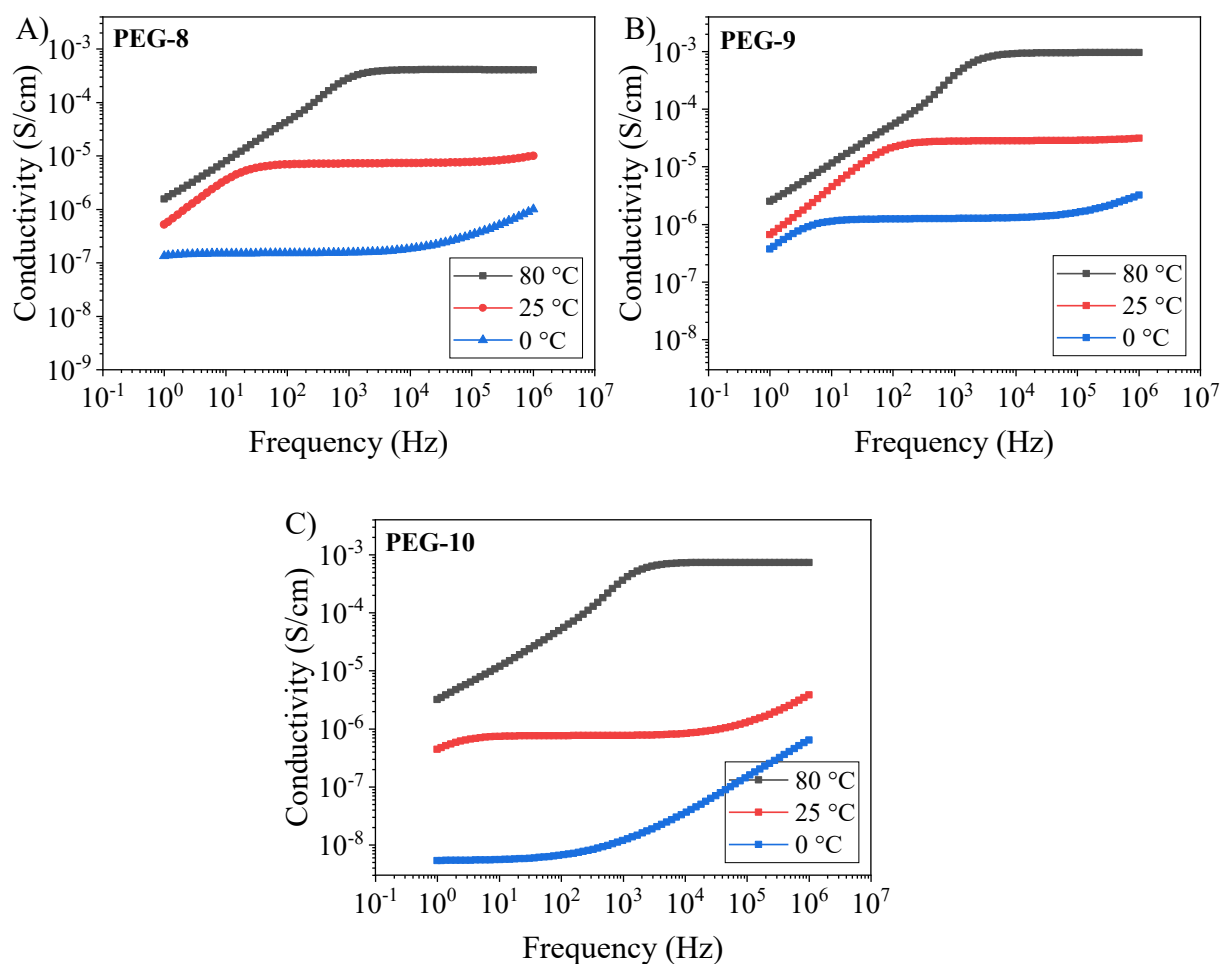
Figure 58. A) BDS measurement of **PEG-8** at different temperatures with the frequency range between 1 to 10^6 Hz, B) BDS measurement of **PEG-9** at different temperatures with the frequency range between 1 to 10^6 Hz, C) BDS measurement of **PEG-10** at different temperatures with the frequency range between 1 to 10^6 Hz.
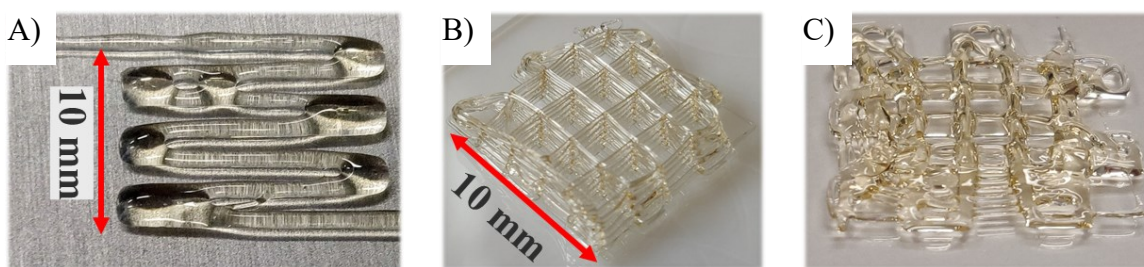
Figure 59. A) FDM of **PEG-1** at 70 °C (for storage tank and printing head) on the glass surface, the needle size 0.33 mm, normal laboratory conditions, B) FDM of **PEG-4** at 90 °C for storage tank and 70 °C for printing head on the glass surface, the needle size 0.33 mm, normal laboratory conditions, C) Printed sample after 1 hour under normal laboratory conditions, shape loss after moisture absorption.

modification of the polymer seems to have a significant impact on the properties. Presumably, strong supramolecular network formed by quadrupole UPy groups is more strongly hindering the ion mobility, compared to the weakly hydrogen bonding barbiturate groups. Additionally, **PEG 1500 UPy** contains a much higher concentration of end groups than **PEG 8000 B₂**. However, the trade-off is the mechanical properties as shorter chains with UPy groups are exhibiting required viscosities for FDM. Figure 59A demonstrates the 3D printing of **PEG-1** (EO / LiTFSI = 5), the printing was conducted at 70 °C for the storage tank and the printing head. The sample did not show shape stability and the polymer spread on the glass surface after the extrusion. Figure 59B displays the FDM of **PEG-4** (EO / LiTFSI = 5, **NP-IL**-15 wt%) into grid shape with 10 mm width. The temperature profile was set at 90 °C for the storage tank and 70 °C for the printing head as this temperature value for the printing head is applicable according to the rheology profile discussed above. The printed shape showed stability and good
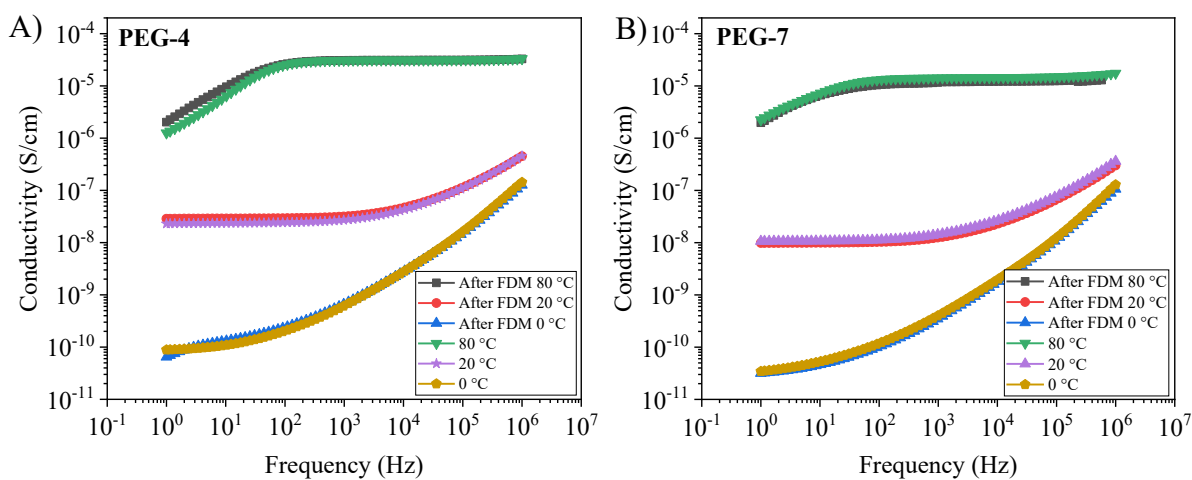
Figure 60. A) BDS measurement of **PEG-4** at different temperatures with the frequency range between 1 to 10^6 Hz, before and after FDM B) BDS measurement of **PEG-7** at different temperatures with the frequency range between 1 to 10^6 Hz, before and after FDM.

adhesion between printed layers (total number of printed layers was set at 6). The sample retains its shape for one hour under normal laboratory conditions. However, the printed grid structure collapses over time (Figure 59C) due the hygroscopic LiTFSI, which absorbs moisture from the air. Importantly, processing *via* FDM does not have impact on the conductivity, which was demonstrated by BDS measurements before and after the printing. The processed composite material was dried under vacuum (24 h, 90 °C) for ensuring the moisture removal. The results are presented in Figure 60, displaying the conductivity vs. frequency overlapping before and after FDM. This indicates that the material can be reprocessed *via* FDM without losing the electrochemical properties. Additionally, the end-group-modified polymers are self-healable, which can be demonstrated *via* a simple experiment shown in Figure 61. The rectangular specimen of **PEG-7** was cut into two pieces and self-healing was conducted at 30 °C for 12 hours (under vacuum). The cut pieces repair their structural integrity due to hydrogen boding and the recovered specimen can resist the stretch test. The tested composite material incorporates additional NPs, which is not hindering the self-healing capabilities.
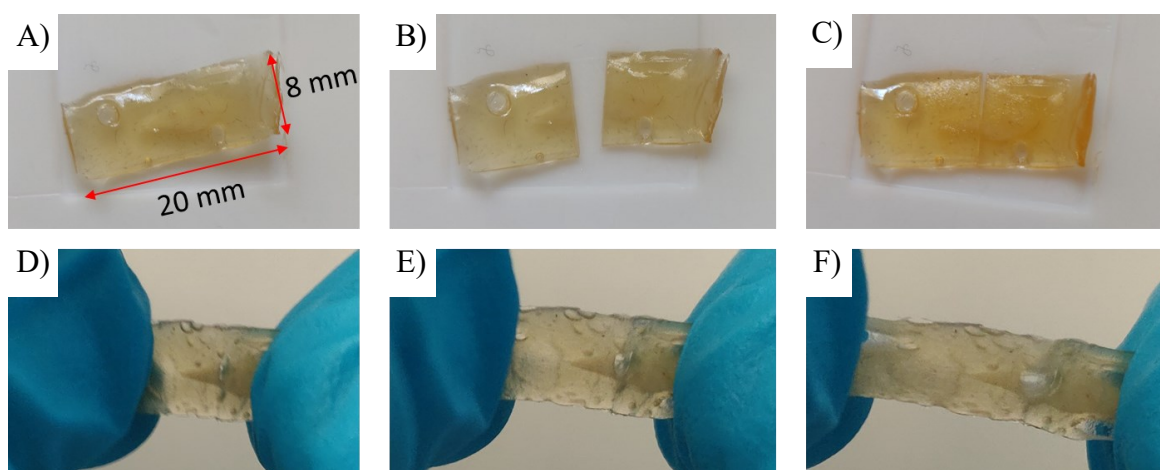
Figure 61. Self-healing test of **PEG-7** A) Rectangular shape specimen, B) Cut specimen into two pieces, C) Reconnected pieces before self-healing, D) E) F) Stretch test after self-healing at 30 °C in the vacuum oven for 12 hours.

6 Poly(ionic liquid) gel electrolytes

A gel polymer electrolyte, comprised of a polymer matrix and a liquid phase as plasticizer, can be considered as promising compromise, offering the advantages of both solid and liquid electrolytes. Beneficial properties of ionic liquids can be incorporated into the gel structure by employing PIL as a polymer matrix and IL as a liquid phase. The presence of polymer matrix holds a three-dimensional structure and prevents the liquid from flowing freely. Here presented material concept was designed to combine supramolecular interaction with the advantageous characteristics of PILs and improve the final materials properties by additional IL and lithium salt (Figure 62A). Additionally, structural stability was enhanced by the covalent crosslinking. Introduction of fluorinated compounds, known for their excellent chemical, electrochemical and thermal stability, should drastically improve the performance of gel polymer

Figure 62. A) Concept of IL-based gel electrolytes, B) Advantages of fluorinated compounds used as electrolyte.
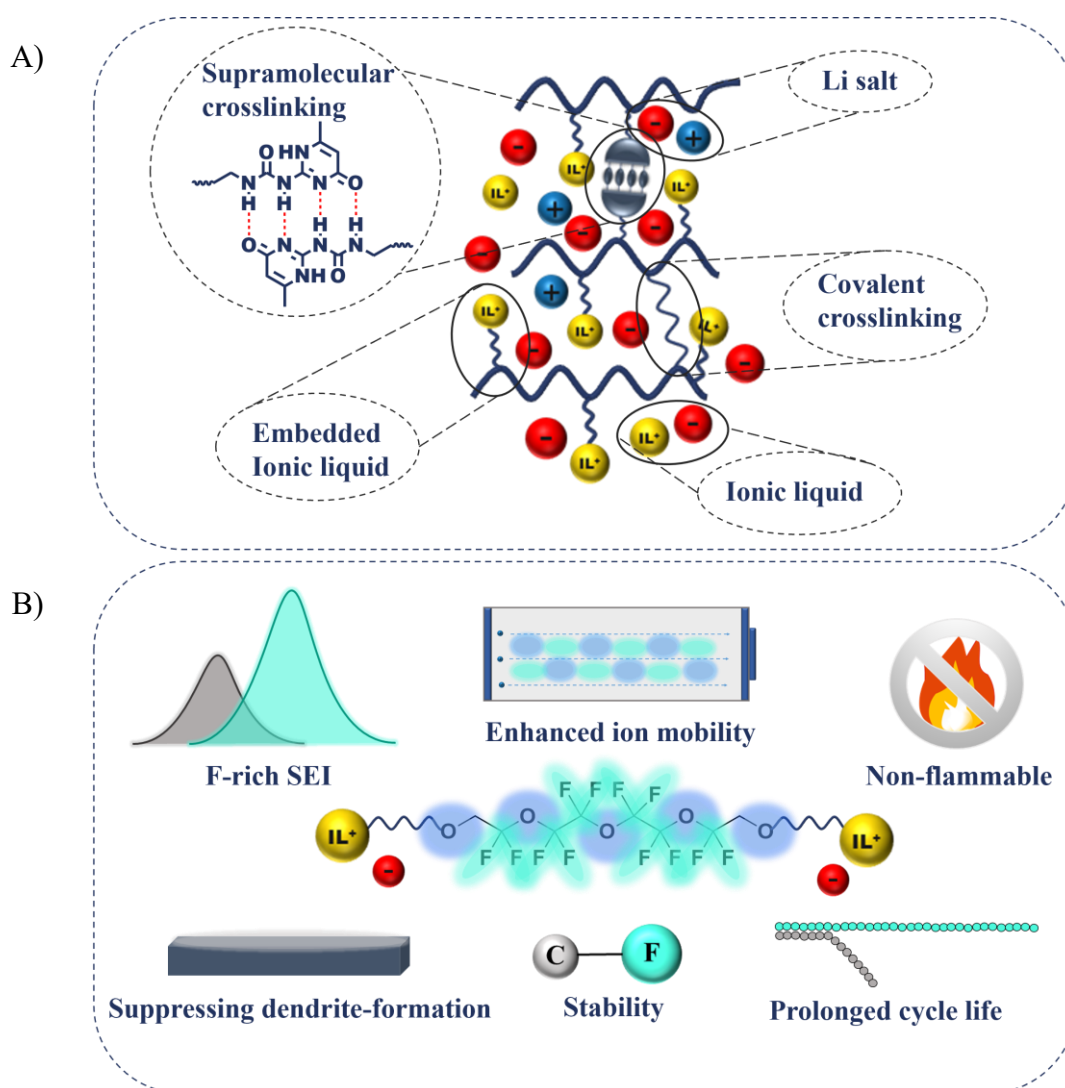
electrolytes.[111,359-361] Fluorinated ethers have been recently presented as a favorable alternative for classical organic liquid electrolytes, exhibiting good ion conductivity and excellent electrochemical stability.[122,362] Thus, in the scope of this work, advantageous properties of ILs are combined with fluorinated ether linker, resulting in a new type of dicationic ILs. Novel dicationic ILs together with expected advantages of fluorination are schematically presented in Figure 62B. One of the important parameters significantly influenced by fluorination is the formation of fluorine-rich SEI, a critical component of the functional battery and a potential determining factor of a cycle life. Additionally, fluorinated compounds are not flammable and can further enhance the thermal stability of ionic liquids. Pyrrolidinium dicationic ILs with different linkers (fluorinated and non-fluorinated) and two different counterions (TFSI and FSI) at varying salt concentrations are comprehensively investigated for their potential use in Li-ion batteries, both as liquid electrolytes as well as liquid phase in gel polymer electrolytes.
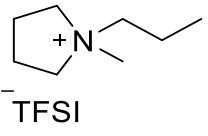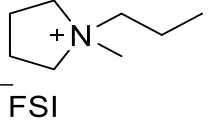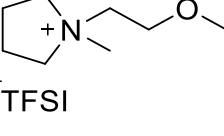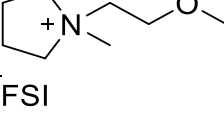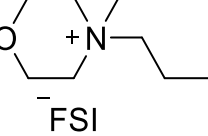
The performance of gel electrolytes can be tuned by changing the ratios and types of incorporated components. Various structures of pyrrolidinium-based ILs, crosslinkers, anions and additives were investigated for yielding the self-standing highly conductive film. The preparation route was based on *in situ* synthesis *via* thermal or photopolymerization. The obtained optimized materials displayed promising properties such as thermal stability, electrochemical stability, high ionic conductivity and relatively easy manufacturing process.

6.1 Ionic liquids for application in gel electrolytes

6.1.1 Ionic liquids for application in electrolytes

As previously mentioned the focus was set on the pyrrolidinium based ILs, due to their high thermal stability and wide electrochemical window (stable up to 5 V).[363,364] In order to estimate their applicability as liquid phase in gel polymer electrolytes selected ILs have been investigated. The obtained conductivity as well as corresponding viscosity values are presented in Table 13. While the presence of the ether group in the alkyl chain does not appear to significantly affect the conductivity and viscosity of the investigated ILs, the switch from TFSI to FSI as an anion results in a notable reduction in viscosity and, consequently, an increase in conductivity. Nevertheless, all four investigated pyrrolidinium ILs are deemed suitable for use as liquid phase in gel electrolytes. In contrast, the analyzed morpholinium-based IL exhibited high viscosity, rendering it unsuitable for further incorporation in gel electrolytes.

Table 13. Ionic liquids and corresponding conductivity and viscosity at 15 and 30 °C.

Ionic liquid	Structure	σ 15 °C mS/cm²	σ 30 °C mS/cm²	η 15 °C mPa × S	η 30 °C mPa × S
1-Methyl-1-propylpyrrolidinium bis(trifluoromethyl sulfonyl)imide	TFSI	2.9	5.6	98.3	50.6
1-Methyl-1-propylpyrrolidinium bis(fluorosulfonyl) imide	FSI	8.7	16.5	59.4	35.9
1-(2-Methoxyethyl)-1-methylpropyl pyrrolidinium bis(trifluoromethyl sulfonyl)imide	TFSI	2.6	5.2	88.1	45.6
1-(2-Methoxyethyl)-1-methylpropyl pyrrolidinium bis(fluorosulfonyl) imide	FSI	5.7	11.0	58.8	34.9
N-Methyl-N-propyl morpholinium bis(fluorosulfonyl) imide	FSI	1.0	2.4	345	145

6.1.2 Fluorinated ionic liquids

Dicationic ionic liquids featuring fluorinated linker and different counterions (Figure 63) were analyzed. Additionally, corresponding non-fluorinated DILs were characterized as a reference. **FIL-TFSI** was analyzed by BDS spectroscopy with different content of LiTFSI varying from 0 M to 1.25 M (where M = mol salt per kg of IL). Figure 64A displays the conductivity and viscosity behavior of **FIL-TFSI** samples with different salt concentration in dependence on temperature. Obtained σ values vary in the range of 10^{-3} S/cm (at 70 °C) to 10^{-9} S/cm (at -20 °C), but the difference is relatively small at higher temperatures. The concentration of LiTFSI plays a crucial role for the performance of **FIL-TFSI**, wherein an increase in salt
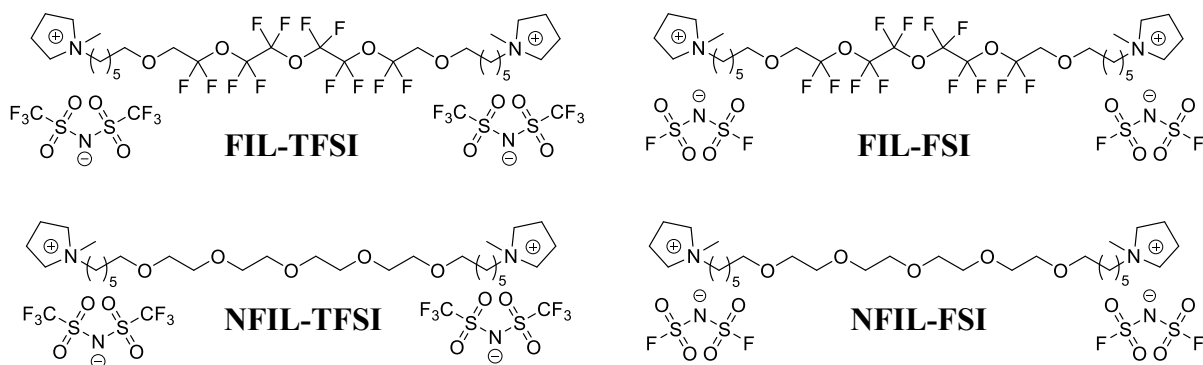
Figure 63. Chemical structures of fluorinated and non-fluorinated dicationic ionic liquids with FSI/TFSI counterion.

content reduces conductivity, and this effect is more pronounced at lower temperature. To provide clearer visualization, a plot of concentration vs. conductivity was generated (Figure 64B), demonstrating a constant linear decrease of σ with an increase in LiTFSI concentration. The reduction can be associated with viscosity changes and formation of ion clusters, restricting the free movement of charged particles.[365-367] The viscosity measurements align with the expected behavior, displaying a notable increase as salt concentration rose (Figure 64A) and inverse relationship with conductivity. Changes in physical properties of IL, specifically viscosity, impacts mobility of charge carriers, which is the key factor governing the ionic conductivity. The relationship is evident across the full measured temperature range. The physical and chemical properties of ILs can be alternated by using different counterions. **FIL-FSI** was characterized analogous to **FIL-TFSI.** Samples with various concentrations of LiFSI were prepared and their respective conductivities were measured using BDS (Figure 64C). The conductivity reached 10^{-3} S/cm at 70 °C and then decreased to 10^{-6} S/cm at -20 °C. The impact of additional salt is less significant compared to **FIL-TFSI**. The increase of concentration of LiFSI only slightly reduces the conductivity, which is observable at temperatures below 10 °C (Figure 64D). The similarities between different concentrations are also reflected in viscosity measurements (Figure 64C). Using FSI as counterion is noticeably reducing the viscosity of the IL in the full temperature range, while the effect of the added salt is almost negligible. The highest viscosity value of 5×10^{-4} mPa × s was reached for **FIL-FSI** while **FIL-TFSI** (1.25 M) reached 5×10^{-6} mPa × s. For better understanding an impact of fluorinated backbone on the overall performance of ILs, analogous structured DILs with aliphatic linker between cationic groups were used as reference and salt containing compositions were investigated. The first noticeable difference was observed in conductivity (Figure 65A). The conductivity of pure **NFIL-TFSI** is significantly lower than **FIL-TFSI** and
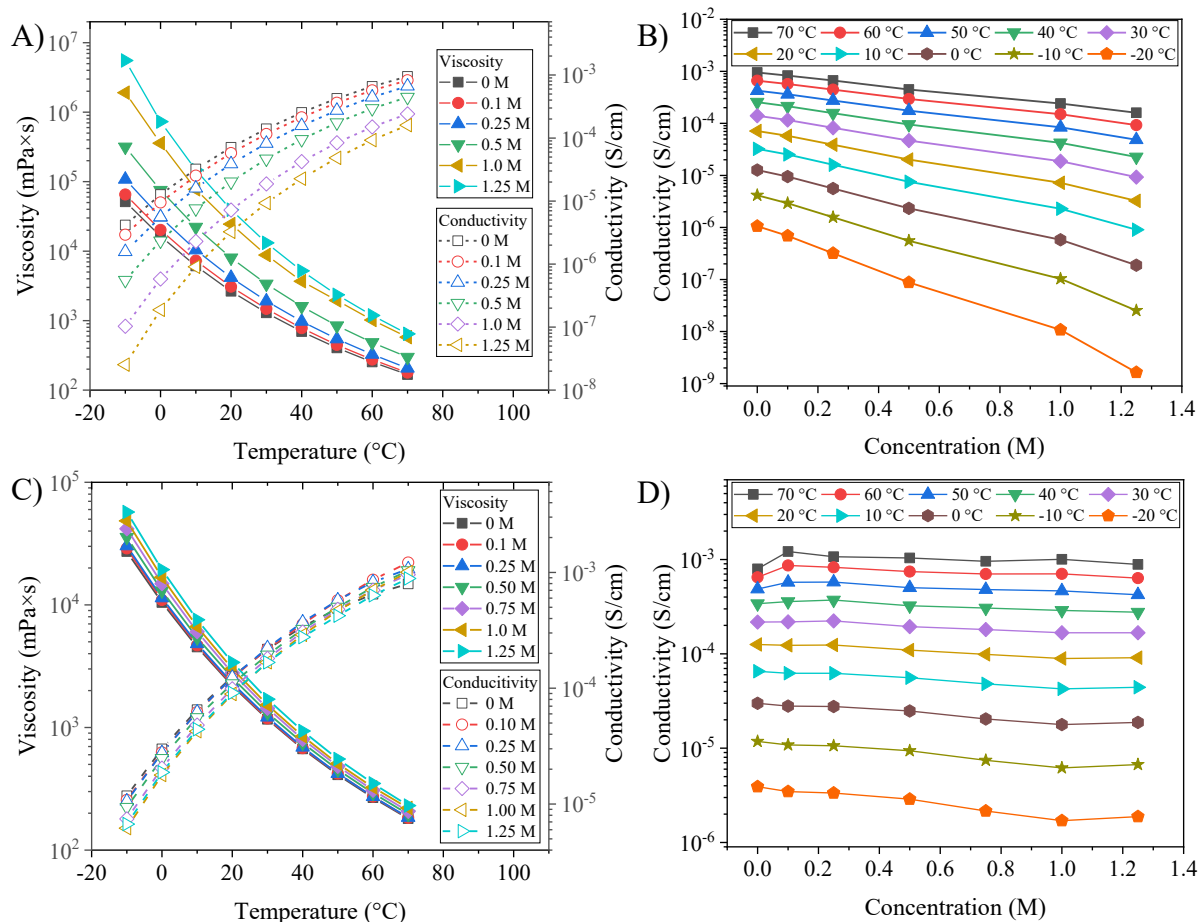
Figure 64. A) Concentration and viscosity as a function of temperature of **FIL-TFSI**/LiTFSI mixtures, B) Conductivity of **FIL-TFSI** as a function of LiTFSI concentration, C) Concentration and viscosity as a function of temperature of **FIL-FSI**/LiFSI mixtures, D) Conductivity of **FIL-FSI** as a function of LiFSI concentration.

the difference becomes more pronounced at lower temperatures. Additionally, the limit of LiTFSI solubility in **NFIL-TFSI** is lower, and the sample with the highest concentration of 1.0 M was prepared. The trend of σ with respect to concentration is similar to **FIL-TFSI**, the values are consistently decreasing with increasing concentrations (Figure 65B). The viscosity of **NFIL-TFSI** exhibits increase compared (Figure 65A) to analogous samples of **FIL-TFSI**, which is also the reason for reduced charge carrier mobility. As expected, the inverse relationship between viscosity and conductivity is also observed for **NFIL-TFSI** (Figure 65A). The results demonstrate that using fluorinated linker significantly impacts the physical properties of the IL, and this effect is also reflected in its electrochemical performance, as indicated by reduction of σ. **NFIL-FSI** based samples display conductivity comparable to **FIL-FSI** compositions, but the lower temperature values are dropping below 10^{-6} S/cm (Figure 65C). It is noticeable that the addition of LiFSI is weakly affecting the behavior
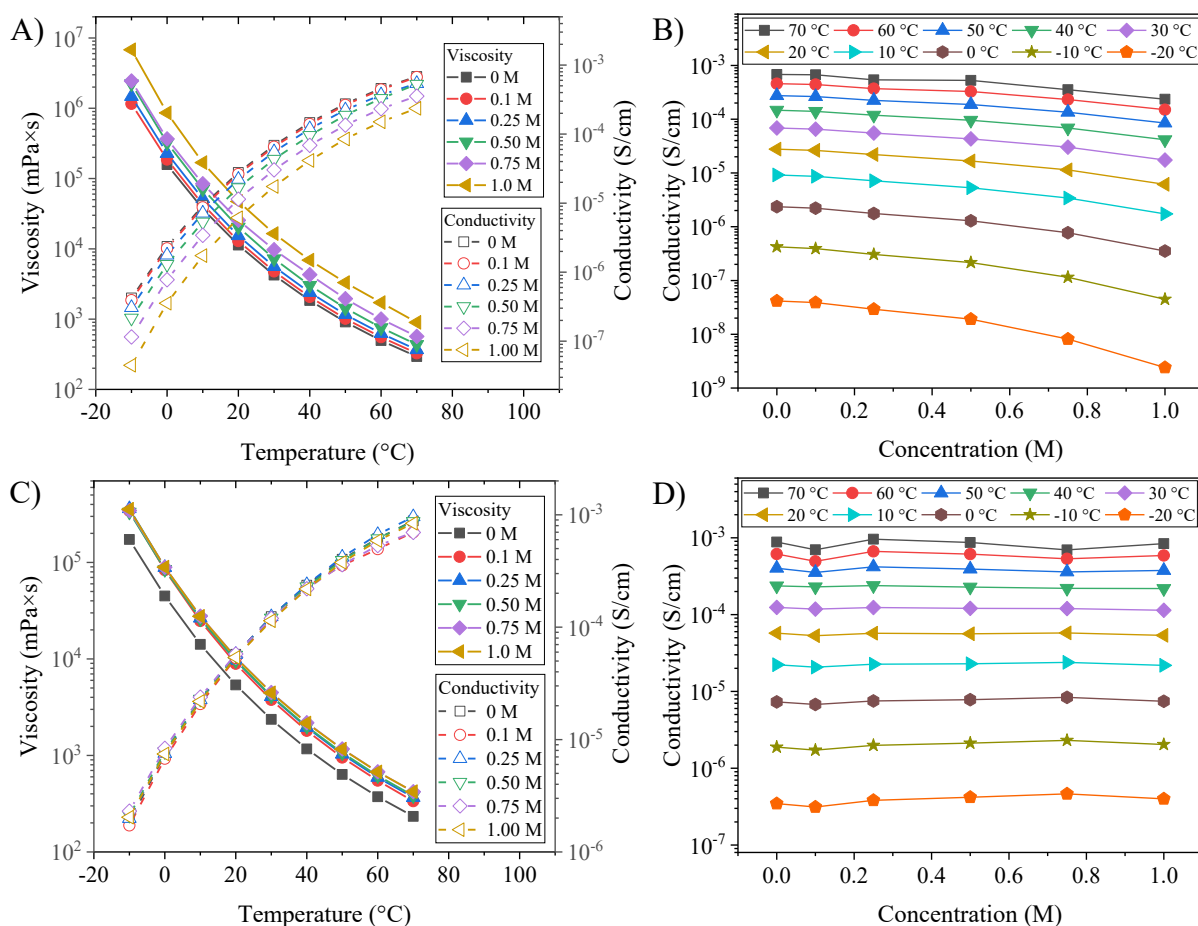
Figure 65. A) Concentration and viscosity as a function of temperature of **NFIL-TFSI**/LiTFSI mixtures, B) Conductivity of **NFIL-TFSI** as a function of LiTFSI concentration, C) Concentration and viscosity as a function of temperature of **NFIL-FSI**/LiFSI mixtures, D) Conductivity of **NFIL-FSI** as a function of LiFSI concentration.

(Figure 65D). The viscosity of **NFIL-FSI** exhibits initial increase with addition of salt and subsequently displays only marginal variations at different concentrations (Figure 65C). After analyzing all types of ILs it can be observed that the viscosity of ILs is increasing in the order of **FIL-FSI** < **FIL-TFSI** < **NFIL-FSI** < **NFIL-TFSI** (Figure 66A) and it follows the VFT behavior. $\eta = \eta_0 \exp[B/(T-T_0)]$ equation describes the temperature dependence of viscosity[368,369] where η_0 is viscosity at high temperature limit and constant, B is the constant related to energy and T_0 Vogel temperature. The fitting parameters are shown in Table 14. T_0 which is associated with the temperature below which molecular motions become significantly restricted, increase in the same order as viscosity. It indicates that **FIL-FSI** has the lowest temperature barrier, and it has crucial contribution for materials viscosity and, correspondingly, for conductivity. η_0 fitting parameter exhibits small deviation in trends.
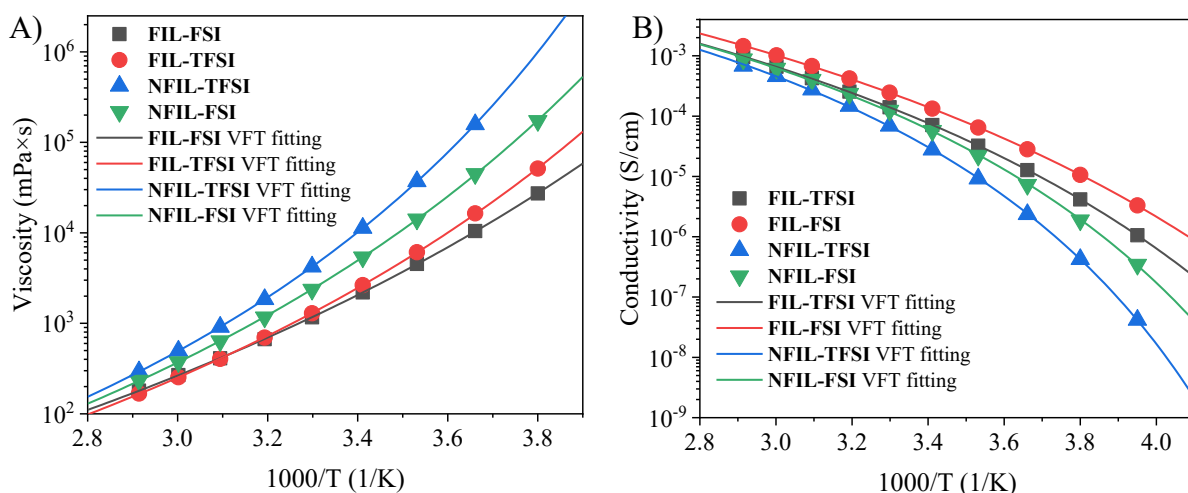
Figure 66. A) Viscosity as a function of inverse temperature of **FIL-TFSI**, **FIL-FSI**, **NFIL-TFSI** and **NFIL-FSI** and corresponding VFT fittings, B) conductivity as a function of inverse temperature of **FIL-TFSI**, **FIL-FSI**, **NFIL-TFSI** and **NFIL-FSI** and corresponding VFT fittings.

Table 14. VFT fitting parameters of **FIL-TFSI**, **FIL-FSI**, **NFIL-TFSI** and **NFIL-FSI** for viscosity.

Sample	$\eta_0/10^{-1}$ mPa × s	$B/10^3$ K	$T_0/$ K	R^2
FIL-TFSI	1.13 ± 0.14	1.32 ± 0.03	161.7 ± 1.6	0.9999
FIL-FSI	1.15 ± 0.12	1.45 ± 0.03	146.1 ± 1.6	0.9999
NFIL-TFSI	1.20 ± 0.01	1.22 ± 0.01	186.5 ± 0.4	0.9999
NFIL-FSI	0.89 ± 0.10	1.38 ± 0.03	168.2 ± 1.3	0.9999

Conductivity of pure DILs is presented in Figure 66B. The values are decreasing in the order of **FIL-FSI** > **FIL-TFSI** > **NFIL-FSI** > **NFIL-TFSI** and the behavior follows VFT model with the equation $\sigma = \sigma_0 \exp[-B/(T-T_0)]$ (described in section 4.2). Fitting parameters are given in Table 15. T_0 as expected displays the highest value for **NFIL-TFSI** and the lowest value for **FIL-FSI**. Moreover, the σ_0 is the highest for **FIL-FSI** followed with **FIL-TFSI**, further proving the advantages of using fluorinated linker in IL. Constant fitting parameter B consistently falls within a similar range. Furthermore, R^2 values indicate the high quality of fitting.

Table 15. VFT fitting parameters of **FIL-TFSI**, **FIL-FSI**, **NFIL-TFSI** and **NFIL-FSI** for conductivity.

Sample	$\sigma_0/10^{-1}$ S/cm	$B/10^3$ K	$T_0/$ K	R^2
FIL-TFSI	8.03 ± 0.83	1.20 ± 0.03	164.7 ± 1.26	0.9999
FIL-FSI	11.65 ± 1.17	1.26 ± 0.03	154.9 ± 1.4	0.9999
NFIL-TFSI	4.86 ± 0.69	0.98 ± 0.03	193.2 ± 1.1	0.9999
NFIL-FSI	4.81 ± 1.19	1.00 ± 0.05	182.5 ± 2.5	0.9998

The impact of fluorinated structures in ILs backbone on thermal properties was investigated *via* TGA measurements (Figure 67A). The highest stability was observed for **FIL-TFSI** reaching 380 °C while analogous non-fluorinated **NFIL-TFSI** displayed a small reduction of stability down to 330 °C. Using FSI as counterion is also impacting the thermal stability of IL. **FIL-FSI** exhibits resistance to degradation up to 270 °C while **NFIL-FSI** shows slightly lower stability at 240 °C. The selection of counterion is directed by the specific application needs. FSI demonstrates superior conductivity, but the compromise is the reduced thermal stability. Nevertheless, these ILs exhibit excellent thermal stability, making them potentially applicable in LiBs. Furthermore, the fluorination led to a significant improvement of the electrochemical stability of DILs (Figure 67B). **FIL-TFSI** displayed the highest stability windows up to 7 V,
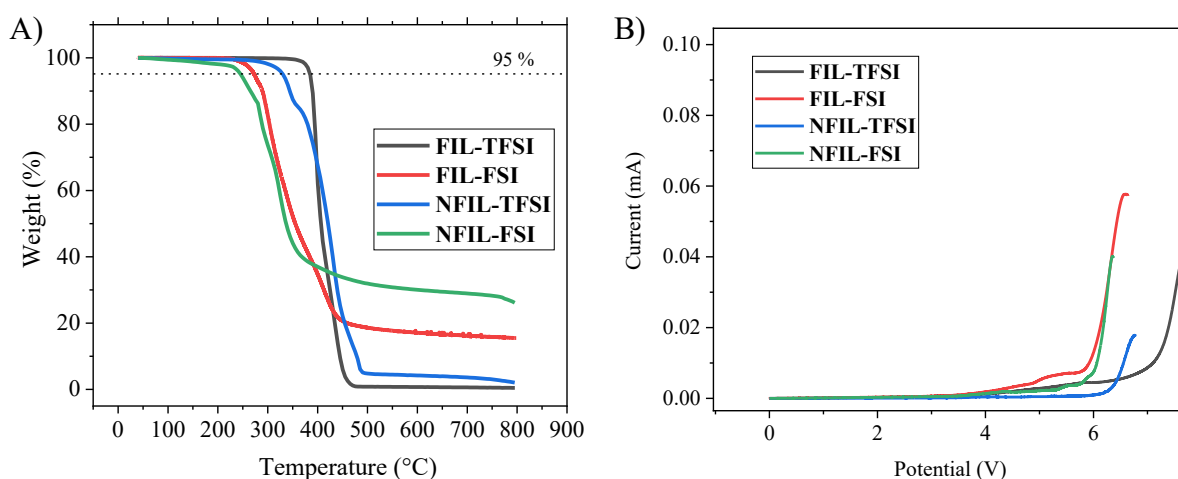
Figure 67. A) TGA measurement of **FIL-TFSI**, **FIL-FSI**, **NFIL-TFSI** and **NFIL-FSI** in the temperature range of 40 °C to 800 °C under nitrogen atmosphere, B) Electrochemical stability windows determined *via* linear sweep voltammetry for **FIL-TFSI**, **FIL-FSI**, **NFIL-TFSI** and **NFIL-FSI**.

which represents a significant increase compared to its nonfluorinated counterpart **NFIL-TFSI**. In contrast, FSI containing DILs exhibit considerably lower stability (up to 6 V). It should be mentioned that a small peak is observed at lower potential, presumably corresponding to traces of moisture. Nevertheless, both fluorinated dicationic ILs fulfill the requirements for the application in next-generation high-voltage LiBs.

Introducing various counterions or altering structural units not only impacts ionic conductivity, viscosity, and thermal properties, but also plays a crucial roles in organizational arrangements and microstructures within IL.[173,186,370,371] X-ray diffraction can be used for investigating the microstructures and the influence of fluorination on the segregation of ILs.[173,372] The WAXD measurements of pure FILs and samples with additional lithium salt are displayed in Figure 68. Scattering vectors (q) correlated to sizes of the heterogeneities by Bragg's law equation of q (q = $4\pi\sin\Theta/\lambda$). Figure 68 displays the peak at ~ q = 13 (d = 0.483 nm) for all FILs and additionally small peak is observed at ~ q = 8.5 (d = 0.739 nm) with different intensities. Deconvolution of existing peaks helps to understand the nanoscale heterogeneities in the samples. In Figure 69A and B signals of **FIL-TFSI** and **FIL-TFSI** mixed with LiTFSI (1 M concentration) can be observed. Higher q value possibly corresponds to charge ordering peak which is characteristic for ionic liquids.[198] This is closely linked to a scenario where ions are surrounded by counterions, ensuring local electroneutrality. Interestingly, the peak intensity remains unaffected by the addition of Li salt. The second peak, observed at the lowest q value, possibly reflects the distances between different ions, which is diminishing upon addition of Li
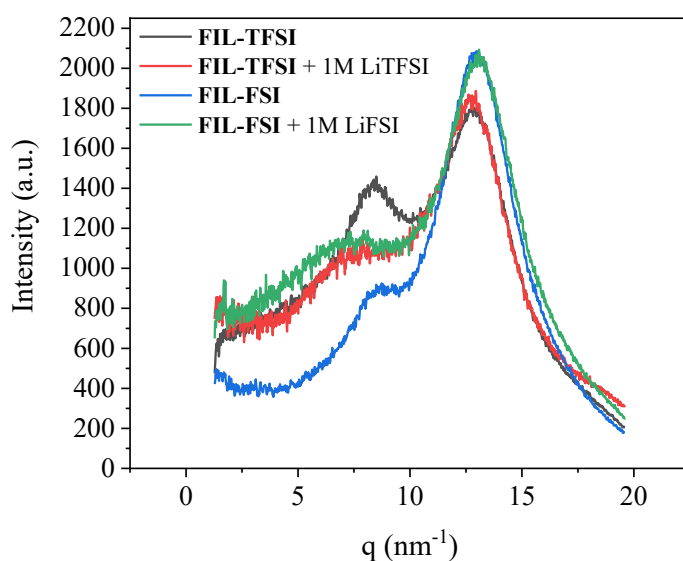
Figure 68. Wide angle X-ray diffraction (WAXD) measurements of **FIL-TFSI** and **FIL-FSI** in pure form and with added salt (1 M concentration).

salt to ILs. In Figure 69C and D signals of **FIL-FSI** and **FIL-FSI** mixed with LiFSI (1 M concentration) can be observed. Similar to **FIL-TFSI** peak at ~ q = 13, related to charge ordering, can be observed and remains unchanged after the salt addition. Additionally, the peak at ~ q = 8.5 is visible, which broadens with the increase in salt content.
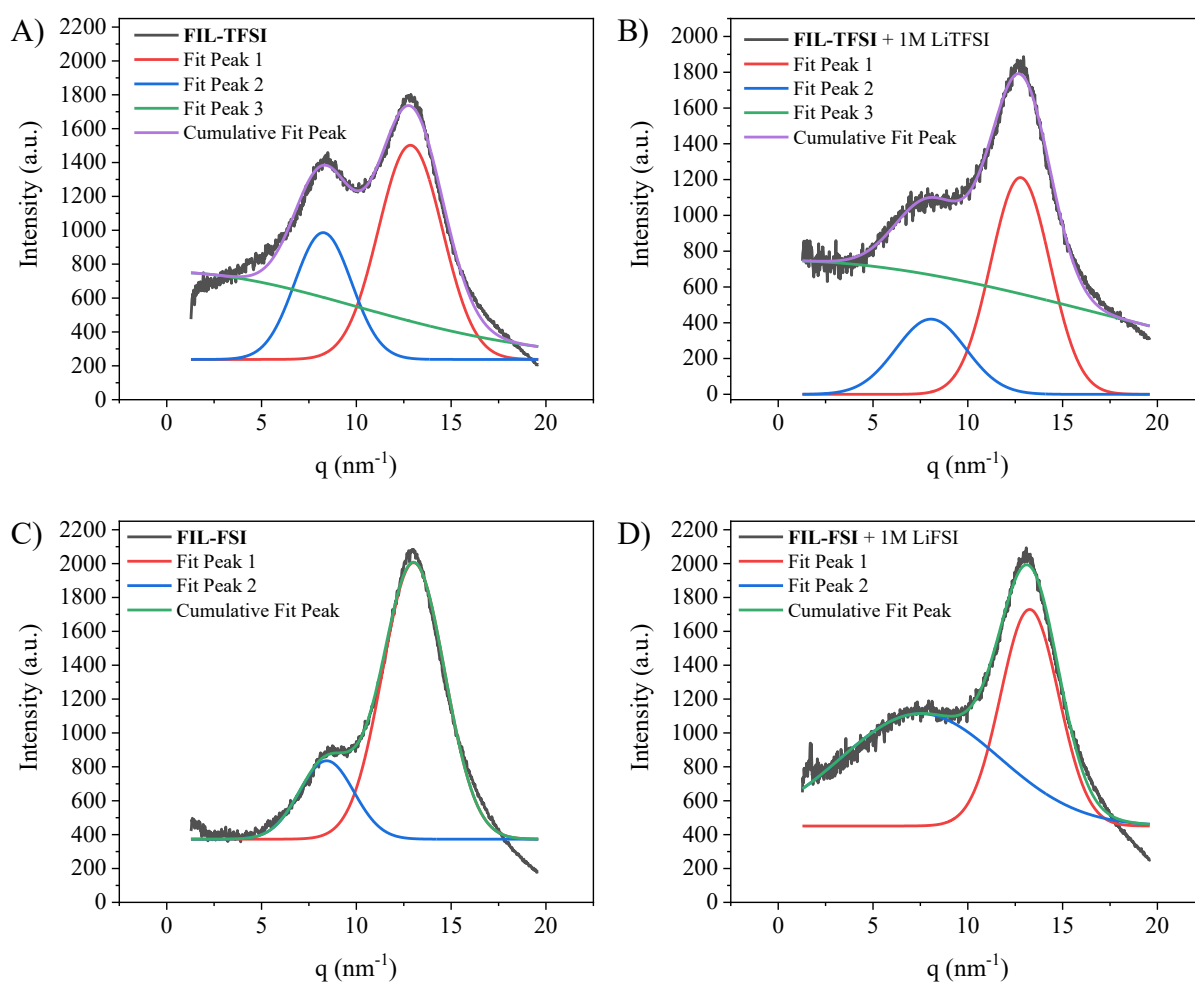
Figure 69. WAXD measurements and corresponding peaks deconvolution of A) **FIL-TFSI** , B) **FIL-TFSI** mixed with LiTFSI (1 M), C) **FIL-FSI** and D) **FIL-FSI** mixed with LiFSI (1 M).

6.1.3   *Fluorinated poly(ionic liquid) copolymers*

Furthermore, fluorinated structures were introduced into poly(ionic liquid)s for potentially incorporating the advantages of fluorination into the polymer matrix of gel electrolytes. N-[(2-acryloyloxy)propyl]-N-methylpyrrolidinium   bis(trifluoromethylsulfonyl)imide   (**4**)   and 2,3,4,5,6-pentafluorostyrene were used for synthesizing block and random copolymers *via* RAFT polymerization. The homopolymer of PIL (**PIL-H**) was prepared (Experimental part 8.6.2) and S,S-dibenzyl trithiocarbonate (DBTTC, **16**) was used as chain transfer agent.

Subsequently, **PIL-H** was used as macroinitiator for synthesizing block copolymer (**PIL-B**) (Experimental part 8.6.3) and a statistical copolymer (**PIL-S**) with comparable molar ratio of monomers was prepared (Experimental part 8.6.4). This methodology aimed to investigate the impact of distinct polymer architecture on materials performance and morphology.

Synthesized materials were analyzed by SEC (Figure 70A). The retention volume of **PIL-B** increased compared to its precursor **PIL-H**, indicating that fluorinated copolymer is noticeably reducing the hydrodynamic volume of polymer chain irrespective of increase in molecular weight. Moreover, **PIL-S** exhibits lower retention volume than **PIL-B** despite the comparable monomer ratio. The influence of architecture on the SEC results is evident, hence molecular weights were determined *via* NMR, while SEC was solely used for assessing PDI values. Figure 70B displays the ^{1}H spectrum of **PIL-B**. Signals from the RAFT agent can be used as a reference for determining molecular weight and the molar ratio of two used monomers. Similarly, values were extracted also for **PIL-H** and **PIL-S** (Table 16).
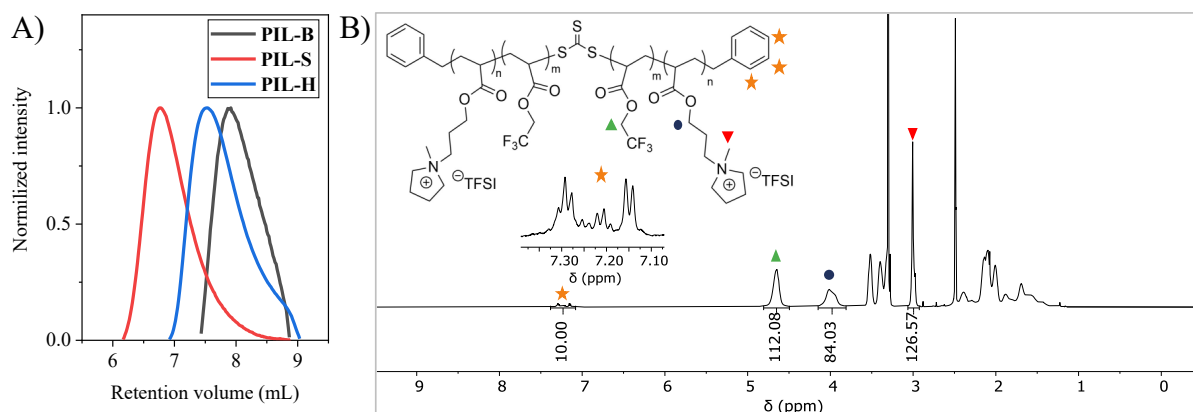
Figure 70. A) SEC analysis of **PIL-B**, **PIL-S** and **PIL-H** in DMF, B) ^{1}H NMR spectrum in CDCl₃ of **PIL-B**.

Table 16. Molecular weight and PDI of **PIL-H**, **PIL-B** and **PIL-S**.

Sample	IL monomer (n)	Fluorinated monomer (m)	PDI (SEC)	Mn (NMR)
PIL-H	38	-	1.4	18 kDa
PIL-B	42	56	1.3	29 kDa
PIL-S	38	53	1.4	26 kDa
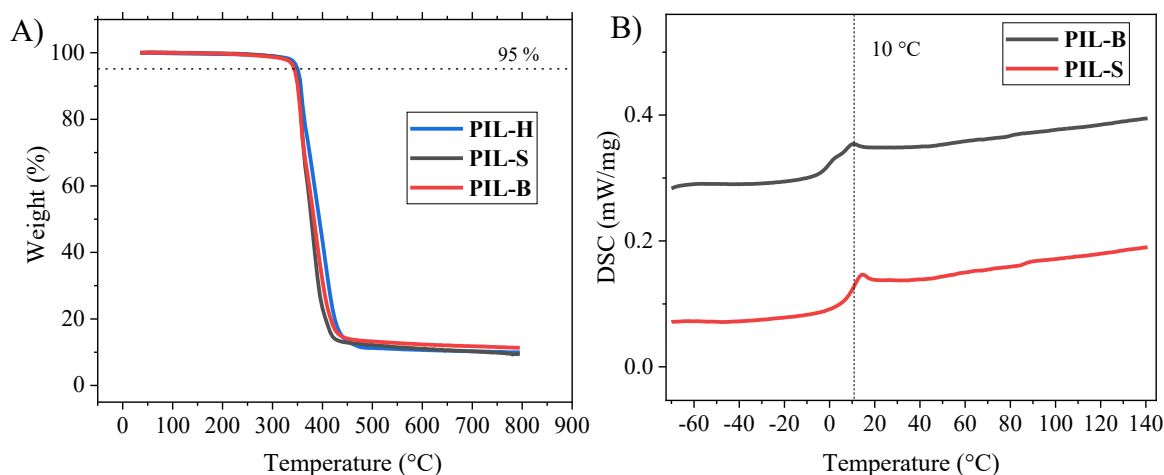
Figure 71. A) TGA measurement of **PIL-H**, **PIL-S and PIL-B** in the temperature range of 40 °C to 800 °C under nitrogen atmosphere, B) DSC measurements of **PIL-B** and **PIL-S** in the temperature range of -70 °C to 140 °C with the heating rate of 10 K min^{-1} under nitrogen atmosphere.

The introduction of fluorinated monomers is impacting the thermal stability of copolymers. Figure 71A, displaying the TGA measurements, reveals that the degradation is only evident above 350 °C, which indicates excellent stability of the material. Moreover, **PIL-B** and **PIL-H** were analyzed *via* DSC (Figure 71B), small variation in T_g were observed, which changed from 9 °C (**PIL-S**) to 6 °C (**PIL-B**). No other structural changes are evident between the statistical and the block copolymers.

In views of conductivity **PIL-S** outperforms **PIL-B** (Figure 72). The values are crossing 10^{-5} S/cm at 70 °C (for **PIL-S**) and gradually dropping with sample cooling. The conductivity
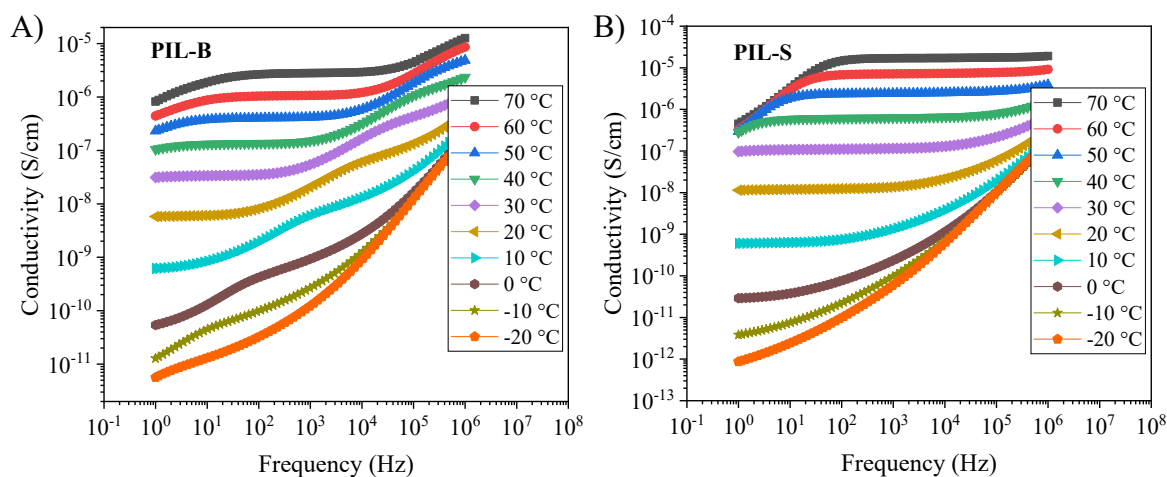
Figure 72. A) BDS measurement of **PIL-B** in the temperature range of -20°C to 70 °C with 10 °C increments, the frequency range between 1 to 10^6 Hz, B) BDS measurement of **PIL-S** in the temperature range of -20°C to 70 °C with 10 °C increments, the frequency range between 1 to 10^6 Hz.

100

at RT could not be explored due to considerable polarization of electrode. It should be noted that the samples do not contain any additional salt which could potentially enhance the performance of the polymers. Nevertheless, due to the only moderate influence of the fluorination on the properties of PILs, these types of polymers have not been further investigated as the polymer matrix for gel electrolytes.

6.2 Synthesis of monomers and gel preparation

Gel electrolytes are prepared from components mixture and consequent crosslinking reaction. The schematic representation of the gel strategy presented here is depicted in Figure 73. All components are dissolved in dry DCM and after solvent removal under vacuum the precursor mixture is transferred onto a petri dish and spread evenly on the surface. The crosslinking reaction is conducted in the glovebox *via* thermal or photo polymerization (exact synthesis procedure can be found in the Experimental part, section 8.7). The final gel electrolyte combines some characteristics properties highlighted in Figure 73: it contains supramolecular and covalent crosslinking, embedded ionic liquid in the polymer backbone and mobile ionic liquid/Li salt mixture.
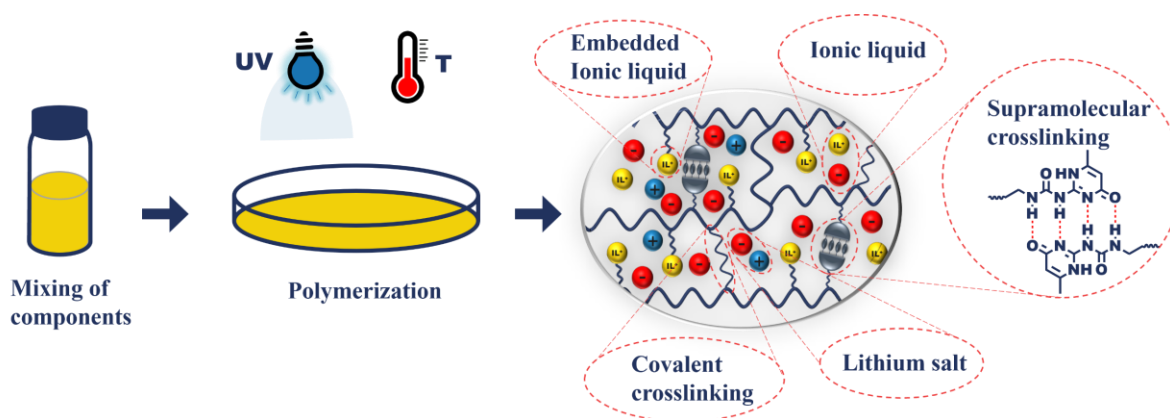
Figure 73. Schematic illustration of gel preparation process *via* thermal or photo initiation and highlighted characteristic properties.

Figure 74 displays the chemical structures of all used components in gel electrolytes. As previously discussed in Chapter 3 the choice of IL monomer was focusing on pyrrolidinium based monomers featuring different linkers between polymerizable group and IL group. The supramolecular bonds in the gel electrolyte are the UPy based monomer (**9**), forming strong quadruple hydrogen bonds. The hydrogen bonds as demonstrated in the previous chapter (5)
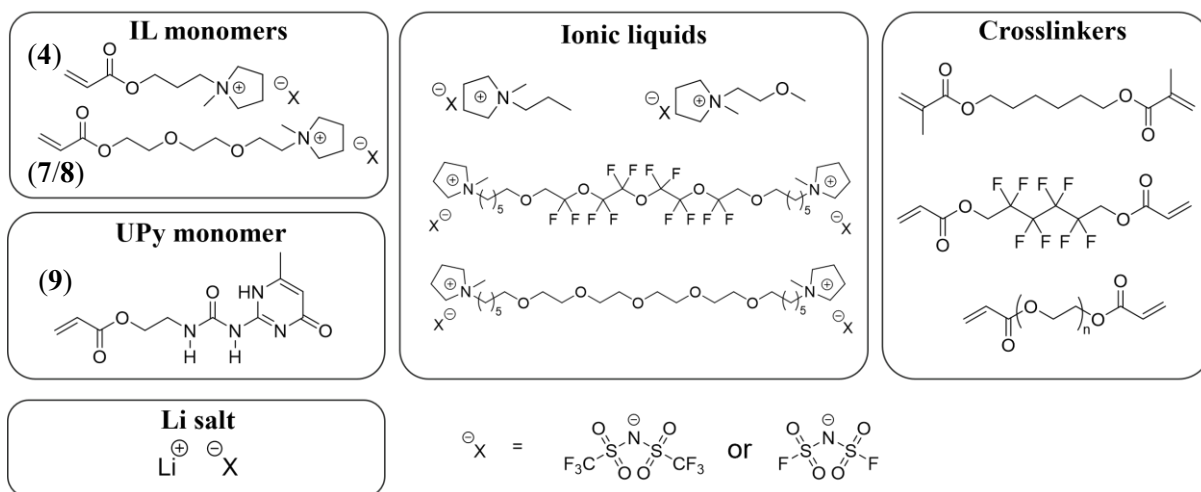
Figure 74. Chemical structures of gel electrolyte components.

can enhance the mechanical properties and potentially make the material self-healable. Additional covalent crosslinking was achieved by using commercially available compounds. Generally, the focus was directed towards a two-sided dimethacrylate crosslinker with different linkers between two polymerizable groups: 1,6-hexanediol dimethacrylate as alkyl linker, poly(ethylene glycol) diacrylate (Mn = 700 Da) having ethylene oxide repeating units between polymerizable groups and 2,2,3,3,4,4,5,5-octafluoro-1,6-hexanediol diacrylate with a fluorinated linker, which is expected to improve electrochemical and thermal stability. As mobile ionic liquid component pyrrolidinium-based mono and DIL with FSI and TFSI counterions were chosen, whereas corresponding Li-salts were used as source of Li-ions.
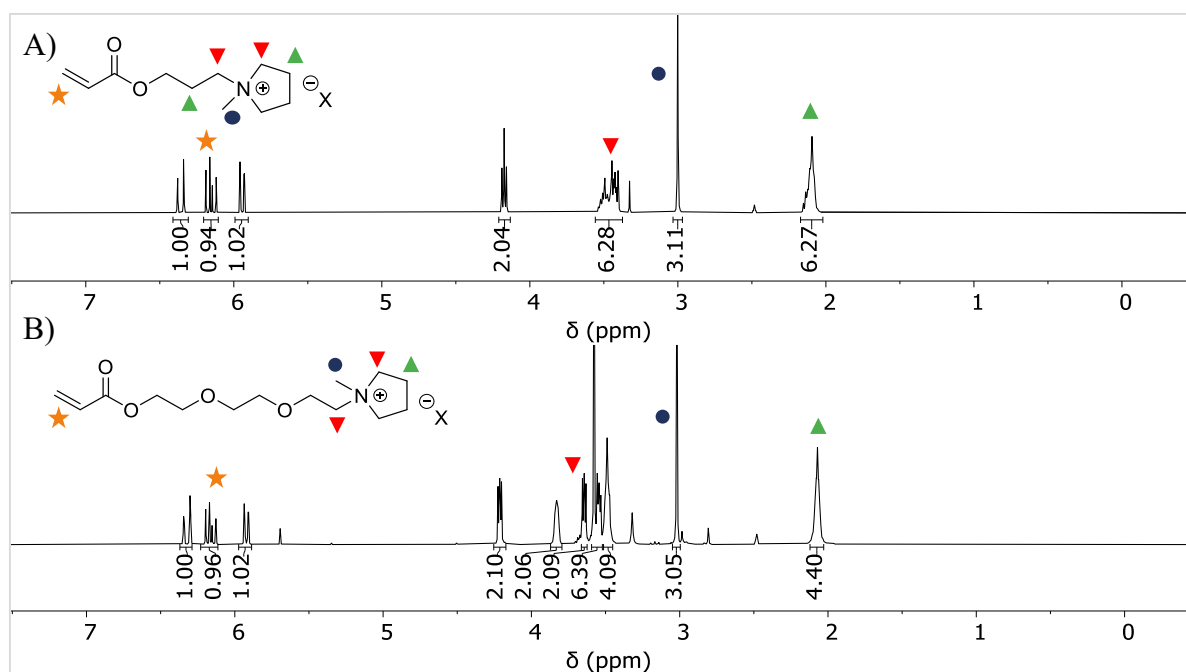
Figure 75. A) ^{1}H NMR spectrum of **4** in DMSO-d$_6$, B) ^{1}H NMR spectrum of **7/8** in DMSO-d$_6$.

102

IL monomers were synthesized in three-step reactions (for detailed information see Experimental section 8.3.2 and 8.3.3). The final monomers were analyzed by ^{1}H NMR and corresponding spectra are shown Figure 75. Characteristic peaks of polymerizable acrylate group are visible on both spectra. Additionally, the pyrrolidinium protons with expected integral values are observable. Moreover, ^{13}C and ^{19}F NMR was recorded and the resulting spectra (Figure S 8, Figure S 9, Figure S 15 and Figure S 16) confirm the successful synthesis.

6.3 Optimization of gel electrolyte preparation and characterization

The properties of gel electrolytes can be adjusted by altering the composition and corresponding ratios of components. For easier understanding of gel properties, the components are split into two groups (Figure 76A), one contributing to the polymer matrix consisting of IL monomer, UPy monomer, crosslinker and initiator. The second group labeled as liquid phase consisting of IL and Li salt. After the polymerization, the gel electrolyte forms self-standing film (Figure 76B) which can be cut into different shapes.
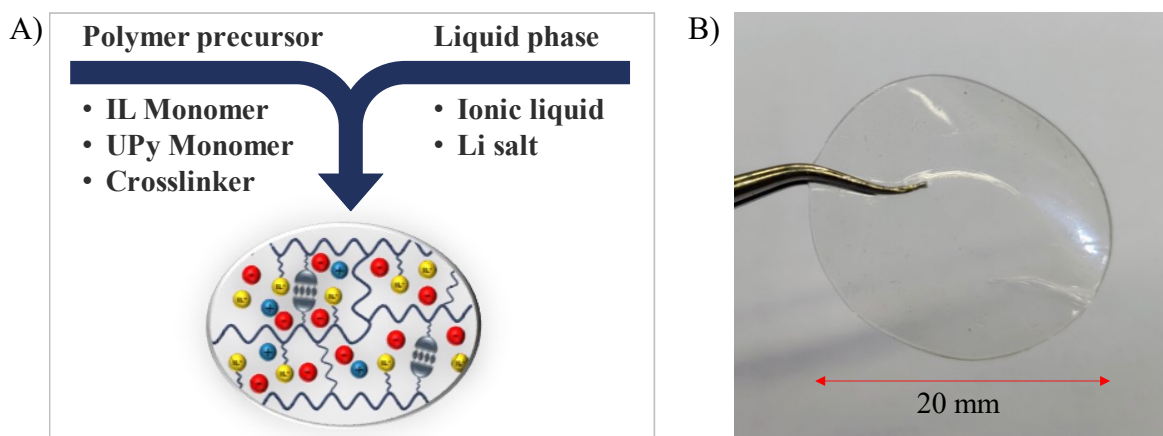
Figure 76. A) Schematic presentation of gel electrolyte components, polymer precursor and liquid phase, B) Self-standing gel electrolyte film.

For optimizing the conductivity different compositions with varying ratio of liquid phase and polymer matrix were tested. Additionally, the content of the UPy monomer in the polymer matrix was alternated. The compositions of all synthesized gels are presented in Table S 1 in the Experimental part. The selected compositions are displayed in Figure 77. The increase of UPy monomer content is negatively affecting the conductivity. This is nicely observable when comparing **G-1** (0 mol% UPy, 60 wt% polymer phase), **G-2** (5 mol% UPy, 60 wt% polymer phase) and **G-5** (15 mol% UPy, 60 wt% polymer phase) samples, with the same content of
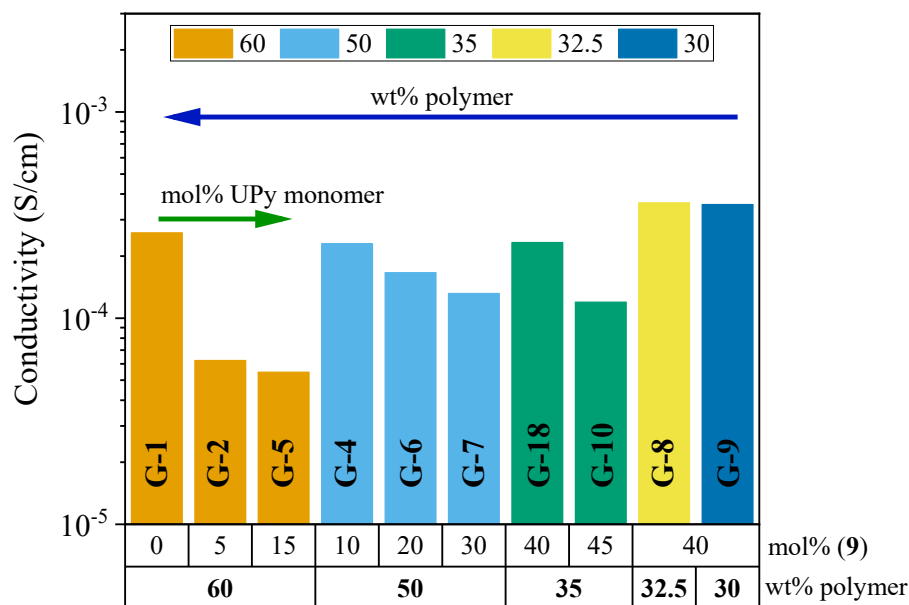
Figure 77. Conductivity dependence on polymer content (in the gel electrolyte) and UPy monomer (**9**) content (in polymer matrix).

polymer and liquid phase but differing in concentration of UPy in the polymer matrix. Although the increased content of the UPy monomer results in decreased conductivity, the tradeoff is the mechanical properties, which for **G-1** is extremely poor and the corresponding film can easily break while handling it. Additionally, there is a limitation of incorporating the UPy in the gel electrolyte due to its poor solubility. The presence of the ionic liquid and the Li salt enhances the solubility of UPy monomer, likely since the ionic groups tend to disrupt hydrogen bonding and facilitate solubilization. Thus, for incorporating more UPy the amount of the liquid phase in the gel needs to be increased as shown in the case of **G-4** (10 mol% UPy, 50 wt% polymer phase), **G-6** (20 mol% UPy, 50 wt% polymer phase) and **G-7** (30 mol% UPy, 50 wt% polymer phase). Although the conductivity shows decrease with increasing UPy content, the values are exceeding the ones observed for **G-2** and **G-5**, whereupon the difference is arising from the increasing content of liquid phase in the sample. The UPy content can be further increased by reducing the polymer content in the gel samples. The samples **G-18** (40 mol% UPy, 35 wt% polymer phase) and **G-10** (45 mol% UPy, 35 wt% polymer phase) exhibit high content of hydrogen forming moieties while still maintaining the conductivity in the range of 10^{-4} S/cm due to increased concentration of liquid phase. The content of liquid phase can be increased further, but it compromises the material's enhanced mechanical properties as the polymer matrix content is dropping to excessively low levels. Moreover, when the polymer content is low, the influence of UPy content on conductivity becomes insignificant which is visible when

comparing **G-8** (40 mol% UPy, 32.5 wt% polymer phase) and **G-9** (40 mol% UPy, 30 wt% polymer phase).

For better visualization of trends, the 3D color map surface was constructed (Figure 78). The uncovered area relates to the compositions which are not easily accessible due to poor solubility of UPy monomer (high UPy content while polymer content in gel is also high) or due to the lack of mechanical properties (< 30 wt% content of polymer matrix). The highest conductivity can be reached when UPy concentration is considerable, strengthening the gels mechanical properties and giving the possibility to incorporate more liquid phase, enhancing the conductivity values. The properties of gel electrolytes can be further tuned by adjusting the components ratios and types. The tensile test was used for characterizing the influence of covalent and supramolecular crosslinking on mechanical properties. Figure 79A displays the tensile measurements of **G-3** (M-IL:M-UPy:C=90:00:10), **G-10** (M-IL:M-UPy:C=57:38:05) and **G-17** (M-IL:M-UPy:C=54:36:10). **G-3** displayed extremely low toughness and breaks at the elongation of approx. 10 %. After introducing the supramolecular crosslinking (while
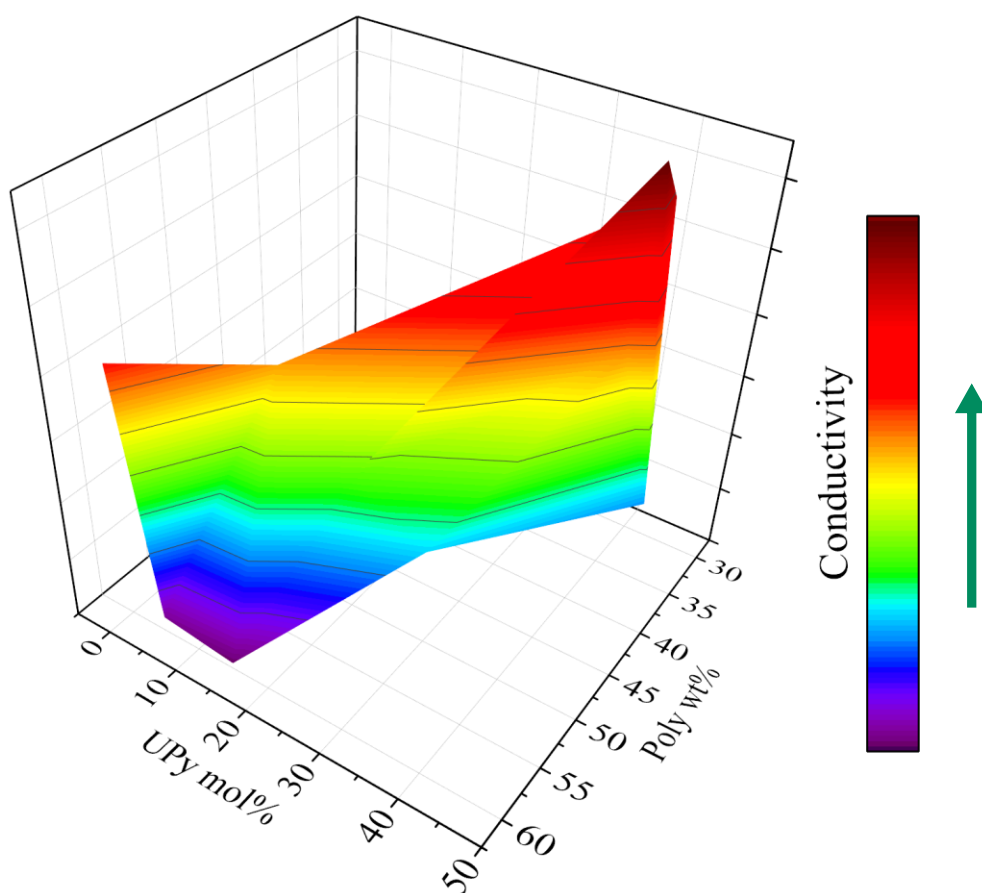
Figure 78. 3D surface demonstrating conductivity dependence on UPy monomer content (in polymer matrix) and polymer content (in gel electrolyte).

maintaining the same amount of covalent crosslinking) the material reached the strain above 100 % (**G-17** vs. **G-3**) and has visibly higher toughness. The effect of covalent crosslinking can be seen when comparing samples **G-10** and **G-17**. The decrease of covalent crosslinking makes the material more elastic leading to a higher deformation of up to 280 %.

Furthermore, the impact of crosslinker type on ionic conductivity was investigated (Figure 79B). Gel electrolytes **G-27** and **G-26** were prepared with the same type of monomers and corresponding ratios, but they differ in the type of the covalent crosslinker, which is 2,2,3,3,4,4,5,5-octafluoro-1,6-hexanediol diacrylate for **G-27** and 1,6-hexanediol dimethacrylate for **G-26**. No significant difference in measured ionic conductivity at RT could be observed (σ(**G-27**) = 5.60 × 10^{-4} S/cm, σ(**G-27**) = 6.3 × 10^{-4} S/cm). This observation was confirmed with samples **G-16** and **G-10**, which also only differ in the type of the crosslinker. **G-10** is crosslinked by 1,6-hexanediol dimethacrylate whereas for **G-16** poly(ethylene glycol) diacrylate (Mn = 700 Da) is used and the RT conductivity values are 1.19 × 10^{-4} S/cm and 1.06 × 10^{-4} S/cm, correspondingly. The lower impact of the crosslinker can be explained by its
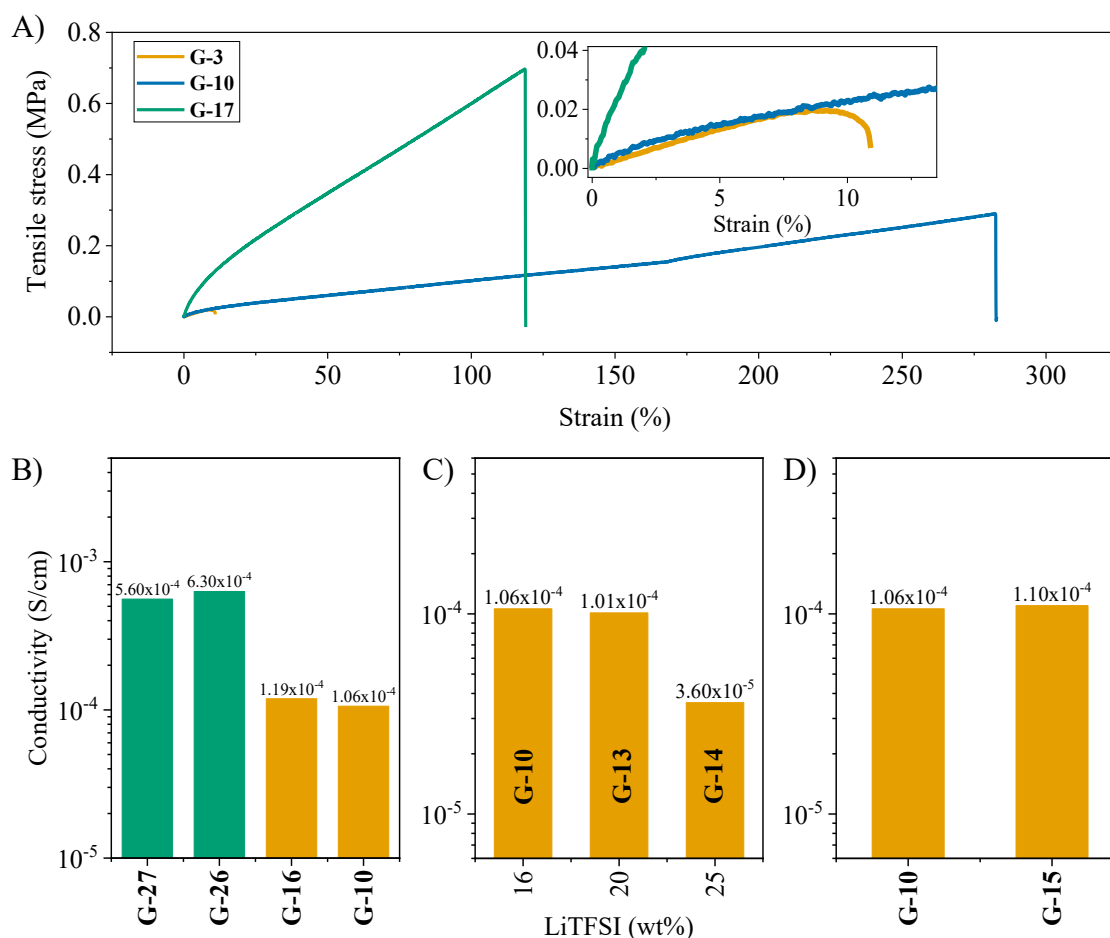
Figure 79. A) Tensile test of **G-3**, **G-10** and **G-17**, conductivity measurements of B) **G-27**, **G-25**, **G-16** and **G-10** at RT, C) **G-10**, **G-13** and **G-14** at RT and D) **G-10** and **G-15** at RT.

relatively low concentration, in the typical synthesized gels the covalent crosslinking was with the molar ratio of 5 to 95 to total monomer molar amount.

The Li salt concentration is also affecting the conductivity as already described in the literature[158,373] and previously observed in section 4.2 for vitrimeric samples. Gel electrolytes with three different salt concentrations were prepared: **G-10** (16 wt% LiTFSI), **G-13** (20 wt% LiTFSI) and **G-14** (25 wt% LiTFSI). The increasing concentration of LiTFSI (above 20 wt%) is reducing the conductivity (Figure 79C), and the corresponding RT value dropped from 1.06×10^{-4} S/cm (**G-10**) to 3.6×10^{-5} S/cm (**G-14**).

Additionally, the influence of different types of ionic liquid as liquid phase was investigated. For this purpose, gel sample **G-10** with typically used 1-methyl-1-propylpyrrolidinium bis(trifluoromehylsulfonyl)imide IL was compared with gel sample **G-15** containing 1-(2-methoxyethyl)-1-methylpropylpyrrolidinium bis(trifluoromethylsulfonyl)imide IL, while other parameters were kept constant (Figure 79D). Against expectations, the presence of oxygen in the structure of 1-(2-methoxyethyl)-1-methylpropylpyrrolidinium bis(trifluoromethylsulfonyl)imide did not significantly improve the conductivity.

Under the assumption that the presence of the ethylene oxide chains directly incorporated into the IL monomer as linkers/spacers between pyrrolidinium and polymerizable group would have the positive influence on the conductivity due to the ability of EO to coordinate and promote Li ion transport in polymer materials, gel electrolytes were synthesized using different types of ionic liquid monomers. Comparing N-[(2-acryloyloxy)propyl]-N-methylpyrrolidinium bis(trifluoromethylsulfonyl)imide (**4**)-based gel electrolyte (**G-11**) vs. N-(2-(2-(2-(acryloyloxy)ethoxy)ethoxy)ethyl)-N-methylpyrrolidinium bis(trifluoromethylsulfonyl)imide (**7**)-based gel (**G-24**) the conductivity is increased from 8.3×10^{-5} S/cm up to 1.32×10^{-4} S/cm (Figure 80A). Moreover, using the FSI counterion instead of TFSI in the monomer as well as in the additional ionic liquid is further improving the conductivity, reaching the values up to 6.28×10^{-4} S/cm (**G-24** vs. **G-26**). The increase in conductivity observed when using FSI as the counterion can be attributed to its higher ionic mobility, promoting the transport of Li ions within the gel, which is in accordance with the literature.[364,374] However, although recent reports highlight the ability of FSI anion to efficiently passivate the surface of anode materials in LIBs,[375-377] it should be noted that the tradeoff associated with use of FSI is the impact on thermal and electrochemical stability. As depicted in Figure 80B TGA measurements of gels based on different kinds of IL monomers display the stability of these materials. The

measurement reveals that the use of FSI counterion is reducing the degradation temperature to 250 °C (**G-26**) compared to 350 °C for TFSI based materials (**G-8** and **G-24**). Additionally, the use of ethylene oxide as a linker appears to have a neglectable influence on thermal stability and TGA curves are almost overlapping for **G-8** and **G-24.** In the broader context, all gel electrolytes based on ILs displayed resistance to temperatures above typical working temperatures of LiBs. Apart from thermal stability the crucial requirement for the materials to be applicable for LiBs is their electrochemical stability window. Linear sweep voltammetry was used for determining the electrochemical stability window of the prepared gel materials. As illustrated in Figure 80C studied gel materials exhibit excellent stability up to 5 V.

Creating gels can prove challenging when aiming to obtain materials with the desired properties. Not only does it require the optimization of compositions but also adaptation of the manufacturing methods. Materials were prepared on the glass surface *via* thermal (AIBN as
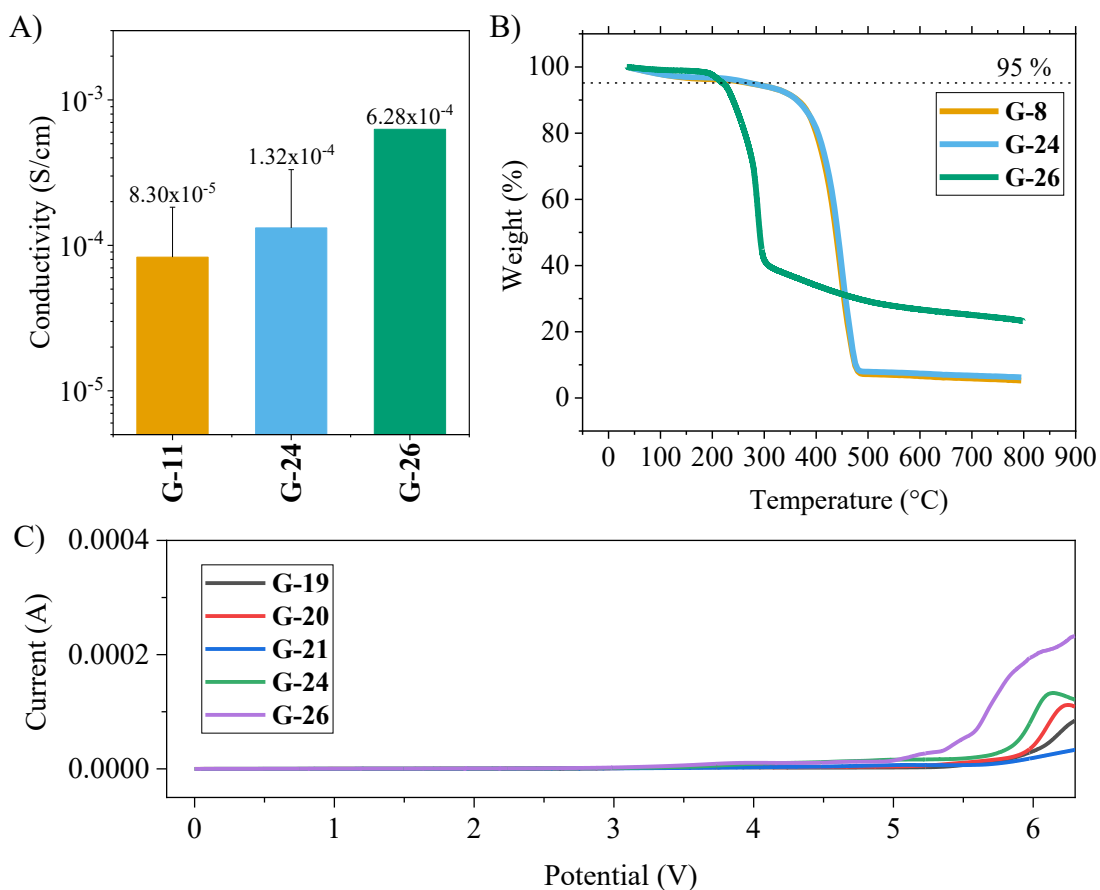
Figure 80. A) Conductivity measurements of **G-11**, **G-24** and **G-26** at 20 °C, B) TGA measurement of **G-8**, **G-24** and **G-26** in the temperature range of 35 °C to 800 °C under nitrogen atmosphere, C) Electrochemical stability windows determined *via* linear sweep voltammetry for **G-19**, **G-20**, **G-21**, **G-24** and **G-26**.

initiator) and photo (DMPA as initiator) polymerization techniques. Obtained gels were peeled off from the surface and needed shapes of specimens were cut for further investigations. Samples containing only TFSI counterion but different linker in the IL monomer were measured by BDS in wide range of temperature from 70°C to -20 °C. Typical frequency vs. conductivity displays gradual decrease of σ with reducing temperature (Figure 81A). N-[(2-acryloyloxy)propyl]-N-methylpyrrolidinium bis(trifluoromethylsulfonyl)imide (**4**)-based gels prepared *via* thermal (**G-11**) and photo (**G-12**) crosslinking exhibited closely aligned properties (Figure 81B). The conductivity curves almost overlap indicating that both methods can be successfully implemented. Moreover, photoinitiation offers distinct advantages by drastically reducing the polymerization time. In analogous manner N-(2-(2-(2-(acryloyloxy)ethoxy)ethoxy)ethyl)-N-methylpyrrolidinium bis(trifluoromethylsulfonyl)imide
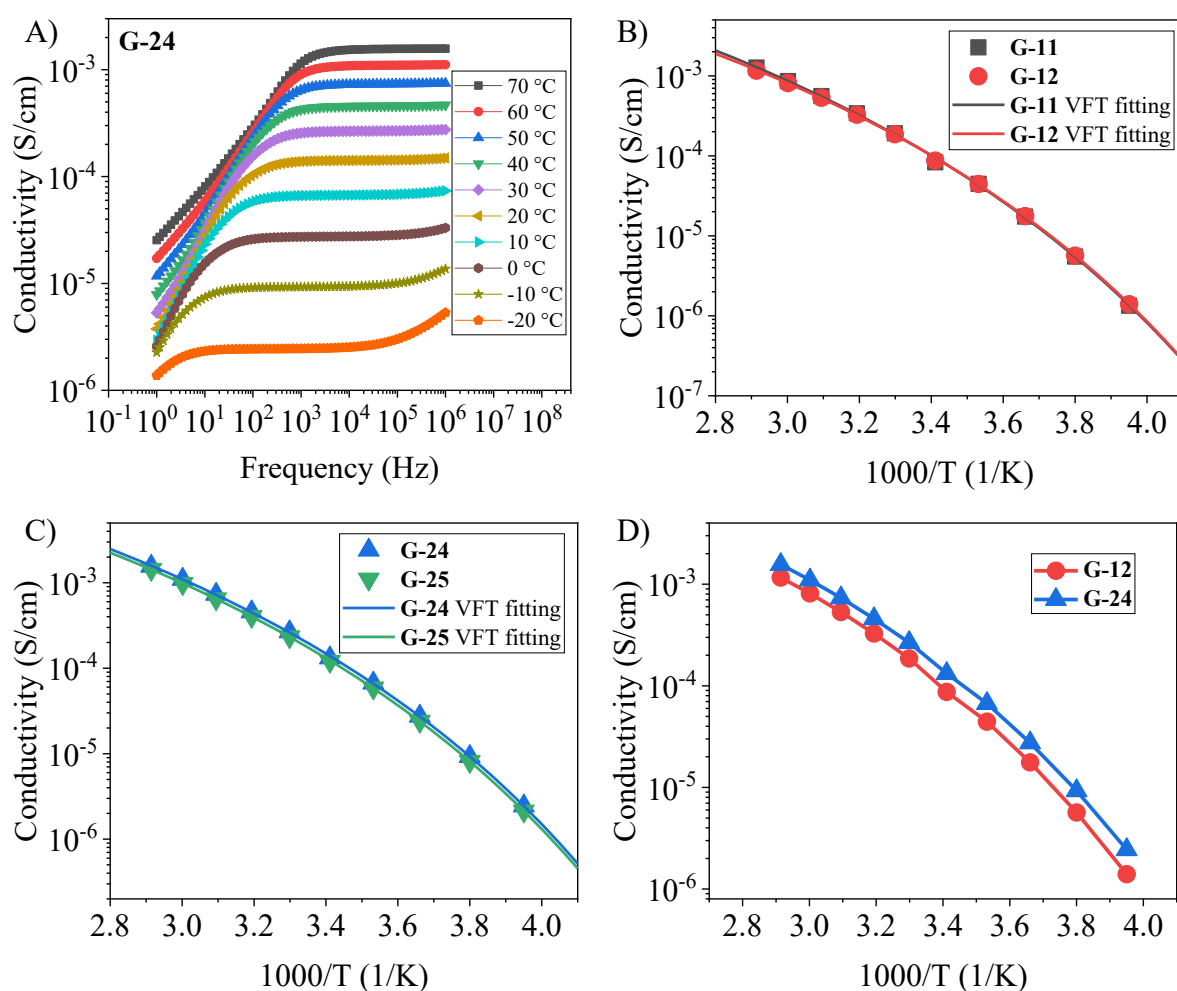
Figure 81. A) BDS measurement of **G-24** in the temperature range of -20 °C to 70 °C with 10 °C increments, the frequency range between 1 to 10^6 Hz, Conductivity as a function of temperature of B) **G-11**, **G-12,** C) **G-24**, **G-25**, D) **G-12** and **G-24** and corresponding VFT fittings.

(**7**)-based materials **G-24** (thermal polymerization) and **G-25** (photopolymerization) were characterized. As expected, no significant difference in performance could be seen between the two employed preparation methods (Figure 81C). Additionally, the comparison of the two used monomers with different linker in the wide range of temperature is depicted in Figure 81D. Using EO linker has a positive impact irrespective of temperature. All measured conductivities follow VFT equation and corresponding fitting parameters are shown in the Table 17. The σ_0 pre-exponential factor also standing for the materials conductivity at infinite temperature is relatively high for **G-11** compared to other samples, presumably due to the fitting quality, since it also displays highest error. However, **G-24** and **G-25** exhibit nearly the same values of σ_0. T_0 also known as Vogel temperature, indicating the low temperature limit for the conductivity is in the similar range (166-173 K) for both types of monomer-based gels.

Table 17. VFT fitting parameters of **G-11**, **G-12**, **G-21**, **G-22**, **G-23**, **G-24** and **G-25** for conductivity.

Sample	$\sigma_0/\ 10^{-1}$ S/cm	$B/\ 10^3$ K	$T_0/$ K	R^2
G-11	9.41 ± 3.72	1.17 ± 0.10	166.4 ± 4.8	0.9994
G-12	6.02 ± 1.41	1.08 ± 0.06	169.8 ± 2.9	0.9998
G-21	12.45 ± 0.46	1.47 ± 0.01	167.9 ± 0.3	0.9999
G-22	7.07 ± 0.82	1.17 ± 0.02	191.3 ± 0.8	0.9999
G-23	6.09 ± 0.30	1.05 ± 0.04	173.8 ± 0.6	0.9999
G-24	6.51 ± 1.02	1.05 ± 0.04	169.5 ± 2.0	0.9999
G-25	6.43 ± 0.39	1.07 ± 0.01	168.6 ± 0.8	0.9999

Gel electrolytes were prepared also with previously mentioned fluorinated ILs **FIL-TFSI** and **NFIL-TFSI** (Chapter 6.1.2) The different structure of ILs is dramatically reducing the solubility of UPy monomer in gel precursor. Due to this reason the typical composition used for other gel samples was not accessible, new ratios were adapted with **FIL-TFSI** (**G-21**) / **NFIL-TFSI** ILs (**G-22**) and corresponding sample with 1-methyl-1-propylpyrrolidinium bis(trifluoromehylsulfonyl)imide as reference was prepared (**G-23**) (exact composition can be found in Table S 1). Introducing fluorinated ILs enhances properties of materials, but at the expense of reduced conductivity, which is displayed in Figure 82A. Comparing **G-21** with
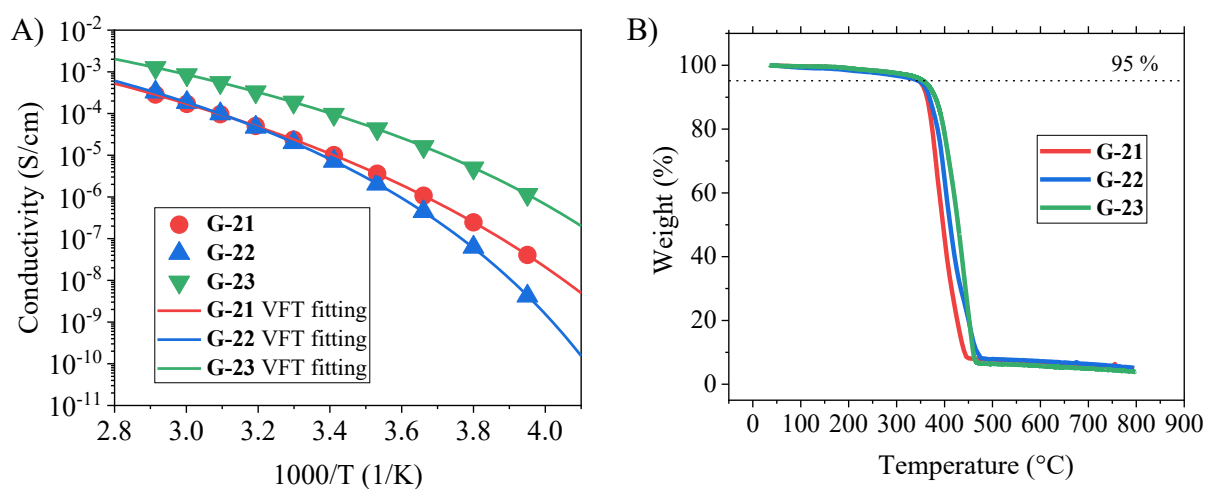
Figure 82. A) Conductivity as a function of temperature of **G-21**, **G-22**, **G-23** and corresponding VFT fitting, B) TGA measurement of **G-21**, **G-22** and **G-23** in the temperature range of 35 °C to 800 °C under nitrogen atmosphere.

G-23 the conductivity is one order of magnitude lowered in the full range of measured temperature. **G-22** (non-fluorinated) follows the behavior of **G-21** at higher temperatures, but values are dropping while cooling. Gel samples follow the typical VFT behavior (fitting parameters are presented in Table 17). σ_0 also indicates the drawbacks of **FIL-TFSI** and **NFIL-TFSI**-based gels, being almost 2 times lower for dicationic ILs compared to the reference sample. This behavior can be partially related to the glass transition temperature or Vogel temperature. **NFIL-TFSI**-based gel displayed lowest T_0 at 191 K, while **FIL-TFSI** exhibits 174 K. In the context of thermal stability samples exhibit excellent properties, stating degradation above 350 °C (Figure 82B).

The electrochemical properties and overall performance of gels can be enhanced in various ways. Mixing TFSI/FSI anions was reported to be an interesting approach for improving the performance of electrolyte.[181] An alternative strategy involves incorporating additives or nanofillers including MOFs and COFs.[378,379] Trying to combine both strategies, nickel-based MOF (Figure 83A) was successfully incorporated in gel composition containing N-[(2-acryloyloxy)propyl]-N-methylpyrrolidinium-TFSI (**4**) monomer, 1-methyl-1-propylpyrrolidinium bis(fluorosulfonyl)imide (FSI-based IL) and LiTFSI. Resulted materials exhibit a noticeable visual difference (Figure 83B and C), the sample with MOF become black opaque. **G-19** and **G-20** demonstrated remarkable electrochemical stability (Figure 80C) reaching values up to 5.5 V. Furthermore, the materials resist thermal degradation up to 350 °C (Figure 83D). However, in the context of conductivity, the incorporation of the MOF did not reveal any noticeable enhancement (Figure 83E).
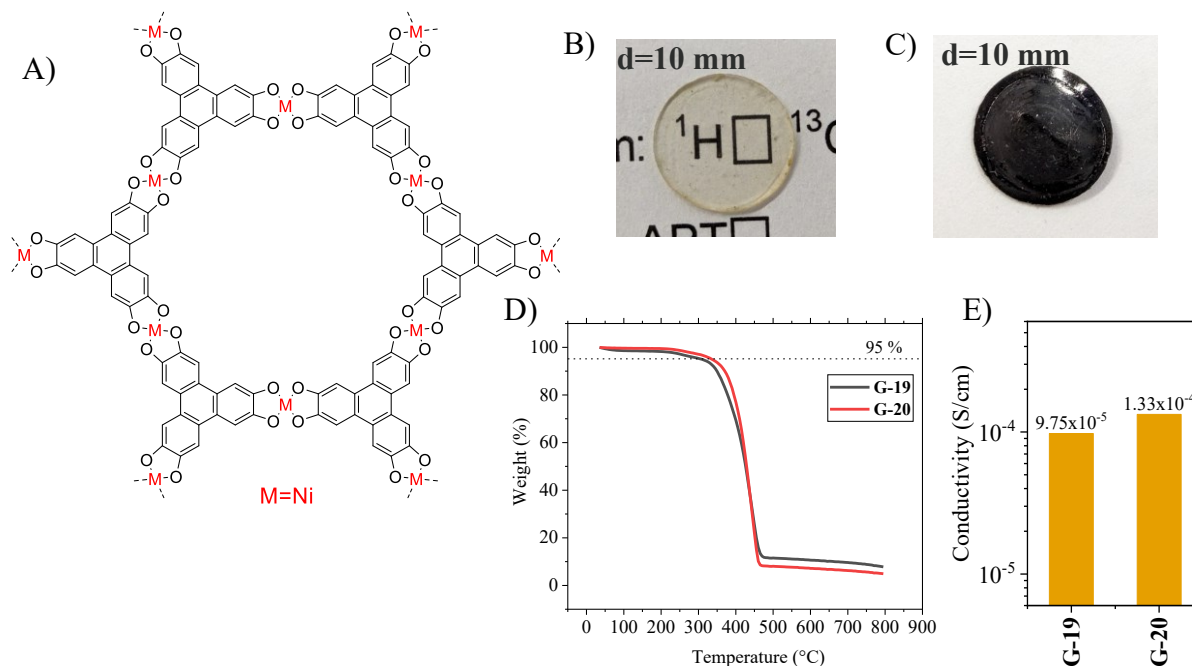
Figure 83. A) Chemical structure of MOF, B) Photo of gel electrolyte (**G-20**), C) Photo of gel electrolyte with embedded MOF (**G-19**), D) TGA measurement of **G-19** and **G-20** in the temperature range of 35 °C to 800 °C under nitrogen atmosphere E) Conductivity measurements of **G-19** and **G-20** at 20 °C.

The properties and performance of gel electrolytes can be improved in various ways, by different components or additives, as described above. The concept of vitrimers can also be used in gel electrolyte by replacing covalent crosslinking by dynamic covalent bonds. Polymer precursor containing ionic liquid monomer, UPy monomer and additional monomer with terminal OH (discussed in Section 4) was prepared (Experimental part 8.3.9) and characterized by SEC and ^{1}H NMR (Figure 86). On the ^{1}H NMR spectrum the incorporation of all monomers can be observed and with the corresponding signals the ratios can be calculated. Polymer precursor was mixed with IL/ LiTFSI in dry ACN in the presence of boric acid for subsequent crosslinking and samples were dried under vacuum at 120 °C. The yielded materials did not show good shape stability and were not able to form self-standing films. Presumably, the dynamic covalent crosslinking does not have sufficient strength to keep the integrity of the structure. On the other hand, the increase of UPy content can compensate for the lack of mechanical strength, but incorporating high concentration of UPy in copolymers can become challenging due to poor solubility.

Although the preparation of gel electrolyte can be complex due to numerous components and varied structures, this complexity can serve as a valuable tool for adjusting and fine-tuning of properties tailored for specific applications.
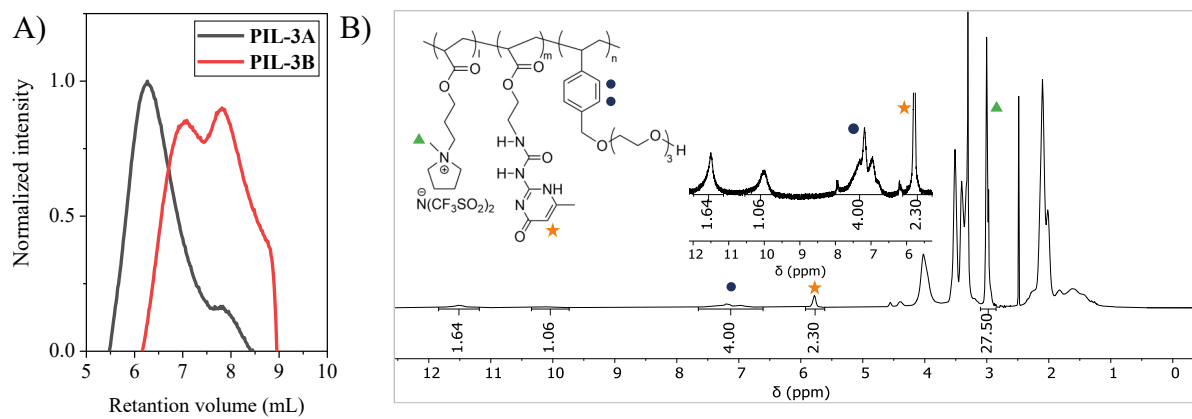
Figure 84. A) SEC analysis of **PIL-3A** and **PIL-3B** in DMF, B) ^{1}H NMR spectrum in CDCl$_3$ of **PIL-3B**.

7 Summary

In the scope of this work novel ionic liquid-based electrolytes were prepared and investigated for their potential application in next-generation LiBs. The first material concept aimed to introduce vitrimeric nature into poly(ionic liquid)-based material was successfully accomplished. The synthesis included preparation of polymerizable ionic liquids which were copolymerized with 2-[2-[2-[(4-ethenylphenyl)methoxy]ethoxy]ethoxy]ethanol monomer, bearing free OH group capable to form dynamic covalent network with boric acid. Subsequently the vitrimeric network was formed by mixing the copolymer precursor, boric acid and LiTFSI. Dynamic borate-ester bonds enabled excellent self-healing ability with high
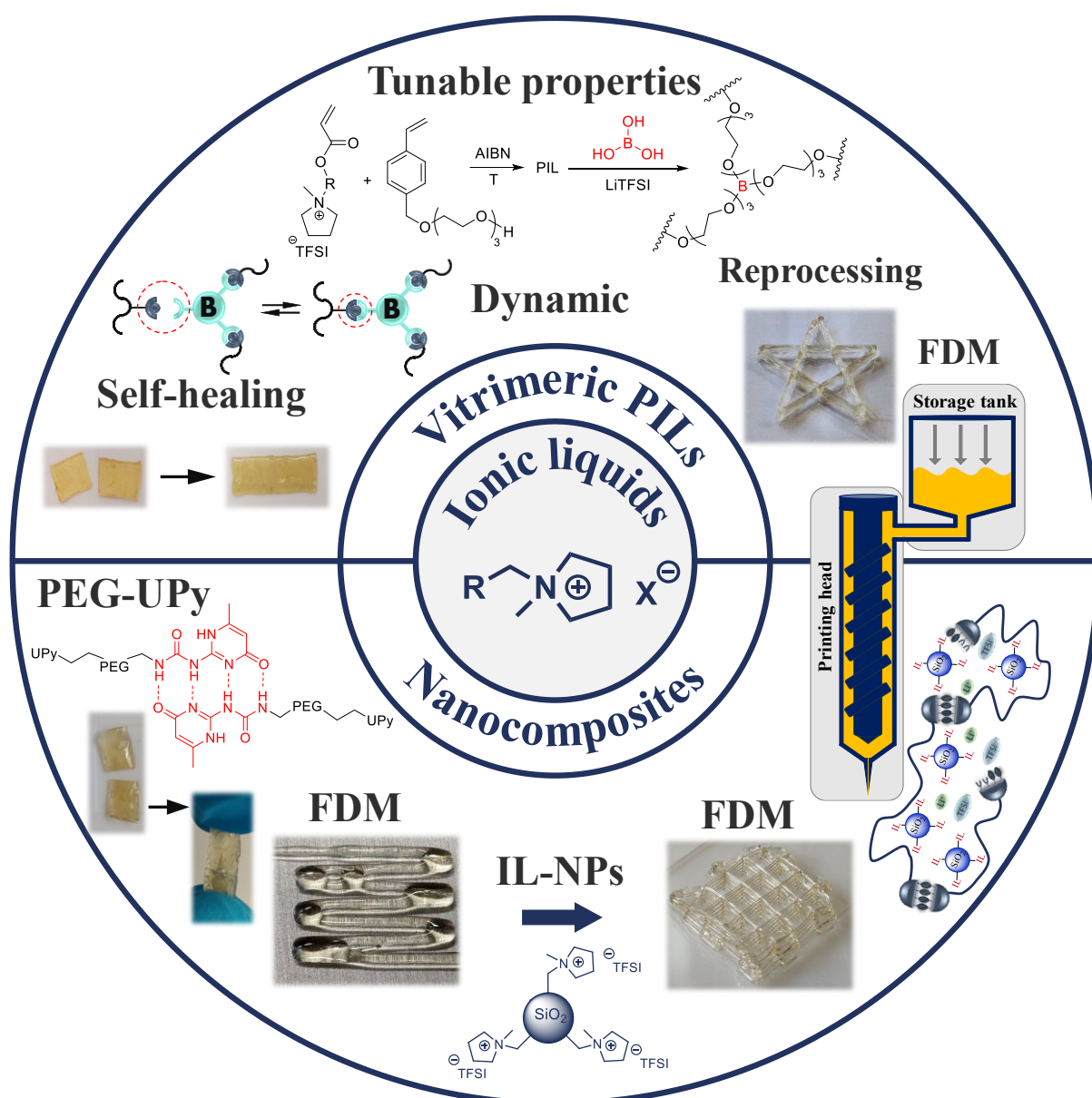
Figure 85. Key summary points for *Material concept I - Vitrimeric poly(ionic liquid)s* and *Material concept - II Nanocomposites*.

efficiency. Moreover, the material can be reprocessed e.g. *via* a hot press to form self-standing films. The dynamic nature of covalent dynamic bonds within material enables it to exhibit the required viscosity for FDM. Thus, the successful printing of complex electrolyte shapes such as star formations with the resolution of 0.33 mm (at 120 °C) was achieved. Vitrimeric PILs were also investigated for thermal stability and ionic conductivity with varied crosslinking density and LiTFSI concentration. PILs are thermally stable up to 300 °C and can reach conductivity in the range of 1.8×10^{-5} S/cm at 50 °C (**V1-4**) and 1.1×10^{-4} S/cm at 50 °C (**V2-1**) for optimized compositions with two types of IL-monomers.

The second material concept involved preparation of nanocomposite electrolytes by combining PEG-based electrolyte with silica nanoparticles. Initially supramolecular interactions were incorporated in PEG *via* end group modification with UPy and barbiturates. The resulting polymers underwent rheology measurement at different temperatures to investigate their potential for FDM. For enhancing the mechanical properties of polymers different amounts of nanoparticles were incorporated, and their surface was modified for better compatibility and dispersivity within the polymer matrix. The surface of the silica NPs was successfully modified either with IL or with alkyl chains. For comparison, unmodified hydroxyl functionalized silica NPs have also been investigated. The IL modification was achieved *via* three step reactions, and successful covalent bonding was confirmed by solid state and liquid NMR, FT-IR and TGA measurements. NPs with organic IL surface exhibit good thermal stability up to 300 °C. Different surfaces of nanoparticles displayed varying dispersity in the polymer matrix, significantly influencing rheological properties. The polymer composite with IL modified nanoparticles and additional LiTFSI displayed improved printability (at 90 °C for storage tank and 70 °C for printing head), forming stable shape and can be self-healed at elevated temperatures. Additionally, IL-particles positively impacted the conductivity (measured by BDS), which increased from 2.8×10^{-5} S/cm at 80 °C to 3.2×10^{-5} S/cm. Remarkably, the ionic conductivity was retained even after reprocessing the composite *via* FDM.

In the third material concept of this work novel dicationic ionic liquids were investigated. These ILs contained a fluorinated linker to enhance electrochemical properties, such as stability windows and the SEI formation ability. Two different counterions, TFSI and FSI, were used for the ILs. Ionic conductivities for four different ILs (fluorinated ones and their nonfluorinated analogs) were investigated with the varied concentration of lithium salt with corresponding anion. Fluorinated ILs display superior physical and electrochemical properties reaching the conductivity in the range of $10^{-3} - 10^{-6}$ S/cm. The difference compared to their nonfluorinated

counterparts becomes more significant at lower temperatures. Additionally, the choice of counterion revealed advantages in using FSI due to reduced viscosity and increased conductivity. The electrochemical stability of fluorinated ILs is remarkably high, reaching 7 V for **FIL-TFSI**, whereas the FSI analog is stable until approximately 6 V. The observed values confirmed expectations that the fluorinated dicationic ILs are suitable for the application in advanced LiBs. However, ILs with FSI counterion exhibited lower thermal stability compared to their TFSI counterparts (330 °C for **NFIL-TFSI** vs. 240 °C for **NFIL-FSI** and 380 °C for **FIL-TFSI** vs. 270 °C for **FIL-FSI**). WAXD measurements revealed the presence of nanoscale heterogeneities that persisted even after the salt addition. The advantageous properties of
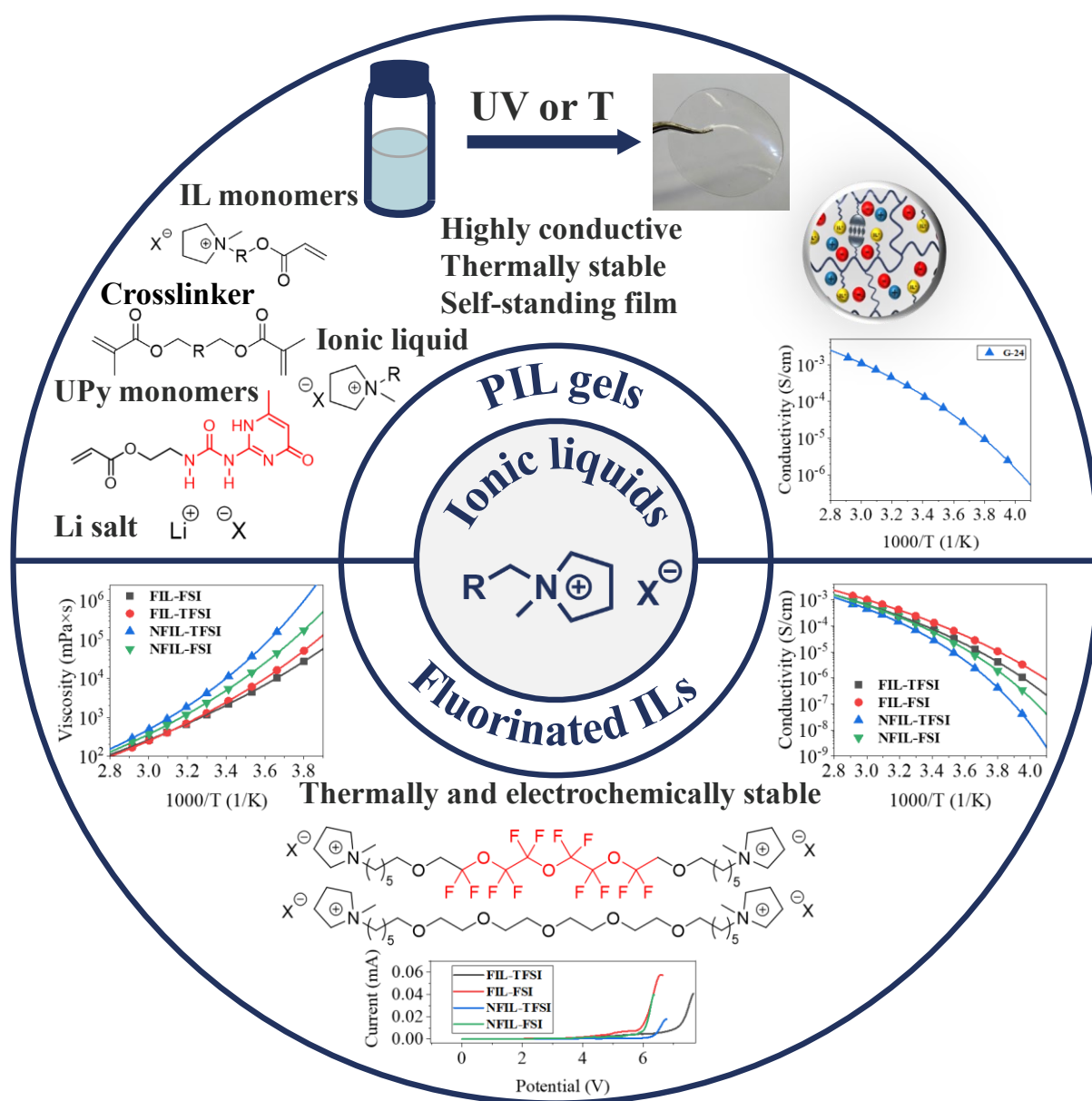
Figure 86. Key summary points for *Material concept - III Fluorinated ionic liquids* and *Material concept - IV Poly(ionic liquid) gel electrolytes*.

fluorinated ILs were explored for incorporation into PIL by copolymerizing fluorinated acrylate and IL-monomer. The resulting polymer displayed high thermal stability but requires further investigation for improving the ionic conductivity.

In the final part of the thesis, ionic liquid-based gel electrolytes were prepared. Multicomponent mixtures containing IL monomer, UPy monomer, crosslinker, IL, lithium salt and initiator were polymerized *via* thermal and photo initiation. The resulting gel retains almost 60 wt% of IL/salt mixture and combines various interactions such as supramolecular hydrogen bonding (UPy monomer), ionic interactions and covalent crosslinking. Such combination enabled formation of self-standing films with good mechanical properties and ionic conductivities. Optimization of the composition of gels involved altering component ratios, chemical structures and polymerization techniques, achieving a room temperature ionic conductivity exceeding 10^{-4} S/cm, an electrochemical stability surpassing 5 V, and thermal stability exceeding 250 °C (for FSI containing gel). Moreover, comparing polymerization techniques revealed consistent performance, indicating that using UV initiation can be more advantageous due to reduced preparation time.

In summary, various approaches were conducted for incorporating IL beneficial properties into polymer electrolytes. The work demonstrated that meticulous material design can enhance the properties, enabling reprocessing, self-healing, fuse deposition modeling, while simultaneously maintaining high-performance standards.

8 Experimental part

8.1 Materials

All other chemicals were used without further purification unless otherwise stated.

3-Chloropropanol (CAS: 627-30-5), N-methylpyrrolidine (CAS: 120-94-5), silica nanoparticles Ludox-sm® (CAS: 7631-86-9), Nanopowder (surface area 175-225 m^2/g (BET)) (CAS: 7631-86-9), hexamethylene diisocyanate (CAS: 822-06-0), PEG 1500 (CAS: 25322-68-3), methylsulfonyl chloride (CAS: 124-63-0), sodium azide (CAS: 26628-22-8), sodium hydride (60 % dispersion in mineral oil) (CAS: 7646-69-7), tri(ethylene glycol) (CAS: 112-27-6), 4-vinylbenzyl chloride (CAS: 1592-20-7), 2,2′-azobis(2-methylpropionitrile) (AIBN) (CAS: 78-67-1), 2,2-dimethoxy-2-phenylacetophenone (DMPA) (CAS: 24650-42-8), triphenylphosphine (CAS: 603-35-0), boric acid (CAS: 10043-35-3), chloro(dodecyl)-dimethylsilane (CAS: 66604-31-7), carbon disulfide (CAS: 75-15-0) and benzyl chloride (CAS: 100-44-7) were purchased from Sigma Aldrich.

2-amino-6-methyl-1H-pyrimidin-4-one (CAS: 3977-29-5), isocyanatoethyl acrylate (CAS: 13641-96-8), 2-(2-(2-chloroethoxy)ethoxy)ethanol (CAS: 5197-62-6), 6-methyl-isocytoside (CAS: 3977-29-5) and 2,2,2-trifluoroethyl acrylate (CAS: 407-47-6) were obtained from TCI.

Triethylamine (CAS: 121-44-8) and (3-chloropropyl)trimethoxysilane (CAS: 2530-87-2) were purchased from Alfa Aesar.

Acryloyl chloride (CAS: 814-68-6) and 2,3,4,5,6-pentafluorostyrene (CAS: 653-34-9) were obtained from abcr.

Io-li-tec provided lithium bis(trifluoromethylsulfonyl)imide (LiTFSI) (CAS: 90076-65-6), lithium bis(fluorosulfonyl)imide (LiFSI) (CAS: 171611-11-3), 1-methyl-1-propyl-pyrrolidinium bis(trifluoromehylsulfonyl)imide (CAS: 223437-05-6), 1-methyl-1-propyl-pyrrolidinium bis(fluorosulfonyl)imide (CAS: 852620-97-4), 1-(2-methoxyethyl)-1-methylpropylpyrrolidinium bis(trifluoromethylsulfonyl)imide (CAS: 757240-24-7), 1-(2-Methoxyethyl)-1-methylpropylpyrrolidinium bis(fluorosulfonyl)imide and N-Methyl-N-propylmorpholinium bis(fluorosulfonyl)imide.

AIBN was recrystallized in methanol. 2,3,4,5,6-Pentafluorostyrene and 2,2,2-trifluoroethyl acrylate were passed through a basic alumina column prior to polymerization. DCM and chloroform were dried by refluxing over calcium hydride. Dry DMF, THF and ACN were collected from solvent purification system (mBraun SPS5).

MOFs have been obtained from Prof. Xinliang Feng, Molecular Functional Materials, Technical University Dresden.

8.2 Methods

NMR - ^{1}H NMR, ^{13}C NMR and ^{19}F NMR spectra were recorded using Varian VnmrS 400 MHz NMR spectrometer at 27 °C. Deuterated chloroform and deuterated dimethyl sulfoxide were used as solvents. Chemical shifts (δ) were given in parts per million (ppm) and coupling constants in Hertz. MestReNova (14.2.1.) was used for spectra interpretations.

Solid state NMR - ^{29}Si MAS NMR spectra of samples were recorded on a Bruker Avance II 400 spectrometer, 4 mm MAS probe, MAS 5 kHz, with CP time of 10 ms and repetition delay of 5s.

Size exclusion chromatography (SEC) measurements were performed on a Viscotek GPCmax VE 2001 equipped with CLM3008 and GMHHRN18055 columns. 10 mM LiTFSI in DMF was used as a solvent and poly(styrene) (PS) was used as calibration standard.

Thermogravimetric analysis (TGA) was conducted on Netzsch TG 209 F3. Samples (5-15 mg) were placed in alumina crucibles and heated from 35 °C to 800 °C with the heating rate of 10 K/min under nitrogen atmosphere (flow rate 20 mL/min). The NETZSCH Proteus was used for analyzing the recorded data.

Differential scanning calorimetry (DSC). DSC data for vitrimeric samples were collected using a PerkinElmer Pyris7. Thermal history was removed by heating up to 120 °C and holding the respective sample at 120 °C for 30 min. The samples were subsequently cooled to -80 °C with a cooling rate of 5 K/min. Heating curves were recorded from -80 °C to 120 °C (heating rate 5 K/min). Temperature calibration was performed manually using OriginLab2023. Substances for temperature calibration were water, indium, tin and lead.

NetzschDSC 204 F1 was used for DSC measurement of PEG-based samples. Samples were dried before measurement in vacuum at 80 °C and placed in aluminum pans, with

measurements being conducted under nitrogen atmosphere. The thermal history was removed by heating samples up to 100 °C followed by cooling down to -20 °C with the rate 5 K/min. Heating curves were recorded up to 170 °C with the heating rate 5 K/min. Collected data were evaluated with Netzsch Proteus Analytic software.

Fourier-transform infrared spectroscopy (FT-IR) analysis was conducted using attenuated total reflection technique on VERTEX 70 v FT-IR Spectrometer (Bruker) equipped with the golden gate diamond ATR unit. Measurements were conducted at room temperature and covered spectral range was from 550 cm^{-1} to 4000 cm^{-1}.

Broadband Dielectric Spectroscopy (BDS) Novocontrol "Alpha analyzer" was used for investigating ionic conductivities. Liquid and viscous samples were placed in a cell containing two brass electrodes (d = 20 mm, h = 2.5 mm), small pressure on cell (heating up to 80 °C for highly viscous polymer samples) was applied for ensuring proper contact between electrodes and samples. PIL gels were placed between two brass electrodes (d = 20 mm) and the thickness of each sample gel was measured individually. Measuring cell was placed in a cryostat with a constant flow of dry nitrogen. Ionic conductivity was recorded in the frequency range 1 – 10^6 Hz and different temperatures. Ion conductivity values were extracted from the plateau of σ vs. T.

3D printing was performed on RegenHU 3D Discovery equipped with a heatable storage tank and an extrusion printing head. A needle with the size of 0.33 mm was connected to the printing head and a pressure of 0.15 MPa − 0.2 MPa was applied for generating a constant flow of polymer sample through the nozzle. 120 °C was chosen (for the nozzle and storage tank) for FDM of vitrimeric samples, 70 °C (printing head) and 90 °C (storage tank) for FDM of PEG/nanocomposite samples. BioCAD™ program was used for designing shapes for printing. FMD was performed directly on glass surfaces under normal laboratory conditions.

Tensile tests were performed using a universal testing machine Instron® at room temperature with the strain rate of 20 mm/min.

Rheological measurements were performed on Anton Paar MCR-101 DSO rheometer equipped with parallel plate-plate geometry (d = 8 mm, for highly viscous samples) or cone-plate (d = 25 mm, for less vicious samples). The device was equipped with Peltier-temperature control for ensuring accurate temperature control and nitrogen gas flushing. All samples were pre-dried (under vacuum at 60 − 80 °C) before measurements. Recorded data were analyzed *via* RheoCompass™.

Dynamic light scattering (DLS) measurements were conducted on Litesizer 500, Anton Paar at 25 °C. Sample concentration was kept in the range of 1-3 mg/ml in THF.

Linear Sweep Voltammetry (LSV) measurements were conducted in a glovebox using potentiostat Autolab PGSTAT 204 with FRA32M module running on Nova 2.1.5 Software. A sample (10 mm diameter) was placed between stainless steel electrodes and measurement was conducted in the range of 0 - 8 V at 1 mV/s rate. Before each measurement, both electrodes are polished with 1 μm and 0.3 μm aluminum oxide suspension for 5 minutes.

Transmission Electron Microscopy (TEM) was performed on electron microscope EM 900 from Zeiss with an acceleration voltage of 80 kV. ImageSP Viewer was used for analyzing images.

The wide-angle X-ray diffraction (WAXD) measurements of vitrimeric samples were performed in transmission mode using a SAXSLAB laboratory setup (Retro-F) equipped with an AXO microfocus X-ray source and an AXO multilayer X-ray optic (ASTIX) as monochromator for Cu Kα radiation (λ = 1.54 Å). A DECTRIS PILATUS3 R 300K detector was used to record the 2D scattering patterns. The 2D WAXD pattern was integrated *via* SAXSGUI in order to obtain 1D WAXD pattern. The sample to detector distance was about 10 cm. A twin pinhole system was used for the measurements with an aperture size of about 0.9 mm and 0.4 mm. The polymer film was placed on a Linkam stage and fixed with double sided adhesive tape. The measurement was performed under vacuum at a temperature of 21 °C with a measurement time of 5 min.

WAXD measurements of ionic liquids were performed with an Incoatec (Geesthacht, Germany) IμS equipped with a microfocus source and a monochromator for CuKa radiation (lamda=1.5406A). 2D scattering patterns are recorded with a Vantec 500 2D detector (Bruker AXS, Karlsruhe). Samples are filled in 0.5 mm diameter capillaries for measurement.

8.3 Synthesis of vitrimeric poly(ionic liquid)s

8.3.1 Synthesis of 2-[2-[2-[(4-ethenylphenyl)methoxy]ethoxy]ethoxy]ethanol (1)

1
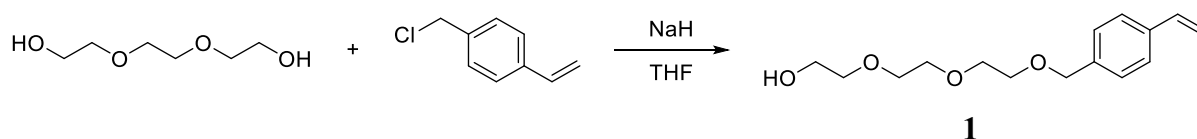
The synthesis was adapted from the literature.[380,381] To the mixture of dry THF (30 mL) and NaH (1.67 g, 0.042 mol), tri(ethylene glycol) (15 g, 0.1 mol) was gradually added under cooling with an ice bath. The reaction mixture was stirred for one hour, followed by the dropwise addition of 4-vinylbenzyl chloride (3 g, 0.02 mol). Finally, the mixture was refluxed at 65 °C for 6 hours under inert atmosphere. The reaction was quenched with water (20 mL), followed by the removal of THF by a rotavapor. The crude product was extracted by chloroform. The organic phase was dried over anhydrous Na_2SO_4 and the solvent was removed under reduced pressure. The product was purified by silica gel column chromatography with ethyl acetate as an eluent ($R_f = 0.37$), giving a light-yellow liquid (3.5 g). Yield 70%.

^{1}H NMR (CDCl$_3$, 400 MHz, δ in ppm): 7.42 – 7.34 (m, 2H), 7.33 – 7.26 (m, 2H), 6.70 (dd, J = 17.6, 10.9 Hz, 1H), 5.73 (dd, J = 17.6, 0.9 Hz, 1H), 5.23 (dd, J = 10.9, 0.9 Hz, 1H), 4.55 (s, 2H), 3.76 – 3.57 (m, 12H), 2.53 (t, J = 6.1 Hz, 1H).

8.3.2 Synthesis of N-[(2-acryloyloxy)propyl]-N-methylpyrrolidinium bis(trifluoromethylsulfonyl)imide (4)

8.3.2.1 Synthesis of 3-chloropropyl acrylate (2)

2
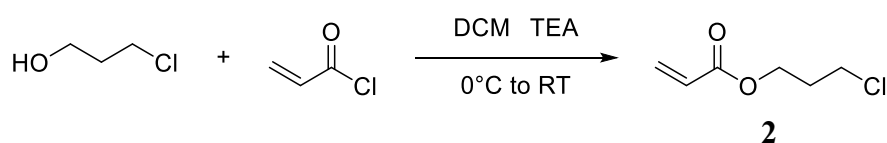
The synthesis was adapted from the literature.[327] A two-neck flask was equipped with a septum and a magnetic stirring bar. To the solution of 3-chloropropanol (3.1 g, 33 mmol) and triethylamine (5.20 mL, 37 mmol) in dry DCM (50 mL) acryloyl chloride (3.17 g, 35 mmol) was slowly added while stirring. The reaction mixture was cooled to 0 °C in an ice bath. After complete addition, the reaction mixture was allowed to warm up to room temperature and kept for stirring for 16 hours. Reaction mixture was poured into saturated NaHCO$_3$ solution (25 mL). The organic layer was collected, washed three times with water (3 × 15 mL), dried

over anhydrous Na_2SO_4 and filtered. Subsequently, the solvent was removed under vacuum at 35 °C. Product was isolated *via* distillation at 0.04 − 0.05 mbar pressure at 35 °C as colorless transparent liquid. Yield 80 %.

^{1}H NMR (CDCl$_3$, 400 MHz, δ in ppm): 6.40 (dd, J = 17.3, 1.4 Hz, 1H), 6.11 (dd, J = 17.3, 10.4 Hz, 1H), 5.83 (dd, J = 10.4, 1.4 Hz, 1H), 4.30 (t, J = 6.1 Hz, 2H), 3.62 (t, J = 6.4 Hz, 2H), 2.14 (p, J = 6.3 Hz, 2H)

^{13}C NMR (CDCl$_3$, 101 MHz, δ in ppm): 165.95, 130.94, 128.17, 61.20, 41.13, 31.59.

8.3.2.2 Synthesis of N-[(2-acryloyloxy)propyl]-N-methylpyrrolidinium chloride (3)
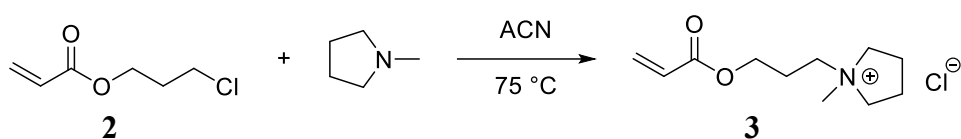
The synthesis was adapted from the literature.[327] 3-chloropropyl acetate (**2**) (5.2 g, 28 mmol) and N-methyl pyrrolidine (2.42 g, 28 mmol) in dry ACN (80 mL) was refluxed overnight at 80 °C in a one neck flask equipped with a reflux condenser and a magnetic stirring bar (under inert atmosphere). The solvent was removed under vacuum at 35 °C. After removing the solvent, the crude product was dissolved in water and washed three times using DCM. Water was evaporated under reduced pressure and the product was obtained as viscous oil. Yield 85 %.

^{1}H NMR (DMSO-d$_6$, 400 MHz, δ in ppm): 6.36 (dd, J = 17.3, 1.5 Hz, 1H), 6.16 (dd, J = 17.3, 10.4 Hz, 1H), 5.97 (dd, J = 10.4, 1.5 Hz, 1H), 4.16 (t, J = 6.2 Hz, 2H), 3.61 – 3.38 (m, 6H), 3.01 (s, 3H), 2.16 – 2.02 (m, 6H).

^{13}C NMR (DMSO-d$_6$, 100 MHz, δ in ppm): 165.78, 132.43, 128.49, 63.99, 61.79, 60.62, 47.98, 23.34, 21.51.

8.3.2.3 Synthesis of N-[(2-acryloyloxy)propyl]-N-methylpyrrolidinium
bis(trifluoromethylsulfonyl)imide (4)
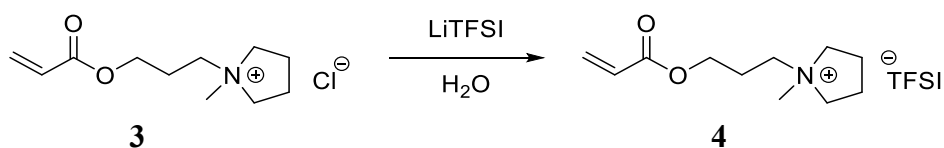
The synthesis was adapted from the literature.[327] N-[(2-acryloyloxy)propyl]-N-methyl pyrrolidinium chloride (**3**) (5.0 g, 21 mmol) was dissolved in 50 mL of water and solution of

lithium bis(trifluoromethylsulfonyl)imide (8.7 g, 25 mmol) in 50 mL water was added. The mixture was kept for stirring at room temperature overnight. Product was extracted using DCM (3 x 50 mL). The organic phase was washed with water (4 × 25 mL) and dried over anhydrous MgSO₄. Solvent was removed under the vacuum and colorless (very slightly yellowish) viscous oil was obtained as a final product. Yield 78 %.

^{1}H NMR (DMSO-d₆, 400 MHz, δ in ppm): 6.36 (dd, J = 17.3, 1.5 Hz, 1H), 6.16 (dd, J = 17.3, 10.4 Hz, 1H), 5.97 (dd, J = 10.4, 1.5 Hz, 1H), 4.17 (t, J = 6.2 Hz, 2H), 3.56 – 3.39 (m, 6H), 2.99 (s, 3H), 2.19 – 2.04 (m, 6H).

^{13}C NMR (DMSO-d₆, 101 MHz, δ in ppm): 165.75, 132.33, 128.48, 125.51 – 114.58 (m), 64.04, 61.73, 60.78, 47.96, 23.30, 21.51.

^{19}F NMR (DMSO-d₆, 400 MHz, δ in ppm): -78.74.

8.3.3 Synthesis of N-(2-(2-(2-(acryloyloxy)ethoxy)ethoxy)ethyl)-N-methylpyrrolidinium bis(trifluoromethylsulfonyl)imide (7) / bis(fluorosulfonyl)imide (8)

8.3.3.1 Synthesis of 2-(2-(2-chloroethoxy)ethoxy)ethyl acrylate (5)
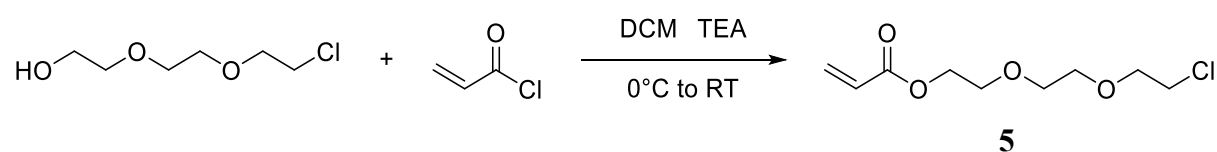
A two-neck flask was equipped with a septum and a magnetic stirring bar. To the solution of the 2-(2-(2-chloroethoxy)ethoxy)ethanol (10 mL, 68.8 mmol) in dry DCM (150 mL) triethylamine (10.6 mL, 75 mmol) was added slowly while cooling to 0 °C, followed with the dropwise addition of acryloyl chloride (5.66 mL, 70 mmol). Reaction mixture was kept in ice bath. After the addition was completed the reaction mixture was allowed to warm up to room temperature and kept for stirring for 16 hours under inert atmosphere. Mixture was filtered and filtrate was poured into saturated NaHCO₃ solution (50 mL). The organic layer was collected and washed three times with water (3 × 20 mL) and subsequently dried over anhydrous Na₂SO₄. After filtration solvent was removed under vacuum at 35 °C. Purification of the product was done by silica column chromatography (DCM / ethyl acetate ratio 40 / 1, Rf = 0.65). Yield 65%.

^{1}H NMR (CDCl₃, 400 MHz, δ in ppm): 6.41 (dd, J = 17.3, 1.4 Hz, 1H), 6.14 (dd, J = 17.3, 10.5 Hz, 1H), 5.82 (dd, J = 10.4, 1.4 Hz, 1H), 4.34 – 4.27 (m, 2H), 3.76 – 3.71 (m, 4H), 3.66 (s, 4H), 3.61 (t, J = 5.8 Hz, 2H).

^{13}C NMR (CDCl$_3$, 101 MHz, δ in ppm): 166.10, 130.96, 128.25, 71.39, 70.62, 69.17, 63.60, 42.67.

8.3.3.2 *N-(2-(2-(2-(acryloyloxy)ethoxy)ethoxy)ethyl)-N-methylpyrrolidinium chloride (6)*

5   + $\xrightarrow[75\ °C]{\text{ACN}}$ **6**
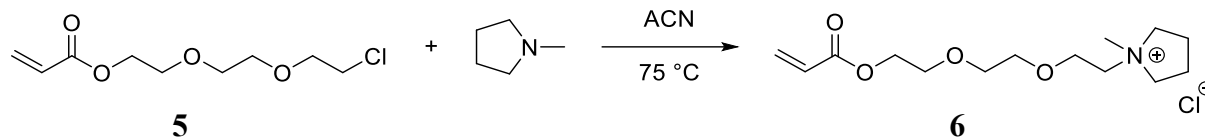
2-(2-(2-chloroethoxy)ethoxy)ethyl acrylate (**5**) (6.7 g, 30 mmol) and N-methyl pyrrolidine (3.2 mL, 30 mmol) in ACN (50 mL) were refluxed overnight at 80 °C in the one neck flask equipped with the reflux condenser and the magnetic stirring bar. The solvent was removed under vacuum at 35 °C. After removing the solvent, water (50 mL) was added to the mixture and the solution was washed three times using DCM (3 × 15 mL). Water was removed under reduced pressure and the product was obtained as viscous oil. Yield 40%.

^{1}H NMR (DMSO-d$_6$, 400 MHz, δ in ppm): 6.32 (dd, J = 17.3, 1.7 Hz, 1H), 6.17 (dd, J = 17.2, 10.3 Hz, 1H), 5.94 (m, 1H), 4.24 – 4.17 (m, 2H), 3.82 (m, 2H), 3.63 (m, 2H), 3.56 (m, 6H), 3.53 – 3.44 (m, 4H), 3.02 (s, 3H), 2.05 (m, J = 3.3 Hz, 4H).

^{13}C NMR (DMSO-d$_6$, 101 MHz, δ in ppm): 165.88, 132.13, 128.61, 69.89, 68.63, 64.91, 64.66, 63.85, 62.57, 48.47, 21.33.

8.3.3.3 *Synthesis of N-(2-(2-(2-(acryloyloxy)ethoxy)ethoxy)ethyl)-N-methylpyrrolidinium bis(trifluoromethylsulfonyl)imide (7) / bis(fluorosulfonyl)imide (8)*

6 $\xrightarrow[\text{H}_2\text{O}]{\text{LiTFSI}}$ **7** TFSI$^{\ominus}$

6 $\xrightarrow[\text{H}_2\text{O}]{\text{LiFSI}}$ **8** FSI$^{\ominus}$
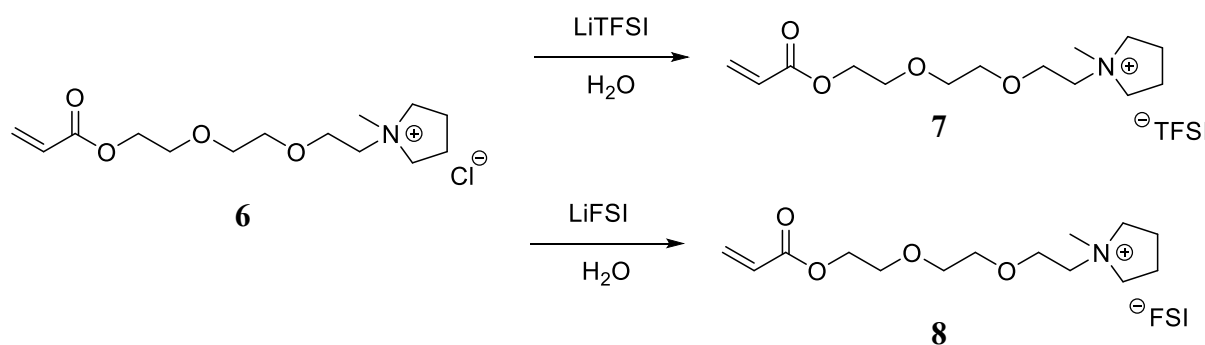
N-(2-(2-(2-(acryloyloxy)ethoxy)ethoxy)ethyl)-N-methylpyrrolidinium chloride (**6**) (3.4 g, 11 mmol) was dissolved in 30 mL of water and solution of lithium bis(trifluoromethylsulfonyl)imide (3.7 g, 13 mmol) in 20 mL water was added. The mixture was kept for stirring at room temperature overnight. N-(2-(2-(2-(acryloyloxy)ethoxy)ethoxy)-ethyl)-N-methylpyrrolidinium bis(trifluoromethylsulfonyl)imide was extracted using DCM

(3 × 15 mL). The organic phase was washed with water (4 × 10 mL) and dried over anhydrous Na_2SO_4. Solvent was removed under the vacuum and final product was dried under high vacuum for 24 hours over P_2O_5. Yield 65%.

^{1}H NMR (DMSO-d$_6$, 400 MHz, δ in ppm): 6.32 (dd, J = 17.3, 1.6 Hz, 1H), 6.17 (dd, J = 17.2, 10.3 Hz, 1H), 5.99 – 5.90 (m, 1H), 4.28 – 4.17 (m, 2H), 3.82 (m, 2H), 3.66 – 3.62 (m, 2H), 3.61 – 3.51 (m, 6H), 3.51 – 3.43 (m, 4H), 3.00 (s, 3H), 2.05 (m, 4H).

^{13}C NMR (DMSO-d$_6$, 101 MHz, δ in ppm): 165.88, 132.13, 128.61, 119.92 (q, J = 321.9 Hz), 69.89, 68.63, 64.91, 64.66, 63.85, 62.57, 48.47, 21.33.

^{19}F NMR (DMSO-d$_6$, 376 MHz, δ in ppm): -78.76.

Similarly, N-(2-(2-(2-(acryloyloxy)ethoxy)ethoxy)ethyl)-N-methylpyrrolidinium bis(fluorosulfonyl)imide was synthesized by using LiFSI for anion exchange. Yield 65%.

^{1}H NMR (DMSO-d$_6$, 400 MHz, δ in ppm): 6.32 (dd, J = 17.3, 1.6 Hz, 1H), 6.17 (dd, J = 17.2, 10.3 Hz, 1H), 5.99 – 5.90 (m, 1H), 4.28 – 4.17 (m, 2H), 3.82 (m, 2H), 3.66 – 3.62 (m, 2H), 3.61 – 3.51 (m, 6H), 3.51 – 3.43 (m, 4H), 3.00 (s, 3H), 2.05 (m, 4H).

^{13}C NMR (DMSO-d$_6$, 101 MHz, δ in ppm): 165.88, 132.13, 128.61, 69.89, 68.63, 64.91, 64.66, 63.85, 62.57, 48.47, 21.33.

^{19}F NMR (DMSO-d$_6$, 376 MHz, δ in ppm): 53.19.

*8.3.4   Synthesis of PIL-copolymer (**PIL-1A, PIL-1B, PIL-1C***)

4   **1**   **PIL-1A**
                                                                        PIL-1B
                                                                        PIL-1C
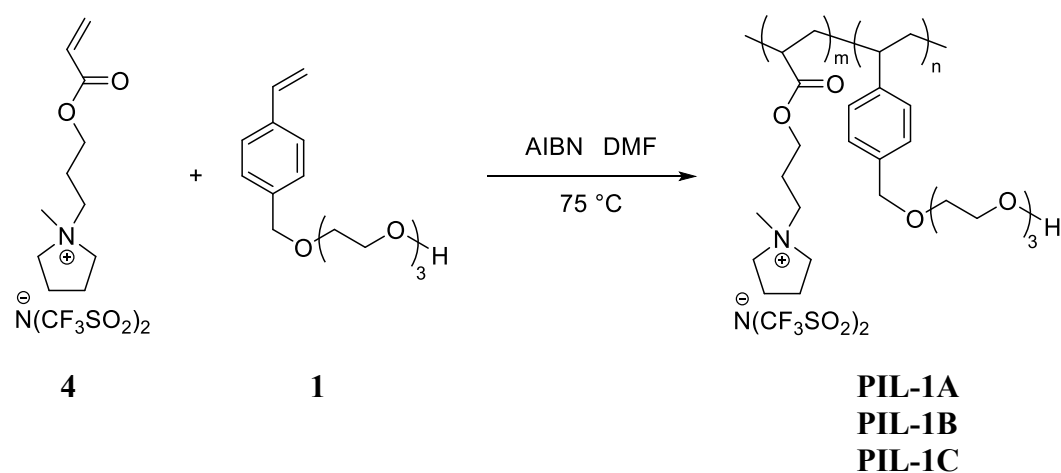
Polymer with the monomer molar ratio of 9 : 1 (m:n) was synthesized *via* the following procedure: 4 g (8.37 mmol) N-[(2-acryloyloxy)propyl]-N-methylpyrrolidinium bis(trifluoro-methylsulfonyl)imide (**4**), 0.234 g (0.93 mmol) 2-[2-[2-[(4-ethenylphenyl)methoxy]-

ethoxy]ethoxy]ethanol (**1**) and 21 mg AIBN were dissolved in dry DMF (4 mL). After freeze thaw cycles (3 x) the mixture was placed in an oil bath at 70 °C overnight (under the inert atmosphere). The reaction product was precipitated into DCM. A highly viscous polymer was collected *via* decantation, dissolved in 5 mL acetone and precipitated again in DCM. Previous purification steps were repeated 3 times. Finally, the polymer (**PIL-1A**) was dried in a vacuum oven at 65 °C for 18 hours. Yield 90%.

Polymers with the monomer molar ratio of 1 : 1 (m:n) (**PIL-1B**) and 1 : 9 (m:n) (**PIL-1C**) were synthesized similarly. DCM/hexane with volume ratio of 1/1 was used for precipitation step.

8.3.5   Synthesis of vitrimeric PIL (*V1-X*)

PIL-1A   **V1-X**
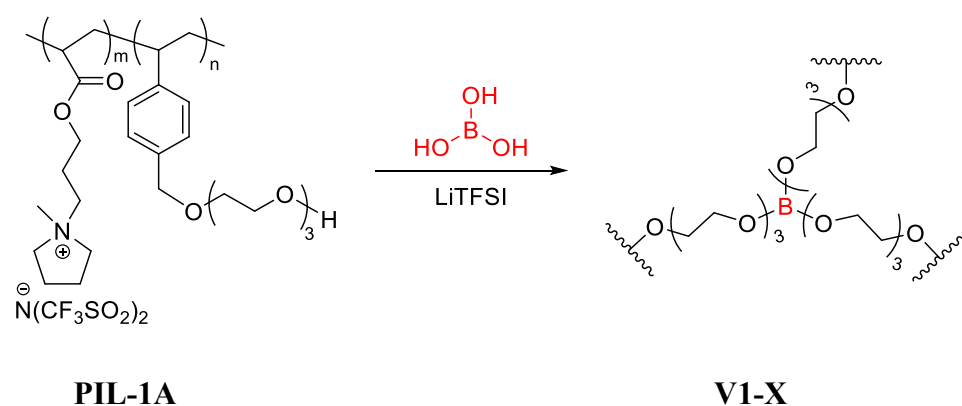
1.5 g **PIL-1A** (m:n = 9 : 1) was dissolved in 5 mL dry acetonitrile. Appropriate amount of dry LiTFSI was dissolved in 1 mL ACN and added to the polymer solution. Boric acid was dissolved in methanol (0.1 g/mL stock solution) and an appropriate amount was added to the mixture. The solution was kept stirring at 40 °C for 30 min. The temperature was gradually increased to 100 °C while the flask was under a constant flow of nitrogen for letting the ACN evaporate. A highly viscous product was transferred to a Teflon mold and dried in vacuum oven at 120 °C for 48 hours.

Similarly, vitrimeric PILs were prepared using PIL copolymer with the monomer ratio of m:n = 1 : 1 (**PIL-1B**). 1 g starting polymer was dissolved in 30 mL of dry acetonitrile and followed same procedures.

Similarly, vitrimeric PILs were prepared using PIL copolymer with the monomer ratio of m:n = 1 : 9 (**PIL-1C**). 1 g starting polymer was dissolved in 50 mL of dry acetonitrile and followed the same procedures.

V1-X compositions are given in the table below.

Sample	Precursor	Polymer (g)	LiTFSI/ EO	LiTFSI (mg)	LiTFSI (mmol)	Boric acid (mg)	Boric acid (mmol)
V1-1	PIL-1A	1.5	0	0	0	6.8	0.11
V1-2	PIL-1A	1.5	0.1	28.3	0.10	6.8	0.11
V1-3	PIL-1A	1.5	0.2	56.5	0.20	6.8	0.11
V1-4	PIL-1A	1.5	0.3	84.8	0.30	6.8	0.11
V1-5	PIL-1A	1.5	0.4	113.1	0.39	6.8	0.11
V1-6	PIL-1A	1.5	0.5	141.4	0.49	6.8	0.11
V1-7	PIL-1A	1.5	1	282.7	0.98	6.8	0.11
V1-8	PIL-1A	1.5	2	565.5	1.97	6.8	0.11
V1-9	PIL-1C	1	0	0	0	64.6	1.05
V1-10	PIL-1B	1	0	0	0	27.7	0.45
V1-11	PIL-1B	1	0.1	115.7	0.40	27.7	0.45
V1-12	PIL-1B	1	0.2	231.5	0.81	27.7	0.45
V1-13	PIL-1B	1	0.3	347.2	1.21	27.7	0.45
V1-14	PIL-1B	1	0.4	462.9	1.61	27.7	0.45
V1-15	PIL-1B	1	0.5	578.6	2.02	27.7	0.45
V1-16	PIL-1B	1	1	1157.3	4.03	27.7	0.45
V1-17	PIL-1B	1	2	2314.5	8.06	27.7	0.45

8.3.6   Synthesis of PIL-copolymer (PIL-2)
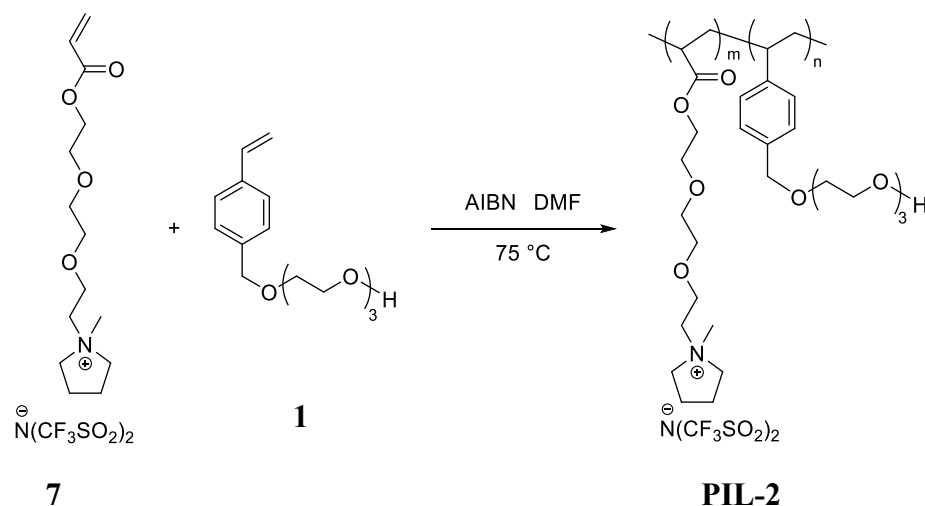
5.46 g (9.89 mmol) N. N-(2-(2-(2-(acryloyloxy)ethoxy)ethoxy)ethyl)-N-methylpyrrolidinium bis(trifluoromethylsulfonyl)imide (**7**), 0.30 g (1.13 mmol) 2-[2-[2-[(4-ethenylphenyl)-methoxy]ethoxy]ethoxy]ethanol (**1**) and 28 mg AIBN were dissolved in dry DMF (6 mL). After freeze thaw cycles (3 x) the mixture was placed in an oil bath at 70 °C overnight (under inert atmosphere). The reaction product was precipitated into DCM/hexane with volume ratios

of 1/1. Polymer was collected, dissolved in 5 mL acetone and precipitated again in DCM/hexane mixture. Previous purification steps were repeated 3 times. Finally, the polymer was dried in a vacuum oven at 65 °C for 18 hours. Yield 80%.

8.3.7 Synthesis of vitrimeric PIL (*V2-X*)
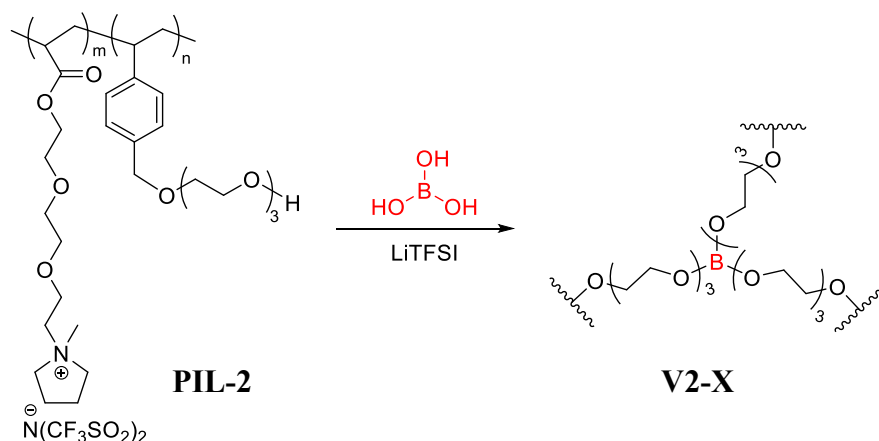
Vitrimeric PILs were synthesized similarly to **V1-X**. 0.5 g **PIL-2** was dissolved in 10 mL dry ACN and an appropriate amount of LiTFSI and boric acid was added to the solution. **V2-X** compositions are given in the table below.

Sample	Polymer (g)	LiTFSI/EO	LiTFSI (mg)	LiTFSI (mmol)	Boric acid (mg)	Boric acid (mmol)
V2-1	0.5	0	0	0	1.97	0.032
V2-2	0.5	0.1	82.3	0.29	1.97	0.032
V2-3	0.5	0.2	164.5	0.57	1.97	0.032
V2-4	0.5	0.3	246.8	0.86	1.97	0.032
V2-5	0.5	0.5	411.3	1.43	1.97	0.032
V2-6	0.5	1	822.5	2.87	1.97	0.032

8.3.8 Synthesis of 2-(3-(4-methyl-6-oxo-1,6-dihydropyrimidin-2-yl)ureido)ethyl acrylate (UPy monomer) (*9*)
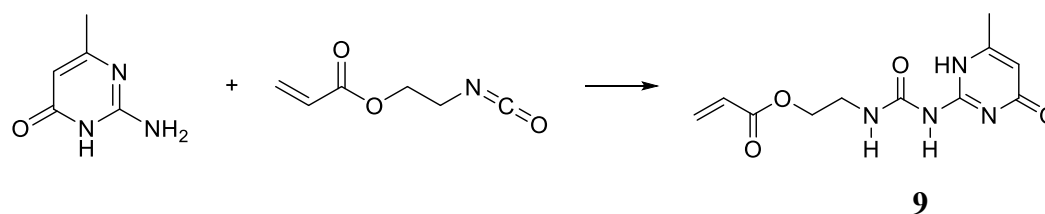
The synthesis was adapted from the literature.[382] 2-amino-6-methyl-1H-pyrimidin-4-one (3.13 g, 25 mmol) was dissolved in 80 mL DMSO at 120 °C. Solution was let to cool down to approx. 80 °C, followed by the addition of isocyanatoethyl acrylate (25 mmol). The mixture

was kept for stirring at RT for 3 hours. Formed white precipitate was collected using filtration, washed two times using hexane, one time with acetone. The final product was dried under high vacuum for 48 hours. Yield 85 %.

^{1}H NMR (CDCl$_3$, 400 MHz, δ in ppm): 12.96 (s, 1H), 11.94 (s, 1H), 10.47 (s, 1H), 6.44 (dd, J = 17.3, 1.5 Hz, 1H), 6.13 (dd, J = 17.3, 10.5 Hz, 1H), 5.91 – 5.70 (m, 2H), 4.29 (t, J = 5.7 Hz, 2H), 3.57 (q, J = 5.7 Hz, 2H), 2.23 (s, 3H).

8.3.9   Synthesis of PIL-copolymer (*PIL-3*)
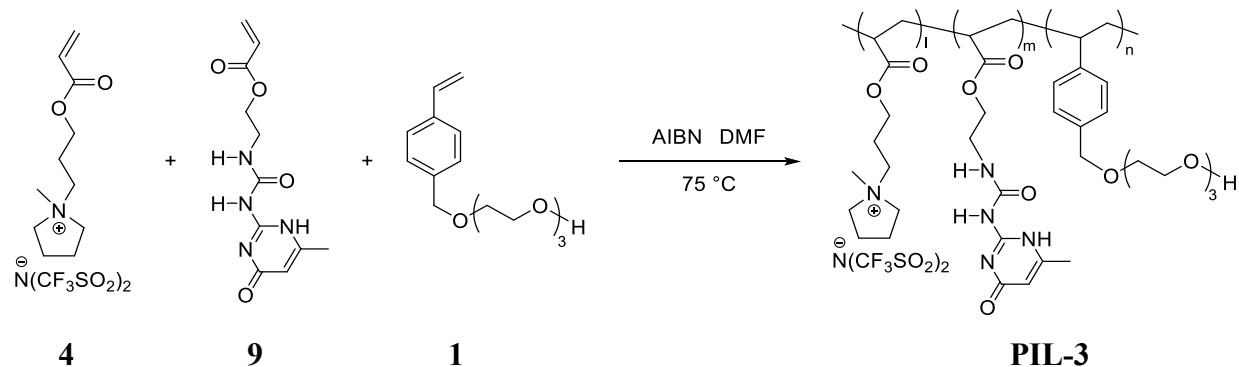
PIL (**PIL-3A**) with the monomer molar ratio of 9 : 1 : 1 (l:m:n) was synthesized *via* following procedure: 1.4 g (3 mmol) N-[(2-acryloyloxy)propyl]-N-methylpyrrolidinium bis(trifluoro-methylsulfonyl)imide (**4**), 88.7 mg (0.33 mmol) 2-[2-[2-[(4-ethenylphenyl)-methoxy]ethoxy]ethoxy]ethanol (**1**) and 88.7 mg (0.33 mmol) UPy monomer (**9**) were dissolved in dry DMF (2.5 mL). Subsequently to freeze thaw cycles (3 x) the mixture was placed in an oil bath at 100 °C. After complete dissolution of components, the temperature was reduced to 75 °C and 8 mg AIBN (dissolved in 0.1 mL dry DMF) was added. Polymerization was done for 16 hours at 75 °C under inert atmosphere. The reaction product was precipitated into DCM. The product was re-dissolved in 5 mL acetone and precipitated again in DCM. Previous precipitation steps were repeated 3 times. Finally, the polymer (**PIL-3**) was dried in a vacuum oven at 60 °C for 24 hours. Yield 60%.

Similarly, PIL (**PIL-3B**) containing monomers with the ratio 9 : 2 : 1 (l:m:n) were prepared.

8.3.10 Synthesis of vitrimeric PIL gel electrolyte (V3-X)

PIL-3   **V3-X**
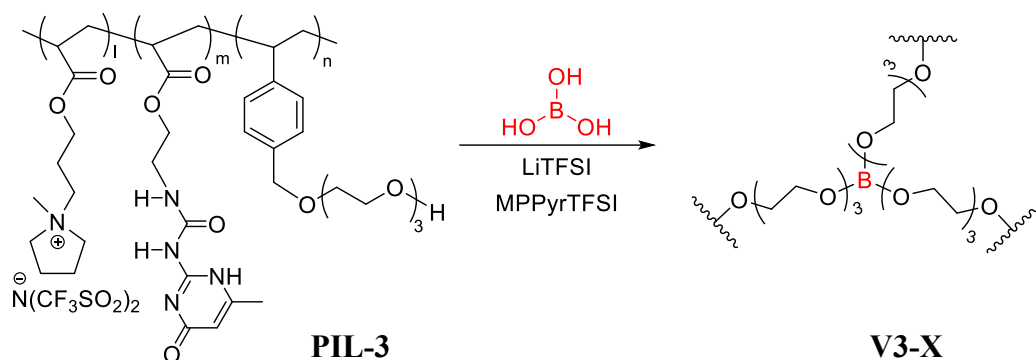
Vitrimeric PILs were synthesized by mixing components in dry ACN. After mixing the solvent was removed at 80 °C followed with drying in vacuum at 100 °C.

Sample	Polymer-type	Polymer (g)	MPPyrTFSI (mg)	LiTFSI (mg)	LiTFSI (mmol)	Boric acid (mg)	Boric acid (mmol)
V3 -1	PIL-3A	0.5	0	0	0	0.98	0.016
V3 -2	PIL-3A	0.5	338	113	0.4	0.98	0.016
V3 -3	PIL-3B	0.5	0	0	0	1.19	0.019
V3 -4	PIL-3B	0.5	338	113	0.4	1.19	0.019

8.4 Surface modification of silica nanoparticles

8.4.1 Synthesis of N-[3-(trimethoxysilyl)propyl]-N-methylpyrrolidinium chloride (10)

10
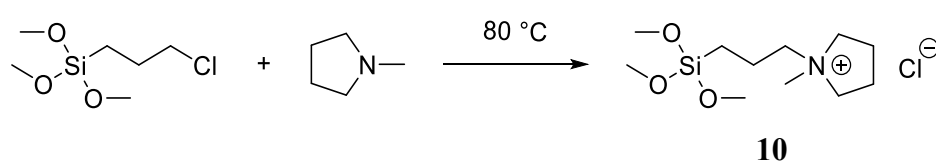
The synthesis was adapted from the literature.[383] N-Methylpyrrolidinium (5 mL, 47 mmol) and (3-chloropropyl)trimethoxysilane (8.57 mL, 47 mmol) mixture was kept at 80 °C while stirring for 48 hours under inert atmosphere. Red/orangish mixture was washed using diethyl ether (4 times) and formed N-[3-(trimethoxysilyl)propyl]-N-methylpyrrolidinium chloride was dried in vacuum. Yellowish brownish solid product was obtained. Yield 45%.

^{1}H NMR (CDCl$_3$, 400 MHz, δ in ppm): 3.78 – 3.61 (m, 4H), 3.54 – 3.47 (m, 2H), 3.45 (s, 9H), 3.19 (s, 3H), 2.27 – 2.08 (m, 4H), 1.80 – 1.68 (m, 2H), 0.61 – 0.53 (m, 2H).

^{13}C NMR (CDCl$_3$, 101 MHz, δ in ppm): 65.36, 64.15, 50.62, 48.40, 21.57, 17.59, 5.77.

8.4.2 Synthesis of LUDOX® SM silica via N-[3-(trimethoxysilyl)propyl]-N-methylpyrrolidinium chloride (11)

10   **11**
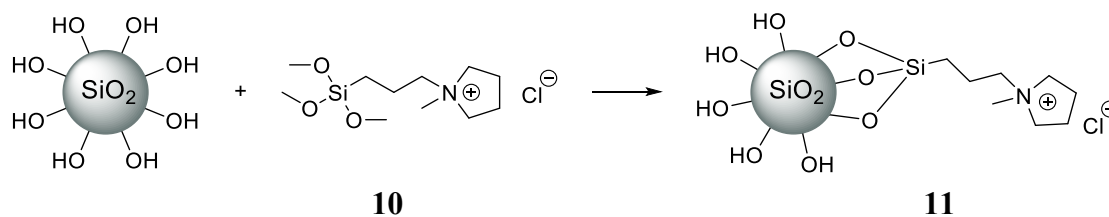
The synthesis was adapted from the literature.[257] Silica nanoparticles Ludox-sm® solution (3 g) was diluted using deionized water (100 g) and 0.7 g (2.5 mmol) of N-[3-(trimethoxysilyl)propyl]-N-methylpyrrolidinium chloride (**10**) were added to the solution. The mixture was kept stirring at 80°C for 24 hours. Solution containing the modified nanoparticles were concentrated using a rotary evaporator and precipitated into acetone. NPs were collected using centrifugation and washed with acetone three more times.

8.4.3 Synthesis of LUDOX® SM silica N-methylpyrrolidinium bis(trifluoromethylsulfonyl)imide (NP-IL)

11   **NP-IL**
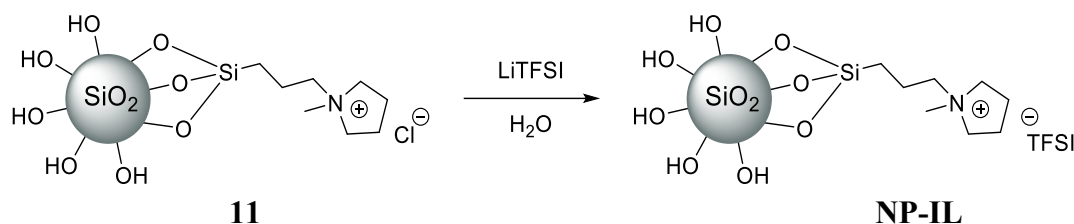
N-methylpyrrolidinium chloride modified nanoparticles (**11**) (4.5 g) were dissolved in 120 mL deionized water and mixed with 20 mL of a solution containing 4 g (14 mmol) LiTFSI. The mixture was kept for stirring for 8 hours at room temperature, after which the final product was collected *via* centrifugation and washed with deionized water (4 times). NPs were dried under vacuum at 70 °C for 24 hours.

8.4.4 Surface modification of Nanopowder (NP-alk)

NP-alk
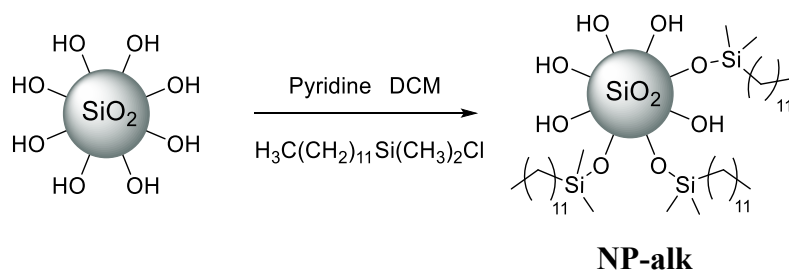
The synthesis was adapted from the literature.[384,385] 1 g of dried (170 °C for 72 hours) Nanopowder was dispersed in 50 mL of dry DCM. Chloro(dodecyl)dimethylsilane (3.0 mL, 10 mmol) and pyridine (0.9 mL, 10 mmol) were added to the suspension and stirred for 8 hours at room temperature. Surface modified nanoparticles were collected using centrifugation, re-dispersed in cold dry DCM and collected again. This washing procedure was repeated three times and the product (**NP-alk**) was dried in high vacuum at 50 °C for 24 hours.

8.5 Preparation of silica NP/PEG composites

8.5.1 Synthesis of 2-(6-isocyanato-hexylamino)-6-methyl-4[1H]-pyrimidone (UPy isocyanate) (12)

12
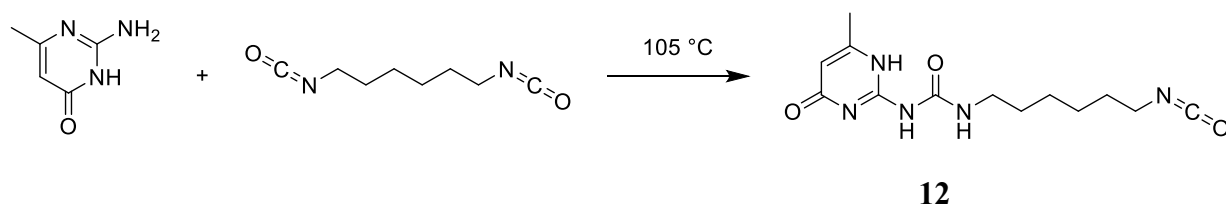
The synthesis was adapted from the literature.[386] 6-Methylisocytoside (3 g, 24 mmol) and hexamethylene diisocyanate (30 mL, 187 mmol) were mixed in the flask under inert atmosphere. The reaction mixture was stirred at 105 °C for 16 hours. After cooling down the mixture the product was precipitated in n-hexane and washed 4 times (by n-hexane). The final product was dried in vacuum. Yield 94 %.

^{1}H NMR (CDCl$_3$, 400 MHz, δ in ppm): 13.10 (s, 1H), 11.85 (s, 1H), 10.17 (t, J = 5.4 Hz, 1H), 5.81 (t, J = 1.3 Hz, 1H), 3.33 – 3.20 (m, 4H), 2.22 (d, J = 1.0 Hz, 3H), 1.67 – 1.55 (m, 5H), 1.40 (m, 4H).

^{13}C NMR (CDCl$_3$, 101 MHz, δ in ppm): 173.03, 156.59, 154.70, 148.24, 106.67, 42.87, 39.77, 31.18, 29.28, 26.21, 26.15, 18.91.

8.5.2 Synthesis of PEG 1500 dimesylate (13)

13
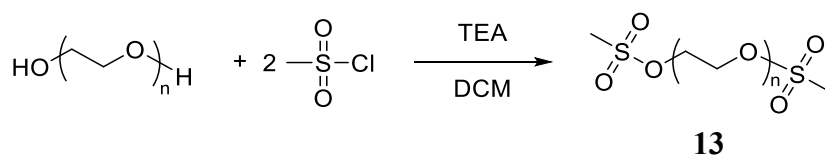
The synthesis was adapted from the literature.[387] PEG 1500 was dried in high vacuum at 60 °C for 8 hours prior the use. PEG 1500 (15 g, 10 mmol) was dissolved in 200 mL dry DCM and

triethylamine (14.5 mL, 100 mmol) was added. Methylsulfonyl chloride (7.7 mL, 100 mmol) was added dropwise to the mixture at 0 °C. The reaction mixture was stirred for 16 hours followed by filtration. Filtrate was washed with water (2 × 40 mL) and with brine (40 mL). Organic phase was dried using Na_2SO_4, concentrated and precipitated in cold diethyl ether. The product was collected and dried under vacuum at 50 °C. Yield 75%.

^{1}H NMR (CDCl$_3$, 400 MHz, δ in ppm): 4.39 – 4.34 (m, 4H), 3.77 – 3.73 (m, 4H), 3.68 – 3.57 (m, 128H), 3.06 (s, 6H).

^{13}C NMR (CDCl$_3$, 101 MHz, δ in ppm): 70.55, 69.27, 69.00, 37.72.

8.5.3 Synthesis of PEG 1500 diazide (14)

13   **14**
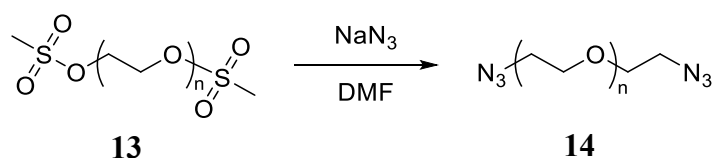
The synthesis was adapted from the literature.[267] PEG 1500 dimesylate (**13**) (12 g, 7.3 mmol) was dissolved in 100 mL dry DMF and sodium azide (5.2 g, 80 mmol) was added to the solution. The reaction mixture was stirred at room temperature for 2 hours and at 50 °C for 24 hours under inert atmosphere. After filtration DMF was removed using a rotary. Crude polymer was dissolved in deionized water (150 mL) and the product was extracted with DCM (4 × 20 mL). Organic phase was dried using MgSO$_4$ and after filtration, the solvent was removed under reduced pressure. PEG 1500 diazide was dried under vacuum for 24 hours. Yield 92%.

^{1}H NMR (CDCl$_3$, 500 MHz, δ in ppm): 3.69 – 3.58 (m, 132H), 3.36 (t, J = 5.1 Hz, 4H).

8.5.4 Synthesis of PEG 1500 diamine (15)

14   **15**
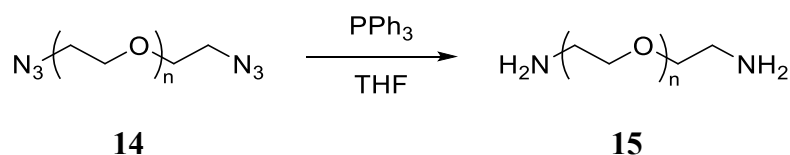
The synthesis was adapted from the literature.[388] PEG 1500 diazide (**14**) (4 g, 2.7 mmol) and triphenylphosphine (4.2 g, 16 mmol) were dissolved in 40 mL THF. The solution was stirred for 1 hour at RT, followed with the addition of 1 mL water. The reaction mixture stirred for 24 hours. The solvent was removed under reduced pressure and 40 mL water was added to the mixture and stirred for an additional 30 min. Opaque mixture was filtered and the filtrate was

concentrated using a rotary. Transparent, slightly yellowish residue was dissolved in 5 mL DCM and precipitated in cold diethyl ether. The precipitate was collected using filtration and dried in vacuum. Yield 85%.

^{1}H NMR (CDCl$_3$, 400 MHz, δ in ppm): 3.67 – 3.57 (m, 134H), 3.50 (t, J = 5.2 Hz, 4H), 2.85 (t, J = 5.2 Hz, 4H).

8.5.5 Synthesis of PEG 1500 UPy (**PEG-UPy**)
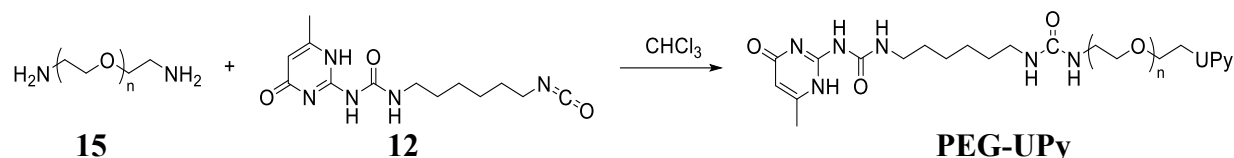
The synthesis was adapted from the literature.[355] PEG 1500 diamine (**15**) (3 g, 2 mmol) and UPy isocyanate (**12**) (1.5 g, 5.1 mmol) were pre-dried in high vacuum for 4 hours and subsequently dissolved in dry chloroform (200 mL). The reaction mixture was refluxed for 48 hours under inert atmosphere. Followed with the addition of $0.5 - 1$ g silica gel and $4 - 5$ drops of dibutyl tin dilaurate. After refluxing for an additional three hours the reaction mixture was filtered and the filtrate was concentrated under reduced pressure. Polymer solution was precipitated in cold diethyl ether. The final product was collected using filtration and dried in vacuum at 40 °C for 24 hours. Yield 90%.

^{1}H NMR (CDCl$_3$, 400 MHz, δ in ppm): 13.11 (s, 2H), 11.83 (s, 2H), 10.09 (s, 2H), 5.81 (s, 2H), 5.12 (d, J = 32.5 Hz, 4H), 3.62 (d, J = 3.1 Hz, 131H), 3.53 (t, J = 5.0 Hz, 4H), 3.39 – 3.06 (m, 14H), 2.21 (s, 7H), 1.64 – 1.28 (m, 20H).

8.5.6 Synthesis of PEG 8000 barbiturate (**PEG 8000 B$_2$**)
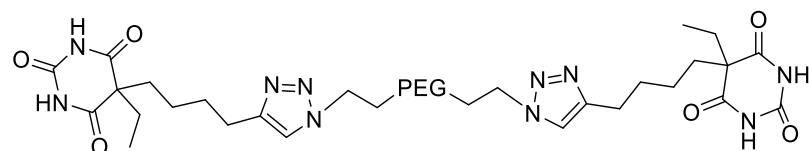
PEG 8000 B$_2$ was previously prepared according to the reported literature.[267]

8.5.7 Preparation of silica NP/PEG composites

Appropriate amounts of polymer, LiTFSI and nanoparticles were mixed in $1 - 2$ mL dry acetonitrile. Solvent was removed in the oven at 80 °C overnight and samples were dried at 80 °C under vacuum for 48 hours. NP-OH was obtained by drying LUDOX® SM on freeze

dryer followed by keeping particles over P$_2$O$_5$ in vacuum. Nanocomposite compositions are given in the table below.

Sample	Polymer-type	Polymer (mg)	LiTFSI (mg)	LiTFSI (mmol)	EO/ LiTFSI	NPs-type	NPs (mg)	NPs (wt%)
PEG-1	PEG 1500 UPY	100	130.1	453	5	-		
PEG-2	PEG 1500 UPY	100	130.1	453	5	NP-IL	12.1	5
PEG-3	PEG 1500 UPY	100	130.1	453	5	NP-IL	25.6	10
PEG-4	PEG 1500 UPY	100	130.1	453	5	NP-IL	40.6	15
PEG-5	PEG 1500 UPY	100	130.1	453	5	NP-OH	12.1	5
PEG-6	PEG 1500 UPY	100	130.1	453	5	NP-OH	25.6	10
PEG-7	PEG 1500 UPY	100	130.1	453	5	NP-OH	40.6	15
PEG-8	PEG 8000 B$_2$	100	121.5	423	5	-		
PEG-9	PEG 8000 B$_2$	100	60.8	212	10	-		
PEG-10	PEG 8000 B$_2$	100	30.4	106	20	-		
PEG-11	PEG 8000 B$_2$	100	121.5	423	5	NP-alk	39.1	5
PEG-12	PEG 8000 B$_2$	100	121.5	423	5	NP-alk	24.6	10
PEG-13	PEG 8000 B$_2$	100	121.5	423	5	NP-alk	11.7	15
PEG-14	PEG 8000 B$_2$	100	121.5	423	5	NP-IL	24.6	10
PEG-15	PEG 8000 B$_2$	100	121.5	423	-	NP-OH	39.1	5
PEG-16	PEG 8000 B$_2$	100	121.5	423	-	NP-OH	24.6	10
PEG-17	PEG 8000 B$_2$	100	121.5	423	-	NP-OH	11.7	15
PEG-18	PEG 8000 B$_2$	100	121.5	423	-	NP-alk	39.1	5
PEG-19	PEG 8000 B$_2$	100	121.5	423	-	NP-alk	24.6	10
PEG-20	PEG 8000 B$_2$	100	121.5	423	-	NP-alk	11.7	15

8.6 Synthesis of fluorinated block copolymers

8.6.1 Synthesis of S,S-dibenzyl trithiocarbonate (DBTTC, 16)

16
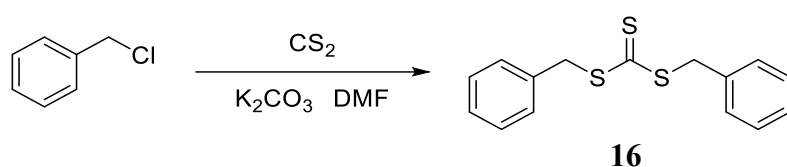
The synthesis was adapted from the literature.[389] Carbon disulfide (0.80 g, 10.5 mmol) and benzyl chloride (1.26 g, 10 mmol) were dissolved in DMF (10 mL) in a one neck flask equipped with the magnetic sitting bar. To the resulting mixture potassium carbonate (1.4 g, 10 mmol)

was added. The reaction mixture was heated to 40 °C and kept for stirring for 16 hours. The reaction was quenched by pouring mixture into ice water. The product was extracted using ethyl acetate. The organic phase was dried over anhydrous Na_2SO_4, filtrated and the solvent was removed under vacuum. The product was purified using column chromatography in hexane to yield a yellow crystal ($R_f = 0.2$). Yield 85 %.

^{1}H-NMR (CDCl$_3$, 400 MHz, δ in ppm): 7.38 – 7.27 (m, 10H), 4.63 (s, 4H).

^{13}C NMR (CDCl$_3$, 100 MHz, δ in ppm): 222.73, 134.95, 129.27, 128.73, 127.80, 41.57.

8.6.2   Synthesis of PIL homopolymer (PIL-H)
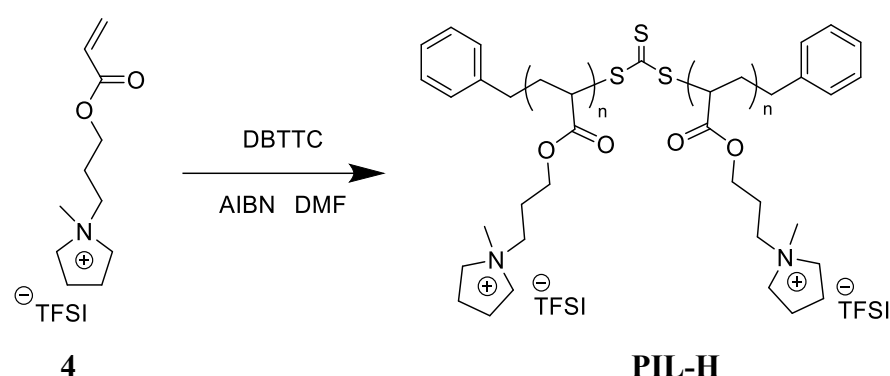
4 g (8.37 mmol) N-[(2-acryloyloxy)propyl]-N-methylpyrrolidinium bis(trifluoro-methylsulfonyl)imide (4), 80 mg (0.28 mmol) DBTTC (16) and 9.2 mg (0.06 mmol) AIBN were dissolved in dry DMF (6 mL) in a Schlenk tube. After freeze thaw cycles (4 x) the reaction mixture was stirred at 70 °C for 16 hours under inert atmosphere. The product was precipitated in DCM and collected by centrifuge. Polymer was redissolved in acetone (5 mL) and precipitated again in DCM. Purification steps were repeated 3 times. The final product (PIL-H) was dried under vacuum at 50 °C. Yield 75%.

8.6.3   Synthesis of fluorinated block (PIL-B) copolymer
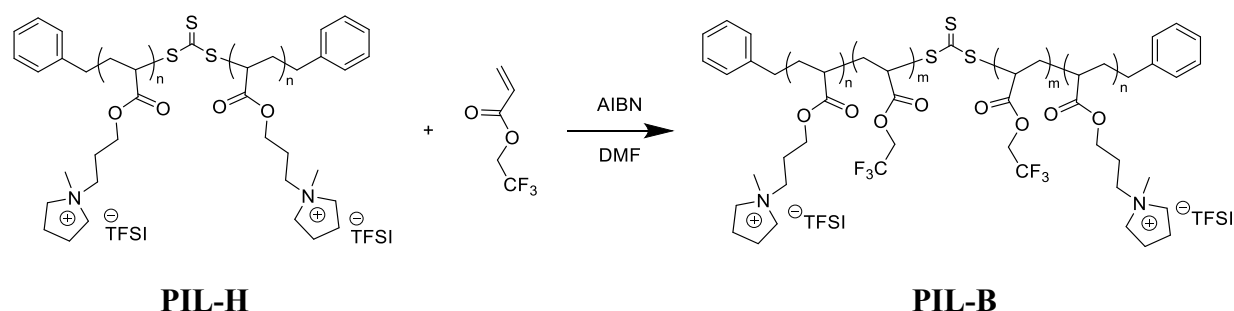
For block copolymer (**PIL-B**) synthesis, 0.8 g (5.2 mmol) 2,2,2-trifluoroethyl acrylate, 1.87 g (0.1 mmol) **PIL-H** and 3.4 mg (0.02 mmol) AIBN were dissolved in dry DMF (4 mL) in a Schlenk tube. After freeze thaw cycles (4 x) the reaction mixture was stirred at 70 °C for 16 hours under inert atmosphere. The product was precipitated in MeOH/ H$_2$O (1/1 volume ratio) and collected by centrifuge. Polymer was redissolved in acetone (5 mL) and precipitated again in MeOH/H$_2$O. Purification steps were repeated 3 times. Final product (**PIL-B**) was dried under vacuum at 50 °C. Yield 70%.

8.6.4 Synthesis of fluorinated statistical (PIL-S) copolymer

4 **PIL-S**
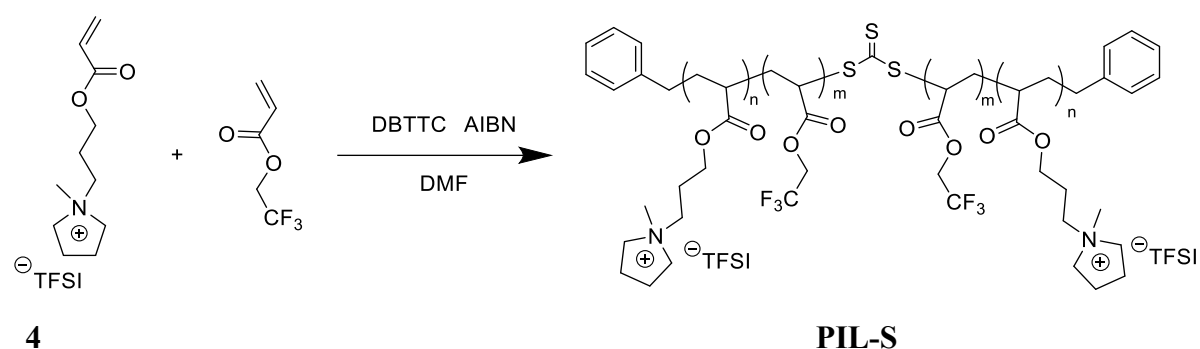
For statistical copolymer (**PIL-S**) synthesis, 0.6 g (3.9 mmol) 2,2,2-trifluoroethyl acrylate, 1.38 g (2.9 mmol) N-[(2-acryloyloxy)propyl]-N-methylpyrrolidinium bis(trifluoro-methylsulfonyl)imide (**4**), 22.5 mg (0.078 mmol) DBTTC (**16**) and 2.6 mg (0.016 mmol) AIBN were dissolved in dry DMF (4 mL) in a Schlenk tube. After freeze thaw cycles (4 x) the reaction mixture was stirred at 70 °C for 16 hours under inert atmosphere. The product was precipitated in MeOH/ H$_2$O (1/1 volume ratio) and collected by centrifuge. Polymer was redissolved in acetone (5 mL) and precipitated again in MeOH/ H$_2$O. Purification steps were repeated 3 times. Final product (**PIL-S**) was dried under vacuum at 50 °C. Yield 65%.
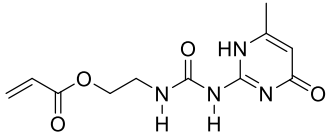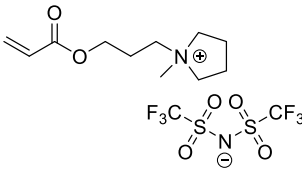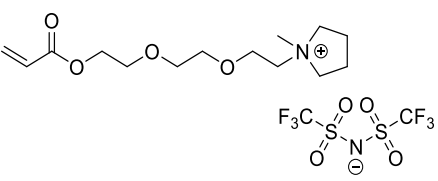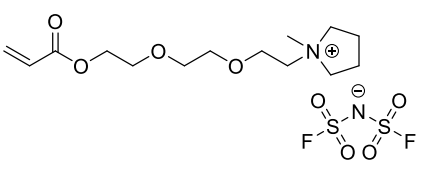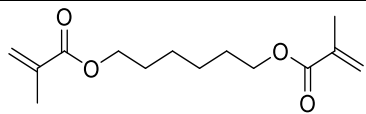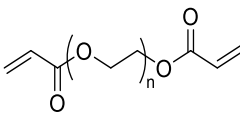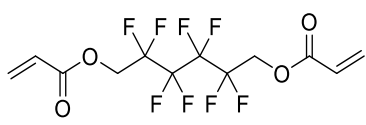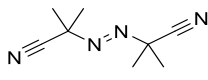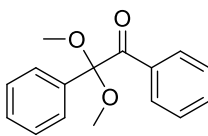
8.7 Synthesis of PIL gels

Poly(ionic liquid) gels were synthesized with the following procedure: dry components were mixed in dry DCM and stirred in a closed vial until a clear solution was formed. Solvent was removed under reduced pressure. The mixture was transpired into glove-box, spread on the glass surface and polymerized at 75 °C for 16 hours (AIBN, thermal initiation) or under UV light (365 nm, 4 watts, distance from the lamp 10-20 mm) for 1 hour (DMPA,

photopolymerization). Formed gels were removed from the glass and cut into round shapes with various diameters. All components and compositions are given below.

PIL gel components

	Compound	structure	Abbreviation
Monomers*	2-(3-(4-Methyl-6-oxo-1,6-dihydropyrimidin-2-yl)ureido)ethyl acrylate		**M-UPy**
	N-[(2-acryloyloxy)propyl]-N-methylpyrrolidinium bis(trifluoro-methylsulfonyl)imide		**M-IL-1**
	N-(2-(2-(2-(acryloyloxy)ethoxy)-ethoxy)ethyl)-N-methylpyrrolidinium bis(trifluoromethylsulfonyl)imide		**M-IL-2**
	N-(2-(2-(2-(acryloyloxy)ethoxy)-ethoxy)ethyl)-N-methylpyrrolidinium bis(fluorosulfonyl)imide		**M-IL-3**
Crosslinkers	1,6-Hexanediol dimethacrylate		**C-1**
	Poly(ethylene glycol) diacrylate (Mn = 700)		**C-2**
	2,2,3,3,4,4,5,5-octafluoro-1,6-hexanediol diacrylate		**C-3**
Initiator	Azobisisobutyronitrile		**AIBN**
	2,2-Dimethoxy-2-phenylacetophenone		**DMPA**

Ionic liquid	1-Methyl-1-propylpyrrolidinium bis(trifluoromehylsulfonyl)imide		**MPPyrTFSI**
	1-Methyl-1-propylpyrrolidinium bis(fluorosulfonyl)imide		**MPPyrFSI**
	1-(2-Methoxyethyl)-1-methylpropylpyrrolidinium bis(trifluoromethylsulfonyl)imide		**MeOEMpyr TFSI**
	Fluorinated IL		**FIL-TFSI**
	Non-Fluorinated IL		**NFIL-TFSI**
Lithium salt	Lithium bis(trifluoromethylsulfonyl)imide		**LiTFSI**
	Lithium bis(fluorosulfonyl)imide		**LiFSI**
Additives	LUDOX® SM silica methylpyrrolidinium chloride bis(trifluoromethylsulfonyl)imide		**NP-IL**
	Nickel-based metal-organic framework		**MOF**

*Monomers were dried over P_2O_5 under high vacuum (< 0.010 mbar) for 36 hours at RT.

Table S 1. Composition of gel electrolyte samples.

Sample	Monomer	Crosslinker	Molar ratio M-IL/M-UPy/C	IL	IL (wt%)	Li salt	Li salt (wt%)	Mode of CL
G-1	M-IL-1	C-1	95:00:05	MPPyrTFSI	30.00	LiTFSI	10.00	T
G-2	M-IL-1	C-1	90:05:05	MPPyrTFSI	30.00	LiTFSI	10.00	T
G-3	M-IL-1	C-1	90:00:10	MPPyrTFSI	36.50	LiTFSI	13.50	T
G-4	M-IL-1	C-1	86:10:05	MPPyrTFSI	37.50	LiTFSI	12.50	T
G-5	M-IL-1	C-1	81:14:05	MPPyrTFSI	30.00	LiTFSI	10.00	T
G-6	M-IL-1	C-1	76:19:05	MPPyrTFSI	37.50	LiTFSI	12.50	T
G-7	M-IL-1	C-1	67:29:05	MPPyrTFSI	37.50	LiTFSI	12.50	T
G-8	M-IL-1	C-1	57:38:05	MPPyrTFSI	50.63	LiTFSI	16.88	T
G-9	M-IL-1	C-1	57:38:05	MPPyrTFSI	52.50	LiTFSI	17.50	T
G-10	M-IL-1	C-1	57:38:05	MPPyrTFSI	48.70	LiTFSI	16.25	T
G-11	M-IL-1	C-1	57:38:05	MPPyrTFSI	48.70	LiTFSI	16.25	T
G-12	M-IL-1	C-1	57:38:05	MPPyrTFSI	48.70	LiTFSI	16.25	UV
G-13	M-IL-1	C-1	57:38:05	MPPyrTFSI	44.85	LiTFSI	20.15	T
G-14	M-IL-1	C-1	57:38:05	MPPyrTFSI	40.00	LiTFSI	25.00	T
G-15	M-IL-1	C-1	57:38:05	MeOEMpyrTFSI	48.70	LiTFSI	16.25	T
G-16	M-IL-1	C-2	57:38:05	MPPyrTFSI	48.70	LiTFSI	16.25	T
G-17	M-IL-1	C-1	54:36:10	MPPyrTFSI	45.00	LiTFSI	15.00	T
G-18	M-IL-1	C-1	52:43:05	MPPyrTFSI	48.70	LiTFSI	17.50	T
G-19	M-IL-1	C-1	57:38:05	MPPyrFSI	48.70	LiTFSI	16.25	T
G-20	M-IL-1	C-1	57:38:05	MPPyrFSI	48.70	LiTFSI	16.25	T
G-21	M-IL-2	C-1	81:14:05	FIL-TFSI	45.00	LiTFSI	15.00	UV
G-22	M-IL-2	C-1	81:14:05	NFIL-TFSI	45.00	LiTFSI	15.00	UV
G-23	M-IL-2	C-1	81:14:05	MPPyrTFSI	45.00	LiTFSI	15.00	UV

G-24	M-IL-2	C-1	57:38:05	MPPyrTFSI	48.70	LiTFSI	16.25	T
G-25	M-IL-2	C-1	57:38:05	MPPyrTFSI	48.70	LiTFSI	16.25	UV
G-26	M-IL-3	C-1	58:37:05	MPPyrFSI	48.70	LiFSI	16.25	T
G-27	M-IL-3	C-3	58:37:05	MPPyrFSI	48.70	LiFSI	16.25	T
G-28	M-IL-3	C-1	58:37:05	MPPyrFSI	48.70	LiTFSI	16.25	T

9 References

1. Kebede, A. A., Kalogiannis, T., Van Mierlo, J. & Berecibar, M. A comprehensive review of stationary energy storage devices for large scale renewable energy sources grid integration. *Renewable and Sustainable Energy Reviews,* **2022**, *159*, 112213. https://doi.org/10.1016/j.rser.2022.112213

2. Wang, W., Yuan, B., Sun, Q. & Wennersten, R. Application of energy storage in integrated energy systems — A solution to fluctuation and uncertainty of renewable energy. *Journal of Energy Storage,* **2022**, *52*, 104812. https://doi.org/10.1016/j.est.2022.104812

3. May, G. J., Davidson, A. & Monahov, B. Lead batteries for utility energy storage: A review. *Journal of Energy Storage,* **2018**, *15*, 145-157. https://doi.org/10.1016/j.est.2017.11.008

4. Liang, Y., Zhao, C.-Z., Yuan, H., Chen, Y., Zhang, W., Huang, J.-Q., Yu, D., Liu, Y., Titirici, M.-M., Chueh, Y.-L., Yu, H. & Zhang, Q. A review of rechargeable batteries for portable electronic devices. *InfoMat,* **2019**, *1*, 6-32. https://doi.org/10.1002/inf2.12000

5. Olabi, A. G., Abbas, Q., Shinde, P. A. & Abdelkareem, M. A. Rechargeable batteries: Technological advancement, challenges, current and emerging applications. *Energy,* **2023**, *266*, 126408. https://doi.org/10.1016/j.energy.2022.126408

6. Park, J. O., Kim, M., Kim, J.-H., Choi, K. H., Lee, H. C., Choi, W., Ma, S. B. & Im, D. A 1000 Wh kg^{-1} Li–Air battery: Cell design and performance. *Journal of Power Sources,* **2019**, *419*, 112-118. https://doi.org/10.1016/j.jpowsour.2019.02.057

7. Evers, S. & Nazar, L. F. New Approaches for High Energy Density Lithium–Sulfur Battery Cathodes. *Accounts of Chemical Research,* **2013**, *46*, 1135-1143. https://doi.org/10.1021/ar3001348

8. Liu, Y.-T., Liu, S., Li, G.-R. & Gao, X.-P. Strategy of Enhancing the Volumetric Energy Density for Lithium–Sulfur Batteries. *Advanced Materials,* **2021**, *33*, 2003955. https://doi.org/10.1002/adma.202003955

9. Cheng, X.-B., Zhang, R., Zhao, C.-Z. & Zhang, Q. Toward Safe Lithium Metal Anode in Rechargeable Batteries: A Review. *Chemical Reviews,* **2017**, *117*, 10403-10473. https://doi.org/10.1021/acs.chemrev.7b00115

10. Placke, T., Kloepsch, R., Dühnen, S. & Winter, M. Lithium ion, lithium metal, and alternative rechargeable battery technologies: the odyssey for high energy density. *Journal of Solid State Electrochemistry,* **2017**, *21*, 1939-1964. https://doi.org/10.1007/s10008-017-3610-7

11. Xu, X., Hui, K. S., Hui, K. N., Shen, J., Zhou, G., Liu, J. & Sun, Y. Engineering strategies for low-cost and high-power density aluminum-ion batteries. *Chemical Engineering Journal,* **2021**, *418*, 129385. https://doi.org/10.1016/j.cej.2021.129385

12. Studer, G., Schmidt, A., Büttner, J., Schmidt, M., Fischer, A., Krossing, I. & Esser, B. On a high-capacity aluminium battery with a two-electron phenothiazine redox polymer as a positive electrode. *Energy & Environmental Science,* **2023**, *16*, 3760-3769. https://doi.org/10.1039/D3EE00235G

13. Das, S. K., Mahapatra, S. & Lahan, H. Aluminium-ion batteries: developments and challenges. *Journal of Materials Chemistry A,* **2017**, *5*, 6347-6367. https://doi.org/10.1039/C7TA00228A

14. Liu, J., Bao, Z., Cui, Y., Dufek, E. J., Goodenough, J. B., Khalifah, P., Li, Q., Liaw, B. Y., Liu, P., Manthiram, A., Meng, Y. S., Subramanian, V. R., Toney, M. F., Viswanathan, V. V., Whittingham, M. S., Xiao, J., Xu, W., Yang, J., Yang, X.-Q. & Zhang, J.-G. Pathways for practical high-energy long-cycling lithium metal batteries. *Nature Energy,* **2019**, *4*, 180-186. https://doi.org/10.1038/s41560-019-0338-x

15. Ma, J., Li, Y., Grundish, N. S., Goodenough, J. B., Chen, Y., Guo, L., Peng, Z., Qi, X., Yang, F., Qie, L., Wang, C.-A., Huang, B., Huang, Z., Chen, L., Su, D., Wang, G., Peng, X., Chen, Z., Yang, J., He, S., Zhang, X., Yu, H., Fu, C., Jiang, M., Deng, W., Sun, C.-F., Pan, Q., Tang, Y., Li, X., Ji, X., Wan, F., Niu, Z., Lian, F., Wang, C., Wallace, G. G., Fan, M., Meng, Q., Xin,

S., Guo, Y.-G. & Wan, L.-J. The 2021 battery technology roadmap. *Journal of Physics D: Applied Physics,* **2021**, *54*, 183001. https://doi.org/10.1088/1361-6463/abd353

16. Lopes, P. P. & Stamenkovic, V. R. Past, present, and future of lead–acid batteries. *Science,* **2020**, *369*, 923-924. https://doi.org/10.1126/science.abd3352

17. Petrovic, S. Battery Technology Crash Course: A Concise Introduction. (*Springer International Publishing*, **2021**), ISBN: 978-3-030-57268-6.

18. Jeyaseelan, C., Jain, A., Khurana, P., Kumar, D. & Thatai, S. Rechargeable Batteries: History, Progress, and Applications. (*Scrivener Publishing LLC*, **2020**), ISBN: 9781119661191.

19. Al-Thyabat, S., Nakamura, T., Shibata, E. & Iizuka, A. Adaptation of minerals processing operations for lithium-ion (LiBs) and nickel metal hydride (NiMH) batteries recycling: Critical review. *Minerals Engineering,* **2013**, *45*, 4-17. https://doi.org/10.1016/j.mineng.2012.12.005

20. Kumar, D., Rajouria, S. K., Kuhar, S. B. & Kanchan, D. K. Progress and prospects of sodium-sulfur batteries: A review. *Solid State Ionics,* **2017**, *312*, 8-16. https://doi.org/10.1016/j.ssi.2017.10.004

21. Wang, Y., Zhou, D., Palomares, V., Shanmukaraj, D., Sun, B., Tang, X., Wang, C., Armand, M., Rojo, T. & Wang, G. Revitalising sodium–sulfur batteries for non-high-temperature operation: a crucial review. *Energy & Environmental Science,* **2020**, *13*, 3848-3879. https://doi.org/10.1039/D0EE02203A

22. Wang, Y.-X., Zhang, B., Lai, W., Xu, Y., Chou, S.-L., Liu, H.-K. & Dou, S.-X. Room-Temperature Sodium-Sulfur Batteries: A Comprehensive Review on Research Progress and Cell Chemistry. *Advanced Energy Materials,* **2017**, *7*, 1602829. https://doi.org/10.1002/aenm.201602829

23. Zhao, M., Li, B.-Q., Zhang, X.-Q., Huang, J.-Q. & Zhang, Q. A Perspective toward Practical Lithium–Sulfur Batteries. *ACS Central Science,* **2020**, *6*, 1095-1104. https://doi.org/10.1021/acscentsci.0c00449

24. Peng, H.-J., Huang, J.-Q., Cheng, X.-B. & Zhang, Q. Review on High-Loading and High-Energy Lithium–Sulfur Batteries. *Advanced Energy Materials,* **2017**, *7*, 1700260. https://doi.org/10.1002/aenm.201700260

25. Usiskin, R., Lu, Y., Popovic, J., Law, M., Balaya, P., Hu, Y.-S. & Maier, J. Fundamentals, status and promise of sodium-based batteries. *Nature Reviews Materials,* **2021**, *6*, 1020-1035. https://doi.org/10.1038/s41578-021-00324-w

26. Shah, R., Mittal, V., Matsil, E. & Rosenkranz, A. Magnesium-ion batteries for electric vehicles: Current trends and future perspectives. *Advances in Mechanical Engineering,* **2021**, *13*, 16878140211003398. https://doi.org/10.1177/16878140211003398

27. Bae, J., Park, H., Guo, X., Zhang, X., Warner, J. H. & Yu, G. High-performance magnesium metal batteries via switching the passivation film into a solid electrolyte interphase. *Energy & Environmental Science,* **2021**, *14*, 4391-4399. https://doi.org/10.1039/D1EE00614B

28. Tao, R., Fu, H., Gao, C., Fan, L., Xie, E., Lyu, W., Zhou, J. & Lu, B. Tailoring Interface to Boost the High-Performance Aqueous Al Ion Batteries. *Advanced Functional Materials,* **2023**, *33*, 2303072. https://doi.org/10.1002/adfm.202303072

29. Lin, M.-C., Gong, M., Lu, B., Wu, Y., Wang, D.-Y., Guan, M., Angell, M., Chen, C., Yang, J., Hwang, B.-J. & Dai, H. An ultrafast rechargeable aluminium-ion battery. *Nature,* **2015**, *520*, 324-328. https://doi.org/10.1038/nature14340

30. Imanishi, N. & Yamamoto, O. Perspectives and challenges of rechargeable lithium–air batteries. *Materials Today Advances,* **2019**, *4*, 100031. https://doi.org/10.1016/j.mtadv.2019.100031

31. Liu, T., Vivek, J. P., Zhao, E. W., Lei, J., Garcia-Araez, N. & Grey, C. P. Current Challenges and Routes Forward for Nonaqueous Lithium–Air Batteries. *Chemical Reviews,* **2020**, *120*, 6558-6625. https://doi.org/10.1021/acs.chemrev.9b00545

32. Matsuda, S., Ono, M., Yamaguchi, S. & Uosaki, K. Criteria for evaluating lithium–air batteries in academia to correctly predict their practical performance in industry. *Materials Horizons,* **2022**, *9*, 856-863. https://doi.org/10.1039/D1MH01546J

33. Bruce, P. G., Freunberger, S. A., Hardwick, L. J. & Tarascon, J.-M. Li–O₂ and Li–S batteries with high energy storage. *Nature Materials,* **2012**, *11*, 19-29. https://doi.org/10.1038/nmat3191

34. Larcher, D. & Tarascon, J. M. Towards greener and more sustainable batteries for electrical energy storage. *Nature Chemistry,* **2015**, *7*, 19-29. https://doi.org/10.1038/nchem.2085

35. dos Reis, G., Strange, C., Yadav, M. & Li, S. Lithium-ion battery data and where to find it. *Energy and AI,* **2021**, *5*, 100081. https://doi.org/10.1016/j.egyai.2021.100081

36. Tarascon, J. M. & Armand, M. Issues and challenges facing rechargeable lithium batteries. *Nature,* **2001**, *414*, 359-367. https://doi.org/10.1038/35104644

37. Goodenough, J. B. & Kim, Y. Challenges for Rechargeable Li Batteries. *Chemistry of Materials,* **2010**, *22*, 587-603. https://doi.org/10.1021/cm901452z

38. Goodenough, J. B. & Park, K.-S. The Li-Ion Rechargeable Battery: A Perspective. *Journal of the American Chemical Society,* **2013**, *135*, 1167-1176. https://doi.org/10.1021/ja3091438

39. Kim, T., Song, W., Son, D.-Y., Ono, L. K. & Qi, Y. Lithium-ion batteries: outlook on present, future, and hybridized technologies. *Journal of Materials Chemistry A,* **2019**, *7*, 2942-2964. https://doi.org/10.1039/C8TA10513H

40. Marinow, A., Katcharava, Z. & Binder, W. H. Self-Healing Polymer Electrolytes for Next-Generation Lithium Batteries. *Polymers,* **2023**, *15*, 1145. https://doi.org/10.3390/polym15051145

41. Chen, S., Gao, Z. & Sun, T. Safety challenges and safety measures of Li-ion batteries. *Energy Science & Engineering,* **2021**, *9*, 1647-1672. https://doi.org/10.1002/ese3.895

42. Nitta, N., Wu, F., Lee, J. T. & Yushin, G. Li-ion battery materials: present and future. *Materials Today,* **2015**, *18*, 252-264. https://doi.org/10.1016/j.mattod.2014.10.040

43. Deng, D. Li-ion batteries: basics, progress, and challenges. *Energy Science & Engineering,* **2015**, *3*, 385-418. https://doi.org/10.1002/ese3.95

44. Casimir, A., Zhang, H., Ogoke, O., Amine, J. C., Lu, J. & Wu, G. Silicon-based anodes for lithium-ion batteries: Effectiveness of materials synthesis and electrode preparation. *Nano Energy,* **2016**, *27*, 359-376. https://doi.org/10.1016/j.nanoen.2016.07.023

45. Feng, K., Li, M., Liu, W., Kashkooli, A. G., Xiao, X., Cai, M. & Chen, Z. Silicon-Based Anodes for Lithium-Ion Batteries: From Fundamentals to Practical Applications. *Small,* **2018**, *14*, 1702737. https://doi.org/10.1002/smll.201702737

46. Jin, Y., Zhu, B., Lu, Z., Liu, N. & Zhu, J. Challenges and Recent Progress in the Development of Si Anodes for Lithium-Ion Battery. *Advanced Energy Materials,* **2017**, *7*, 1700715. https://doi.org/10.1002/aenm.201700715

47. Shao-Horn, Y., Croguennec, L., Delmas, C., Nelson, E. C. & O'Keefe, M. A. Atomic resolution of lithium ions in LiCoO₂. *Nature Materials,* **2003**, *2*, 464-467. https://doi.org/10.1038/nmat922

48. Zhang, T., Li, D., Tao, Z. & Chen, J. Understanding electrode materials of rechargeable lithium batteries via DFT calculations. *Progress in Natural Science: Materials International,* **2013**, *23*, 256-272. https://doi.org/10.1016/j.pnsc.2013.04.005

49. Ling, J., Karuppiah, C., Krishnan, S. G., Reddy, M. V., Misnon, I. I., Ab Rahim, M. H., Yang, C.-C. & Jose, R. Phosphate Polyanion Materials as High-Voltage Lithium-Ion Battery Cathode: A Review. *Energy & Fuels,* **2021**, *35*, 10428-10450. https://doi.org/10.1021/acs.energyfuels.1c01102

50. Manthiram, A. A reflection on lithium-ion battery cathode chemistry. *Nature Communications,* **2020**, *11*, 1550. https://doi.org/10.1038/s41467-020-15355-0

51. Li, M., Lu, J., Chen, Z. & Amine, K. 30 Years of Lithium-Ion Batteries. *Advanced Materials,* **2018**, *30*, 1800561. https://doi.org/10.1002/adma.201800561

52.   Wang, X., Ding, Y.-L., Deng, Y.-P. & Chen, Z. Ni-Rich/Co-Poor Layered Cathode for Automotive Li-Ion Batteries: Promises and Challenges. *Advanced Energy Materials,* **2020**, *10*, 1903864. https://doi.org/10.1002/aenm.201903864

53.   Huang, Y., Dong, Y., Li, S., Lee, J., Wang, C., Zhu, Z., Xue, W., Li, Y. & Li, J. Lithium Manganese Spinel Cathodes for Lithium-Ion Batteries. *Advanced Energy Materials,* **2021**, *11*, 2000997. https://doi.org/10.1002/aenm.202000997

54.   Gong, Z. & Yang, Y. Recent advances in the research of polyanion-type cathode materials for Li-ion batteries. *Energy & Environmental Science,* **2011**, *4*, 3223-3242. https://doi.org/10.1039/C0EE00713G

55.   Eftekhari, A. LiFePO$_4$/C nanocomposites for lithium-ion batteries. *Journal of Power Sources,* **2017**, *343*, 395-411. https://doi.org/10.1016/j.jpowsour.2017.01.080

56.   Jones, C., Gilbert, P. & Stamford, L. Assessing the Climate Change Mitigation Potential of Stationary Energy Storage for Electricity Grid Services. *Environmental Science & Technology,* **2020**, *54*, 67-75. https://doi.org/10.1021/acs.est.9b06231

57.   Xu, K. Electrolytes and interphases in Li-ion batteries and beyond. *Chemical Reviews,* **2014**, *114*, 11503-11618. https://doi.org/10.1021/cr500003w

58.   Li, Q., Chen, J., Fan, L., Kong, X. & Lu, Y. Progress in electrolytes for rechargeable Li-based batteries and beyond. *Green Energy & Environment,* **2016**, *1*, 18-42. https://doi.org/10.1016/j.gee.2016.04.006

59.   Xu, K. Nonaqueous Liquid Electrolytes for Lithium-Based Rechargeable Batteries. *Chemical Reviews,* **2004**, *104*, 4303-4418. https://doi.org/10.1021/cr030203g

60.   Shen, C., Wang, S., Jin, Y. & Han, W.-Q. In Situ AFM Imaging of Solid Electrolyte Interfaces on HOPG with Ethylene Carbonate and Fluoroethylene Carbonate-Based Electrolytes. *ACS Applied Materials & Interfaces,* **2015**, *7*, 25441-25447. https://doi.org/10.1021/acsami.5b08238

61.   Jiang, J. & Dahn, J. R. Effects of solvents and salts on the thermal stability of LiC$_6$. *Electrochimica Acta,* **2004**, *49*, 4599-4604. https://doi.org/10.1016/j.electacta.2004.05.014

62.   Kalhoff, J., Eshetu, G. G., Bresser, D. & Passerini, S. Safer Electrolytes for Lithium-Ion Batteries: State of the Art and Perspectives. *ChemSusChem,* **2015**, *8*, 2154-2175. https://doi.org/10.1002/cssc.201500284

63.   Aravindan, V., Gnanaraj, J., Madhavi, S. & Liu, H.-K. Lithium-Ion Conducting Electrolyte Salts for Lithium Batteries. *Chemistry – A European Journal,* **2011**, *17*, 14326-14346. https://doi.org/10.1002/chem.201101486

64.   Han, J.-G., Kim, K., Lee, Y. & Choi, N.-S. Scavenging Materials to Stabilize LiPF$_6$-Containing Carbonate-Based Electrolytes for Li-Ion Batteries. *Advanced Materials,* **2019**, *31*, 1804822. https://doi.org/10.1002/adma.201804822

65.   Marom, R., Haik, O., Aurbach, D. & Halalay, I. C. Revisiting LiClO$_4$ as an Electrolyte for Rechargeable Lithium-Ion Batteries. *Journal of The Electrochemical Society,* **2010**, *157*, A972. https://doi.org/10.1149/1.3447750

66.   Newman, G. H., Francis, R. W., Gaines, L. H. & Rao, B. M. L. Hazard Investigations of LiClO4 / Dioxolane Electrolyte. *Journal of The Electrochemical Society,* **1980**, *127*, 2025. https://doi.org/10.1149/1.2130056

67.   Zhang, S. S., Xu, K. & Jow, T. R. A new approach toward improved low temperature performance of Li-ion battery. *Electrochemistry Communications,* **2002**, *4*, 928-932. https://doi.org/10.1016/S1388-2481(02)00490-3

68.   Ue, M. & Mori, S. Mobility and Ionic Association of Lithium Salts in a Propylene Carbonate-Ethyl Methyl Carbonate Mixed Solvent. *Journal of The Electrochemical Society,* **1995**, *142*, 2577. https://doi.org/10.1149/1.2050056

69.   Andersson, A. M., Herstedt, M., Bishop, A. G. & Edström, K. The influence of lithium salt on the interfacial reactions controlling the thermal stability of graphite anodes. *Electrochimica Acta,* **2002**, *47*, 1885-1898. https://doi.org/10.1016/S0013-4686(02)00044-0

70. Koch, V. R. Reactions of Tetrahydrofuran and Lithium Hexafluoroarsenate with Lithium. *Journal of The Electrochemical Society,* **1979**, *126*, 181. https://doi.org/10.1149/1.2129002

71. Xu, K., Zhang, S., Jow, T. R., Xu, W. & Angell, C. A. LiBOB as Salt for Lithium-Ion Batteries:A Possible Solution for High Temperature Operation. *Electrochemical and Solid-State Letters,* **2002**, *5*, A26. https://doi.org/10.1149/1.1426042

72. Barthel, J., Buestrich, R., Gores, H. J., Schmidt, M. & Wühr, M. A New Class of Electrochemically and Thermally Stable Lithium Salts for Lithium Battery Electrolytes: IV. Investigations of the Electrochemical Oxidation of Lithium Organoborates. *Journal of The Electrochemical Society,* **1997**, *144*, 3866. https://doi.org/10.1149/1.1838103

73. Han, H.-B., Zhou, S.-S., Zhang, D.-J., Feng, S.-W., Li, L.-F., Liu, K., Feng, W.-F., Nie, J., Li, H., Huang, X.-J., Armand, M. & Zhou, Z.-B. Lithium bis(fluorosulfonyl)imide (LiFSI) as conducting salt for nonaqueous liquid electrolytes for lithium-ion batteries: Physicochemical and electrochemical properties. *Journal of Power Sources,* **2011**, *196*, 3623-3632. https://doi.org/10.1016/j.jpowsour.2010.12.040

74. Logan, E. R., Eldesoky, A., Eastwood, E., Hebecker, H., Aiken, C. P., Metzger, M. & Dahn, J. R. The Use of LiFSI and LiTFSI in LiFePO4/Graphite Pouch Cells to Improve High-Temperature Lifetime. *Journal of The Electrochemical Society,* **2022**, *169*, 040560. https://doi.org/10.1149/1945-7111/ac67f9

75. Zhang, S. S. A review on the separators of liquid electrolyte Li-ion batteries. *Journal of Power Sources,* **2007**, *164*, 351-364. https://doi.org/10.1016/j.jpowsour.2006.10.065

76. Yu, Y., Liu, M., Chen, Z., Zhang, Z., Qiu, T., Hu, Z., Xiang, H., Zhu, L., Xu, G. & Zhu, M. Advances in Nonwoven-Based Separators for Lithium-Ion Batteries. *Advanced Fiber Materials,* **2023**, *5*, 1827-1851. https://doi.org/10.1007/s42765-023-00322-3

77. Costa, C. M., Lee, Y.-H., Kim, J.-H., Lee, S.-Y. & Lanceros-Méndez, S. Recent advances on separator membranes for lithium-ion battery applications: From porous membranes to solid electrolytes. *Energy Storage Materials,* **2019**, *22*, 346-375. https://doi.org/10.1016/j.ensm.2019.07.024

78. Lagadec, M. F., Zahn, R. & Wood, V. Characterization and performance evaluation of lithium-ion battery separators. *Nature Energy,* **2019**, *4*, 16-25. https://doi.org/10.1038/s41560-018-0295-9

79. Zhong, S., Yuan, B., Guang, Z., Chen, D., Li, Q., Dong, L., Ji, Y., Dong, Y., Han, J. & He, W. Recent progress in thin separators for upgraded lithium ion batteries. *Energy Storage Materials,* **2021**, *41*, 805-841. https://doi.org/10.1016/j.ensm.2021.07.028

80. Lee, H., Yanilmaz, M., Toprakci, O., Fu, K. & Zhang, X. A review of recent developments in membrane separators for rechargeable lithium-ion batteries. *Energy & Environmental Science,* **2014**, *7*, 3857-3886. https://doi.org/10.1039/C4EE01432D

81. Liu, K., Liu, Y., Lin, D., Pei, A. & Cui, Y. Materials for lithium-ion battery safety. *Science Advances,* **2018**, *4*, eaas9820. https://doi.org/10.1126/sciadv.aas9820

82. Chen, Y., Kang, Y., Zhao, Y., Wang, L., Liu, J., Li, Y., Liang, Z., He, X., Li, X., Tavajohi, N. & Li, B. A review of lithium-ion battery safety concerns: The issues, strategies, and testing standards. *Journal of Energy Chemistry,* **2021**, *59*, 83-99. https://doi.org/10.1016/j.jechem.2020.10.017

83. Wu, J., Zheng, M., Liu, T., Wang, Y., Liu, Y., Nai, J., Zhang, L., Zhang, S. & Tao, X. Direct recovery: A sustainable recycling technology for spent lithium-ion battery. *Energy Storage Materials,* **2023**, *54*, 120-134. https://doi.org/10.1016/j.ensm.2022.09.029

84. Fan, E., Li, L., Wang, Z., Lin, J., Huang, Y., Yao, Y., Chen, R. & Wu, F. Sustainable Recycling Technology for Li-Ion Batteries and Beyond: Challenges and Future Prospects. *Chemical Reviews,* **2020**, *120*, 7020-7063. https://doi.org/10.1021/acs.chemrev.9b00535

85. Wu, X., Ma, J., Wang, J., Zhang, X., Zhou, G. & Liang, Z. Progress, Key Issues, and Future Prospects for Li-Ion Battery Recycling. *Global Challenges,* **2022**, *6*, 2200067. https://doi.org/10.1002/gch2.202200067

86.   Feng, X., Ouyang, M., Liu, X., Lu, L., Xia, Y. & He, X. Thermal runaway mechanism of lithium ion battery for electric vehicles: A review. *Energy Storage Materials,* **2018**, *10*, 246-267. https://doi.org/10.1016/j.ensm.2017.05.013

87.   Doughty, D. H. & Roth, E. P. A General Discussion of Li Ion Battery Safety. *The Electrochemical Society Interface,* **2012**, *21*, 37. https://doi.org/10.1149/2.F03122if

88.   Song, L., Zheng, Y., Xiao, Z., Wang, C. & Long, T. Review on Thermal Runaway of Lithium-Ion Batteries for Electric Vehicles. *Journal of Electronic Materials,* **2022**, *51*, 30-46. https://doi.org/10.1007/s11664-021-09281-0

89.   Feng, X., Zheng, S., Ren, D., He, X., Wang, L., Cui, H., Liu, X., Jin, C., Zhang, F., Xu, C., Hsu, H., Gao, S., Chen, T., Li, Y., Wang, T., Wang, H., Li, M. & Ouyang, M. Investigating the thermal runaway mechanisms of lithium-ion batteries based on thermal analysis database. *Applied Energy,* **2019**, *246*, 53-64. https://doi.org/10.1016/j.apenergy.2019.04.009

90.   Ren, D., Feng, X., Liu, L., Hsu, H., Lu, L., Wang, L., He, X. & Ouyang, M. Investigating the relationship between internal short circuit and thermal runaway of lithium-ion batteries under thermal abuse condition. *Energy Storage Materials,* **2021**, *34*, 563-573. https://doi.org/10.1016/j.ensm.2020.10.020

91.   Feng, X., Ren, D., He, X. & Ouyang, M. Mitigating Thermal Runaway of Lithium-Ion Batteries. *Joule,* **2020**, *4*, 743-770. https://doi.org/10.1016/j.joule.2020.02.010

92.   Wang, Q., Mao, B., Stoliarov, S. I. & Sun, J. A review of lithium ion battery failure mechanisms and fire prevention strategies. *Progress in Energy and Combustion Science,* **2019**, *73*, 95-131. https://doi.org/10.1016/j.pecs.2019.03.002

93.   Chen, X.-R., Zhao, B.-C., Yan, C. & Zhang, Q. Review on Li Deposition in Working Batteries: From Nucleation to Early Growth. *Advanced Materials,* **2021**, *33*, 2004128. https://doi.org/10.1002/adma.202004128

94.   Akolkar, R. Modeling dendrite growth during lithium electrodeposition at sub-ambient temperature. *Journal of Power Sources,* **2014**, *246*, 84-89. https://doi.org/10.1016/j.jpowsour.2013.07.056

95.   Chu, Z., Feng, X., Ouyang, M., Wang, Z., Lu, L., Li, J. & Han, X. Optimal charge current of lithium ion battery. *Energy Procedia,* **2017**, *142*, 1867-1873. https://doi.org/10.1016/j.egypro.2017.12.577

96.   Guo, Z., Zhu, J., Feng, J. & Du, S. Direct in situ observation and explanation of lithium dendrite of commercial graphite electrodes. *RSC Advances,* **2015**, *5*, 69514-69521. https://doi.org/10.1039/C5RA13289D

97.   Khurana, R., Schaefer, J. L., Archer, L. A. & Coates, G. W. Suppression of Lithium Dendrite Growth Using Cross-Linked Polyethylene/Poly(ethylene oxide) Electrolytes: A New Approach for Practical Lithium-Metal Polymer Batteries. *Journal of the American Chemical Society,* **2014**, *136*, 7395-7402. https://doi.org/10.1021/ja502133j

98.   Zhang, X., Wang, A., Liu, X. & Luo, J. Dendrites in Lithium Metal Anodes: Suppression, Regulation, and Elimination. *Accounts of Chemical Research,* **2019**, *52*, 3223-3232. https://doi.org/10.1021/acs.accounts.9b00437

99.   Zeng, Z., Murugesan, V., Han, K. S., Jiang, X., Cao, Y., Xiao, L., Ai, X., Yang, H., Zhang, J.-G., Sushko, M. L. & Liu, J. Non-flammable electrolytes with high salt-to-solvent ratios for Li-ion and Li-metal batteries. *Nature Energy,* **2018**, *3*, 674-681. https://doi.org/10.1038/s41560-018-0196-y

100.   Gond, R., van Ekeren, W., Mogensen, R., Naylor, A. J. & Younesi, R. Non-flammable liquid electrolytes for safe batteries. *Materials Horizons,* **2021**, *8*, 2913-2928. https://doi.org/10.1039/D1MH00748C

101.   Zhu, B., Wang, X., Yao, P., Li, J. & Zhu, J. Towards high energy density lithium battery anodes: silicon and lithium. *Chemical Science,* **2019**, *10*, 7132-7148. https://doi.org/10.1039/C9SC01201J

102. Fichtner, M., Edström, K., Ayerbe, E., Berecibar, M., Bhowmik, A., Castelli, I. E., Clark, S., Dominko, R., Erakca, M., Franco, A. A., Grimaud, A., Horstmann, B., Latz, A., Lorrmann, H., Meeus, M., Narayan, R., Pammer, F., Ruhland, J., Stein, H., Vegge, T. & Weil, M. Rechargeable Batteries of the Future—The State of the Art from a BATTERY 2030+ Perspective. *Advanced Energy Materials,* **2022**, *12*, 2102904. https://doi.org/10.1002/aenm.202102904

103. Harper, G., Sommerville, R., Kendrick, E., Driscoll, L., Slater, P., Stolkin, R., Walton, A., Christensen, P., Heidrich, O., Lambert, S., Abbott, A., Ryder, K., Gaines, L. & Anderson, P. Recycling lithium-ion batteries from electric vehicles. *Nature,* **2019**, *575*, 75-86. https://doi.org/10.1038/s41586-019-1682-5

104. Jin, S., Mu, D., Lu, Z., Li, R., Liu, Z., Wang, Y., Tian, S. & Dai, C. A comprehensive review on the recycling of spent lithium-ion batteries: Urgent status and technology advances. *Journal of Cleaner Production,* **2022**, *340*, 130535. https://doi.org/10.1016/j.jclepro.2022.130535

105. Li, M., Wang, C., Chen, Z., Xu, K. & Lu, J. New Concepts in Electrolytes. *Chemical Reviews,* **2020**, *120*, 6783-6819. https://doi.org/10.1021/acs.chemrev.9b00531

106. Xu, L., Tang, S., Cheng, Y., Wang, K., Liang, J., Liu, C., Cao, Y.-C., Wei, F. & Mai, L. Interfaces in Solid-State Lithium Batteries. *Joule,* **2018**, *2*, 1991-2015. https://doi.org/10.1016/j.joule.2018.07.009

107. Liu, Q., Jiang, W., Xu, J., Xu, Y., Yang, Z., Yoo, D.-J., Pupek, K. Z., Wang, C., Liu, C., Xu, K. & Zhang, Z. A fluorinated cation introduces new interphasial chemistries to enable high-voltage lithium metal batteries. *Nature Communications,* **2023**, *14*, 3678. https://doi.org/10.1038/s41467-023-38229-7

108. Zhao, Y., Zhou, T., Ashirov, T., Kazzi, M. E., Cancellieri, C., Jeurgens, L. P. H., Choi, J. W. & Coskun, A. Fluorinated ether electrolyte with controlled solvation structure for high voltage lithium metal batteries. *Nature Communications,* **2022**, *13*, 2575. https://doi.org/10.1038/s41467-022-29199-3

109. Lin, Y., Yu, Z., Yu, W., Liao, S.-L., Zhang, E., Guo, X., Huang, Z., Chen, Y., Qin, J., Cui, Y. & Bao, Z. Impact of Fluorination Degree of Ether-Based Electrolyte Solvent on Li-metal Battery Performance. *Journal of Materials Chemistry A,* **2024**, https://doi.org/10.1039/D3TA05535C

110. Fan, X., Chen, L., Ji, X., Deng, T., Hou, S., Chen, J., Zheng, J., Wang, F., Jiang, J., Xu, K. & Wang, C. Highly Fluorinated Interphases Enable High-Voltage Li-Metal Batteries. *Chem,* **2018**, *4*, 174-185. https://doi.org/10.1016/j.chempr.2017.10.017

111. von Aspern, N., Röschenthaler, G.-V., Winter, M. & Cekic-Laskovic, I. Fluorine and Lithium: Ideal Partners for High-Performance Rechargeable Battery Electrolytes. *Angewandte Chemie International Edition,* **2019**, *58*, 15978-16000. https://doi.org/10.1002/anie.201901381

112. Wang, Y., Li, Z., Hou, Y., Hao, Z., Zhang, Q., Ni, Y., Lu, Y., Yan, Z., Zhang, K., Zhao, Q., Li, F. & Chen, J. Emerging electrolytes with fluorinated solvents for rechargeable lithium-based batteries. *Chemical Society Reviews,* **2023**, *52*, 2713-2763. https://doi.org/10.1039/D2CS00873D

113. Bolloli, M., Alloin, F., Kalhoff, J., Bresser, D., Passerini, S., Judeinstein, P., Leprêtre, J.-C. & Sanchez, J.-Y. Effect of carbonates fluorination on the properties of LiTFSI-based electrolytes for Li-ion batteries. *Electrochimica Acta,* **2015**, *161*, 159-170. https://doi.org/10.1016/j.electacta.2015.02.042

114. Young, B. T., Heskett, D. R., Nguyen, C. C., Nie, M., Woicik, J. C. & Lucht, B. L. Hard X-ray Photoelectron Spectroscopy (HAXPES) Investigation of the Silicon Solid Electrolyte Interphase (SEI) in Lithium-Ion Batteries. *ACS Applied Materials & Interfaces,* **2015**, *7*, 20004-20011. https://doi.org/10.1021/acsami.5b04845

115. Sasaki, Y., Shimazaki, G., Nanbu, N., Takehara, M. & Ue, M. Physical and Electrolytic Properties of Partially Fluorinated Organic Solvents and Its Application to Secondary Lithium Batteries: Partially Fluorinated Dialkoxyethanes. *ECS Transactions,* **2009**, *16*, 23. https://doi.org/10.1149/1.3123124

116. Abouimrane, A., Belharouak, I. & Amine, K. Sulfone-based electrolytes for high-voltage Li-ion batteries. *Electrochemistry Communications,* **2009**, *11*, 1073-1076. https://doi.org/10.1016/j.elecom.2009.03.020

117. Deng, K., Zeng, Q., Wang, D., Liu, Z., Wang, G., Qiu, Z., Zhang, Y., Xiao, M. & Meng, Y. Nonflammable organic electrolytes for high-safety lithium-ion batteries. *Energy Storage Materials,* **2020**, *32*, 425-447. https://doi.org/10.1016/j.ensm.2020.07.018

118. Fan, X. & Wang, C. High-voltage liquid electrolytes for Li batteries: progress and perspectives. *Chemical Society Reviews,* **2021**, *50*, 10486-10566. https://doi.org/10.1039/D1CS00450F

119. Du, F., Ye, T., Wu, Y., Guo, G., Xie, Z., Zhang, Y., Xiao, F. & Liu, J. Computational comparison of oxidation stability: Sulfones vs. fluorinated sulfones. *Chemical Physics,* **2021**, *551*, 111328. https://doi.org/10.1016/j.chemphys.2021.111328

120. Feng, J., Ma, P., Yang, H. & Lu, L. Understanding the interactions of phosphonate-based flame-retarding additives with graphitic anode for lithium ion batteries. *Electrochimica Acta,* **2013**, *114*, 688-692. https://doi.org/10.1016/j.electacta.2013.10.104

121. Xu, K., Zhang, S., Allen, J. L. & Jow, T. R. Nonflammable Electrolytes for Li-Ion Batteries Based on a Fluorinated Phosphate. *Journal of The Electrochemical Society,* **2002**, *149*, A1079. https://doi.org/10.1149/1.1490356

122. Amanchukwu, C., Yu, Z., Kong, X., Qin, J., Cui, Y. & Bao, Z. A new class of ionically conducting fluorinated ether electrolytes with high electrochemical stability. *Journal of the American Chemical Society,* **2020**, Ahead of Print. https://doi.org/10.1021/jacs.9b11056

123. Nambu, N., Nachi, T., Takehara, M., Ue, M. & Sasaki, Y. Structural Isomerism Effect on Physical and Electrochemical Properties of Monofluorinated Linear Carbonates. *Electrochemistry,* **2012**, *80*, 771-773. https://doi.org/10.5796/electrochemistry.80.771

124. Flamme, B., Rodriguez Garcia, G., Weil, M., Haddad, M., Phansavath, P., Ratovelomanana-Vidal, V. & Chagnes, A. Guidelines to design organic electrolytes for lithium-ion batteries: environmental impact, physicochemical and electrochemical properties. *Green Chemistry,* **2017**, *19*, 1828-1849. https://doi.org/10.1039/C7GC00252A

125. Xu, K. & Angell, C. A. Sulfone-Based Electrolytes for Lithium-Ion Batteries. *Journal of The Electrochemical Society,* **2002**, *149*, A920. https://doi.org/10.1149/1.1483866

126. Xu, K., Ding, M. S., Zhang, S., Allen, J. L. & Jow, T. R. Evaluation of Fluorinated Alkyl Phosphates as Flame Retardants in Electrolytes for Li-Ion Batteries: I. Physical and Electrochemical Properties. *Journal of The Electrochemical Society,* **2003**, *150*, A161. https://doi.org/10.1149/1.1533040

127. Zhao, Q., Stalin, S., Zhao, C.-Z. & Archer, L. A. Designing solid-state electrolytes for safe, energy-dense batteries. *Nature Reviews Materials,* **2020**, *5*, 229-252. https://doi.org/10.1038/s41578-019-0165-5

128. Fenton, D. E., Parker, J. M. & Wright, P. V. Complexes of alkali metal ions with poly(ethylene oxide). *Polymer,* **1973**, *14*, 589. https://doi.org/10.1016/0032-3861(73)90146-8

129. Xue, Z., He, D. & Xie, X. Poly(ethylene oxide)-based electrolytes for lithium-ion batteries. *Journal of Materials Chemistry A,* **2015**, *3*, 19218-19253. https://doi.org/10.1039/C5TA03471J

130. Manuel Stephan, A. Review on gel polymer electrolytes for lithium batteries. *European Polymer Journal,* **2006**, *42*, 21-42. https://doi.org/10.1016/j.eurpolymj.2005.09.017

131. Gadjourova, Z., Andreev, Y. G., Tunstall, D. P. & Bruce, P. G. Ionic conductivity in crystalline polymer electrolytes. *Nature,* **2001**, *412*, 520-523. https://doi.org/10.1038/35087538

132. Xue, S., Liu, Y., Li, Y., Teeters, D., Crunkleton, D. W. & Wang, S. Diffusion of Lithium Ions in Amorphous and Crystalline Poly(ethylene oxide)$_3$:LiCF$_3$SO$_3$ Polymer Electrolytes. *Electrochimica Acta,* **2017**, *235*, 122-128. https://doi.org/10.1016/j.electacta.2017.03.083

133. Quartarone, E. & Mustarelli, P. Electrolytes for solid-state lithium rechargeable batteries: recent advances and perspectives. *Chemical Society Reviews,* **2011**, *40*, 2525-2540. https://doi.org/10.1039/C0CS00081G

134. Aziz, S. B., Woo, T. J., Kadir, M. F. Z. & Ahmed, H. M. A conceptual review on polymer electrolytes and ion transport models. *Journal of Science: Advanced Materials and Devices,* **2018**, *3*, 1-17. https://doi.org/10.1016/j.jsamd.2018.01.002

135. Diederichsen, K. M., Buss, H. G. & McCloskey, B. D. The Compensation Effect in the Vogel–Tammann–Fulcher (VTF) Equation for Polymer-Based Electrolytes. *Macromolecules,* **2017**, *50*, 3831-3840. https://doi.org/10.1021/acs.macromol.7b00423

136. Othman, L., Chew, K. W. & Osman, Z. Impedance spectroscopy studies of poly (methyl methacrylate)-lithium salts polymer electrolyte systems. *Ionics,* **2007**, *13*, 337-342. https://doi.org/10.1007/s11581-007-0120-0

137. Sashmitha, K. & Rani, M. U. A comprehensive review of polymer electrolyte for lithium-ion battery. *Polymer Bulletin,* **2023**, *80*, 89-135. https://doi.org/10.1007/s00289-021-04008-x

138. Diederichsen, K. M., McShane, E. J. & McCloskey, B. D. Promising Routes to a High Li$^+$ Transference Number Electrolyte for Lithium Ion Batteries. *ACS Energy Letters,* **2017**, *2*, 2563-2575. https://doi.org/10.1021/acsenergylett.7b00792

139. Wu, F., Zhang, K., Liu, Y., Gao, H., Bai, Y., Wang, X. & Wu, C. Polymer electrolytes and interfaces toward solid-state batteries: Recent advances and prospects. *Energy Storage Materials,* **2020**, *33*, 26-54. https://doi.org/10.1016/j.ensm.2020.08.002

140. Wang, H., Sheng, L., Yasin, G., Wang, L., Xu, H. & He, X. Reviewing the current status and development of polymer electrolytes for solid-state lithium batteries. *Energy Storage Materials,* **2020**, *33*, 188-215. https://doi.org/10.1016/j.ensm.2020.08.014

141. Devaux, D., Glé, D., Phan, T. N. T., Gigmes, D., Giroud, E., Deschamps, M., Denoyel, R. & Bouchet, R. Optimization of Block Copolymer Electrolytes for Lithium Metal Batteries. *Chemistry of Materials,* **2015**, *27*, 4682-4692. https://doi.org/10.1021/acs.chemmater.5b01273

142. Jiang, Y., Yan, X., Ma, Z., Mei, P., Xiao, W., You, Q. & Zhang, Y. Development of the PEO Based Solid Polymer Electrolytes for All-Solid State Lithium Ion Batteries. *Polymers,* **2018**, *10*, 1237. https://doi.org/10.3390/polym10111237

143. Guo, B., Fu, Y., Wang, J., Gong, Y., Zhao, Y., Yang, K., Zhou, S., Liu, L., Yang, S., Liu, X. & Pan, F. Strategies and characterization methods for achieving high performance PEO-based solid-state lithium-ion batteries. *Chemical Communications,* **2022**, *58*, 8182-8193. https://doi.org/10.1039/D2CC02306G

144. Tsuchida, E., Ohno, H., Tsunemi, K. & Kobayashi, N. Lithium ionic conduction in poly (methacrylic acid)-poly (ethylene oxide) complex containing lithium perchlorate. *Solid State Ionics,* **1983**, *11*, 227-233. https://doi.org/10.1016/0167-2738(83)90028-0

145. Yu, X.-Y., Xiao, M., Wang, S.-J., Zhao, Q.-Q. & Meng, Y.-Z. Fabrication and characterization of PEO/PPC polymer electrolyte for lithium-ion battery. *Journal of Applied Polymer Science,* **2010**, *115*, 2718-2722. https://doi.org/10.1002/app.29915

146. Wong, D. H. C., Vitale, A., Devaux, D., Taylor, A., Pandya, A. A., Hallinan, D. T., Thelen, J. L., Mecham, S. J., Lux, S. F., Lapides, A. M., Resnick, P. R., Meyer, T. J., Kostecki, R. M., Balsara, N. P. & DeSimone, J. M. Phase Behavior and Electrochemical Characterization of Blends of Perfluoropolyether, Poly(ethylene glycol), and a Lithium Salt. *Chemistry of Materials,* **2015**, *27*, 597-603. https://doi.org/10.1021/cm504228a

147. Song, Z., Chen, F., Martinez-Ibanez, M., Feng, W., Forsyth, M., Zhou, Z., Armand, M. & Zhang, H. A reflection on polymer electrolytes for solid-state lithium metal batteries. *Nature Communications,* **2023**, *14*, 4884. https://doi.org/10.1038/s41467-023-40609-y

148. Wu, Z., Xie, Z., Yoshida, A., Wang, Z., Hao, X., Abudula, A. & Guan, G. Utmost limits of various solid electrolytes in all-solid-state lithium batteries: A critical review. *Renewable and Sustainable Energy Reviews,* **2019**, *109*, 367-385. https://doi.org/10.1016/j.rser.2019.04.035

149. Young, W.-S. & Epps, T. H., III. Ionic Conductivities of Block Copolymer Electrolytes with Various Conducting Pathways: Sample Preparation and Processing Considerations. *Macromolecules,* **2012**, *45*, 4689-4697. https://doi.org/10.1021/ma300362f

150. Aldalur, I., Zhang, H., Piszcz, M., Oteo, U., Rodriguez-Martinez, L. M., Shanmukaraj, D., Rojo, T. & Armand, M. Jeffamine® based polymers as highly conductive polymer electrolytes and cathode binder materials for battery application. *Journal of Power Sources,* **2017**, *347*, 37-46. https://doi.org/10.1016/j.jpowsour.2017.02.047

151. Aldalur, I., Martinez-Ibañez, M., Piszcz, M., Rodriguez-Martinez, L. M., Zhang, H. & Armand, M. Lowering the operational temperature of all-solid-state lithium polymer cell with highly conductive and interfacially robust solid polymer electrolytes. *Journal of Power Sources,* **2018**, *383*, 144-149. https://doi.org/10.1016/j.jpowsour.2018.02.066

152. Wang, Q., Zhang, H., Cui, Z., Zhou, Q., Shangguan, X., Tian, S., Zhou, X. & Cui, G. Siloxane-based polymer electrolytes for solid-state lithium batteries. *Energy Storage Materials,* **2019**, *23*, 466-490. https://doi.org/10.1016/j.ensm.2019.04.016

153. Zhou, D., Shanmukaraj, D., Tkacheva, A., Armand, M. & Wang, G. X. Polymer Electrolytes for Lithium-Based Batteries: Advances and Prospects. *Chem,* **2019**, *5*, 2326-2352. https://doi.org/10.1016/j.chempr.2019.05.009

154. Zhang, Z., Sherlock, D., West, R., West, R., Amine, K. & Lyons, L. J. Cross-Linked Network Polymer Electrolytes Based on a Polysiloxane Backbone with Oligo(oxyethylene) Side Chains: Synthesis and Conductivity. *Macromolecules,* **2003**, *36*, 9176-9180. https://doi.org/10.1021/ma0349276

155. Zhang, Z. C., Jin, J. J., Bautista, F., Lyons, L. J., Shariatzadeh, N., Sherlock, D., Amine, K. & West, R. Ion conductive characteristics of cross-linked network polysiloxane-based solid polymer electrolytes. *Solid State Ionics,* **2004**, *170*, 233-238. https://doi.org/10.1016/j.ssi.2004.04.007

156. Tang, L., Chen, B., Zhang, Z., Ma, C., Chen, J., Huang, Y., Zhang, F., Dong, Q., Xue, G., Chen, D., Hu, C., Li, S., Liu, Z., Shen, Y., Chen, Q. & Chen, L. Polyfluorinated crosslinker-based solid polymer electrolytes for long-cycling 4.5 V lithium metal batteries. *Nature Communications,* **2023**, *14*, 2301. https://doi.org/10.1038/s41467-023-37997-6

157. Subba Reddy, C. V., Wu, G. P., Zhao, C. X., Jin, W., Zhu, Q. Y., Chen, W. & Mho, S.-i. Mesoporous silica (MCM-41) effect on (PEO+LiAsF$_6$) solid polymer electrolyte. *Current Applied Physics,* **2007**, *7*, 655-661. https://doi.org/10.1016/j.cap.2007.03.001

158. Lascaud, S., Perrier, M., Vallee, A., Besner, S., Prud'homme, J. & Armand, M. Phase Diagrams and Conductivity Behavior of Poly(ethylene oxide)-Molten Salt Rubbery Electrolytes. *Macromolecules,* **1994**, *27*, 7469-7477. https://doi.org/10.1021/ma00103a034

159. Ibrahim, S., Yassin, M. M., Ahmad, R. & Johan, M. R. Effects of various LiPF$_6$ salt concentrations on PEO-based solid polymer electrolytes. *Ionics,* **2011**, *17*, 399-405. https://doi.org/10.1007/s11581-011-0524-8

160. Appetecchi, G. B., Zane, D. & Scrosati, B. PEO-Based Electrolyte Membranes Based on LiBC$_4$O$_8$ Salt. *Journal of The Electrochemical Society,* **2004**, *151*, A1369. https://doi.org/10.1149/1.1774488

161. Jacob, M. M. E., Prabaharan, S. R. S. & Radhakrishna, S. Effect of PEO addition on the electrolytic and thermal properties of PVDF-LiClO4 polymer electrolytes. *Solid State Ionics,* **1997**, *104*, 267-276. https://doi.org/10.1016/S0167-2738(97)00422-0

162. Singh, M., Odusanya, O., Wilmes, G. M., Eitouni, H. B., Gomez, E. D., Patel, A. J., Chen, V. L., Park, M. J., Fragouli, P., Iatrou, H., Hadjichristidis, N., Cookson, D. & Balsara, N. P. Effect of Molecular Weight on the Mechanical and Electrical Properties of Block Copolymer Electrolytes. *Macromolecules,* **2007**, *40*, 4578-4585. https://doi.org/10.1021/ma0629541

163. Walkowiak, M., Schroeder, G., Gierczyk, B., Waszak, D. & Osińska, M. New lithium ion conducting polymer electrolytes based on polysiloxane grafted with Si-tripodand centers. *Electrochemistry Communications,* **2007**, *9*, 1558-1562. https://doi.org/10.1016/j.elecom.2007.02.019

164. Tominaga, Y. & Yamazaki, K. Fast Li-ion conduction in poly(ethylene carbonate)-based electrolytes and composites filled with TiO_2 nanoparticles. *Chemical Communications,* **2014**, *50*, 4448-4450. https://doi.org/10.1039/C3CC49588D

165. Chai, J., Liu, Z., Ma, J., Wang, J., Liu, X., Liu, H., Zhang, J., Cui, G. & Chen, L. In Situ Generation of Poly (Vinylene Carbonate) Based Solid Electrolyte with Interfacial Stability for $LiCoO_2$ Lithium Batteries. *Advanced Science,* **2017**, *4*, 1600377. https://doi.org/10.1002/advs.201600377

166. Wilkes, J. S. A short history of ionic liquids—from molten salts to neoteric solvents. *Green Chemistry,* **2002**, *4*, 73-80. https://doi.org/10.1039/B110838G

167. Hallett, J. P. & Welton, T. Room-Temperature Ionic Liquids: Solvents for Synthesis and Catalysis. 2. *Chemical Reviews,* **2011**, *111*, 3508-3576. https://doi.org/10.1021/cr1003248

168. Qian, W., Texter, J. & Yan, F. Frontiers in poly(ionic liquid)s: syntheses and applications. *Chemical Society Reviews,* **2017**, *46*, 1124-1159. https://doi.org/10.1039/C6CS00620E

169. Zhou, T., Gui, C., Sun, L., Hu, Y., Lyu, H., Wang, Z., Song, Z. & Yu, G. Energy Applications of Ionic Liquids: Recent Developments and Future Prospects. *Chemical Reviews,* **2023**, *123*, 12170-12253. https://doi.org/10.1021/acs.chemrev.3c00391

170. MacFarlane, D. R., Tachikawa, N., Forsyth, M., Pringle, J. M., Howlett, P. C., Elliott, G. D., Davis, J. H., Watanabe, M., Simon, P. & Angell, C. A. Energy applications of ionic liquids. *Energy & Environmental Science,* **2014**, *7*, 232-250. https://doi.org/10.1039/C3EE42099J

171. Yang, Q., Zhang, Z., Sun, X.-G., Hu, Y.-S., Xing, H. & Dai, S. Ionic liquids and derived materials for lithium and sodium batteries. *Chemical Society Reviews,* **2018**, *47*, 2020-2064. https://doi.org/10.1039/C7CS00464H

172. Hayes, R., Warr, G. G. & Atkin, R. Structure and Nanostructure in Ionic Liquids. *Chemical Reviews,* **2015**, *115*, 6357-6426. https://doi.org/10.1021/cr500411q

173. Triolo, A., Russina, O., Bleif, H. J. & Di Cola, E. Nanoscale segregation in room temperature ionic liquids. *The Journal of Physical Chemistry B,* **2007**, *111*, 4641-4644. https://doi.org/10.1021/jp067705t

174. Canongia Lopes, J. N. A. & Pádua, A. A. H. Nanostructural Organization in Ionic Liquids. *The Journal of Physical Chemistry B,* **2006**, *110*, 3330-3335. https://doi.org/10.1021/jp056006y

175. Watanabe, M., Thomas, M. L., Zhang, S., Ueno, K., Yasuda, T. & Dokko, K. Application of Ionic Liquids to Energy Storage and Conversion Materials and Devices. *Chemical Reviews,* **2017**, *117*, 7190-7239. https://doi.org/10.1021/acs.chemrev.6b00504

176. Liu, H. & Yu, H. Ionic liquids for electrochemical energy storage devices applications. *Journal of Materials Science & Technology,* **2019**, *35*, 674-686. https://doi.org/10.1016/j.jmst.2018.10.007

177. Liu, K., Wang, Z., Shi, L., Jungsuttiwong, S. & Yuan, S. Ionic liquids for high performance lithium metal batteries. *Journal of Energy Chemistry,* **2021**, *59*, 320-333. https://doi.org/10.1016/j.jechem.2020.11.017

178. Tang, X., Lv, S. Y., Jiang, K., Zhou, G. H. & Liu, X. M. Recent development of ionic liquid-based electrolytes in lithium-ion batteries. *Journal of Power Sources,* **2022**, *542* https://doi.org/10.1016/j.jpowsour.2022.231792

179. Mahmood, H., Moniruzzaman, M., Yusup, S. & Welton, T. Ionic liquids assisted processing of renewable resources for the fabrication of biodegradable composite materials. *Green Chemistry,* **2017**, *19*, 2051-2075. https://doi.org/10.1039/C7GC00318H

180. Zhong, C., Deng, Y., Hu, W., Qiao, J., Zhang, L. & Zhang, J. A review of electrolyte materials and compositions for electrochemical supercapacitors. *Chemical Society Reviews,* **2015**, *44*, 7484-7539. https://doi.org/10.1039/C5CS00303B

181. Kerner, M., Plylahan, N., Scheers, J. & Johansson, P. Ionic liquid based lithium battery electrolytes: fundamental benefits of utilising both TFSI and FSI anions? *Physical Chemistry Chemical Physics,* **2015**, *17*, 19569-19581. https://doi.org/10.1039/C5CP01891A

182. Wang, X., Salari, M., Jiang, D.-e., Chapman Varela, J., Anasori, B., Wesolowski, D. J., Dai, S., Grinstaff, M. W. & Gogotsi, Y. Electrode material–ionic liquid coupling for electrochemical energy storage. *Nature Reviews Materials,* **2020**, *5*, 787-808. https://doi.org/10.1038/s41578-020-0218-9

183. Galiński, M., Lewandowski, A. & Stępniak, I. Ionic liquids as electrolytes. *Electrochimica Acta,* **2006**, *51*, 5567-5580. https://doi.org/10.1016/j.electacta.2006.03.016

184. Lewandowski, A. & Galinski, M. Practical and theoretical limits for electrochemical double-layer capacitors. *Journal of Power Sources,* **2007**, *173*, 822-828. https://doi.org/10.1016/j.jpowsour.2007.05.062

185. Hayyan, M., Mjalli, F. S., Hashim, M. A., AlNashef, I. M. & Mei, T. X. Investigating the electrochemical windows of ionic liquids. *Journal of Industrial and Engineering Chemistry,* **2013**, *19*, 106-112. https://doi.org/10.1016/j.jiec.2012.07.011

186. Wang, Y. L., Li, B., Sarman, S., Mocci, F., Lu, Z. Y., Yuan, J., Laaksonen, A. & Fayer, M. D. Microstructural and Dynamical Heterogeneities in Ionic Liquids. *Chemical Reviews,* **2020**, *120*, 5798-5877. https://doi.org/10.1021/acs.chemrev.9b00693

187. Chen, S., Zhang, S., Liu, X., Wang, J., Wang, J., Dong, K., Sun, J. & Xu, B. Ionic liquid clusters: structure, formation mechanism, and effect on the behavior of ionic liquids. *Physical Chemistry Chemical Physics,* **2014**, *16*, 5893-5906. https://doi.org/10.1039/C3CP53116C

188. Gouverneur, M., Schmidt, F. & Schönhoff, M. Negative effective Li transference numbers in Li salt/ionic liquid mixtures: does Li drift in the "Wrong" direction? *Physical Chemistry Chemical Physics,* **2018**, *20*, 7470-7478. https://doi.org/10.1039/C7CP08580J

189. Niu, H., Wang, L., Guan, P., Zhang, N., Yan, C., Ding, M., Guo, X., Huang, T. & Hu, X. Recent Advances in Application of Ionic Liquids in Electrolyte of Lithium Ion Batteries. *Journal of Energy Storage,* **2021**, *40* https://doi.org/10.1016/j.est.2021.102659

190. Anderson, J. L., Ding, R., Ellern, A. & Armstrong, D. W. Structure and Properties of High Stability Geminal Dicationic Ionic Liquids. *Journal of the American Chemical Society,* **2005**, *127*, 593-604. https://doi.org/10.1021/ja046521u

191. Vélez, J. F., Vazquez-Santos, M. B., Amarilla, J. M., Tartaj, P., Herradón, B., Mann, E., del Río, C. & Morales, E. Asymmetrical imidazolium-trialkylammonium room temperature dicationic ionic liquid electrolytes for Li-ion batteries. *Electrochimica Acta,* **2018**, *280*, 171-180. https://doi.org/10.1016/j.electacta.2018.05.103

192. Yuan, J. Y., Mecerreyes, D. & Antonietti, M. Poly(ionic liquid)s: An update. *Progress in Polymer Science,* **2013**, *38*, 1009-1036. https://doi.org/10.1016/j.progpolymsci.2013.04.002

193. Nulwala, H., Mirjafari, A. & Zhou, X. Ionic liquids and poly(ionic liquid)s for 3D printing – A focused mini-review. *European Polymer Journal,* **2018**, *108*, 390-398. https://doi.org/10.1016/j.eurpolymj.2018.09.023

194. Chen, H., Choi, J.-H., Salas-de la Cruz, D., Winey, K. I. & Elabd, Y. A. Polymerized Ionic Liquids: The Effect of Random Copolymer Composition on Ion Conduction. *Macromolecules,* **2009**, *42*, 4809-4816. https://doi.org/10.1021/ma900713e

195. Choi, J.-H., Ye, Y., Elabd, Y. A. & Winey, K. I. Network Structure and Strong Microphase Separation for High Ion Conductivity in Polymerized Ionic Liquid Block Copolymers. *Macromolecules,* **2013**, *46*, 5290–5300. https://doi.org/10.1021/ma400562a

196. Sharick, S., Koski, J., Riggleman, R. A. & Winey, K. I. Isolating the Effect of Molecular Weight on Ion Transport of Non-Ionic Diblock Copolymer/Ionic Liquid Mixtures. *Macromolecules,* **2016**, *49*, 2245-2256. https://doi.org/10.1021/acs.macromol.5b02445

197. Ye, Y., Choi, J.-H., Winey, K. I. & Elabd, Y. A. Polymerized Ionic Liquid Block and Random Copolymers: Effect of Weak Microphase Separation on Ion Transport. *Macromolecules,* **2012**, *45*, 7027-7035. https://doi.org/10.1021/ma301036b

198. Ferreira, M. L., Pastoriza-Gallego, M. J., Araújo, J. M. M., Canongia Lopes, J. N., Rebelo, L. P. N., M. Piñeiro, M., Shimizu, K. & Pereiro, A. B. Influence of Nanosegregation on the Phase

Behavior of Fluorinated Ionic Liquids. *The Journal of Physical Chemistry C,* **2017**, *121*, 5415-5427. https://doi.org/10.1021/acs.jpcc.7b00516

199. Ichikawa, T., Yoshio, M., Hamasaki, A., Kagimoto, J., Ohno, H. & Kato, T. 3D Interconnected Ionic Nano-Channels Formed in Polymer Films: Self-Organization and Polymerization of Thermotropic Bicontinuous Cubic Liquid Crystals. *Journal of the American Chemical Society,* **2011**, *133*, 2163-2169. https://doi.org/10.1021/ja106707z

200. Carrasco, P. M., Ruiz de Luzuriaga, A., Constantinou, M., Georgopanos, P., Rangou, S., Avgeropoulos, A., Zafeiropoulos, N. E., Grande, H.-J., Cabañero, G., Mecerreyes, D. & Garcia, I. Influence of Anion Exchange in Self-Assembling of Polymeric Ionic Liquid Block Copolymers. *Macromolecules,* **2011**, *44*, 4936-4941. https://doi.org/10.1021/ma200213s

201. Mecerreyes, D. Polymeric ionic liquids: Broadening the properties and applications of polyelectrolytes. *Progress in Polymer Science,* **2011**, *36*, 1629-1648. https://doi.org/10.1016/j.progpolymsci.2011.05.007

202. Nirmale, T. C., Khupse, N. D., Kalubarme, R. S., Kulkarni, M. V., Varma, A. J. & Kale, B. B. Imidazolium-Based Dicationic Ionic Liquid Electrolyte: Strategy toward Safer Lithium-Ion Batteries. *ACS Sustainable Chemistry & Engineering,* **2022**, *10*, 8297-8304. https://doi.org/10.1021/acssuschemeng.2c00767

203. Vélez, J. F., Vázquez-Santos, M. B., Amarilla, J. M., Herradón, B., Mann, E., del Río, C. & Morales, E. Geminal pyrrolidinium and piperidinium dicationic ionic liquid electrolytes. Synthesis, characterization and cell performance in $LiMn_2O_4$ rechargeable lithium cells. *Journal of Power Sources,* **2019**, *439*, 227098. https://doi.org/10.1016/j.jpowsour.2019.227098

204. Zhang, H., Feng, W., Zhou, Z. & Nie, J. Composite electrolytes of lithium salt/polymeric ionic liquid with bis(fluorosulfonyl)imide. *Solid State Ionics,* **2014**, *256*, 61-67. https://doi.org/10.1016/j.ssi.2014.01.003

205. Ohno, H. & Ito, K. Room-Temperature Molten Salt Polymers as a Matrix for Fast Ion Conduction. *Chemistry Letters,* **1998**, *27*, 751-752. https://doi.org/10.1246/cl.1998.751

206. Zhang, H., Li, L., Feng, W., Zhou, Z. & Nie, J. Polymeric ionic liquids based on ether functionalized ammoniums and perfluorinated sulfonimides. *Polymer,* **2014**, *55*, 3339-3348. https://doi.org/10.1016/j.polymer.2014.03.041

207. Ogihara, W., Washiro, S., Nakajima, H. & Ohno, H. Effect of cation structure on the electrochemical and thermal properties of ion conductive polymers obtained from polymerizable ionic liquids. *Electrochimica Acta,* **2006**, *51*, 2614-2619. https://doi.org/10.1016/j.electacta.2005.07.043

208. Shaplov, A. S., Vlasov, P. S., Armand, M., Lozinskaya, E. I., Ponkratov, D. O., Malyshkina, I. A., Vidal, F., Okatova, O. V., Pavlov, G. M., Wandrey, C., Godovikov, I. A. & Vygodskii, Y. S. Design and synthesis of new anionic "polymeric ionic liquids" with high charge delocalization. *Polymer Chemistry,* **2011**, *2*, 2609-2618. https://doi.org/10.1039/C1PY00282A

209. Jones, S. D., Nguyen, H., Richardson, P. M., Chen, Y.-Q., Wyckoff, K. E., Hawker, C. J., Clément, R. J., Fredrickson, G. H. & Segalman, R. A. Design of Polymeric Zwitterionic Solid Electrolytes with Superionic Lithium Transport. *ACS Central Science,* **2022**, *8*, 169-175. https://doi.org/10.1021/acscentsci.1c01260

210. Huang, Z., Choudhury, S., Gong, H., Cui, Y. & Bao, Z. A Cation-Tethered Flowable Polymeric Interface for Enabling Stable Deposition of Metallic Lithium. *Journal of the American Chemical Society,* **2020**, *142*, 21393-21403. https://doi.org/10.1021/jacs.0c09649

211. Almdal, K., Dyre, J., Hvidt, S. & Kramer, O. Towards a phenomenological definition of the term 'gel'. *Polymer Gels and Networks,* **1993**, *1*, 5-17. https://doi.org/10.1016/0966-7822(93)90020-I

212. Zhu, M., Wu, J., Wang, Y., Song, M., Long, L., Siyal, S. H., Yang, X. & Sui, G. Recent advances in gel polymer electrolyte for high-performance lithium batteries. *Journal of Energy Chemistry,* **2019**, *37*, 126-142. https://doi.org/10.1016/j.jechem.2018.12.013

213. Hu, Z., Li, G., Wang, A., Luo, J. & Liu, X. Recent Progress of Electrolyte Design for Lithium Metal Batteries. *Batteries & Supercaps,* **2020**, *3*, 331-335. https://doi.org/10.1002/batt.201900191

214. Ren, W., Ding, C., Fu, X. & Huang, Y. Advanced gel polymer electrolytes for safe and durable lithium metal batteries: Challenges, strategies, and perspectives. *Energy Storage Materials,* **2021**, *34*, 515-535. https://doi.org/10.1016/j.ensm.2020.10.018

215. Arya, A. & Sharma, A. L. Polymer electrolytes for lithium ion batteries: a critical study. *Ionics,* **2017**, *23*, 497-540. https://doi.org/10.1007/s11581-016-1908-6

216. Marcinek, M., Syzdek, J., Marczewski, M., Piszcz, M., Niedzicki, L., Kalita, M., Plewa-Marczewska, A., Bitner, A., Wieczorek, P., Trzeciak, T., Kasprzyk, M., P.Łężak, Zukowska, Z., Zalewska, A. & Wieczorek, W. Electrolytes for Li-ion transport – Review. *Solid State Ionics,* **2015**, *276*, 107-126. https://doi.org/10.1016/j.ssi.2015.02.006

217. Patel, M., Gnanavel, M. & Bhattacharyya, A. J. Utilizing an ionic liquid for synthesizing a soft matter polymer "gel" electrolyte for high rate capability lithium-ion batteries. *Journal of Materials Chemistry,* **2011**, *21*, 17419-17424. https://doi.org/10.1039/C1JM12269J

218. Abitelli, E., Ferrari, S., Quartarone, E., Mustarelli, P., Magistris, A., Fagnoni, M., Albini, A. & Gerbaldi, C. Polyethylene oxide electrolyte membranes with pyrrolidinium-based ionic liquids. *Electrochimica Acta,* **2010**, *55*, 5478-5484. https://doi.org/10.1016/j.electacta.2010.04.099

219. Tripathi, A. K. Ionic liquid–based solid electrolytes (ionogels) for application in rechargeable lithium battery. *Materials Today Energy,* **2021**, *20*, 100643. https://doi.org/10.1016/j.mtener.2021.100643

220. Baskoro, F., Wong, H. Q. & Yen, H.-J. Strategic Structural Design of a Gel Polymer Electrolyte toward a High Efficiency Lithium-Ion Battery. *ACS Applied Energy Materials,* **2019**, *2*, 3937-3971. https://doi.org/10.1021/acsaem.9b00295

221. Li, L., Wang, J., Yang, P., Guo, S., Wang, H., Yang, X., Ma, X., Yang, S. & Wu, B. Preparation and characterization of gel polymer electrolytes containing N-butyl-N-methylpyrrolidinium bis(trifluoromethanesulfonyl) imide ionic liquid for lithium ion batteries. *Electrochimica Acta,* **2013**, *88*, 147-156. https://doi.org/10.1016/j.electacta.2012.10.018

222. Li, Q. & Ardebili, H. Flexible thin-film battery based on solid-like ionic liquid-polymer electrolyte. *Journal of Power Sources,* **2016**, *303*, 17-21. https://doi.org/10.1016/j.jpowsour.2015.10.099

223. Shalu, Singh, V. K. & Singh, R. K. Development of ion conducting polymer gel electrolyte membranes based on polymer PVdF-HFP, BMIMTFSI ionic liquid and the Li-salt with improved electrical, thermal and structural properties. *Journal of Materials Chemistry C,* **2015**, *3*, 7305-7318. https://doi.org/10.1039/C5TC00940E

224. Sirisopanaporn, C., Fernicola, A. & Scrosati, B. New, ionic liquid-based membranes for lithium battery application. *Journal of Power Sources,* **2009**, *186*, 490-495. https://doi.org/10.1016/j.jpowsour.2008.10.036

225. Ye, H., Huang, J., Xu, J. J., Khalfan, A. & Greenbaum, S. G. Li Ion Conducting Polymer Gel Electrolytes Based on Ionic Liquid/PVDF-HFP Blends. *Journal of The Electrochemical Society,* **2007**, *154*, A1048. https://doi.org/10.1149/1.2779962

226. Fasciani, C., Panero, S., Hassoun, J. & Scrosati, B. Novel configuration of poly(vinylidenedifluoride)-based gel polymer electrolyte for application in lithium-ion batteries. *Journal of Power Sources,* **2015**, *294*, 180-186. https://doi.org/10.1016/j.jpowsour.2015.06.068

227. Wang, Z., Zhang, J., Liu, J., Hao, S., Song, H. & Zhang, J. 3D Printable, Highly Stretchable, Superior Stable Ionogels Based on Poly(ionic liquid) with Hyperbranched Polymers as Macro-cross-linkers for High-Performance Strain Sensors. *ACS Applied Materials & Interfaces,* **2021**, *13*, 5614-5624. https://doi.org/10.1021/acsami.0c21121

228. D'Angelo, A. J. & Panzer, M. J. Design of Stretchable and Self-Healing Gel Electrolytes via Fully Zwitterionic Polymer Networks in Solvate Ionic Liquids for Li-Based Batteries. *Chemistry of Materials,* **2019**, *31*, 2913-2922. https://doi.org/10.1021/acs.chemmater.9b00172

229. Zhou, T., Zhao, Y., Choi, J. W. & Coskun, A. Ionic Liquid Functionalized Gel Polymer Electrolytes for Stable Lithium Metal Batteries. *Angewandte Chemie International Edition,* **2021**, *60*, 22791-22796. https://doi.org/10.1002/anie.202106237

230. Appetecchi, G. B., Kim, G. T., Montanino, M., Carewska, M., Marcilla, R., Mecerreyes, D. & De Meatza, I. Ternary polymer electrolytes containing pyrrolidinium-based polymeric ionic liquids for lithium batteries. *Journal of Power Sources,* **2010**, *195*, 3668-3675. https://doi.org/10.1016/j.jpowsour.2009.11.146

231. Manthiram, A., Yu, X. & Wang, S. Lithium battery chemistries enabled by solid-state electrolytes. *Nature Reviews Materials,* **2017**, *2*, 16103. https://doi.org/10.1038/natrevmats.2016.103

232. Schnell, J., Günther, T., Knoche, T., Vieider, C., Köhler, L., Just, A., Keller, M., Passerini, S. & Reinhart, G. All-solid-state lithium-ion and lithium metal batteries – paving the way to large-scale production. *Journal of Power Sources,* **2018**, *382*, 160-175. https://doi.org/10.1016/j.jpowsour.2018.02.062

233. Zhang, L., Liu, Y., You, Y., Vinu, A. & Mai, L. NASICONs-type solid-state electrolytes: The history, physicochemical properties, and challenges. *Interdisciplinary Materials,* **2023**, *2*, 91-110. https://doi.org/10.1002/idm2.12046

234. Matsuo, M., Remhof, A., Martelli, P., Caputo, R., Ernst, M., Miura, Y., Sato, T., Oguchi, H., Maekawa, H., Takamura, H., Borgschulte, A., Züttel, A. & Orimo, S.-i. Complex Hydrides with $(BH_4)^-$ and $(NH_2)^-$ Anions as New Lithium Fast-Ion Conductors. *Journal of the American Chemical Society,* **2009**, *131*, 16389-16391. https://doi.org/10.1021/ja907249p

235. Bates, J. B., Dudney, N. J., Gruzalski, G. R., Zuhr, R. A., Choudhury, A., Luck, C. F. & Robertson, J. D. Electrical properties of amorphous lithium electrolyte thin films. *Solid State Ionics,* **1992**, *53-56*, 647-654. https://doi.org/10.1016/0167-2738(92)90442-R

236. Thangadurai, V. & Weppner, W. $Li_6ALa_2Ta_2O_{12}$ (A = Sr, Ba): Novel Garnet-Like Oxides for Fast Lithium Ion Conduction. *Advanced Functional Materials,* **2005**, *15*, 107-112. https://doi.org/10.1002/adfm.200400044

237. Zhao, Y. & Daemen, L. L. Superionic Conductivity in Lithium-Rich Anti-Perovskites. *Journal of the American Chemical Society,* **2012**, *134*, 15042-15047. https://doi.org/10.1021/ja305709z

238. Kato, Y., Hori, S., Saito, T., Suzuki, K., Hirayama, M., Mitsui, A., Yonemura, M., Iba, H. & Kanno, R. High-power all-solid-state batteries using sulfide superionic conductors. *Nature Energy,* **2016**, *1*, 16030. https://doi.org/10.1038/nenergy.2016.30

239. Lu, J. & Li, Y. Perovskite-type Li-ion solid electrolytes: a review. *Journal of Materials Science: Materials in Electronics,* **2021**, *32*, 9736-9754. https://doi.org/10.1007/s10854-021-05699-8

240. Bachman, J. C., Muy, S., Grimaud, A., Chang, H.-H., Pour, N., Lux, S. F., Paschos, O., Maglia, F., Lupart, S., Lamp, P., Giordano, L. & Shao-Horn, Y. Inorganic Solid-State Electrolytes for Lithium Batteries: Mechanisms and Properties Governing Ion Conduction. *Chemical Reviews,* **2016**, *116*, 140-162. https://doi.org/10.1021/acs.chemrev.5b00563

241. Weston, J. E. & Steele, B. C. H. Effects of inert fillers on the mechanical and electrochemical properties of lithium salt-poly(ethylene oxide) polymer electrolytes. *Solid State Ionics,* **1982**, *7*, 75-79. https://doi.org/10.1016/0167-2738(82)90072-8

242. Yu, X. & Manthiram, A. A review of composite polymer-ceramic electrolytes for lithium batteries. *Energy Storage Materials,* **2021**, *34*, 282-300. https://doi.org/10.1016/j.ensm.2020.10.006

243. Manuel Stephan, A. & Nahm, K. S. Review on composite polymer electrolytes for lithium batteries. *Polymer,* **2006**, *47*, 5952-5964. https://doi.org/10.1016/j.polymer.2006.05.069

244. Liu, Y., Xu, B., Zhang, W., Li, L., Lin, Y. & Nan, C. Composition Modulation and Structure Design of Inorganic-in-Polymer Composite Solid Electrolytes for Advanced Lithium Batteries. *Small,* **2020**, *16*, 1902813. https://doi.org/10.1002/smll.201902813

245. Yang, X., Liu, J., Pei, N., Chen, Z., Li, R., Fu, L., Zhang, P. & Zhao, J. The Critical Role of Fillers in Composite Polymer Electrolytes for Lithium Battery. *Nano-Micro Letters,* **2023**, *15*, 74. https://doi.org/10.1007/s40820-023-01051-3

246. Boaretto, N., Meabe, L., Martinez-Ibañez, M., Armand, M. & Zhang, H. Review—Polymer Electrolytes for Rechargeable Batteries: From Nanocomposite to Nanohybrid. *Journal of The Electrochemical Society,* **2020**, *167*, 070524. https://doi.org/10.1149/1945-7111/ab7221

247. Bao, W., Fan, W., Luo, J., Huo, S., Hu, Z., Jing, X., Chen, W., Long, X. & Zhang, Y. Imidazolium-Type Poly(ionic liquid) Endows the Composite Polymer Electrolyte Membrane with Excellent Interface Compatibility for All-Solid-State Lithium Metal Batteries. *ACS Applied Materials & Interfaces,* **2022**, *14*, 55664-55673. https://doi.org/10.1021/acsami.2c17842

248. Choudhary, S. & Sengwa, R. J. Effects of different inorganic nanoparticles on the structural, dielectric and ion transportation properties of polymers blend based nanocomposite solid polymer electrolytes. *Electrochimica Acta,* **2017**, *247*, 924-941. https://doi.org/10.1016/j.electacta.2017.07.051

249. Li, S., Zhang, S.-Q., Shen, L., Liu, Q., Ma, J.-B., Lv, W., He, Y.-B. & Yang, Q.-H. Progress and Perspective of Ceramic/Polymer Composite Solid Electrolytes for Lithium Batteries. *Advanced Science,* **2020**, *7*, 1903088. https://doi.org/10.1002/advs.201903088

250. Ji, K.-S., Moon, H.-S., Kim, J.-W. & Park, J.-W. Role of functional nano-sized inorganic fillers in poly(ethylene) oxide-based polymer electrolytes. *Journal of Power Sources,* **2003**, *117*, 124-130. https://doi.org/10.1016/S0378-7753(03)00159-9

251. Lin, D., Yuen, P. Y., Liu, Y., Liu, W., Liu, N., Dauskardt, R. H. & Cui, Y. A Silica-Aerogel-Reinforced Composite Polymer Electrolyte with High Ionic Conductivity and High Modulus. *Advanced Materials,* **2018**, *30*, 1802661. https://doi.org/10.1002/adma.201802661

252. Aravindan, V. & Vickraman, P. Characterization of SiO_2 and Al_2O_3 incorporated PVdF-HFP based composite polymer electrolytes with $LiPF_3(CF_3CF_2)_3$. *Journal of Applied Polymer Science,* **2008**, *108*, 1314-1322. https://doi.org/10.1002/app.27824

253. Lin, D., Liu, W., Liu, Y., Lee, H. R., Hsu, P.-C., Liu, K. & Cui, Y. High Ionic Conductivity of Composite Solid Polymer Electrolyte via In Situ Synthesis of Monodispersed SiO_2 Nanospheres in Poly(ethylene oxide). *Nano Letters,* **2016**, *16*, 459-465. https://doi.org/10.1021/acs.nanolett.5b04117

254. Liu, W., Lin, D., Sun, J., Zhou, G. & Cui, Y. Improved Lithium Ionic Conductivity in Composite Polymer Electrolytes with Oxide-Ion Conducting Nanowires. *ACS Nano,* **2016**, *10*, 11407-11413. https://doi.org/10.1021/acsnano.6b06797

255. Lu, Y., Moganty, S. S., Schaefer, J. L. & Archer, L. A. Ionic liquid-nanoparticle hybrid electrolytes. *Journal of Materials Chemistry,* **2012**, *22*, 4066-4072. https://doi.org/10.1039/C2JM15345A

256. Lu, Y., Das, S. K., Moganty, S. S. & Archer, L. A. Ionic Liquid-Nanoparticle Hybrid Electrolytes and their Application in Secondary Lithium-Metal Batteries. *Advanced Materials,* **2012**, *24*, 4430-4435. https://doi.org/10.1002/adma.201201953

257. Moganty, S. S., Srivastava, S., Lu, Y., Schaefer, J. L., Rizvi, S. A. & Archer, L. A. Ionic Liquid-Tethered Nanoparticle Suspensions: A Novel Class of Ionogels. *Chemistry of Materials,* **2012**, *24*, 1386-1392. https://doi.org/10.1021/cm300424v

258. Mu, Y., Chu, Y., Pan, L., Wu, B., Zou, L., He, J., Han, M., Zhao, T. & Zeng, L. 3D printing critical materials for rechargeable batteries: from materials, design and optimization strategies to applications. *International Journal of Extreme Manufacturing,* **2023**, *5*, 042008. https://doi.org/10.1088/2631-7990/acf172

259. Lyu, Z., Lim, G. J. H., Koh, J. J., Li, Y., Ma, Y., Ding, J., Wang, J., Hu, Z., Wang, J., Chen, W. & Chen, Y. Design and Manufacture of 3D-Printed Batteries. *Joule,* **2021**, *5*, 89-114. https://doi.org/10.1016/j.joule.2020.11.010

260. Zhou, S., Li, M., Wang, P., Cheng, L., Chen, L., Huang, Y., Yu, S., Mo, F. & Wei, J. Printed Solid-State Batteries. *Electrochemical Energy Reviews,* **2023**, *6*, 34. https://doi.org/10.1007/s41918-023-00200-x

261. Idrees, M., Batool, S., Din, M. A. U., Javed, M. S., Ahmed, S. & Chen, Z. Material-structure-property integrated additive manufacturing of batteries. *Nano Energy,* **2023**, *109*, 108247. https://doi.org/10.1016/j.nanoen.2023.108247

262. Pang, Y., Cao, Y., Chu, Y., Liu, M., Snyder, K., MacKenzie, D. & Cao, C. Additive Manufacturing of Batteries. *Advanced Functional Materials,* **2020**, *30*, 1906244. https://doi.org/10.1002/adfm.201906244

263. Chang, P., Mei, H., Zhou, S., Dassios, K. G. & Cheng, L. 3D printed electrochemical energy storage devices. *Journal of Materials Chemistry A,* **2019**, *7*, 4230-4258. https://doi.org/10.1039/C8TA11860D

264. Zhou, L.-Y., Fu, J. & He, Y. A Review of 3D Printing Technologies for Soft Polymer Materials. *Advanced Functional Materials,* **2020**, *30*, 2000187. https://doi.org/10.1002/adfm.202000187

265. Zhang, M., Mei, H., Chang, P. & Cheng, L. 3D printing of structured electrodes for rechargeable batteries. *Journal of Materials Chemistry A,* **2020**, *8*, 10670-10694. https://doi.org/10.1039/D0TA02099K

266. Zhang, S., Liu, Y., Hao, J., Wallace, G. G., Beirne, S. & Chen, J. 3D-Printed Wearable Electrochemical Energy Devices. *Advanced Functional Materials,* **2022**, *32*, 2103092. https://doi.org/10.1002/adfm.202103092

267. Rupp, H., Döhler, D., Hilgeroth, P., Mahmood, N., Beiner, M. & Binder, W. H. 3D Printing of Supramolecular Polymers: Impact of Nanoparticles and Phase Separation on Printability. *Macromolecular Rapid Communications,* **2019**, *40*, 1900467. https://doi.org/10.1002/marc.201900467

268. Maurel, A., Courty, M., Fleutot, B., Tortajada, H., Prashantha, K., Armand, M., Grugeon, S., Panier, S. & Dupont, L. Highly Loaded Graphite–Polylactic Acid Composite-Based Filaments for Lithium-Ion Battery Three-Dimensional Printing. *Chemistry of Materials,* **2018**, *30*, 7484-7493. https://doi.org/10.1021/acs.chemmater.8b02062

269. Lawes, S., Sun, Q., Lushington, A., Xiao, B., Liu, Y. & Sun, X. Inkjet-printed silicon as high performance anodes for Li-ion batteries. *Nano Energy,* **2017**, *36*, 313-321. https://doi.org/10.1016/j.nanoen.2017.04.041

270. Sun, K., Wei, T.-S., Ahn, B. Y., Seo, J. Y., Dillon, S. J. & Lewis, J. A. 3D Printing of Interdigitated Li-Ion Microbattery Architectures. *Advanced Materials,* **2013**, *25*, 4539-4543. https://doi.org/10.1002/adma.201301036

271. He, Y., Chen, S., Nie, L., Sun, Z., Wu, X. & Liu, W. Stereolithography Three-Dimensional Printing Solid Polymer Electrolytes for All-Solid-State Lithium Metal Batteries. *Nano Letters,* **2020**, *20*, 7136-7143. https://doi.org/10.1021/acs.nanolett.0c02457

272. McOwen, D. W., Xu, S., Gong, Y., Wen, Y., Godbey, G. L., Gritton, J. E., Hamann, T. R., Dai, J., Hitz, G. T., Hu, L. & Wachsman, E. D. 3D-Printing Electrolytes for Solid-State Batteries. *Advanced Materials,* **2018**, *30*, 1707132. https://doi.org/10.1002/adma.201707132

273. Cheng, Y., Xiao, X., Pan, K. & Pang, H. Development and application of self-healing materials in smart batteries and supercapacitors. *Chemical Engineering Journal,* **2020**, *380*, 122565. https://doi.org/10.1016/j.cej.2019.122565

274. Ezeigwe, E. R., Dong, L., Manjunatha, R., Tan, M., Yan, W. & Zhang, J. A review of self-healing electrode and electrolyte materials and their mitigating degradation of Lithium batteries. *Nano Energy,* **2021**, *84*, 105907. https://doi.org/10.1016/j.nanoen.2021.105907

275. Jadoun, S. Synthesis, Mechanism, and Applications of Self-healing Materials. *Biomedical Materials & Devices,* **2023**, https://doi.org/10.1007/s44174-023-00107-7

159

276. Campanella, A., Dohler, D. & Binder, W. H. Self-Healing in Supramolecular Polymers. *Macromolecular Rapid Communications,* **2018**, *39*, 1700739. https://doi.org/10.1002/marc.201700739

277. Huang, S., Kong, X., Xiong, Y., Zhang, X., Chen, H., Jiang, W., Niu, Y., Xu, W. & Ren, C. An overview of dynamic covalent bonds in polymer material and their applications. *European Polymer Journal,* **2020**, *141*, 110094. https://doi.org/10.1016/j.eurpolymj.2020.110094

278. Zheng, N., Xu, Y., Zhao, Q. & Xie, T. Dynamic Covalent Polymer Networks: A Molecular Platform for Designing Functions beyond Chemical Recycling and Self-Healing. *Chemical Reviews,* **2021**, *121*, 1716-1745. https://doi.org/10.1021/acs.chemrev.0c00938

279. Yang, L., Tan, X., Wang, Z. & Zhang, X. Supramolecular Polymers: Historical Development, Preparation, Characterization, and Functions. *Chemical Reviews,* **2015**, *115*, 7196-7239. https://doi.org/10.1021/cr500633b

280. Aida, T., Meijer, E. W. & Stupp, S. I. Functional Supramolecular Polymers. *Science,* **2012**, *335*, 813-817. https://doi.org/10.1126/science.1205962

281. Herbst, F., Döhler, D., Michael, P. & Binder, W. H. Self-healing polymers via supramolecular forces. *Macromolecular Rapid Communications,* **2013**, *34*, 203-220. https://doi.org/10.1002/marc.201200675

282. Wang, S. & Urban, M. W. Self-healing polymers. *Nature Reviews Materials,* **2020**, *5*, 562-583. https://doi.org/10.1038/s41578-020-0202-4

283. Guadagno, L., Vertuccio, L., Naddeo, C., Calabrese, E., Barra, G., Raimondo, M., Sorrentino, A., Binder, W. H., Michael, P. & Rana, S. Self-healing epoxy nanocomposites via reversible hydrogen bonding. *Composites Part B: Engineering,* **2019**, *157*, 1-13. https://doi.org/10.1016/j.compositesb.2018.08.082

284. Herbst, F., Seiffert, S. & Binder, W. H. Dynamic supramolecular poly(isobutylene)s for self-healing materials. *Polymer Chemistry,* **2012**, *3*, 3084-3092. https://doi.org/10.1039/C2PY20265D

285. Cordier, P., Tournilhac, F., Soulié-Ziakovic, C. & Leibler, L. Self-healing and thermoreversible rubber from supramolecular assembly. *Nature,* **2008**, *451*, 977-980. https://doi.org/10.1038/nature06669

286. Narayan, R., Laberty-Robert, C., Pelta, J., Tarascon, J.-M. & Dominko, R. Self-Healing: An Emerging Technology for Next-Generation Smart Batteries. *Advanced Energy Materials,* **2022**, *12*, 2102652. https://doi.org/10.1002/aenm.202102652

287. Zhou, B., He, D., Hu, J., Ye, Y., Peng, H., Zhou, X., Xie, X. & Xue, Z. A flexible, self-healing and highly stretchable polymer electrolyte via quadruple hydrogen bonding for lithium-ion batteries. *Journal of Materials Chemistry A,* **2018**, *6*, 11725-11733. https://doi.org/10.1039/C8TA01907J

288. Jo, Y. H., Zhou, B., Jiang, K., Li, S., Zuo, C., Gan, H., He, D., Zhou, X. & Xue, Z. Self-healing and shape-memory solid polymer electrolytes with high mechanical strength facilitated by a poly(vinyl alcohol) matrix. *Polymer Chemistry,* **2019**, *10*, 6561-6569. https://doi.org/10.1039/C9PY01406C

289. Guo, P., Zhang, H., Liu, X. & Sun, J. Counteranion-Mediated Intrinsic Healing of Poly(ionic liquid) Copolymers. *ACS Applied Materials & Interfaces,* **2018**, *10*, 2105-2113. https://doi.org/10.1021/acsami.7b16880

290. Zhu, X., Fang, Z., Deng, Q., Zhou, Y., Fu, X., Wu, L., Yan, W. & Yang, Y. Poly(ionic liquid)@PEGMA Block Polymer Initiated Microphase Separation Architecture in Poly(ethylene oxide)-Based Solid-State Polymer Electrolyte for Flexible and Self-Healing Lithium Batteries. *ACS Sustainable Chemistry & Engineering,* **2022**, *10*, 4173-4185. https://doi.org/10.1021/acssuschemeng.1c08306

291. Zhou, B., Jo, Y. H., Wang, R., He, D., Zhou, X., Xie, X. & Xue, Z. Self-healing composite polymer electrolyte formed via supramolecular networks for high-performance lithium-ion

batteries. *Journal of Materials Chemistry A,* **2019**, *7*, 10354-10362. https://doi.org/10.1039/C9TA01214A

292. Li, J., Yang, L., Zhang, H. & Ji, X. Self-healing composite solid electrolytes with enhanced Li$^+$ transport and mechanical properties for safe lithium metal batteries. *Chemical Engineering Journal,* **2022**, *438*, 135418. https://doi.org/10.1016/j.cej.2022.135418

293. Tian, X., Yang, P., Yi, Y., Liu, P., Wang, T., Shu, C., Qu, L., Tang, W., Zhang, Y., Li, M. & Yang, B. Self-healing and high stretchable polymer electrolytes based on ionic bonds with high conductivity for lithium batteries. *Journal of Power Sources,* **2020**, *450*, 227629. https://doi.org/10.1016/j.jpowsour.2019.227629

294. Guo, P., Su, A., Wei, Y., Liu, X., Li, Y., Guo, F., Li, J., Hu, Z. & Sun, J. Healable, Highly Conductive, Flexible, and Nonflammable Supramolecular Ionogel Electrolytes for Lithium-Ion Batteries. *ACS Applied Materials & Interfaces,* **2019**, *11*, 19413-19420. https://doi.org/10.1021/acsami.9b02182

295. Chen, X., Yi, L., Zou, C., Liu, J., Yu, J., Zang, Z., Tao, X., Luo, Z., Guo, X., Chen, G., Chang, B., Shen, Y. & Wang, X. High-Performance Gel Polymer Electrolyte with Self-Healing Capability for Lithium-Ion Batteries. *ACS Applied Energy Materials,* **2022**, *5*, 5267-5276. https://doi.org/10.1021/acsaem.2c00713

296. Davino, S., Callegari, D., Pasini, D., Thomas, M., Nicotera, I., Bonizzoni, S., Mustarelli, P. & Quartarone, E. Cross-Linked Gel Electrolytes with Self-Healing Functionalities for Smart Lithium Batteries. *ACS Applied Materials & Interfaces,* **2022**, *14*, 51941-51953. https://doi.org/10.1021/acsami.2c15011

297. Zhou, B., Zuo, C., Xiao, Z., Zhou, X., He, D., Xie, X. & Xue, Z. Self-Healing Polymer Electrolytes Formed via Dual-Networks: A New Strategy for Flexible Lithium Metal Batteries. *Chemistry – A European Journal,* **2018**, *24*, 19200-19207. https://doi.org/10.1002/chem.201803943

298. Luo, J. C., Demchuk, Z., Zhao, X., Saito, T., Tian, M., Sokolov, A. P. & Cao, P. F. Review Elastic vitrimers: Beyond thermoplastic and thermoset elastomers. *Matter,* **2022**, *5*, 1391-1422. https://doi.org/10.1016/j.matt.2022.04.007

299. Scheutz, G. M., Lessard, J. J., Sims, M. B. & Sumerlin, B. S. Adaptable Crosslinks in Polymeric Materials: Resolving the Intersection of Thermoplastics and Thermosets. *Journal of the American Chemical Society,* **2019**, *141*, 16181-16196. https://doi.org/10.1021/jacs.9b07922

300. Denissen, W., Winne, J. M. & Du Prez, F. E. Vitrimers: permanent organic networks with glass-like fluidity. *Chemical Science,* **2016**, *7*, 30-38. https://doi.org/10.1039/C5SC02223A

301. Krishnakumar, B., Sanka, R. V. S. P., Binder, W. H., Parthasarthy, V., Rana, S. & Karak, N. Vitrimers: Associative dynamic covalent adaptive networks in thermoset polymers. *Chemical Engineering Journal,* **2020**, *385*, 123820. https://doi.org/10.1016/j.cej.2019.123820

302. Lagron, A. B., El-Zaatari, B. M. & Hamachi, L. S. Characterization Techniques to Assess Recyclability in Dynamic Polymer Networks. *Frontiers in Materials,* **2022**, *9* https://doi.org/10.3389/fmats.2022.915296

303. Jourdain, A., Asbai, R., Anaya, O., Chehimi, M. M., Drockenmuller, E. & Montarnal, D. Rheological Properties of Covalent Adaptable Networks with 1,2,3-Triazolium Cross-Links: The Missing Link between Vitrimers and Dissociative Networks. *Macromolecules,* **2020**, *53*, 1884-1900. https://doi.org/10.1021/acs.macromol.9b02204

304. Chen, X., Dam, M. A., Ono, K., Mal, A., Shen, H., Nutt, S. R., Sheran, K. & Wudl, F. A Thermally Re-mendable Cross-Linked Polymeric Material. *Science,* **2002**, *295*, 1698-1702. https://doi.org/10.1126/science.1065879

305. Montarnal, D., Capelot, M., Tournilhac, F. & Leibler, L. Silica-Like Malleable Materials from Permanent Organic Networks. *Science,* **2011**, *334*, 965-968. https://doi.org/10.1126/science.1212648

306. Van Zee, N. J. & Nicolaÿ, R. Vitrimers: Permanently crosslinked polymers with dynamic network topology. *Progress in Polymer Science,* **2020**, *104* https://doi.org/10.1016/j.progpolymsci.2020.101233

307. Ogden, W. A. & Guan, Z. Recyclable, Strong, and Highly Malleable Thermosets Based on Boroxine Networks. *Journal of the American Chemical Society,* **2018**, *140*, 6217-6220. https://doi.org/10.1021/jacs.8b03257

308. Rottger, M., Domenech, T., van der Weegen, R., Breuillac, A., Nicolay, R. & Leibler, L. High-performance vitrimers from commodity thermoplastics through dioxaborolane metathesis. *Science,* **2017**, *356*, 62-65. https://doi.org/10.1126/science.aah5281

309. Marco-Dufort, B. & Tibbitt, M. W. Design of moldable hydrogels for biomedical applications using dynamic covalent boronic esters. *Materials Today Chemistry,* **2019**, *12*, 16-33. https://doi.org/10.1016/j.mtchem.2018.12.001

310. Zhang, V., Kang, B., Accardo, J. V. & Kalow, J. A. Structure–Reactivity–Property Relationships in Covalent Adaptable Networks. *Journal of the American Chemical Society,* **2022**, *144*, 22358-22377. https://doi.org/10.1021/jacs.2c08104

311. Capelot, M., Unterlass, M. M., Tournilhac, F. & Leibler, L. Catalytic Control of the Vitrimer Glass Transition. *ACS Macro Letters,* **2012**, *1*, 789-792. https://doi.org/10.1021/mz300239f

312. Guerre, M., Taplan, C., Winne, J. M. & Du Prez, F. E. Vitrimers: directing chemical reactivity to control material properties. *Chemical Science,* **2020**, *11*, 4855-4870. https://doi.org/10.1039/D0SC01069C

313. Zhang, L., Zhang, P., Chang, C., Guo, W., Guo, Z. H. & Pu, X. Self-Healing Solid Polymer Electrolyte for Room-Temperature Solid-State Lithium Metal Batteries. *ACS Applied Materials & Interfaces,* **2021**, *13*, 46794-46802. https://doi.org/10.1021/acsami.1c14462

314. Jo, Y. H., Li, S., Zuo, C., Zhang, Y., Gan, H., Li, S., Yu, L., He, D., Xie, X. & Xue, Z. Self-Healing Solid Polymer Electrolyte Facilitated by a Dynamic Cross-Linked Polymer Matrix for Lithium-Ion Batteries. *Macromolecules,* **2020**, *53*, 1024-1032. https://doi.org/10.1021/acs.macromol.9b02305

315. Zhou, S., Deng, K., Xu, Z., Xiao, M. & Meng, Y. Highly conductive self-healing polymer electrolytes based on synergetic dynamic bonds for highly safe lithium metal batteries. *Chemical Engineering Journal,* **2022**, *442*, 136083. https://doi.org/10.1016/j.cej.2022.136083

316. Jing, B. B. & Evans, C. M. Catalyst-Free Dynamic Networks for Recyclable, Self-Healing Solid Polymer Electrolytes. *Journal of the American Chemical Society,* **2019**, *141*, 18932-18937. https://doi.org/10.1021/jacs.9b09811

317. Li, F., Nguyen, G. T. M., Vancaeyzeele, C., Vidal, F. & Plesse, C. Healable Ionoelastomer Designed from Polymeric Ionic Liquid and Vitrimer Chemistry. *ACS Applied Polymer Materials,* **2023**, *5*, 529-541. https://doi.org/10.1021/acsapm.2c01635

318. Wan, L., Cao, X., Xue, X., Tong, Y., Ci, S., Huang, H. & Zhou, D. Self-Healing and Flexible Ionic Gel Polymer Electrolyte Based on Reversible Bond for High-Performance Lithium Metal Batteries. *Energy Technology,* **2022**, *10*, 2100749. https://doi.org/10.1002/ente.202100749

319. Whiteley, J. M., Taynton, P., Zhang, W. & Lee, S.-H. Ultra-thin Solid-State Li-Ion Electrolyte Membrane Facilitated by a Self-Healing Polymer Matrix. *Advanced Materials,* **2015**, *27*, 6922-6927. https://doi.org/10.1002/adma.201502636

320. Lin, Y., Chen, Y., Yu, Z., Huang, Z., Lai, J.-C., Tok, J. B. H., Cui, Y. & Bao, Z. Reprocessable and Recyclable Polymer Network Electrolytes via Incorporation of Dynamic Covalent Bonds. *Chemistry of Materials,* **2022**, *34*, 2393-2399. https://doi.org/10.1021/acs.chemmater.1c04396

321. Zhou, X., Li, C., Bhandary, R., Katcharava, Z., Du, F., Androsch, R., Marinow, A. & Binder, W. H. Catalyst-Free, Mechanically Robust, and Ion-Conductive Vitrimers for Self-Healing Ionogel Electrolytes. *ACS Applied Engineering Materials,* **2023**, *1*, 1997-2003. https://doi.org/10.1021/acsaenm.3c00286

322. Arbizzani, C., Gabrielli, G. & Mastragostino, M. Thermal stability and flammability of electrolytes for lithium-ion batteries. *Journal of Power Sources,* **2011**, *196*, 4801-4805. https://doi.org/10.1016/j.jpowsour.2011.01.068

323. Li, B., Chao, Y., Li, M., Xiao, Y., Li, R., Yang, K., Cui, X., Xu, G., Li, L., Yang, C., Yu, Y., Wilkinson, D. P. & Zhang, J. A Review of Solid Electrolyte Interphase (SEI) and Dendrite Formation in Lithium Batteries. *Electrochemical Energy Reviews,* **2023**, *6*, 7. https://doi.org/10.1007/s41918-022-00147-5

324. Xiao, J. How lithium dendrites form in liquid batteries. *Science,* **2019**, *366*, 426-427. https://doi.org/10.1126/science.aay8672

325. Guo, K., Qi, S., Wang, H., Huang, J., Wu, M., Yang, Y., Li, X., Ren, Y. & Ma, J. High-Voltage Electrolyte Chemistry for Lithium Batteries. *Small Science,* **2022**, *2*, 2100107. https://doi.org/10.1002/smsc.202100107

326. Costa, C. M., Barbosa, J. C., Gonçalves, R., Castro, H., Campo, F. J. D. & Lanceros-Méndez, S. Recycling and environmental issues of lithium-ion batteries: Advances, challenges and opportunities. *Energy Storage Materials,* **2021**, *37*, 433-465. https://doi.org/10.1016/j.ensm.2021.02.032

327. Li, C., Bhandary, R., Marinow, A., Ivanov, D., Du, M., Androsch, R. & Binder, W. H. Synthesis and Characterization of Quadrupolar-Hydrogen-Bonded Polymeric Ionic Liquids for Potential Self-Healing Electrolytes. *Polymers,* **2022**, *14*, 4090. https://doi.org/10.3390/polym14194090

328. He, H., Zhong, M., Adzima, B., Luebke, D., Nulwala, H. & Matyjaszewski, K. A simple and universal gel permeation chromatography technique for precise molecular weight characterization of well-defined poly(ionic liquid)s. *Journal of the American Chemical Society,* **2013**, *135*, 4227-4230. https://doi.org/10.1021/ja4012645

329. Cromwell, O. R., Chung, J. & Guan, Z. Malleable and Self-Healing Covalent Polymer Networks through Tunable Dynamic Boronic Ester Bonds. *Journal of the American Chemical Society,* **2015**, *137*, 6492-6495. https://doi.org/10.1021/jacs.5b03551

330. Cash, J. J., Kubo, T., Bapat, A. P. & Sumerlin, B. S. Room-Temperature Self-Healing Polymers Based on Dynamic-Covalent Boronic Esters. *Macromolecules,* **2015**, *48*, 2098-2106. https://doi.org/10.1021/acs.macromol.5b00210

331. Xu, S., Sun, Z., Sun, C., Li, F., Chen, K., Zhang, Z., Hou, G., Cheng, H.-M. & Li, F. Homogeneous and Fast Ion Conduction of PEO-Based Solid-State Electrolyte at Low Temperature. *Advanced Functional Materials,* **2020**, *30*, 2007172. https://doi.org/10.1002/adfm.202007172

332. Döbbelin, M., Azcune, I., Bedu, M., Ruiz de Luzuriaga, A., Genua, A., Jovanovski, V., Cabañero, G. & Odriozola, I. Synthesis of Pyrrolidinium-Based Poly(ionic liquid) Electrolytes with Poly(ethylene glycol) Side Chains. *Chemistry of Materials,* **2012**, *24*, 1583-1590. https://doi.org/10.1021/cm203790z

333. Diederichsen, K. M., Buss, H. G. & McCloskey, B. D. The Compensation Effect in the Vogel-Tammann-Fulcher (VTF) Equation for Polymer-Based Electrolytes. *Macromolecules,* **2017**, *50*, 3832-3841. https://doi.org/10.1021/acs.macromol.7b00423

334. Chintapalli, M., Le, T. N. P., Venkatesan, N. R., Mackay, N. G., Rojas, A. A., Thelen, J. L., Chen, X. C., Devaux, D. & Balsara, N. P. Structure and Ionic Conductivity of Polystyrene-block-poly(ethylene oxide) Electrolytes in the High Salt Concentration Limit. *Macromolecules,* **2016**, *49*, 1770-1780. https://doi.org/10.1021/acs.macromol.5b02620

335. Zhao, Y., Bai, Y., Li, W., Liu, A., An, M., Bai, Y. & Chen, G. Semi closed coordination structure polymer electrolyte combined in situ interface engineering for lithium batteries. *Chemical Engineering Journal,* **2020**, *394*, 124847. https://doi.org/10.1016/j.cej.2020.124847

336. Weber, R. L., Ye, Y., Banik, S. M., Elabd, Y. A., Hickner, M. A. & Mahanthappa, M. K. Thermal and ion transport properties of hydrophilic and hydrophobic polymerized styrenic imidazolium ionic liquids. *Journal of Polymer Science Part B: Polymer Physics,* **2011**, *49*, 1287-1296. https://doi.org/10.1002/polb.22319
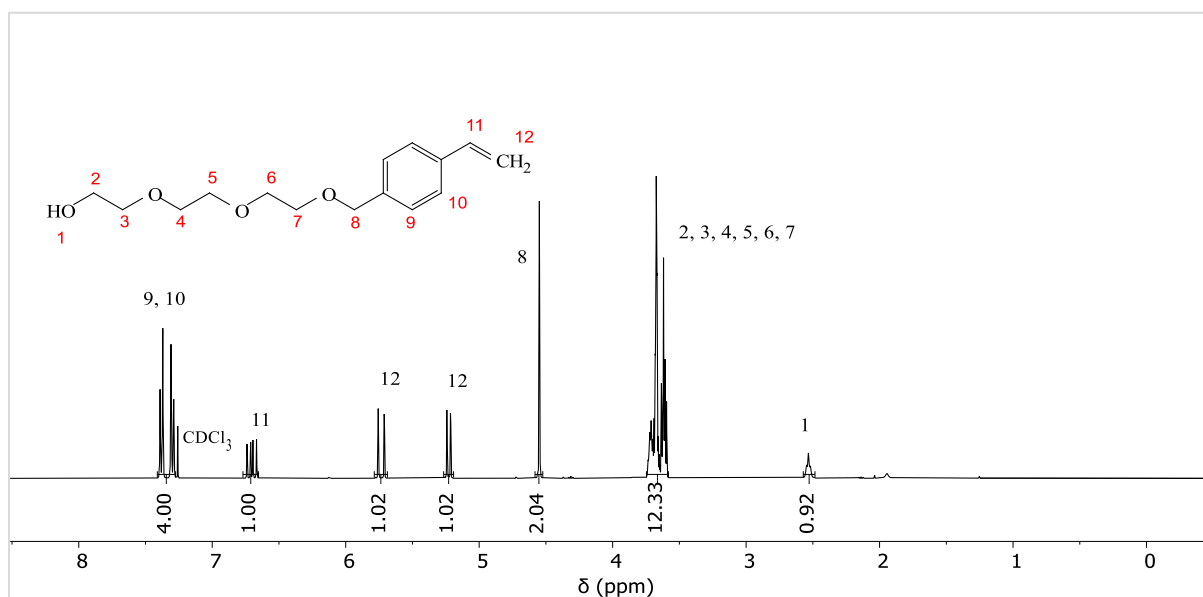
337. Green, M. D., Salas-de la Cruz, D., Ye, Y., Layman, J. M., Elabd, Y. A., Winey, K. I. & Long, T. E. Alkyl-Substituted N-Vinylimidazolium Polymerized Ionic Liquids: Thermal Properties and Ionic Conductivities. *Macromolecular Chemistry and Physics,* **2011**, *212*, 2522-2528. https://doi.org/10.1002/macp.201100389

338. He, R., Echeverri, M., Ward, D., Zhu, Y. & Kyu, T. Highly conductive solvent-free polymer electrolyte membrane for lithium-ion batteries: Effect of prepolymer molecular weight. *Journal of Membrane Science,* **2016**, *498*, 208-217. https://doi.org/10.1016/j.memsci.2015.10.008

339. Elling, B. R. & Dichtel, W. R. Reprocessable Cross-Linked Polymer Networks: Are Associative Exchange Mechanisms Desirable? *ACS Central Science,* **2020**, *6*, 1488-1496. https://doi.org/10.1021/acscentsci.0c00567

340. Nishimura, Y., Chung, J., Muradyan, H. & Guan, Z. Silyl Ether as a Robust and Thermally Stable Dynamic Covalent Motif for Malleable Polymer Design. *Journal of the American Chemical Society,* **2017**, *139*, 14881-14884. https://doi.org/10.1021/jacs.7b08826

341. Porath, L. E. & Evans, C. M. Importance of Broad Temperature Windows and Multiple Rheological Approaches for Probing Viscoelasticity and Entropic Elasticity in Vitrimers. *Macromolecules,* **2021**, *54*, 4782-4791. https://doi.org/10.1021/acs.macromol.0c02800

342. Chen, F., Cheng, Q., Gao, F., Zhong, J., Shen, L., Lin, C. & Lin, Y. The effect of latent plasticity on the shape recovery of a shape memory vitrimer. *European Polymer Journal,* **2021**, *147*, 110304. https://doi.org/10.1016/j.eurpolymj.2021.110304

343. Wang, S., Ma, S., Li, Q., Xu, X., Wang, B., Yuan, W., Zhou, S., You, S. & Zhu, J. Facile in situ preparation of high-performance epoxy vitrimer from renewable resources and its application in nondestructive recyclable carbon fiber composite. *Green Chemistry,* **2019**, *21*, 1484-1497. https://doi.org/10.1039/C8GC03477J

344. Wu, S., Yang, H., Huang, S. & Chen, Q. Relationship between Reaction Kinetics and Chain Dynamics of Vitrimers Based on Dioxaborolane Metathesis. *Macromolecules,* **2020**, *53*, 1180-1190. https://doi.org/10.1021/acs.macromol.9b02162

345. Wu, S., Yang, H., Xu, W.-S. & Chen, Q. Thermodynamics and Reaction Kinetics of Symmetric Vitrimers Based on Dioxaborolane Metathesis. *Macromolecules,* **2021**, *54*, 6799-6809. https://doi.org/10.1021/acs.macromol.1c00697

346. Bragg, W. H. & Bragg, W. L. The reflection of X-rays by crystals. *Proceedings of the Royal Society of London. Series A, Containing Papers of a Mathematical and Physical Character,* **1913**, *88*, 428-438. https://doi.org/10.1098/rspa.1913.0040

347. Singh, P. S. Membrane Characterization. (*Elsevier*, **2017**), ISBN: 978-0-444-63776-5.

348. Liu, Y., Zhang, R., Wang, J. & Wang, Y. Current and future lithium-ion battery manufacturing. *iScience,* **2021**, *24*, 102332. https://doi.org/10.1016/j.isci.2021.102332

349. Le Bideau, J., Viau, L. & Vioux, A. Ionogels, ionic liquid based hybrid materials. *Chemical Society Reviews,* **2011**, *40*, 907-925. https://doi.org/10.1039/c0cs00059k

350. Forsyth, M., Porcarelli, L., Wang, X., Goujon, N. & Mecerreyes, D. Innovative Electrolytes Based on Ionic Liquids and Polymers for Next-Generation Solid-State Batteries. *Accounts of Chemical Research,* **2019**, *52*, 686-694. https://doi.org/10.1021/acs.accounts.8b00566

351. Yang, G., Song, Y., Wang, Q., Zhang, L. & Deng, L. Review of ionic liquids containing, polymer/inorganic hybrid electrolytes for lithium metal batteries. *Materials & Design,* **2020**, *190*, 108563. https://doi.org/10.1016/j.matdes.2020.108563

352. Cheng, M., Jiang, Y., Yao, W., Yuan, Y., Deivanayagam, R., Foroozan, T., Huang, Z., Song, B., Rojaee, R., Shokuhfar, T., Pan, Y., Lu, J. & Shahbazian-Yassar, R. Elevated-Temperature 3D Printing of Hybrid Solid-State Electrolyte for Li-Ion Batteries. *Advanced Materials,* **2018**, *30*, e1800615. https://doi.org/10.1002/adma.201800615

353. Nematdoust, S., Najjar, R., Bresser, D. & Passerini, S. Understanding the Role of Nanoparticles in PEO-Based Hybrid Polymer Electrolytes for Solid-State Lithium–Polymer Batteries. *The Journal of Physical Chemistry C,* **2020**, *124*, 27907-27915. https://doi.org/10.1021/acs.jpcc.0c08749

354. Yao, P., Yu, H., Ding, Z., Liu, Y., Lu, J., Lavorgna, M., Wu, J. & Liu, X. Review on Polymer-Based Composite Electrolytes for Lithium Batteries. *Frontiers in Chemistry,* **2019**, *7*, 522. https://doi.org/10.3389/fchem.2019.00522

355. Rupp, H., Bhandary, R., Kulkarni, A. & Binder, W. Printable Electrolytes: Tuning 3D-Printing by Multiple Hydrogen Bonds and Added Inorganic Lithium-Salts. *Advanced Materials Technologies,* **2022**, *7*, 2200088. https://doi.org/10.1002/admt.202200088

356. Vallée, A., Besner, S. & Prud'Homme, J. Comparative study of poly(ethylene oxide) electrolytes made with $LiN(CF_3SO_2)_2$, $LiCF_3SO_3$ and $LiClO_4$: Thermal properties and conductivity behaviour. *Electrochimica Acta,* **1992**, *37*, 1579-1583. https://doi.org/10.1016/0013-4686(92)80115-3

357. Teran, A. A., Tang, M. H., Mullin, S. A. & Balsara, N. P. Effect of molecular weight on conductivity of polymer electrolytes. *Solid State Ionics,* **2011**, *203*, 18-21. https://doi.org/10.1016/j.ssi.2011.09.021

358. Devaux, D., Bouchet, R., Glé, D. & Denoyel, R. Mechanism of ion transport in PEO/LiTFSI complexes: Effect of temperature, molecular weight and end groups. *Solid State Ionics,* **2012**, *227*, 119-127. https://doi.org/10.1016/j.ssi.2012.09.020

359. Wang, Y., Wu, Z., Azad, F. M., Zhu, Y., Wang, L., Hawker, C. J., Whittaker, A. K., Forsyth, M. & Zhang, C. Fluorination in advanced battery design. *Nature Reviews Materials,* **2023**, https://doi.org/10.1038/s41578-023-00623-4

360. Liu, Q., Hsu, C.-W., Dzwiniel, T. L., Pupek, K. Z. & Zhang, Z. A fluorine-substituted pyrrolidinium-based ionic liquid for high-voltage Li-ion batteries. *Chemical Communications,* **2020**, *56*, 7317-7320. https://doi.org/10.1039/D0CC02184A

361. Fan, X., Ji, X., Chen, L., Chen, J., Deng, T., Han, F., Yue, J., Piao, N., Wang, R., Zhou, X., Xiao, X., Chen, L. & Wang, C. All-temperature batteries enabled by fluorinated electrolytes with non-polar solvents. *Nature Energy,* **2019**, *4*, 882-890. https://doi.org/10.1038/s41560-019-0474-3

362. Boyle, D. T., Kim, S. C., Oyakhire, S. T., Vilá, R. A., Huang, Z., Sayavong, P., Qin, J., Bao, Z. & Cui, Y. Correlating Kinetics to Cyclability Reveals Thermodynamic Origin of Lithium Anode Morphology in Liquid Electrolytes. *Journal of the American Chemical Society,* **2022**, *144*, 20717-20725. https://doi.org/10.1021/jacs.2c08182

363. Qi, H., Ren, Y., Guo, S., Wang, Y., Li, S., Hu, Y. & Yan, F. High-Voltage Resistant Ionic Liquids for Lithium-Ion Batteries. *ACS Applied Materials & Interfaces,* **2020**, *12*, 591-600. https://doi.org/10.1039/c9ta05804d

364. Kerner, M. & Johansson, P. Pyrrolidinium FSI and TFSI-Based Polymerized Ionic Liquids as Electrolytes for High-Temperature Lithium-Ion Batteries. *Batteries,* **2018**, *4*, 10. https://doi.org/10.3390/batteries4010010

365. Monteiro, M. J., Bazito, F. F. C., Siqueira, L. J. A., Ribeiro, M. C. C. & Torresi, R. M. Transport Coefficients, Raman Spectroscopy, and Computer Simulation of Lithium Salt Solutions in an Ionic Liquid. *The Journal of Physical Chemistry B,* **2008**, *112*, 2102-2109. https://doi.org/10.1021/jp077026y

366. Asenbauer, J., Ben Hassen, N., McCloskey, B. D. & Prausnitz, J. M. Solubilities and ionic conductivities of ionic liquids containing lithium salts. *Electrochimica Acta,* **2017**, *247*, 1038-1043. https://doi.org/10.1016/j.electacta.2017.07.053

367. Seki, S., Ohno, Y., Kobayashi, Y., Miyashiro, H., Usami, A., Mita, Y., Tokuda, H., Watanabe, M., Hayamizu, K., Tsuzuki, S., Hattori, M. & Terada, N. Imidazolium-Based Room-Temperature Ionic Liquid for Lithium Secondary Batteries: Effects of Lithium Salt Concentration. *Journal of The Electrochemical Society,* **2007**, *154*, A173. https://doi.org/10.1149/1.2426871

368. Tokuda, H., Hayamizu, K., Ishii, K., Susan, M. A. B. H. & Watanabe, M. Physicochemical Properties and Structures of Room Temperature Ionic Liquids. 2. Variation of Alkyl Chain

Length in Imidazolium Cation. *The Journal of Physical Chemistry B,* **2005**, *109*, 6103-6110. https://doi.org/10.1021/jp044626d

369. Wang, X., Chi, Y. & Mu, T. A review on the transport properties of ionic liquids. *Journal of Molecular Liquids,* **2014**, *193*, 262-266. https://doi.org/10.1016/j.molliq.2014.03.011

370. Zheng, W., Mohammed, A., Hines, L. G., Jr., Xiao, D., Martinez, O. J., Bartsch, R. A., Simon, S. L., Russina, O., Triolo, A. & Quitevis, E. L. Effect of cation symmetry on the morphology and physicochemical properties of imidazolium ionic liquids. *The Journal of Physical Chemistry B,* **2011**, *115*, 6572-6584. https://doi.org/10.1021/jp1115614

371. Russina, O., Triolo, A., Gontrani, L., Caminiti, R., Xiao, D., Hines, L. G., Bartsch, R. A., Quitevis, E. L., Plechkova, N. & Seddon, K. R. Morphology and intermolecular dynamics of 1-alkyl-3-methylimidazolium bis{(trifluoromethane)sulfonyl}amide ionic liquids: structural and dynamic evidence of nanoscale segregation. *Journal of Physics: Condensed Matter,* **2009**, *21*, 424121. https://doi.org/10.1088/0953-8984/21/42/424121

372. Triolo, A., Russina, O., Fazio, B., Triolo, R. & Di Cola, E. Morphology of 1-alkyl-3-methylimidazolium hexafluorophosphate room temperature ionic liquids. *Chemical Physics Letters,* **2008**, *457*, 362-365. https://doi.org/10.1016/j.cplett.2008.04.027

373. He, W., Cui, Z., Liu, X., Cui, Y., Chai, J., Zhou, X., Liu, Z. & Cui, G. Carbonate-linked poly(ethylene oxide) polymer electrolytes towards high performance solid state lithium batteries. *Electrochimica Acta,* **2017**, *225*, 151-159. https://doi.org/10.1016/j.electacta.2016.12.113

374. Chaudoy, V., Jacquemin, J., Tran-Van, F., Deschamps, M. & Ghamouss, F. Effect of mixed anions on the transport properties and performance of an ionic liquid-based electrolyte for lithium-ion batteries. *Pure and Applied Chemistry,* **2019**, *91*, 1361-1381. https://doi.org/10.1515/pac-2018-1006

375. Matsui, Y., Yamagata, M., Murakami, S., Saito, Y., Higashizaki, T., Ishiko, E., Kono, M. & Ishikawa, M. Design of an electrolyte composition for stable and rapid charging–discharging of a graphite negative electrode in a bis(fluorosulfonyl)imide-based ionic liquid. *Journal of Power Sources,* **2015**, *279*, 766-773. https://doi.org/10.1016/j.jpowsour.2015.01.070

376. Kang, S.-J., Park, K., Park, S.-H. & Lee, H. Unraveling the role of LiFSI electrolyte in the superior performance of graphite anodes for Li-ion batteries. *Electrochimica Acta,* **2018**, *259*, 949-954. https://doi.org/10.1016/j.electacta.2017.11.018

377. Kerr, R., Mazouzi, D., Eftekharnia, M., Lestriez, B., Dupré, N., Forsyth, M., Guyomard, D. & Howlett, P. C. High-Capacity Retention of Si Anodes Using a Mixed Lithium/Phosphonium Bis(fluorosulfonyl)imide Ionic Liquid Electrolyte. *ACS Energy Letters,* **2017**, *2*, 1804-1809. https://doi.org/10.1021/acsenergylett.7b00403

378. Huang, W.-H., Li, X.-M., Yang, X.-F., Zhang, X.-X., Wang, H.-H. & Wang, H. The recent progress and perspectives on metal- and covalent-organic framework based solid-state electrolytes for lithium-ion batteries. *Materials Chemistry Frontiers,* **2021**, *5*, 3593-3613. https://doi.org/10.1039/D0QM00936A

379. Fu, X., Yu, D., Zhou, J., Li, S., Gao, X., Han, Y., Qi, P., Feng, X. & Wang, B. Inorganic and organic hybrid solid electrolytes for lithium-ion batteries. *CrystEngComm,* **2016**, *18*, 4236-4258. https://doi.org/10.1039/C6CE00171H

380. Hua, F., Jiang, X., Li, D. & Zhao, B. Well-defined thermosensitive, water-soluble polyacrylates and polystyrenics with short pendant oligo(ethylene glycol) groups synthesized by nitroxide-mediated radical polymerization. *Journal of Polymer Science Part A: Polymer Chemistry,* **2006**, *44*, 2454-2467. https://doi.org/10.1002/pola.21357

381. Zhao, B., Li, D., Hua, F. & Green, D. R. Synthesis of Thermosensitive Water-Soluble Polystyrenics with Pendant Methoxyoligo(ethylene glycol) Groups by Nitroxide-Mediated Radical Polymerization. *Macromolecules,* **2005**, *38*, 9509-9517. https://doi.org/10.1021/ma0514572

382. Yamauchi, K., Lizotte, J. R. & Long, T. E. Thermoreversible Poly(alkyl acrylates) Consisting of Self-Complementary Multiple Hydrogen Bonding. *Macromolecules,* **2003**, *36*, 1083-1088. https://doi.org/10.1021/ma0212801

383. Chrobok, A., Baj, S., Pudło, W. & Jarzębski, A. Supported hydrogensulfate ionic liquid catalysis in Baeyer–Villiger reaction. *Applied Catalysis A: General,* **2009**, *366*, 22-28. https://doi.org/10.1016/j.apcata.2009.06.040

384. Bracho, D., Dougnac, V. N., Palza, H. & Quijada, R. Functionalization of Silica Nanoparticles for Polypropylene Nanocomposite Applications. *Journal of Nanomaterials,* **2012**, *2012*, 263915. https://doi.org/10.1155/2012/263915

385. Yamamoto, E., Shimojima, A., Wada, H. & Kuroda, K. Mesoporous Silica Nanoparticles with Dispersibility in Organic Solvents and Their Versatile Surface Modification. *Langmuir,* **2020**, *36*, 5571-5578. https://doi.org/10.1021/acs.langmuir.0c00729

386. Dankers, P. Y. W., Zhang, Z., Wisse, E., Grijpma, D. W., Sijbesma, R. P., Feijen, J. & Meijer, E. W. Oligo(trimethylene carbonate)-Based Supramolecular Biomaterials. *Macromolecules,* **2006**, *39*, 8763-8771. https://doi.org/10.1021/ma061078o

387. Nakahata, M., Mori, S., Takashima, Y., Yamaguchi, H. & Harada, A. Self-Healing Materials Formed by Cross-Linked Polyrotaxanes with Reversible Bonds. *Chem,* **2016**, *1*, 766-775. https://doi.org/10.1016/j.chempr.2016.09.013

388. Kikkeri, R., Lepenies, B., Adibekian, A., Laurino, P. & Seeberger, P. H. In Vitro Imaging and in Vivo Liver Targeting with Carbohydrate Capped Quantum Dots. *Journal of the American Chemical Society,* **2009**, *131*, 2110-2112. https://doi.org/10.1021/ja807711w

389. Aoyagi, N. & Endo, T. Functional RAFT agents for radical-controlled polymerization: Quantitative synthesis of trithiocarbonates containing functional groups as RAFT agents using equivalent amount of CS_2. *Journal of Polymer Science Part A: Polymer Chemistry,* **2009**, *47*, 3702-3709. https://doi.org/10.1002/pola.23410

10 Appendix

Figure S 1. ^{1}H NMR spectrum of **1** in DMSO-d$_6$.

Figure S 2. ^{13}C NMR spectrum of **1** in DMSO-d$_6$.
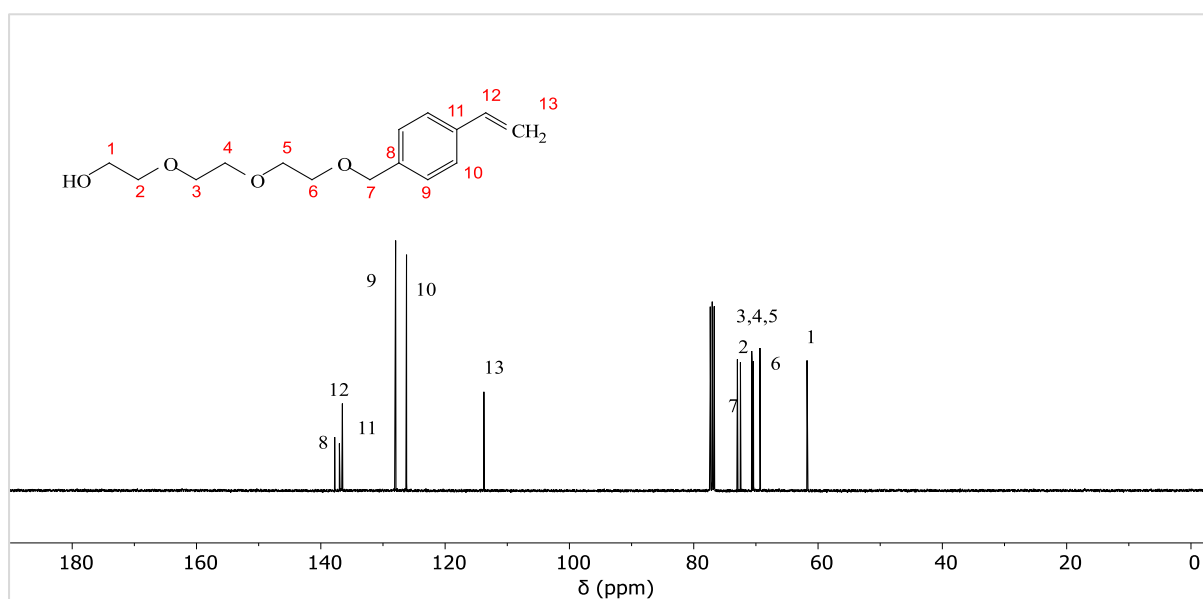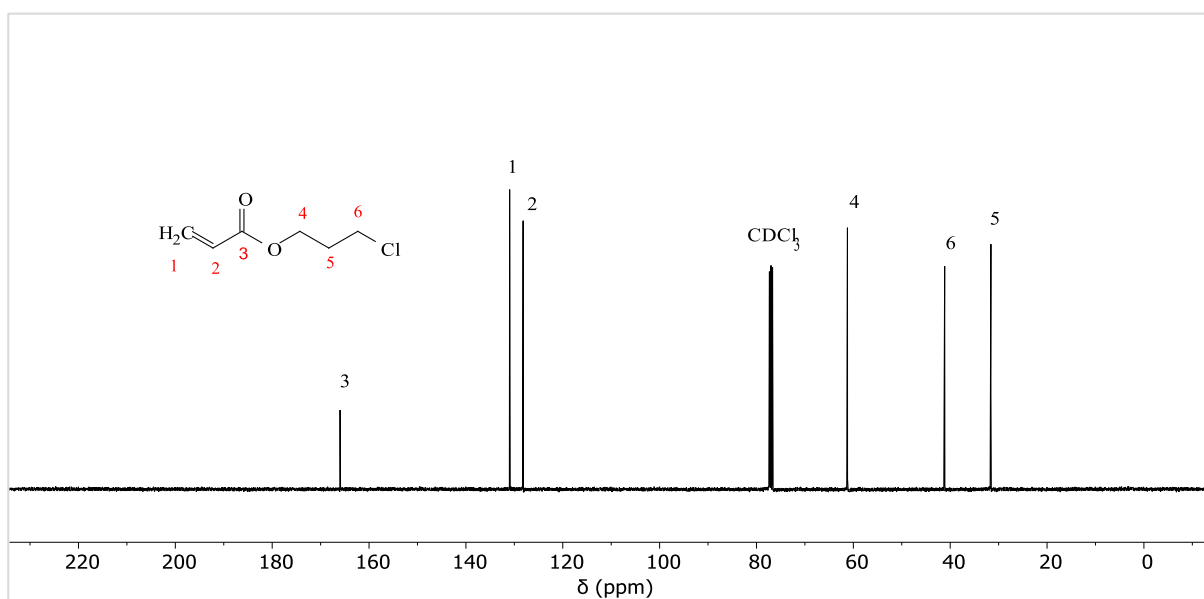
Figure S 3. ^{13}C NMR spectrum of **2** in CDCl$_3$.
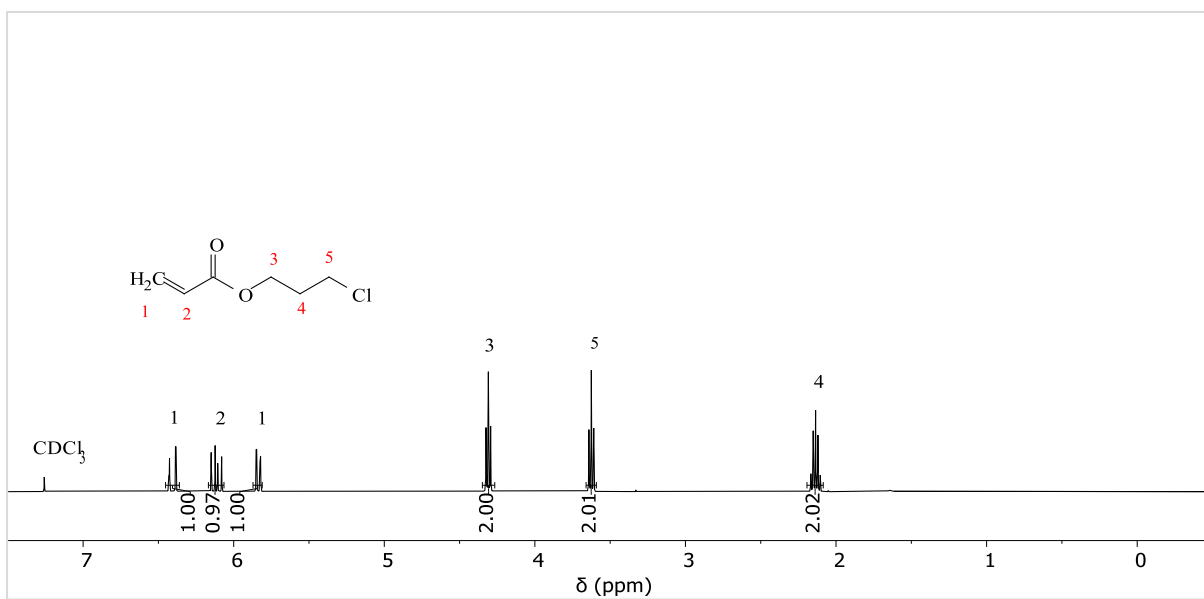
Figure S 4. ^{1}H NMR spectrum of **2** in CDCl$_3$.

169
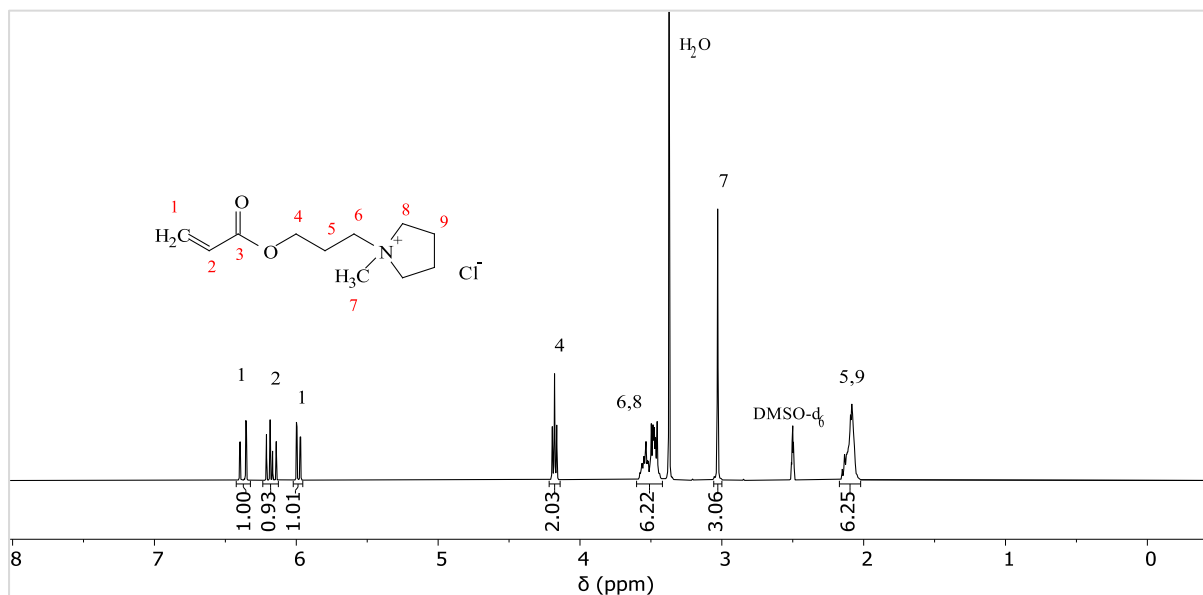
Figure S 5. ^{1}H NMR spectrum of **3** in DMSO-d$_6$.
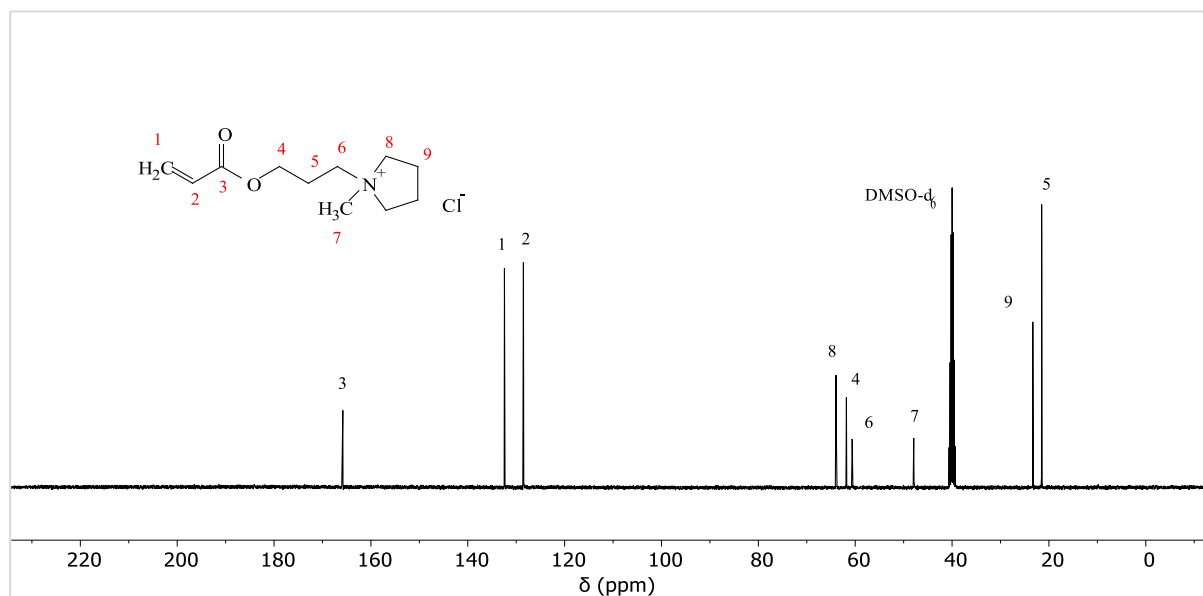
Figure S 6. ^{13}C NMR spectrum of **3** in DMSO-d$_6$.
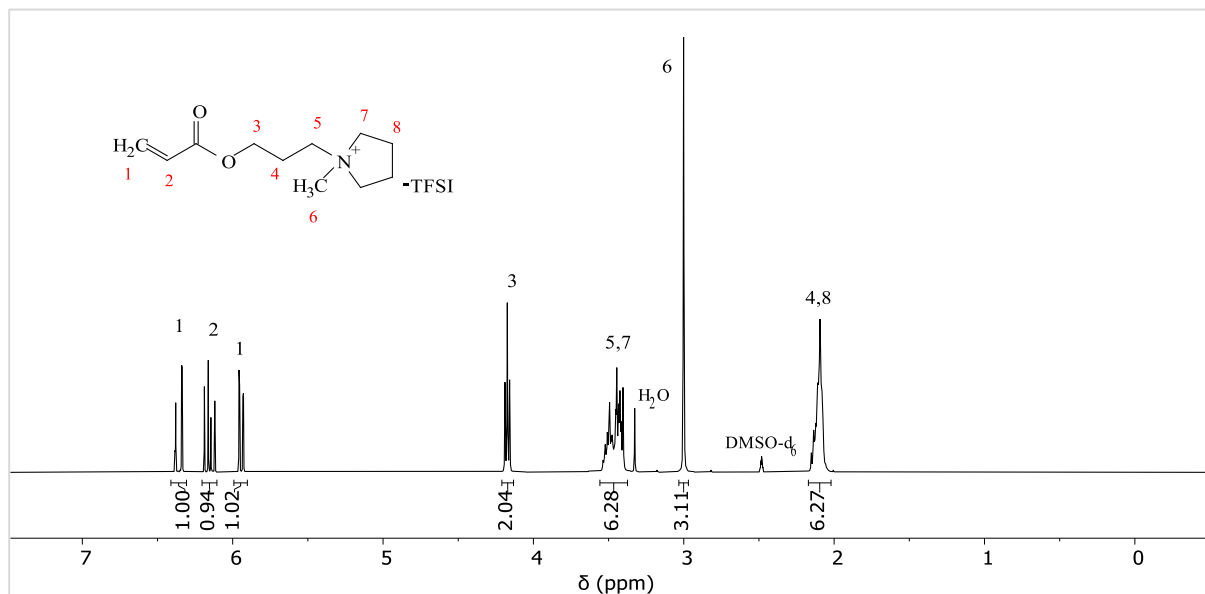
Figure S 7. ^{1}H NMR spectrum of **4** in DMSO-d$_6$.
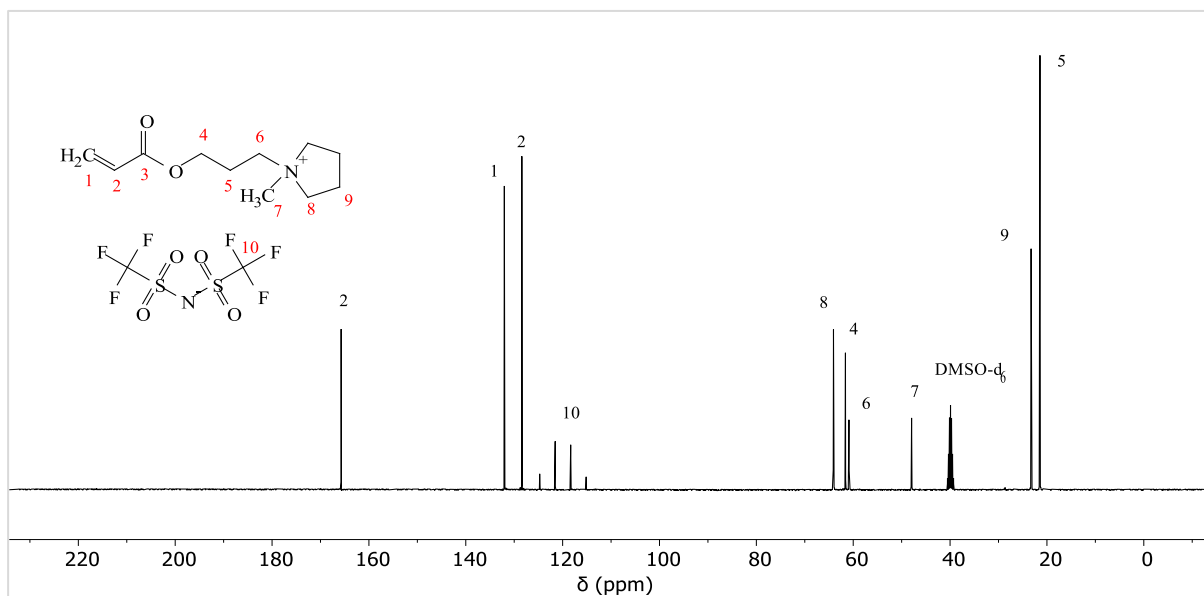
Figure S 8. ^{13}C NMR spectrum of **4** in DMSO-d$_6$.
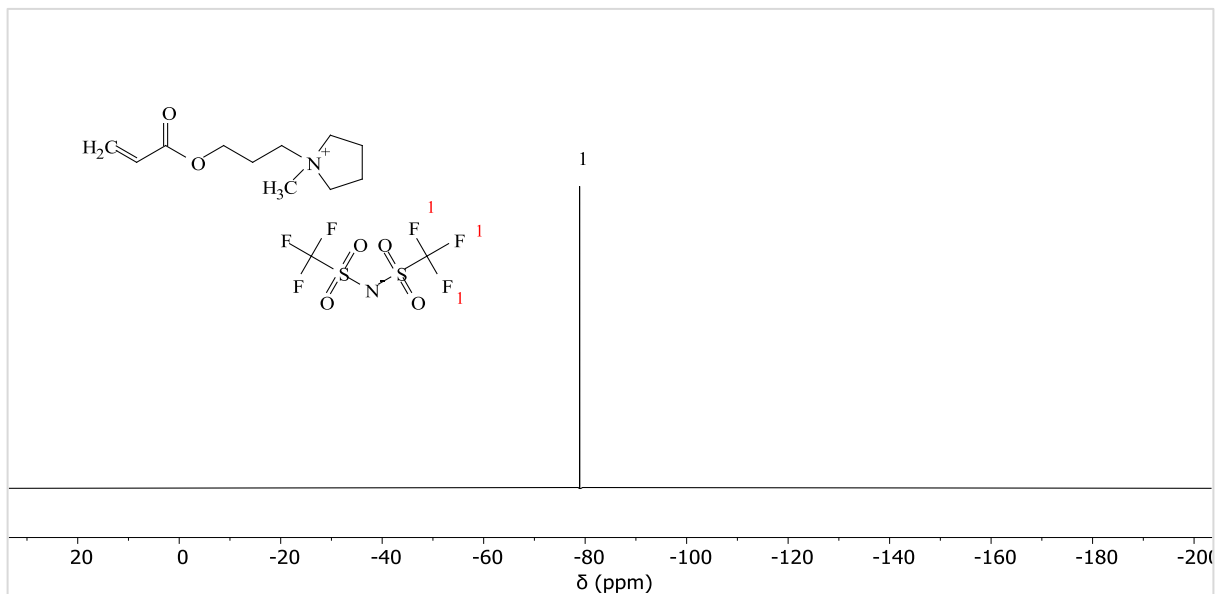
Figure S 9. ^{19}F NMR spectrum of **4** in DMSO-d$_6$.
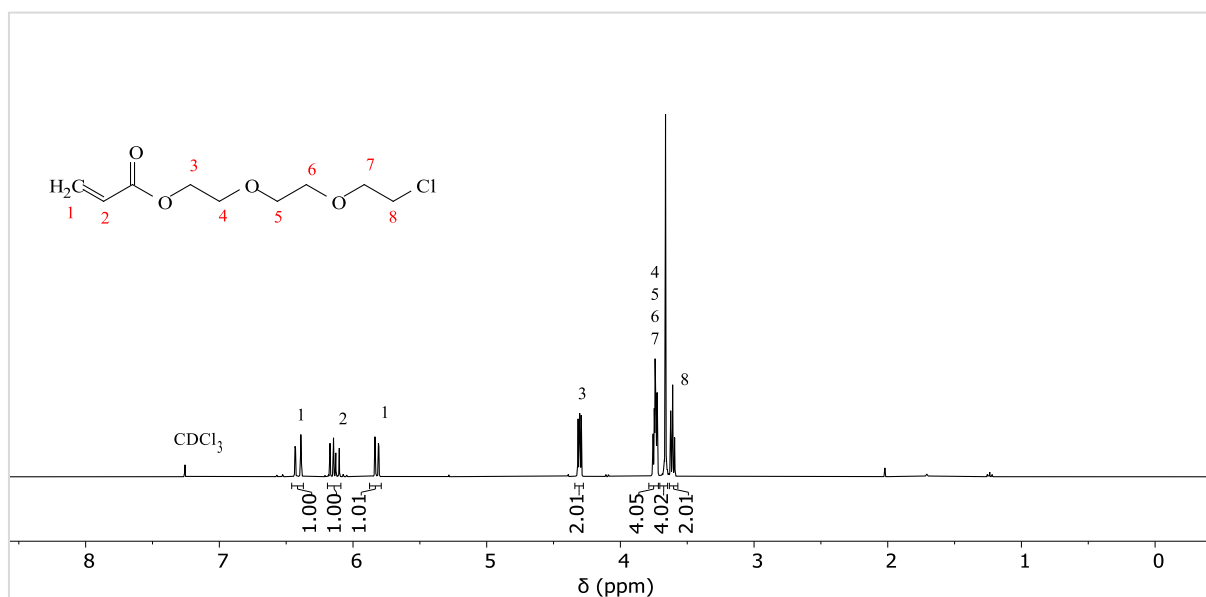
Figure S 10. ^{1}H NMR spectrum of **5** in CDCl$_3$.
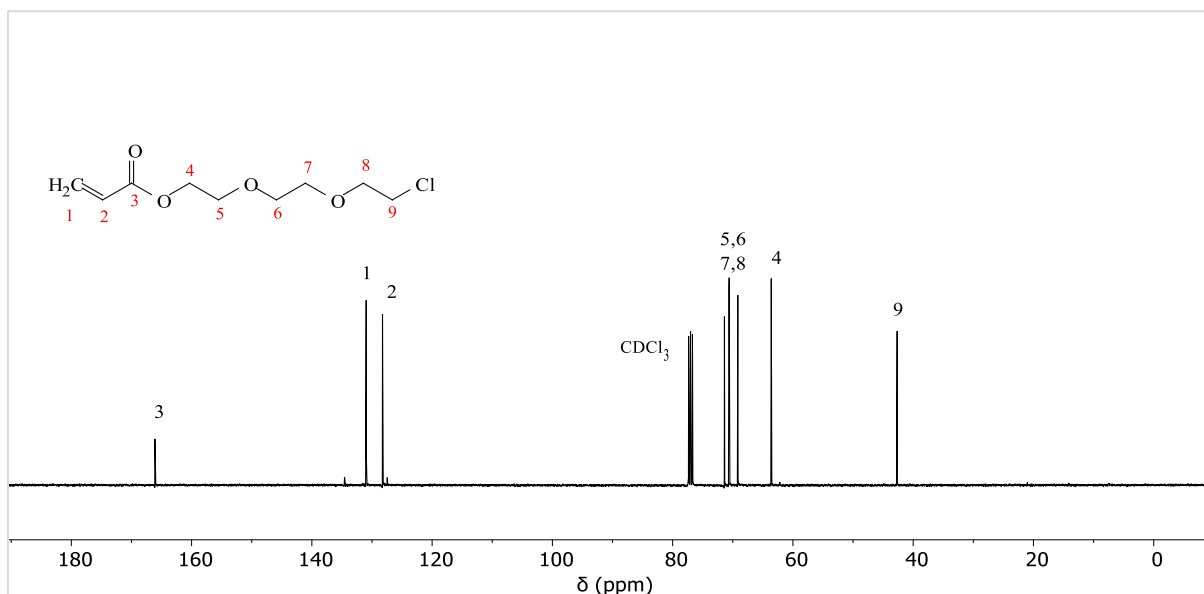
Figure S 11. ^{13}C NMR spectrum of **5** in CDCl$_3$.
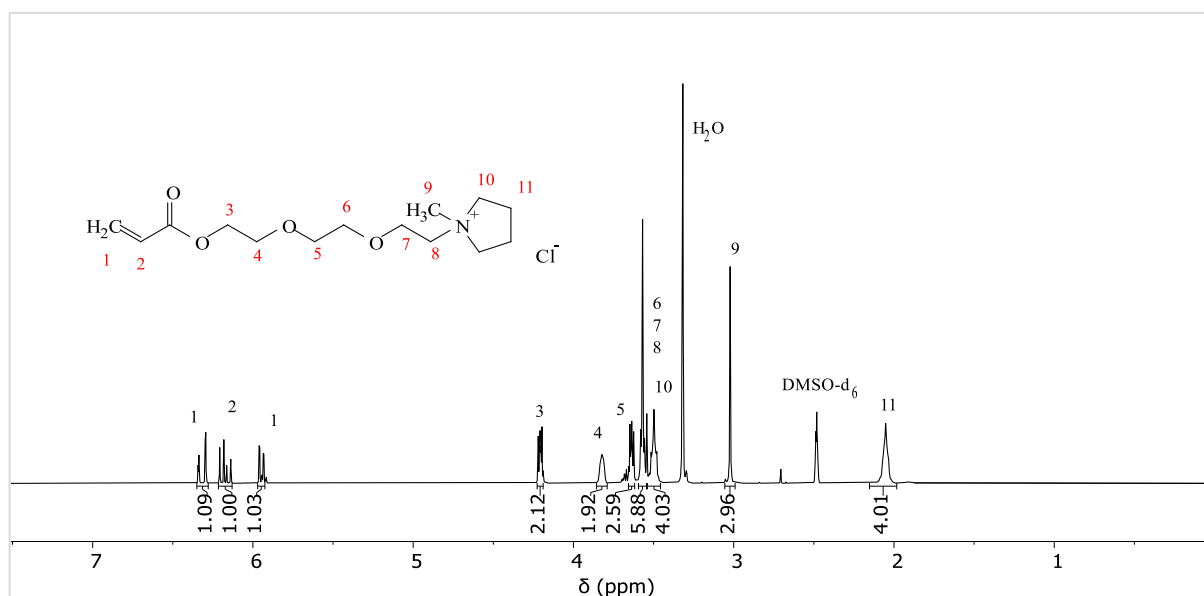
Figure S 12. ^{1}H NMR spectrum of **6** in DMSO-d$_6$.

173
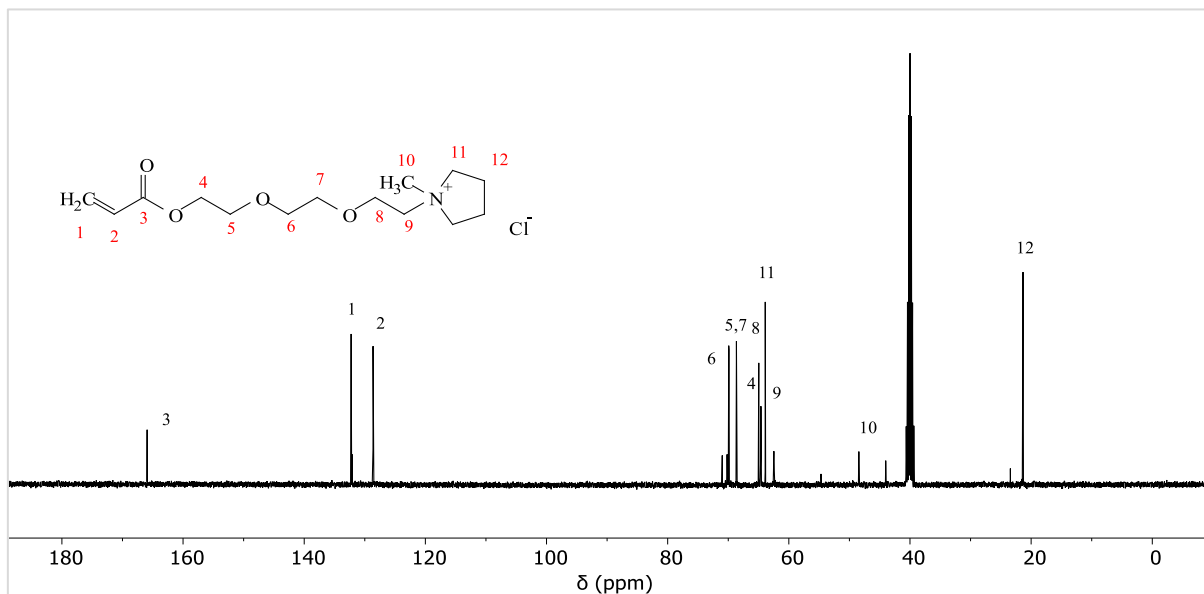
Figure S 13. ^{13}C NMR spectrum of **6** in DMSO-d$_6$.
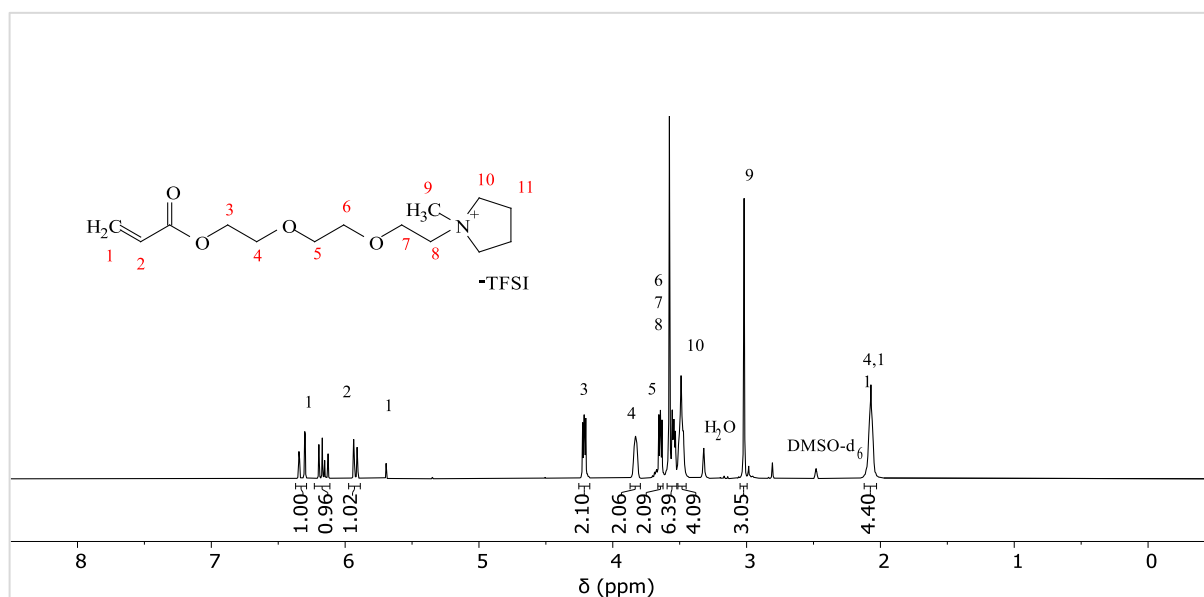
Figure S 14. ^{1}H NMR spectrum of **7** in DMSO-d$_6$.
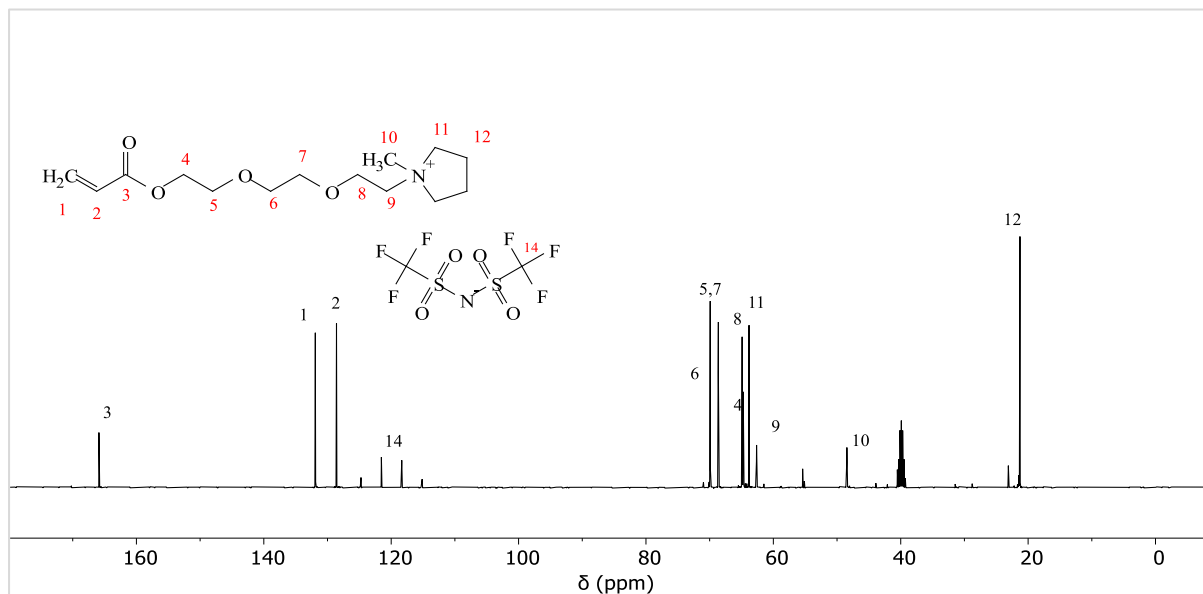
Figure S 15. ^{13}C NMR spectrum of **7** in DMSO-d$_6$.
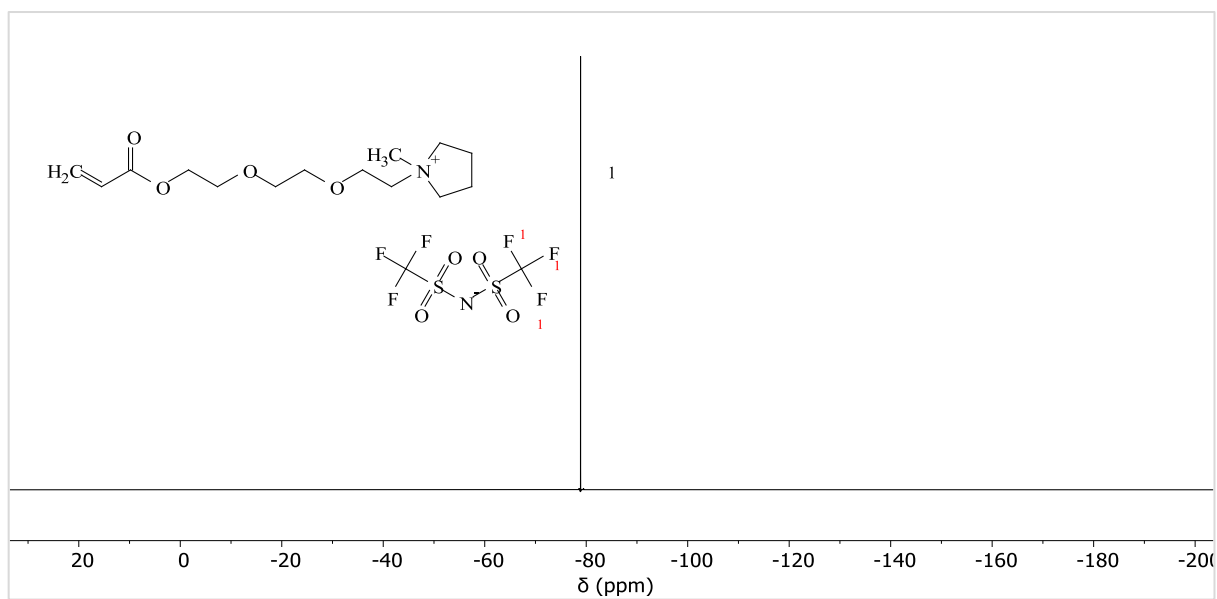
Figure S 16. ^{19}F NMR spectrum of **7** in DMSO-d$_6$.
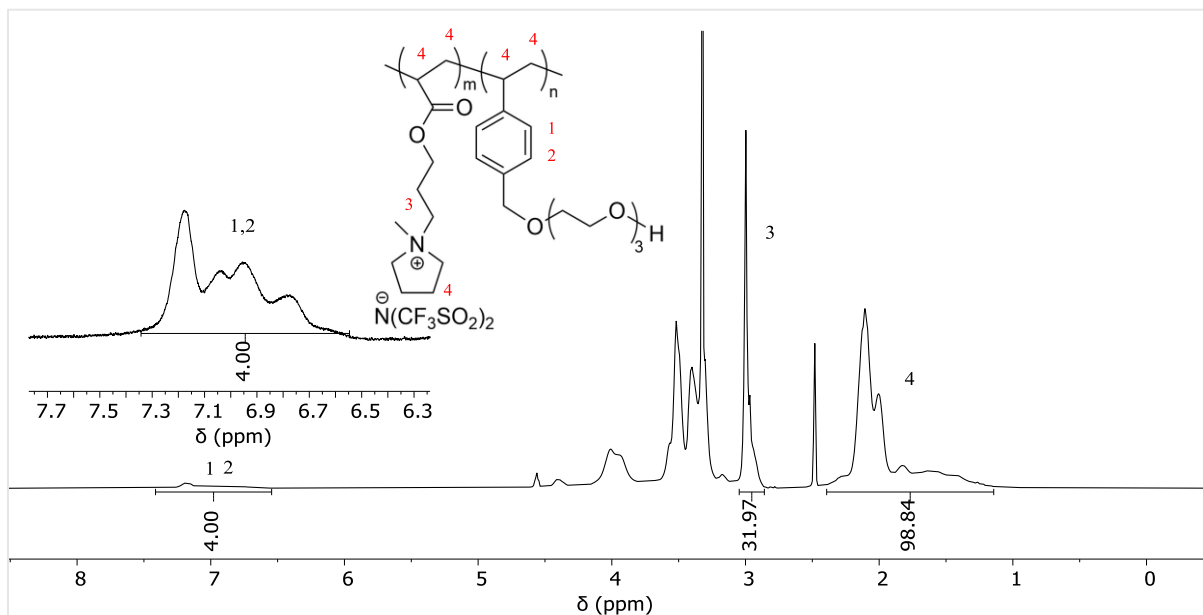
Figure S 17. ^{1}H NMR spectrum of **PIL-1A** in DMSO-d$_6$.
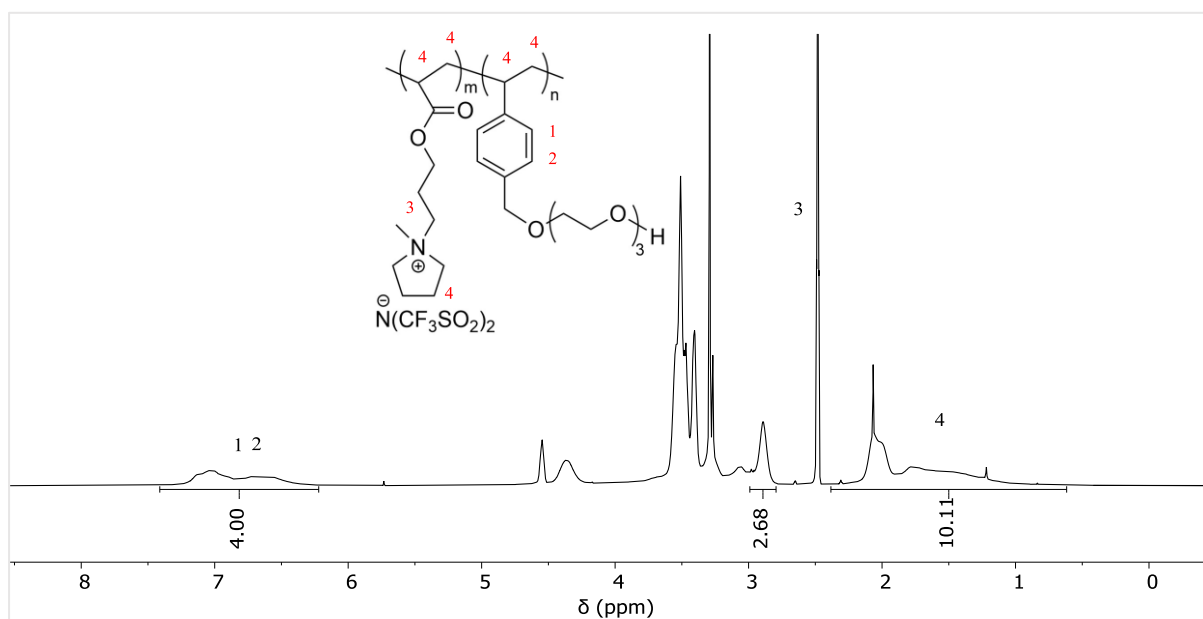
Figure S 18 ^{1}H NMR spectrum of **PIL-1B** in DMSO-d$_6$.
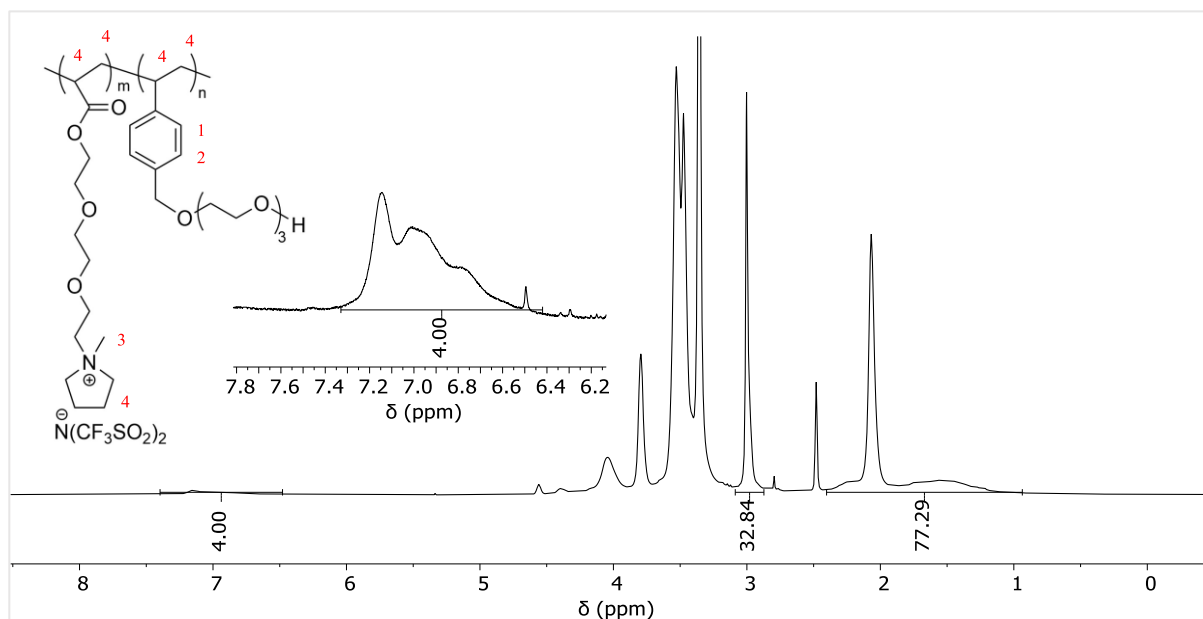
Figure S 19. ^{1}H NMR spectrum of **PIL-2** in DMSO-d$_6$.
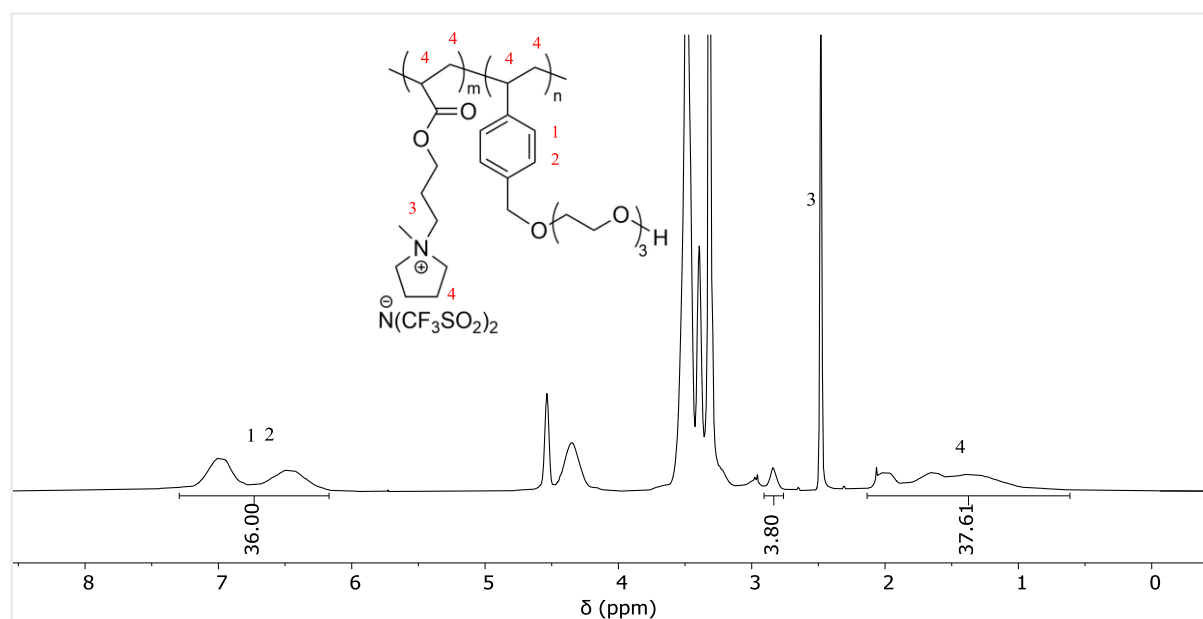
Figure S 20. ^{1}H NMR spectrum of **PIL-1C** in DMSO-d$_6$.
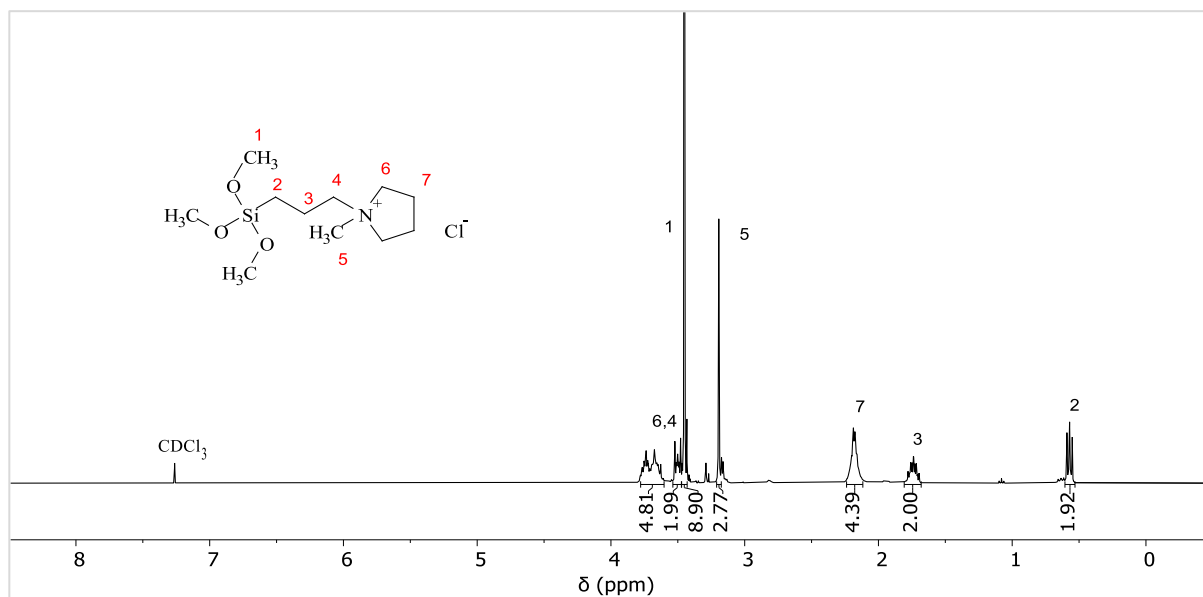
Figure S 21. ^{1}H NMR spectrum of **10** in CDCl$_3$.
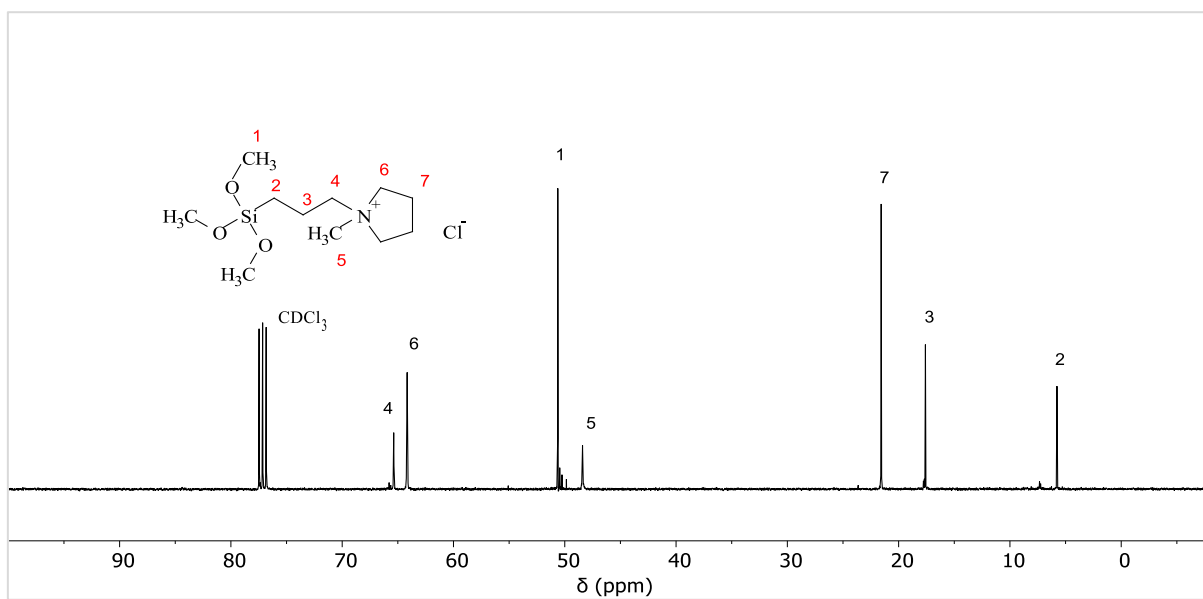
Figure S 22. ^{13}C NMR spectrum of **10** in CDCl$_3$.
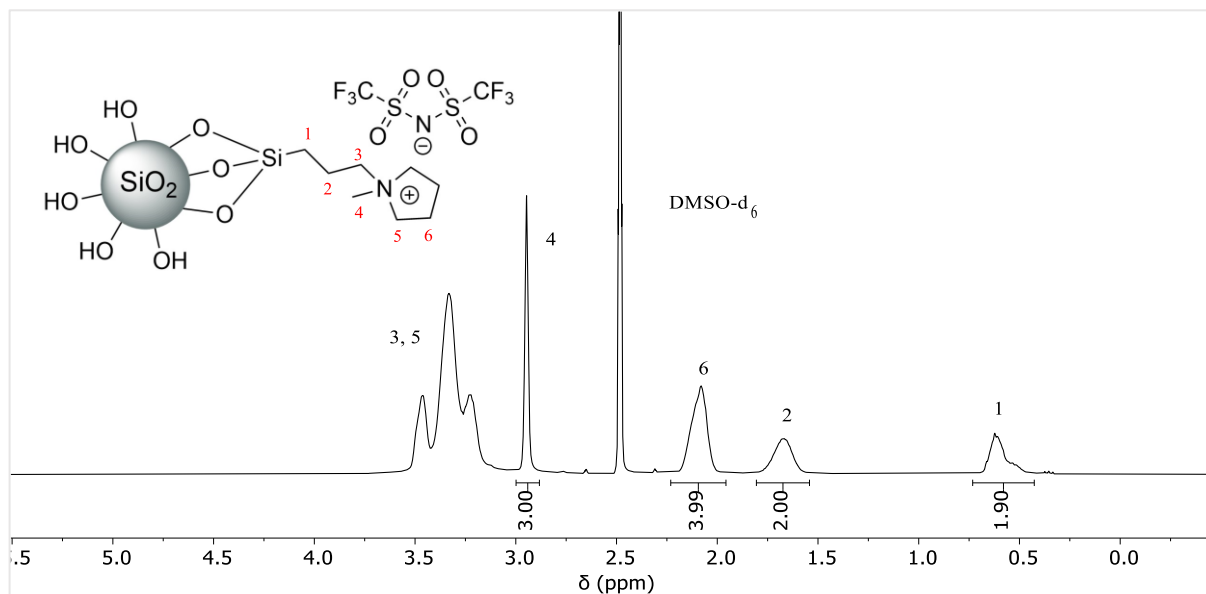
Figure S 23. ^{1}H NMR spectrum of **NP-IL** in DMSO-d$_6$.
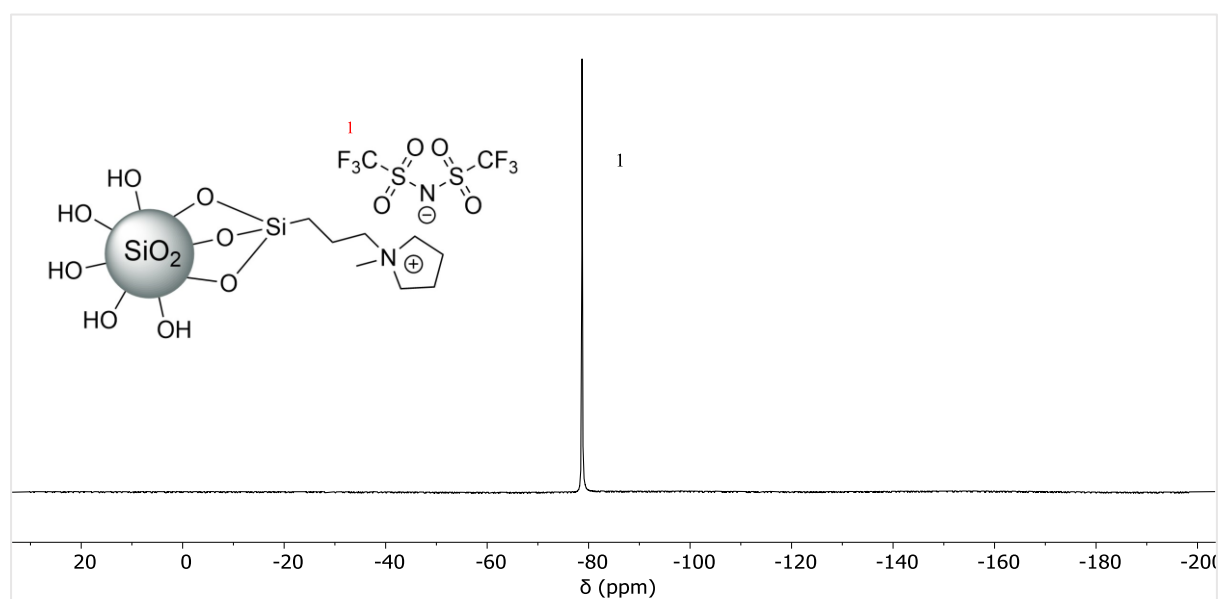
Figure S 24. ^{19}F NMR spectrum of **NP-IL** in DMSO-d$_6$.
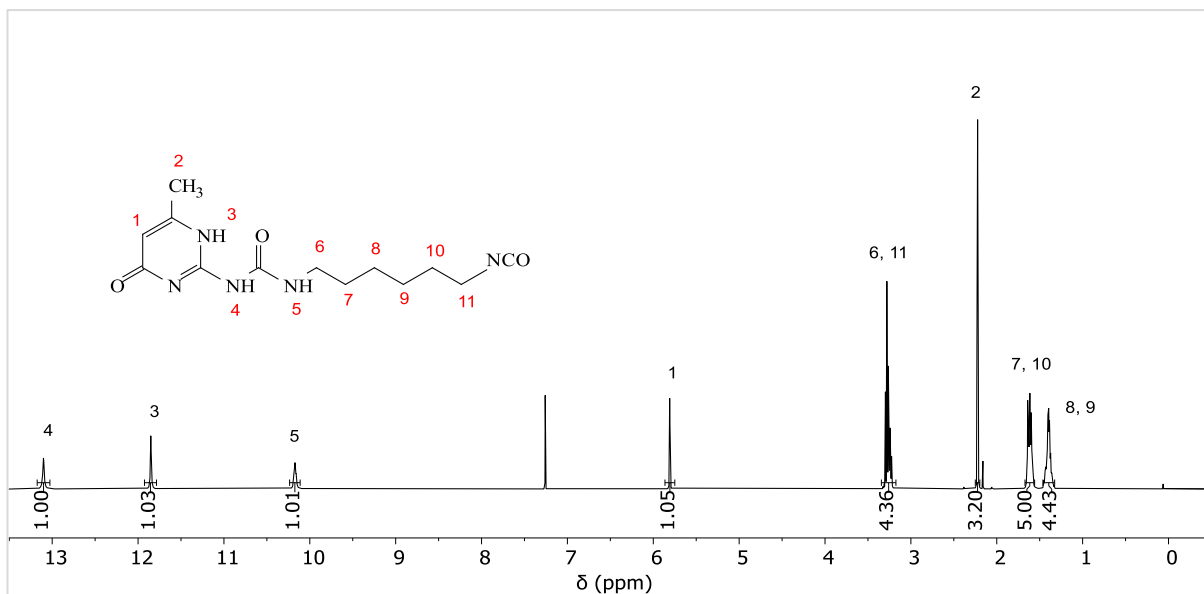
Figure S 25. ^{1}H NMR spectrum of UPy isocyanate **13** in CDCl$_3$.
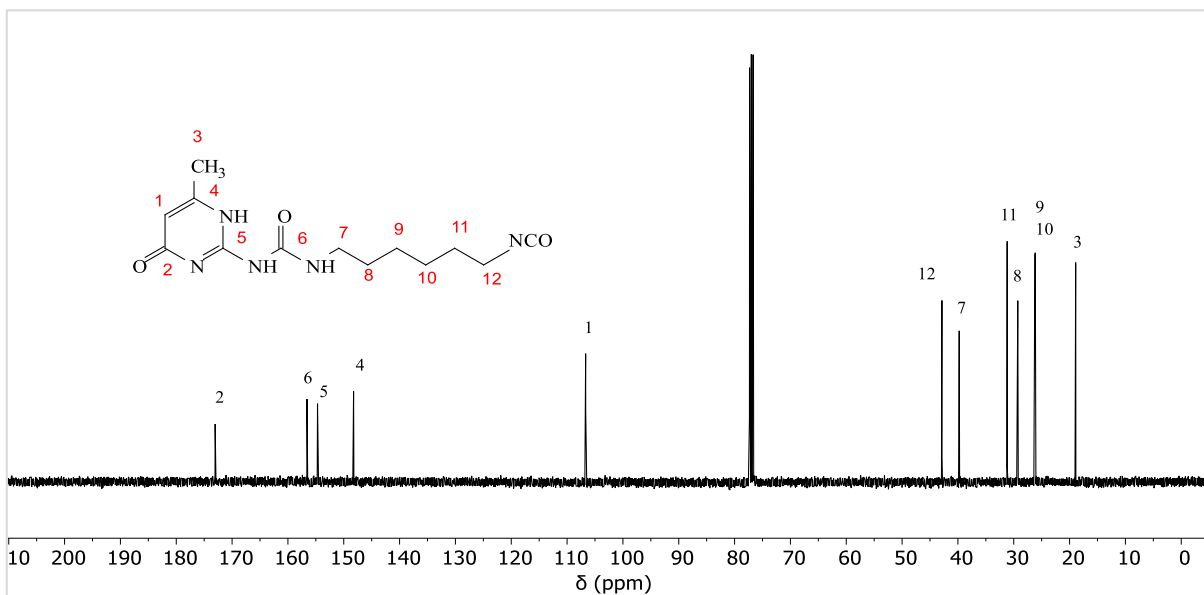
Figure S 26. ^{13}C NMR spectrum of UPy isocyanate **13** in CDCl$_3$.
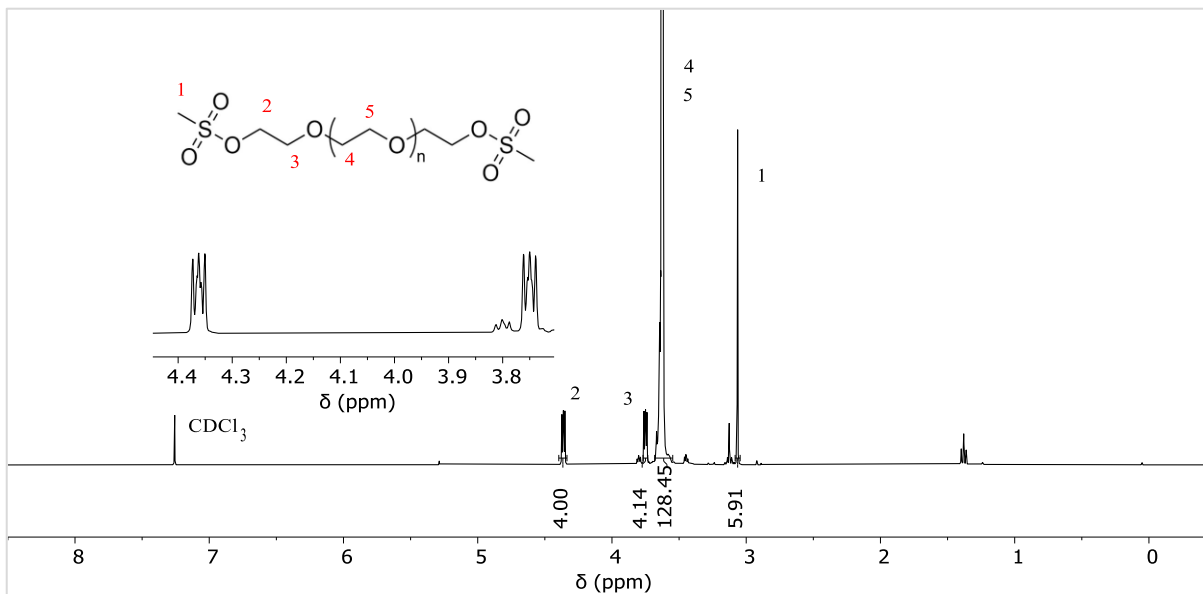
Figure S 27. ^{1}H NMR spectrum of **14** in CDCl$_3$.
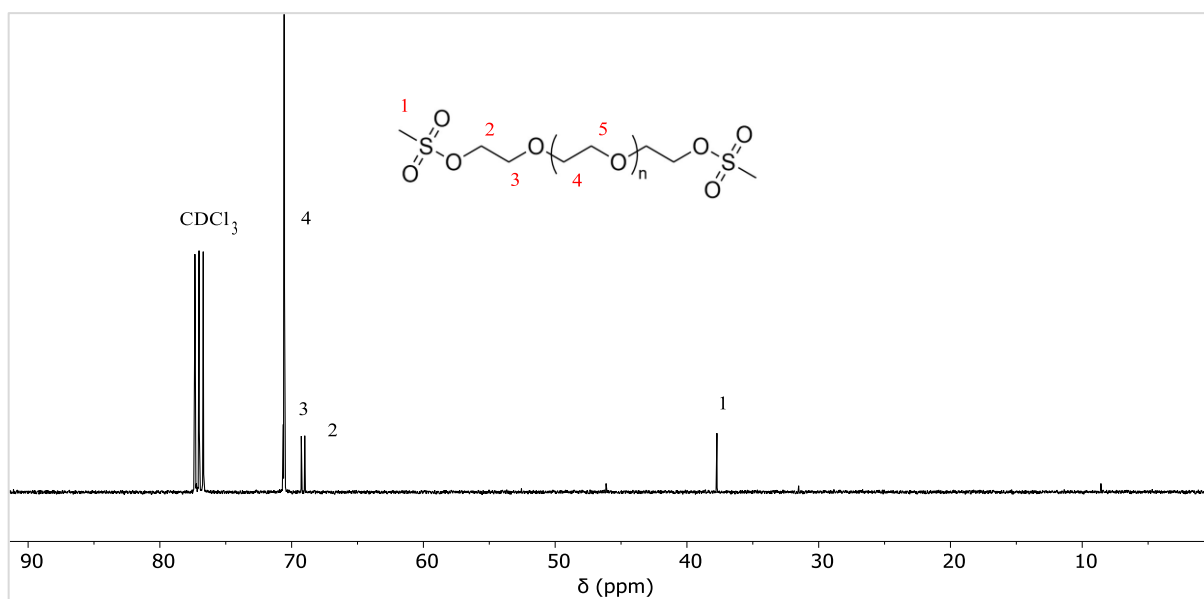
Figure S 28. ^{13}C NMR spectrum of **14** in CDCl$_3$.
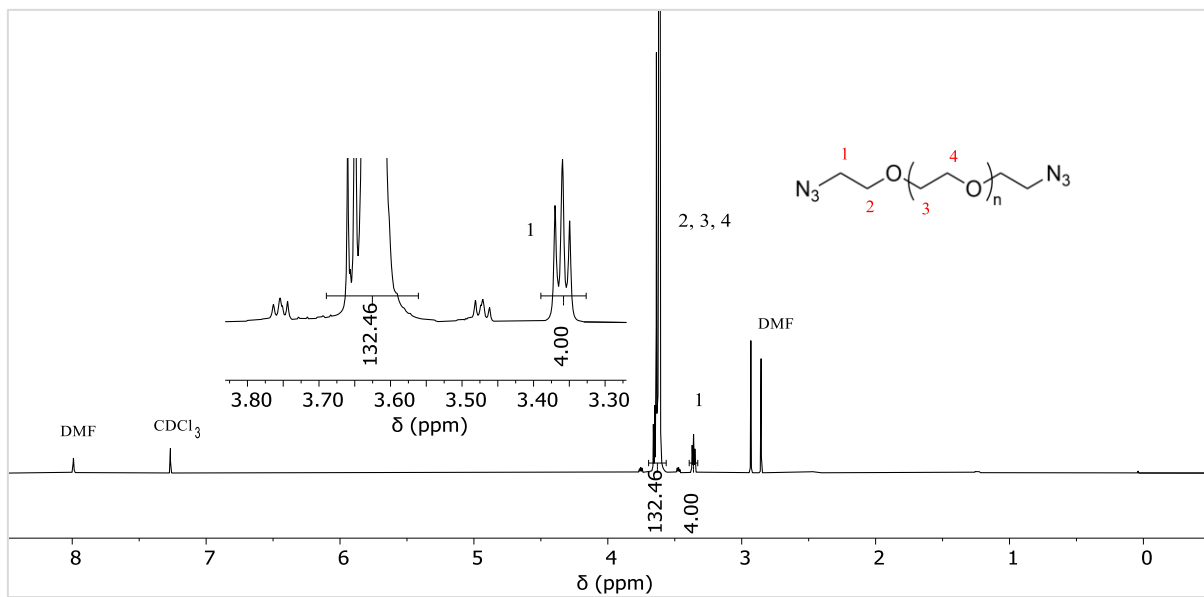
Figure S 30. ^{1}H NMR spectrum of **15** in CDCl$_3$.
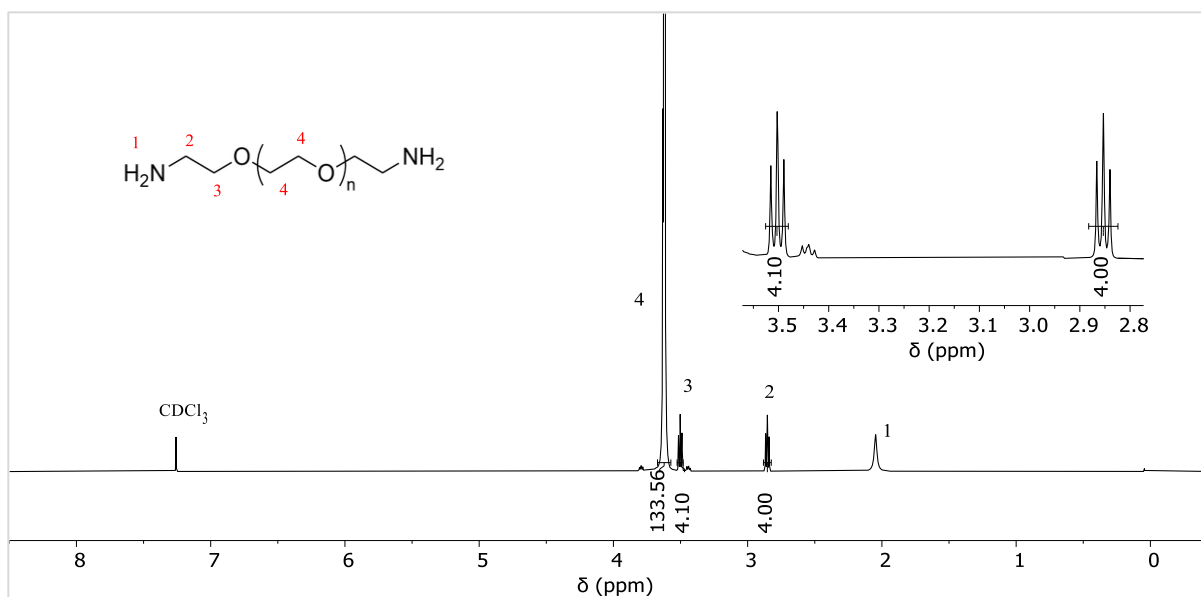
Figure S 29. ^{1}H NMR spectrum of **16** in CDCl$_3$.
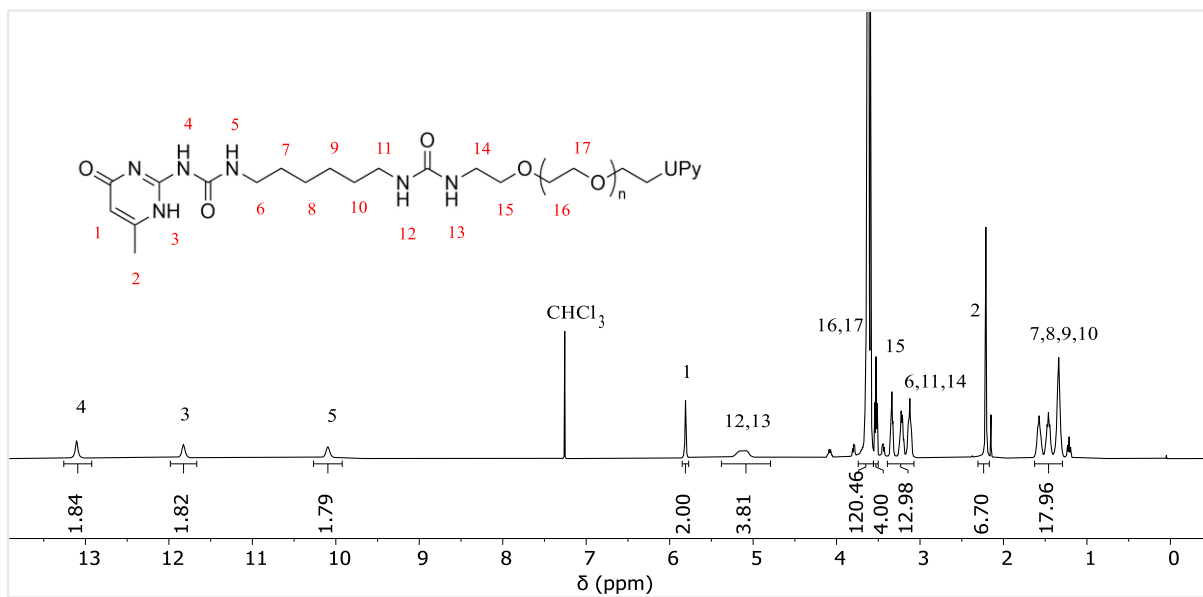
Figure S 31. ^{1}H NMR spectrum of **PEG-UPy** in CDCl$_3$.
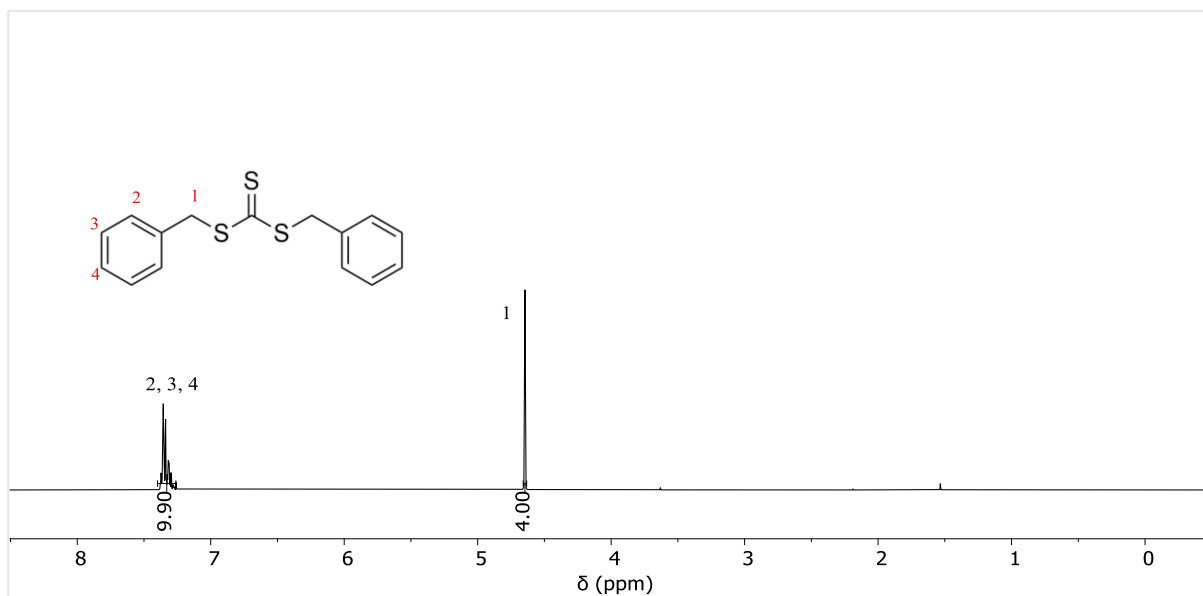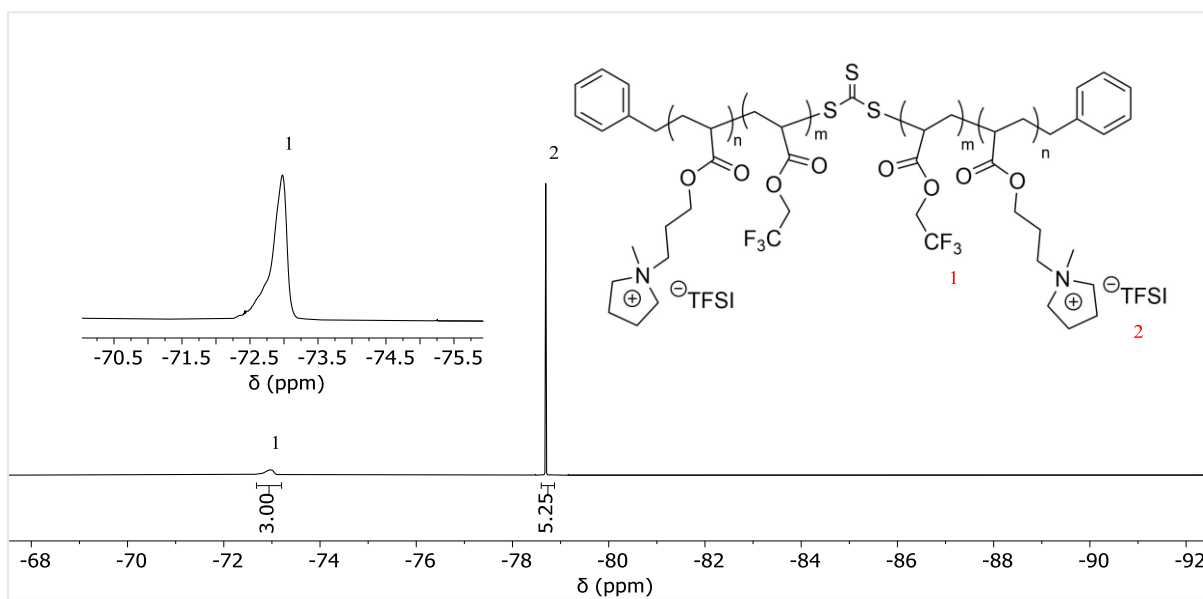

Figure S 32. ^{1}H NMR spectrum of **16** in CDCl$_3$.
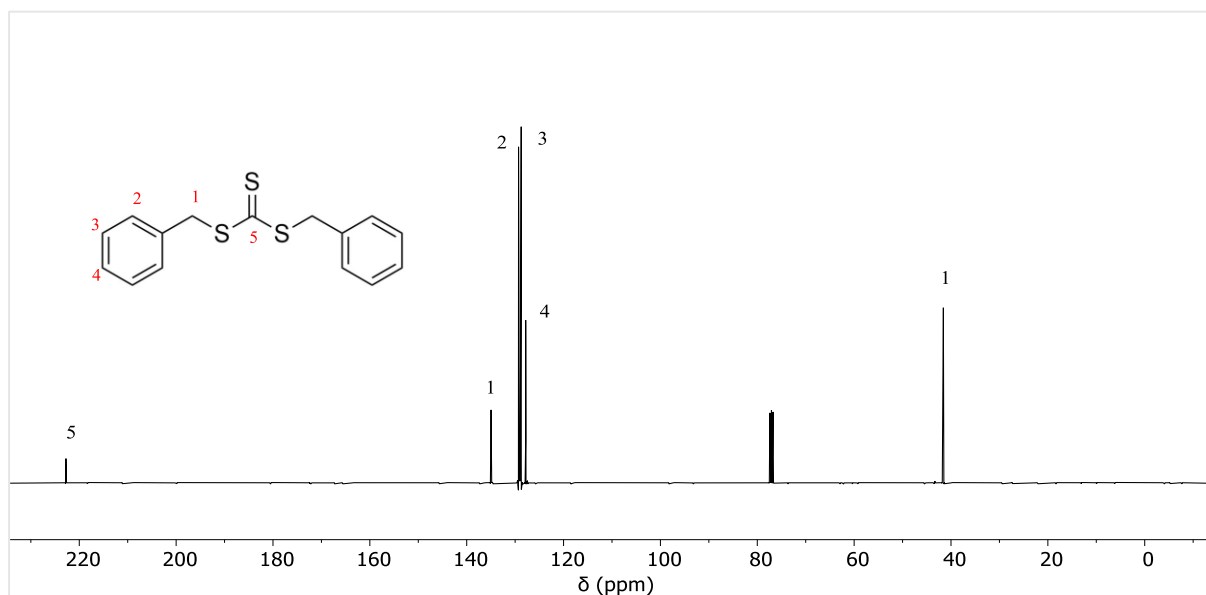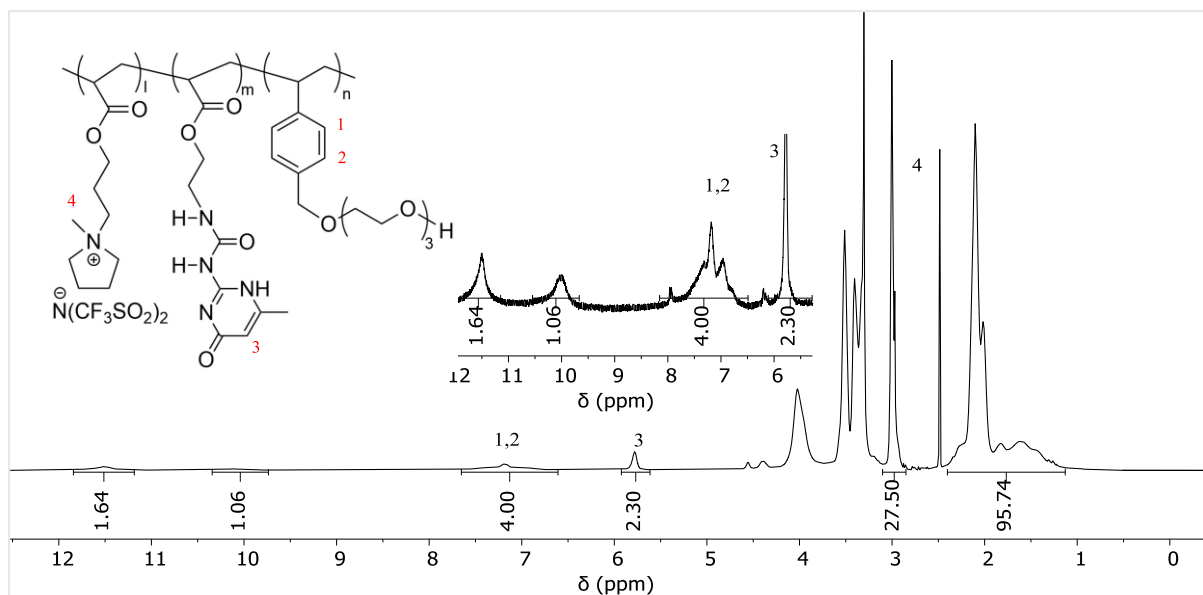
Figure S 33. ^{13}C NMR spectrum of **16** in CDCl$_3$.
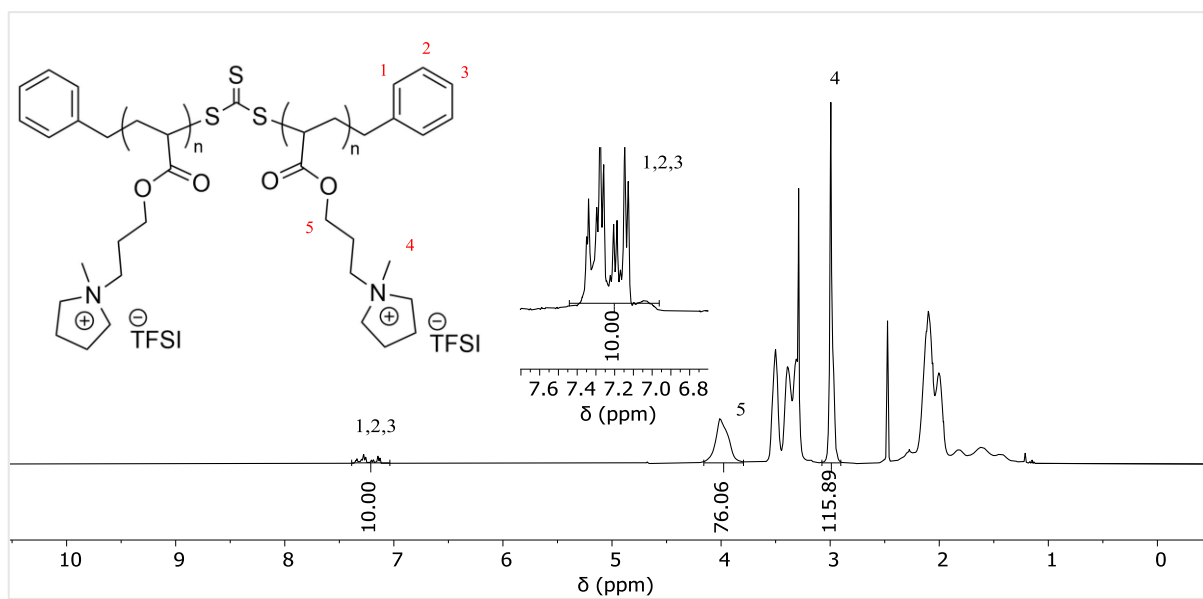
Figure S 34. ^{1}H NMR spectrum of **PIL-H** in DMSO-d$_6$.
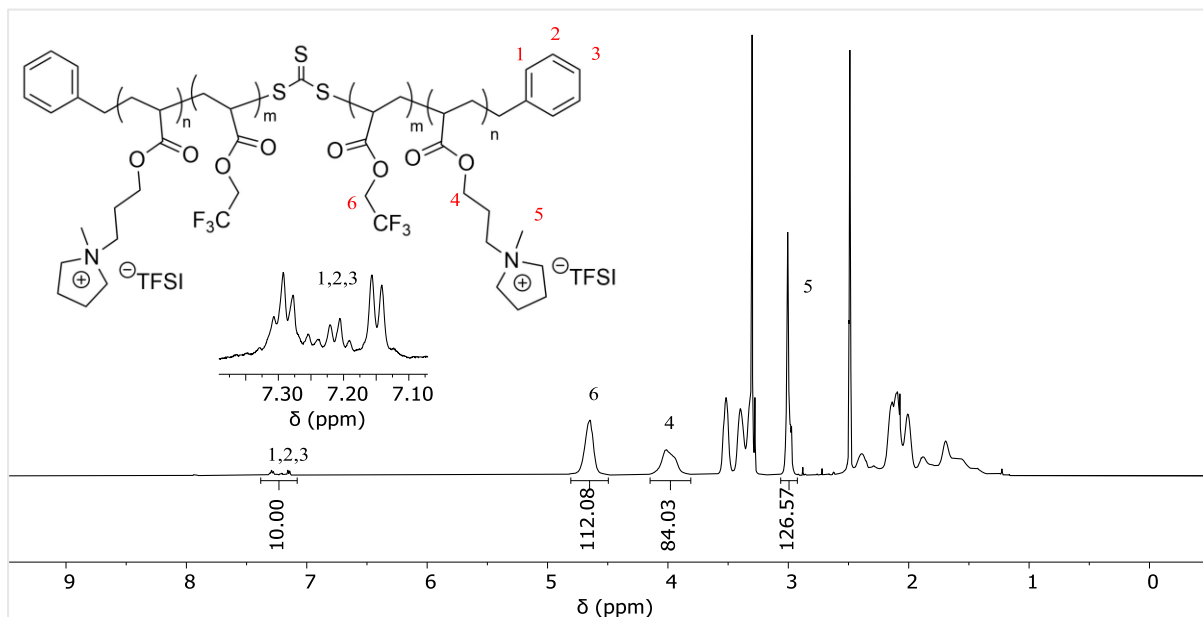
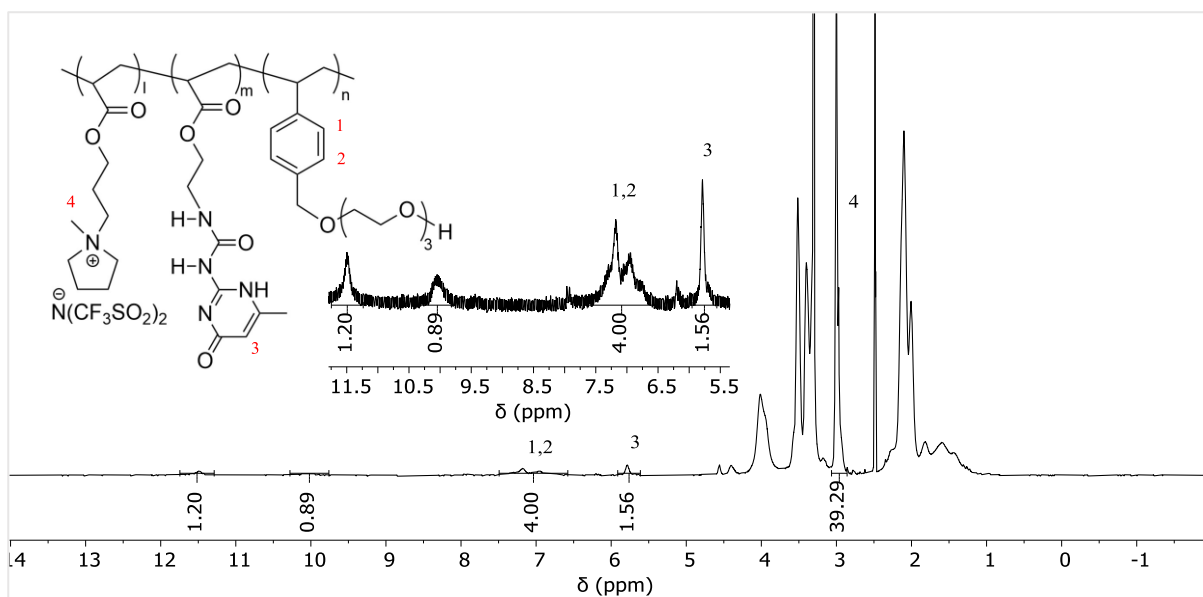**Figure S 35.** ^{1}H NMR spectrum of **PIL-S** in DMSO-d$_6$.

Figure S 36. ^{19}F NMR spectrum of **PIL-S** in DMSO-d$_6$.

Figure S 37. ^{1}H NMR spectrum of **PIL-3B** in DMSO-d[6].
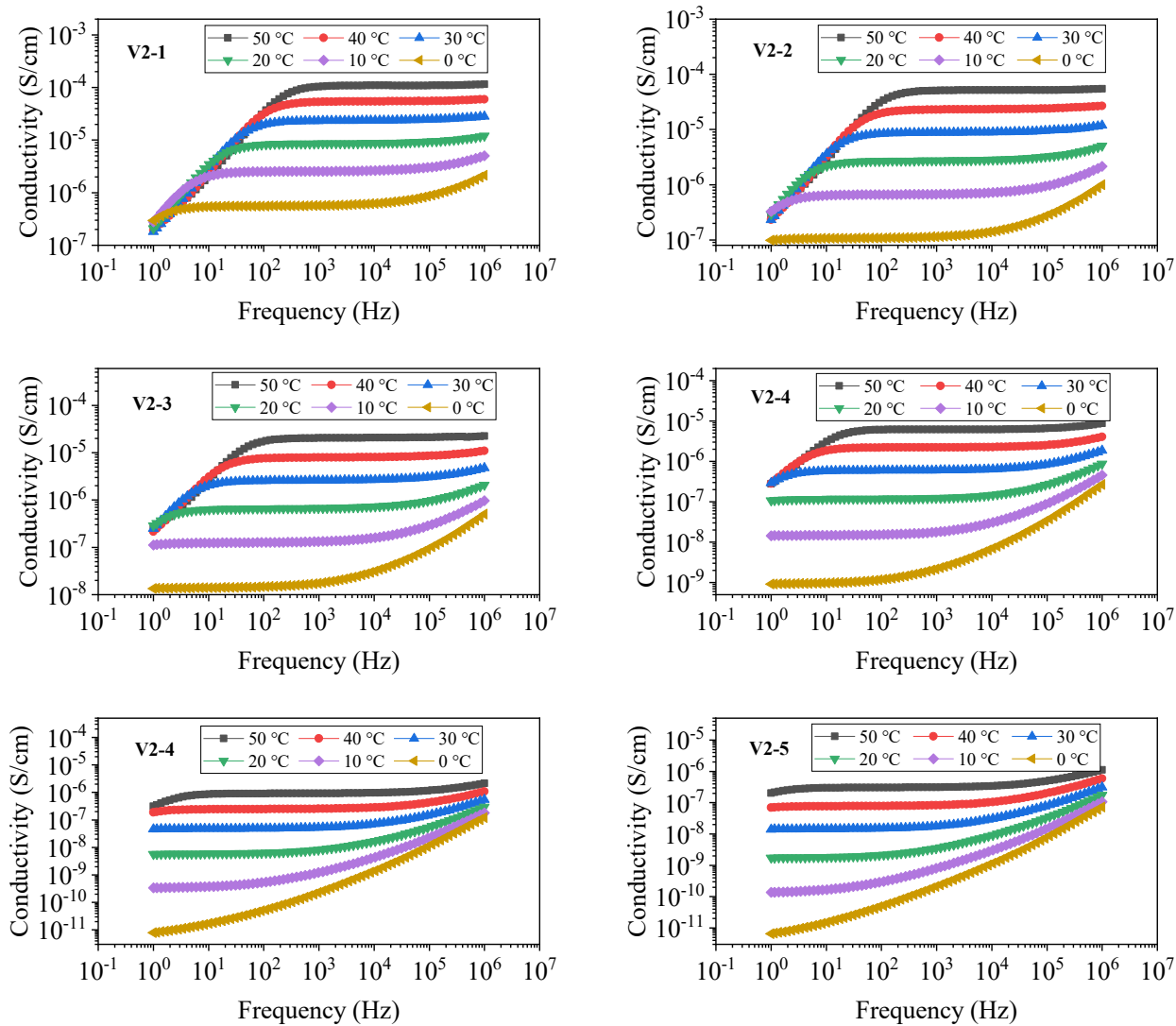

Figure S 38. ^{1}H NMR spectrum of **PIL-3A** in DMSO-d[6].
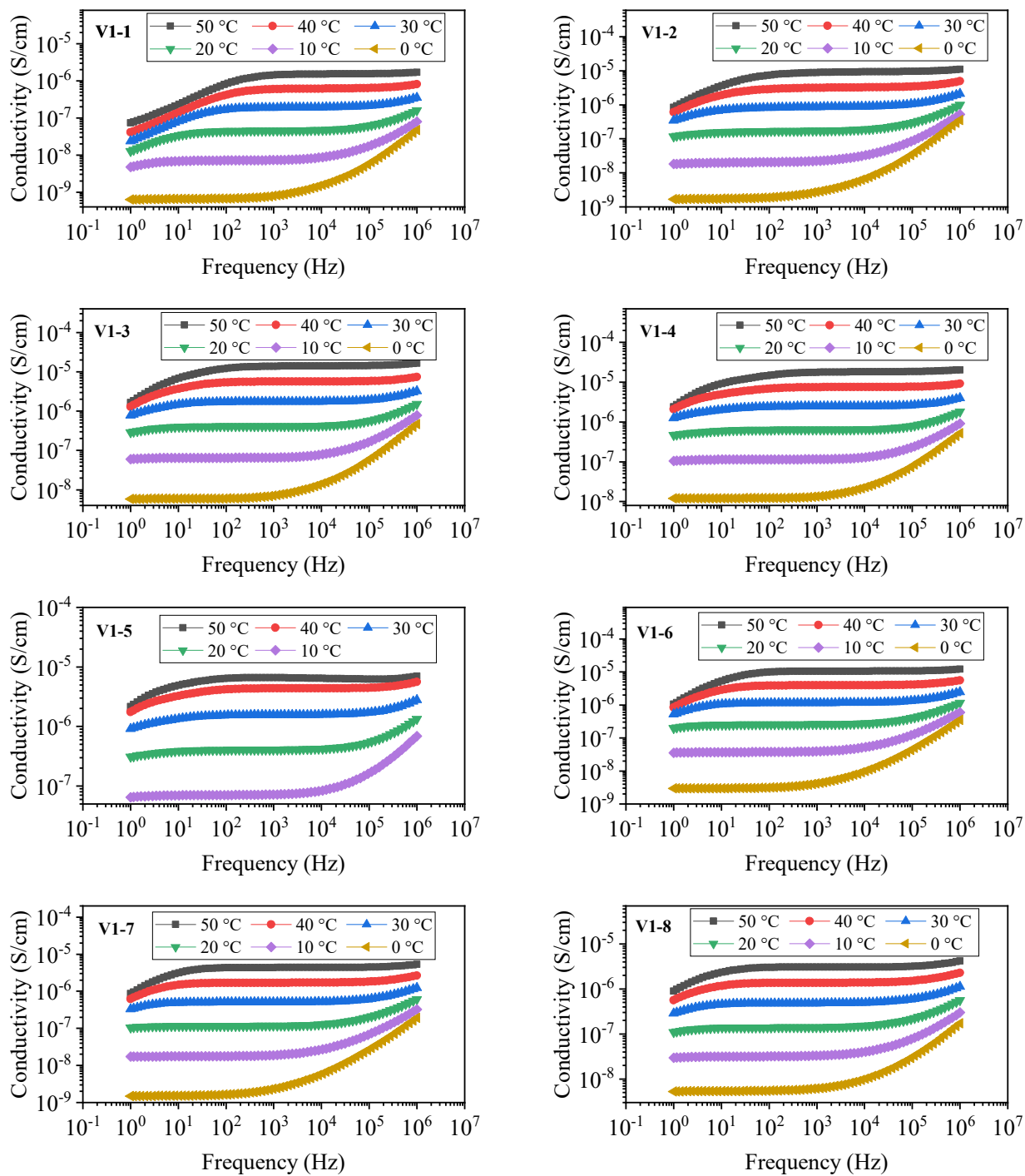
Figure S 39. BDS measurements of **V1-1 − V1-8** in the temperature range of 0°C to 50 °C with 10 °C increments, the frequency range between 1 to 10^6 Hz.
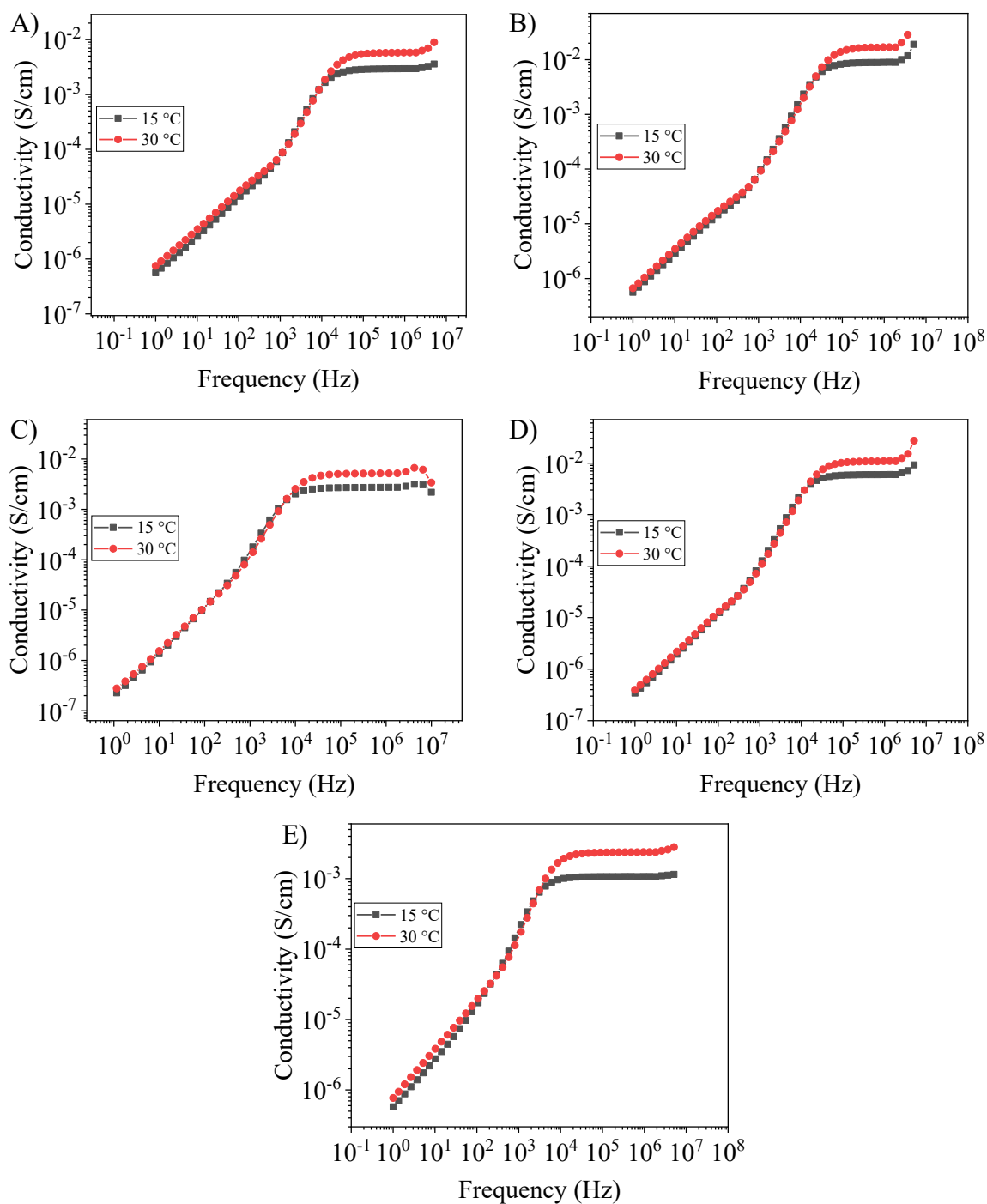
Figure S 40. BDS measurements of **V2-1 – V2-5** in the temperature range of 0 °C to 50 °C with 10 °C increments, the frequency range between 1 to 10^6 Hz.

Figure S 41. BDS measurement of A) 1-Methyl-1-propylpyrrolidinium bis(trifluoromethyl sulfonyl)imide, B) 1-Methyl-1-propylpyrrolidinium bis(fluorosulfonyl)imide, C) 1-(2-Methoxyethyl)-1-methylpropyl pyrrolidinium bis(trifluoromethylsulfonyl)imide, D) 1-(2-Methoxyethyl)-1-methylpropyl pyrrolidinium bis(fluorosulfonyl)imide and E) N-Methyl-N-propyl morpholinium bis(fluorosulfonyl)imide.

Table S 2. Viscosities of **FIL-FSI**, **FIL-TFSI**, **NFIL-TFSI** and **NFIL-FSI** with corresponding salt mixtures at different temperatures.

Ionic liquid	Lithium salt-Concentration (M)	Viscosity (mPa × s)								
		-10 °C	0 °C	10 °C	20 °C	30 °C	40 °C	50 °C	60 °C	70 °C
FIL-FSI	LiFSI - 0	27225	10468	4533	2192	1166	669	411	268	181
FIL-FSI	LiFSI - 0.1	28883	10966	4676	2240	1186	679	421	273	183
FIL-FSI	LiFSI - 0.25	30279	11394	4817	2298	1214	690	421	273	185
FIL-FSI	LiFSI - 0.5	35657	13047	5392	2542	1320	747	453	292	196
FIL-FSI	LiFSI - 0.75	41767	14885	6037	2791	1434	802	483	308	207
FIL-FSI	LiFSI - 1	48490	16768	6643	3017	1529	849	508	325	221
FIL-FSI	LiFSI - 1.25	57192	19392	7563	3395	1702	936	554	350	231
FIL-TFSI	LiTFSI - 0	51336	16389	6114	2645	1292	695	405	254	167
FIL-TFSI	LiTFSI - 0.1	65245	20211	7291	3077	1474	779	447	275	178
FIL-TFSI	LiTFSI - 0.25	108028	30743	10379	4173	1913	977	544	327	206
FIL-TFSI	LiTFSI - 0.5	316072	75086	22195	8008	3372	1606	845	484	298
FIL-TFSI	LiTFSI - 0.75	643808	135136	35778	11877	4691	2119	1067	588	342
FIL-TFSI	LiTFSI - 1	1909189	357373	77637	24469	8801	3686	1955	1019	577
FIL-TFSI	LiTFSI - 1.25	5535512	731752	147043	39401	13141	5198	2349	1186	645
NFIL-TFSI	LiTFSI - 0	-	157816	37004	11293	4224	1843	911	496	293
NFIL-TFSI	LiTFSI - 0.1	1156575	186065	42833	12880	4772	2067	1014	554	327
NFIL-TFSI	LiTFSI - 0.25	1474009	227839	51802	15367	5599	2393	1163	626	367
NFIL-TFSI	LiTFSI - 0.5	2235108	322904	70856	20384	7218	3021	1435	755	435
NFIL-TFSI	LiTFSI - 0.75	2443855	365951	84369	25506	9726	4285	1953	1004	568
NFIL-TFSI	LiTFSI - 1	6780323	858083	168610	47164	16458	6897	3315	1717	898
NFIL-FSI	LiFSI - 0	173193	44925	14158	5381	2365	1170	636	373	234
NFIL-FSI	LiFSI - 0.1	342963	83276	24734	8921	3769	1801	950	548	336
NFIL-FSI	LiFSI - 0.25	361011	88747	26493	9633	4075	1950	1032	593	367
NFIL-FSI	LiFSI - 0.5	332514	84584	25974	9616	4128	1998	1066	616	382
NFIL-FSI	LiFSI - 0.75	345734	89172	27767	10395	4494	2184	1169	678	421
NFIL-FSI	LiFSI - 1	355870	89392	27668	10321	4463	2168	1162	675	422
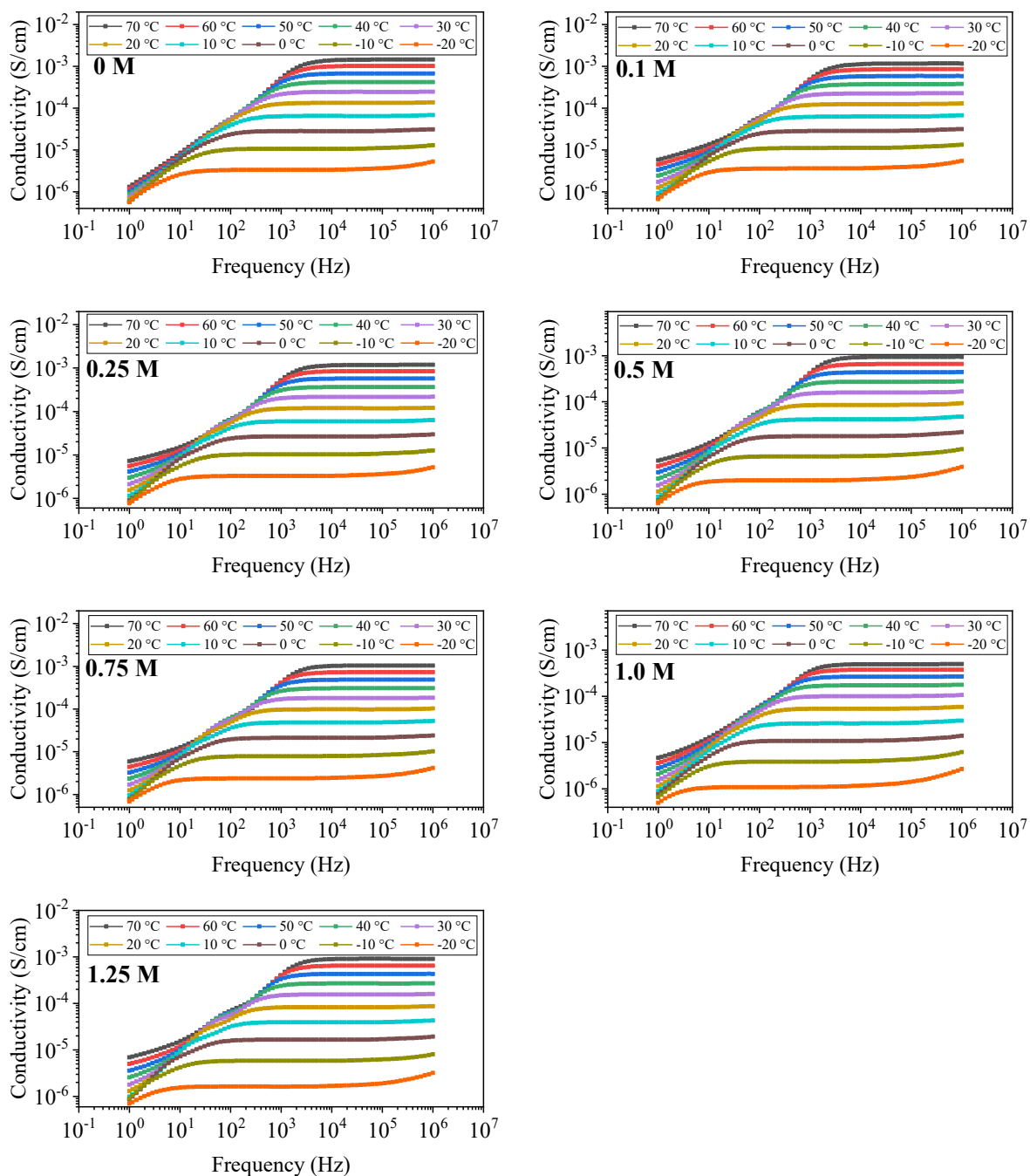
Figure S 42. BDS measurement of **FIL-FSI** with different content of LiFSI in the temperature range of -20 to 70 °C.
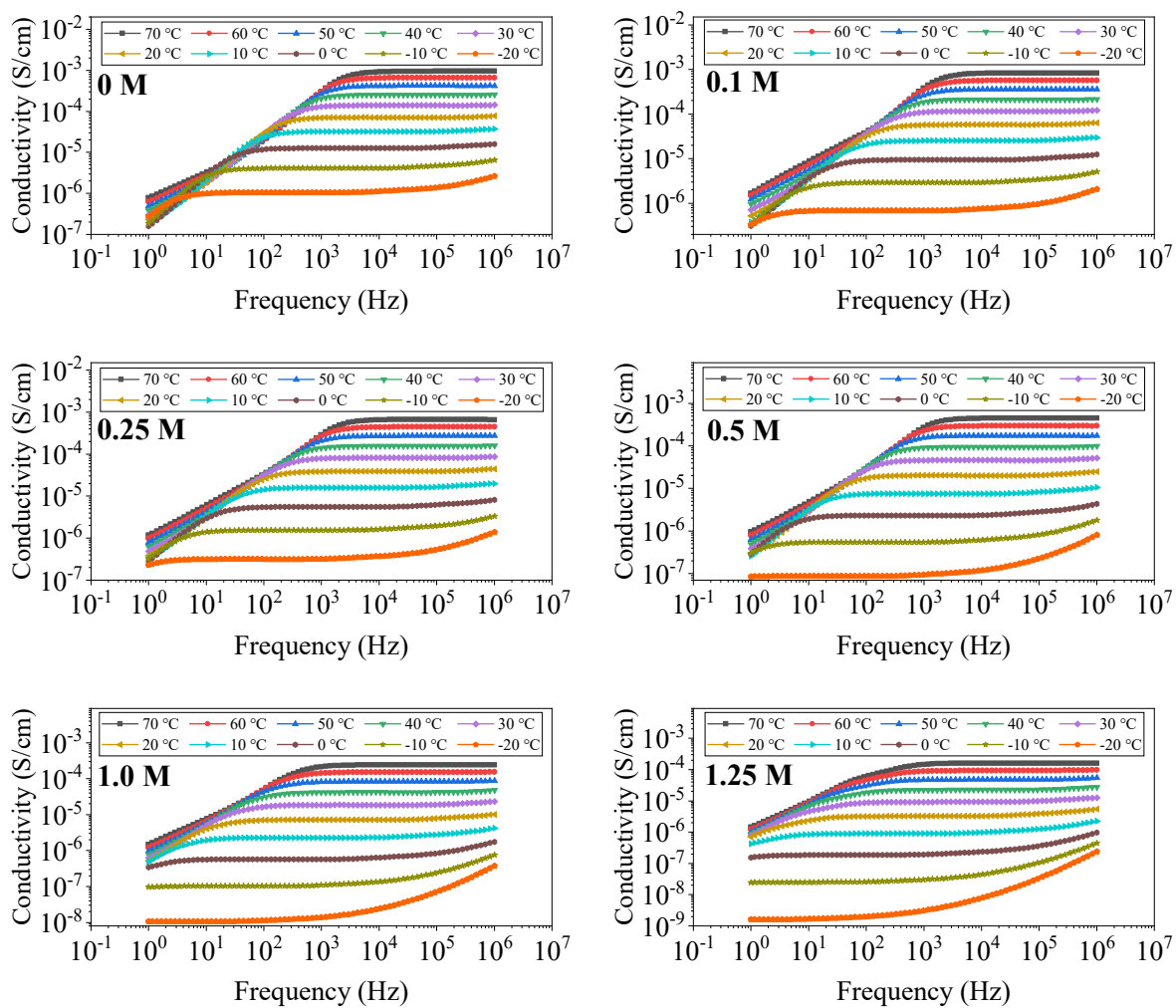
Figure S 43. BDS measurement of **FIL-TFSI** with different content of LiTFSI in the temperature range of -20 to 70 °C.
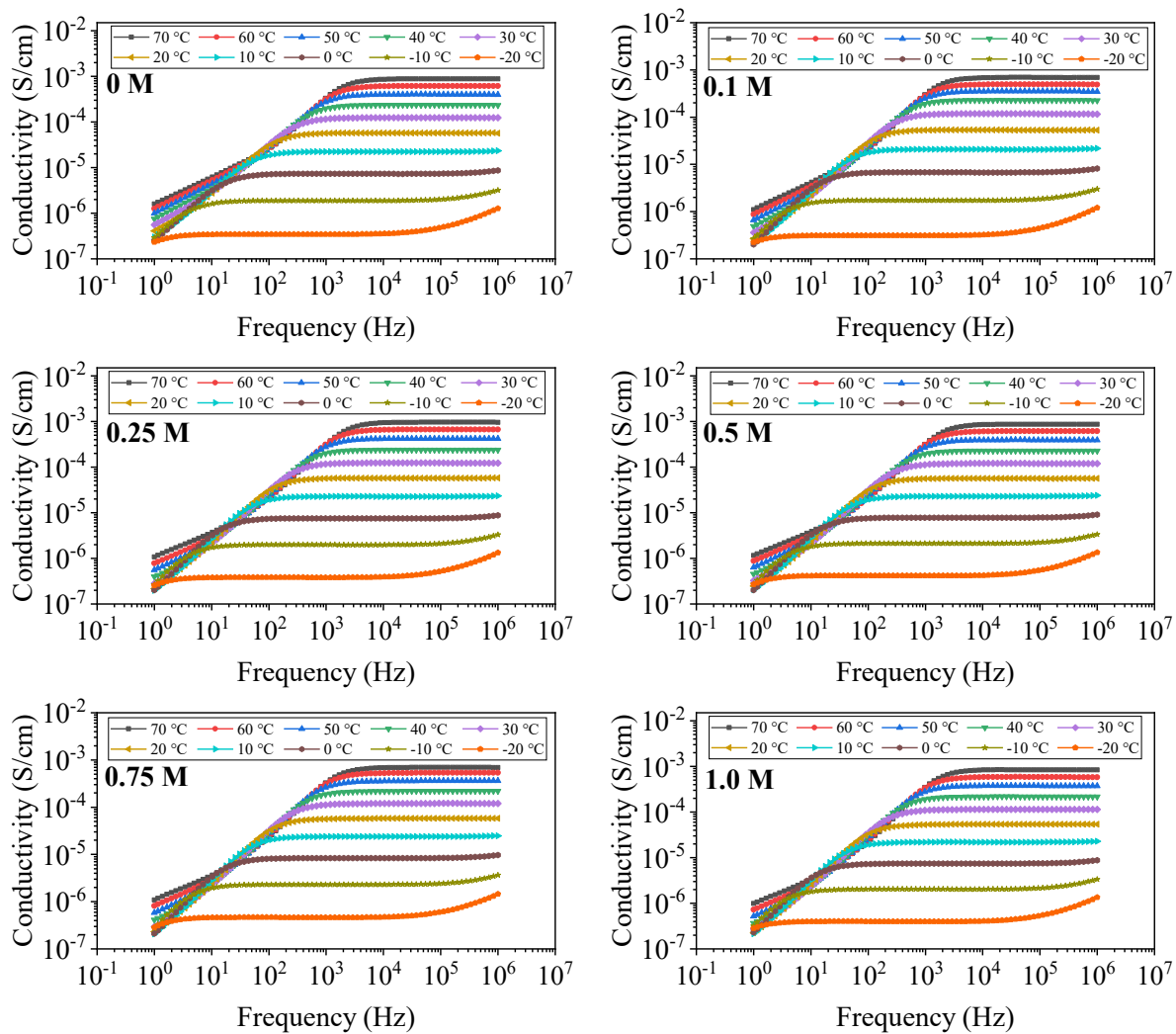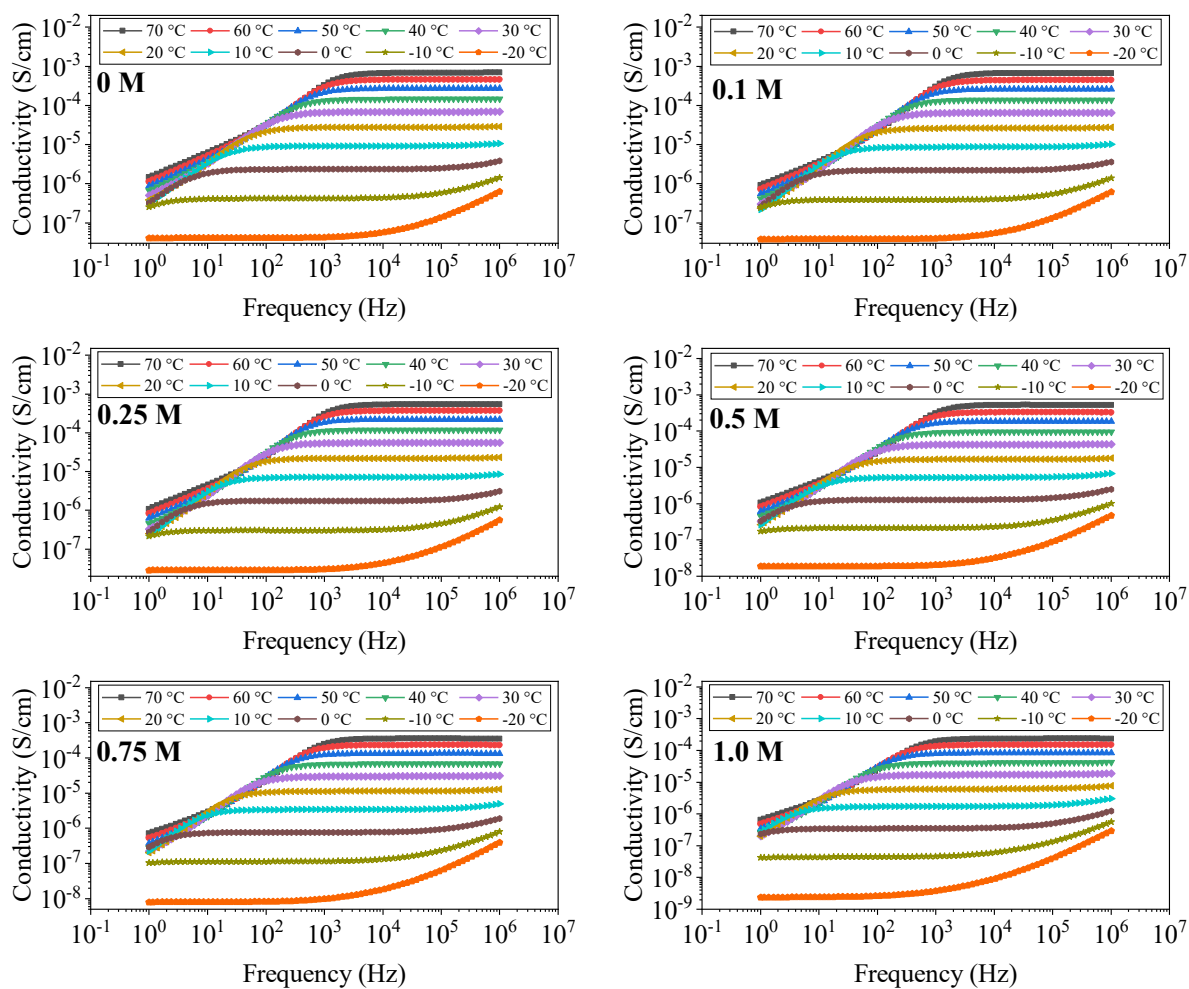
Figure S 44. BDS measurement of **NFIL-FSI** with different content of LiFSI in the temperature range of -20 to 70 °C.
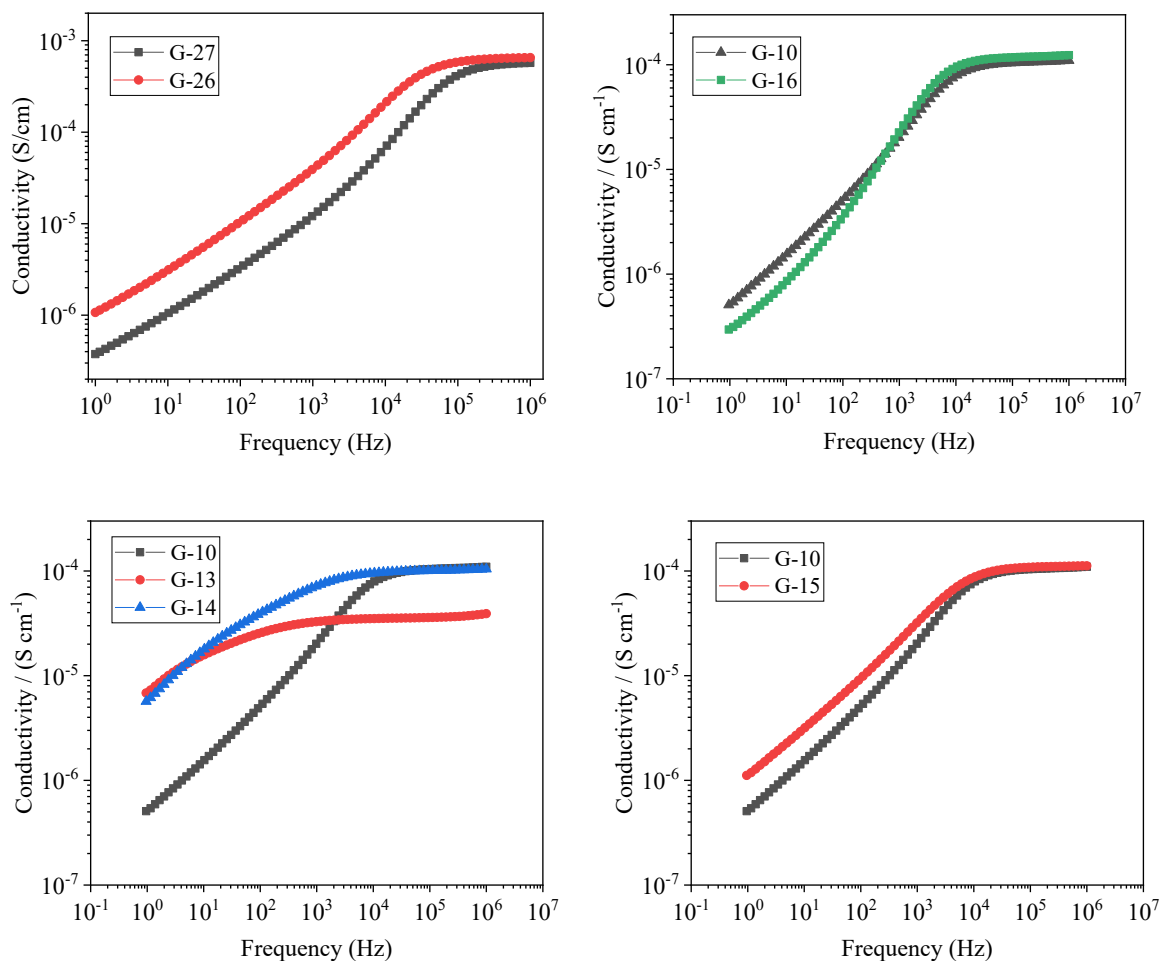
Figure S 45. BDS measurement of **NFIL-TFSI** with different content of LiTFSI in the temperature range of -20 to 70 °C.

Figure S 46 BDS measurements of selected gel compositions (**G - X**) at room temperature, the frequency range between 1 to 10^6 Hz.
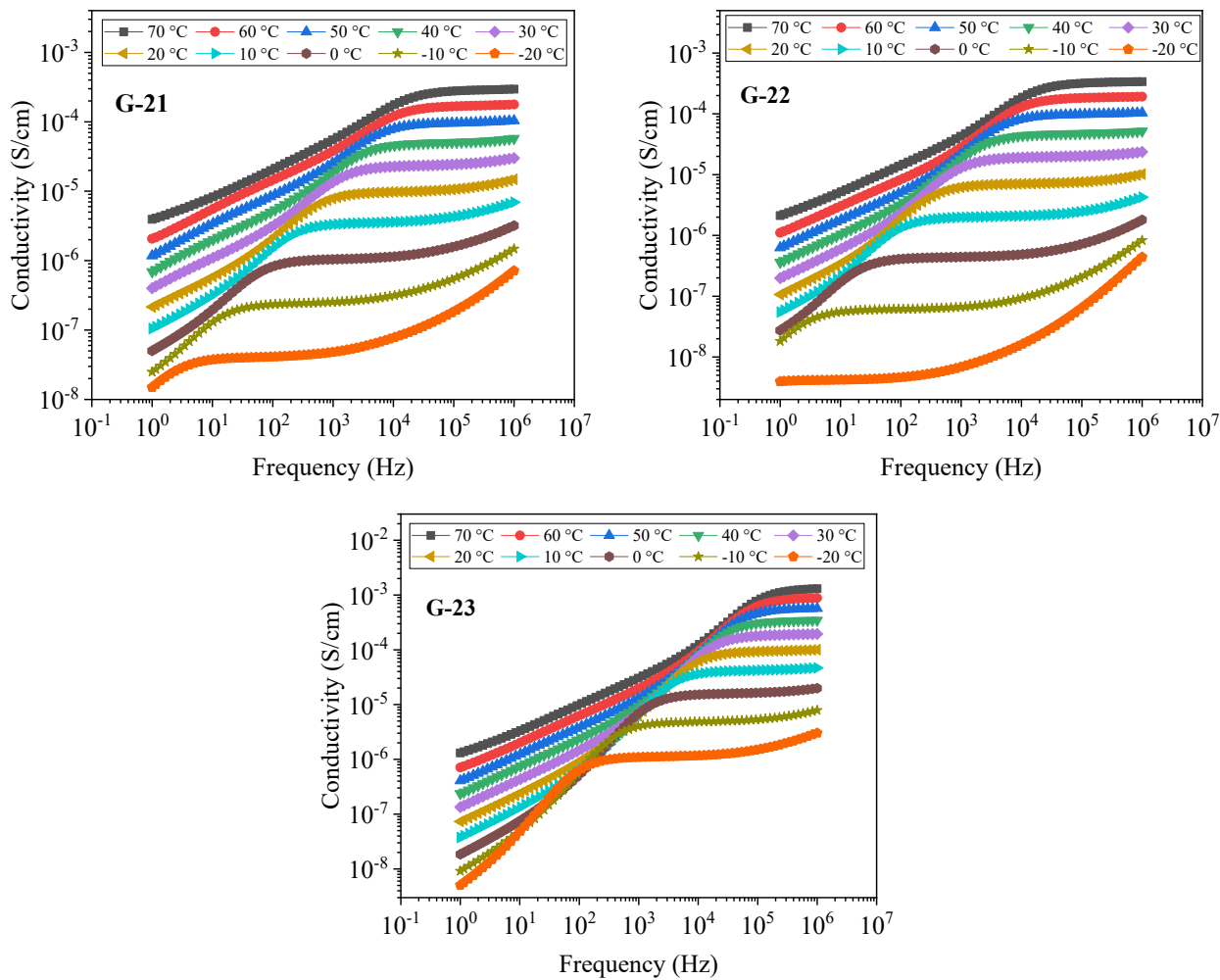
Figure S 47. BDS measurements of **G-21, G-22** and **G-23** in the temperature range of 0°C to 70 °C with 10 °C increments, the frequency range between 1 to 10^6 Hz.
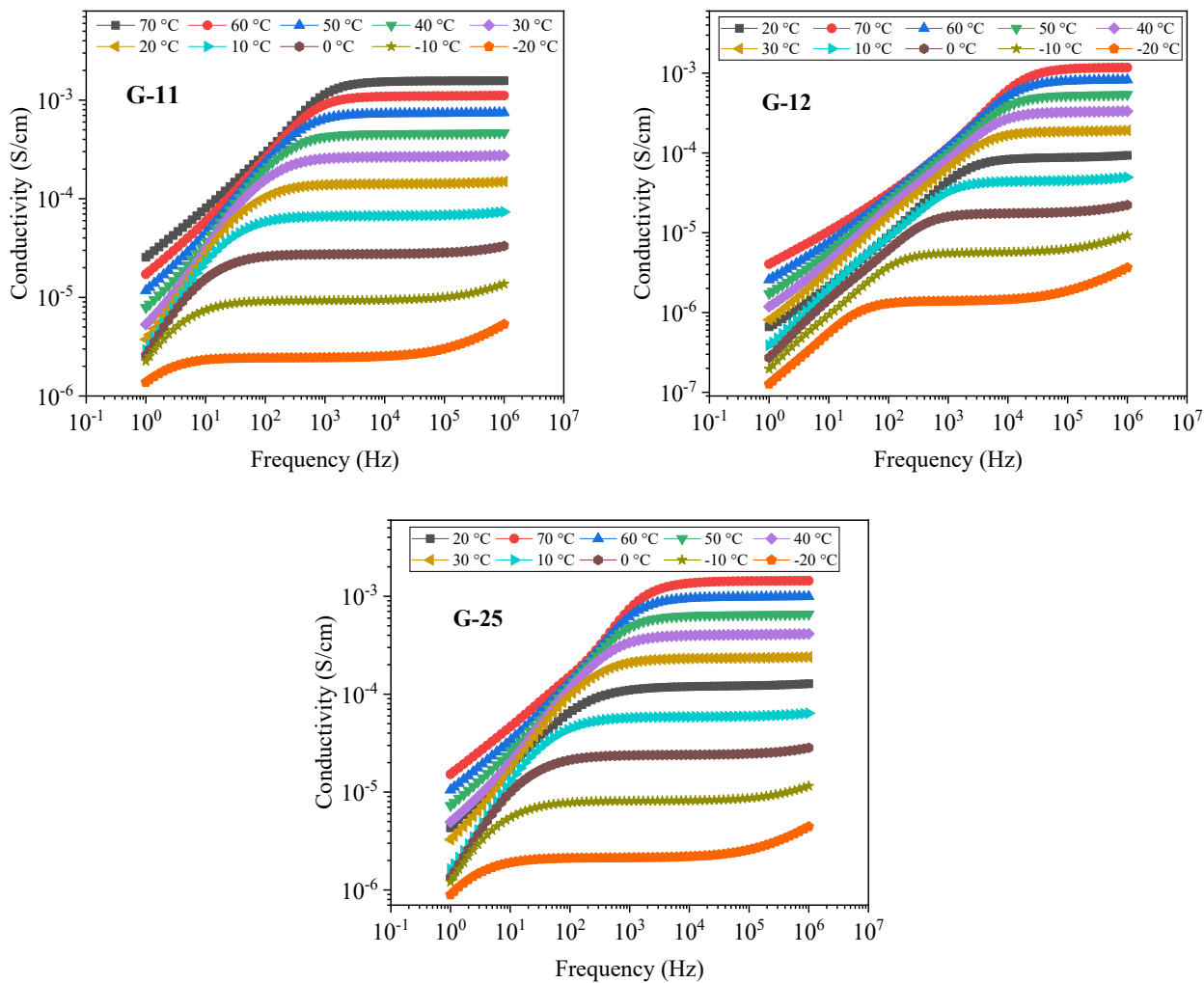
Figure S 48. BDS measurements of **G-11, G-12** and **G-25** in the temperature range of 0°C to 70 °C with 10 °C increments, the frequency range between 1 to 10^6 Hz.

Curriculum Vitae

Zviadi Katcharava

Address: Halle (Saale), Germany
Nationality: Georgian
Gender: Male

Work experience		
	12/2020 – Current	**University research assistant** *Martin Luther University Halle-Wittenberg*

This research was developed under the framework of the BAT4EVER (Autonomous Polymer based Self-Healing Components for high performant LIBs) project. This project has received funding from the European Union's Horizon 2020 research and innovation programme under grant agreement No. 957225.

City: Halle (Saale)
Country: Germany

06/2019 – 11/2020 **Student research assistant (HIWI)**
Martin Luther University Halle-Wittenberg

City: Halle (Saale)
Country: Germany

04/2018 – 09/2018 **Research assistant**
FUMATECH BWT GmbH

City: Bietigheim-Bissingen
Country: Germany

09/2017 – 04/2018 **Research assistant**
Agricultural University of Georgia

VW grant „Novel polymer Electrolyte Membranes for Fuel Cell Application" (Az:93 331)

City: Tbilisi
Country: Georgia

10/2016 – 04/2018 **Student research assistant**
Agricultural University of Georgia

Optimization of sulfonated poly(phenyl sulfone) synthesis (Collaborated with Max Planck Institute for Solid State Research)

City: Tbilisi
Country: Georgia

Education	12/2020 – Current	**PhD in chemistry** *Martin Luther University Halle-Wittenberg*
		City: Halle (Saale) Country: Germany
	10/2018 – 11/2020	**Master of Science (M.Sc.)** *Martin Luther University Halle-Wittenberg*
		Field(s) of study: Polymer Materials Science **Thesis:** Modification of nanocomposites and electrolytes 3D-printing
		City: Halle (Saale) Country: Germany
	09/2013 – 07/2017	**Bachelor of Science (B.Sc)** *Agricultural University of Georgia*
		Field(s) of study: Chemistry **Thesis:** Optimization of half sulfonated poly (phenyl sulfone) synthesis for fuel cell application
		City: Tbilisi Country: Georgia
	2001 – 2013	**General Education Diploma** **Public School N4**
		City: Rustavi Country: Georgia

Honors and awards	04/2018	**Study Scholarships for Graduates of All Disciplines** *German Academic Exchange Service (DAAD)*

Conferences	29/05/2023 – 01/06/2023	**Frontiers in Polymer Science 2023** *Gothenburg, Sweden*
		Oral presentation: Solvent-free vitrimeric poly(ionic liquid) electrolyte for Li-ion batteries
	09/05/2023 – 10/05/2023	**BATTERY 2030+ Annual Conference 2023** *Uppsala, Sweden*
		Poster presentation: Self-healing ionic-liquid-based electrolytes
	23/04/2023 – 27/04/2023	**14th Advanced Polymers *via* Macromolecular Engineering (APME23)** *Paris, France*
		Oral presentation: Vitrimeric poly(ionic liquid) electrolyte for Li-ion batteries
	20/06/2022 – 22/06/2022	**8th International Conference on Self-Healing Materials ICSHM-MILANO 2022** *Milan, Italy*
		Oral presentation: Self-healing poly(ionic liquid)-based iongels as potential electrolytes for lithium-ion batteries

13/06/2022 – 16/06/2022	**Bordeaux Polymer Conference (BPC 2022)** ***Bordeaux, France***
	Poster presentation: Novel 3D printable and self-healing electrolytes for Li-ion batteries
21/02/2018 – 23/02/2018	**Chemistry Conference for Young Scientists (ChemCYS 2018)** ***Blankenberge, Belgium***
	Poster presentation: Optimization of synthesis of half sulfonated poly(phenyl sulfone) – sPSO2-360

Languages

Georgian	Native language
English	Listening – C2; Reading – C2; Writing – C1; Speaking – C1;

Levels: A1 and A2: Basic user; B1 and B2: Independent user; C1 and C2: Proficient user

---

Digital Skills

Microsoft Office / ChemDraw / ChemSketch / OriginPro / MestreNova

Declaration

Hiermit erkläre ich an Eides statt, dass ich die vorliegende Arbeit selbstständig und ohne fremde Hilfe verfasst habe. Andere als die angegebenen Quellen und Hilfsmittel wurden nicht benutzt und die den benutzten Werken wörtlich oder inhaltlich entnommenen Stellen wurden als solche kenntlich gemacht.

Außerdem erkläre ich, dass ich die vorliegende Dissertation an keiner anderen wissenschaftlichen Einrichtung zur Erlangung eines akademischen Grades eingereicht zu haben.

Halle (Saale), den   _____

                                                                    Zviadi Katcharava